Development of grafting strategies for the polymer functionalisation of graphene

Yin-Nei Heather Au

Department of Chemistry, Imperial College London

2017

Submitted in partial fulfilment of the requirements for the degree of

Doctor of Philosophy of Imperial College London

Abstract

Graphene is well-known for its exceptional mechanical, electrical, and thermal properties, but its potential is yet to be fully realised in bulk applications due to difficulties in obtaining a large yield of high-quality individually-dispersed graphene sheets. In this thesis, reductive exfoliation of bulk graphite is demonstrated as a promising and versatile method which allows the isolation of single- and few-layer graphenes; the production of reduced graphene, or 'graphenide', solutions shows varying efficiency in different solvents. Subsequent functionalisation of graphenide dispersions with various electrophiles, including 1-bromododecane, anionic monomers such as methyl methacrylate, and bromine, results in increased solubility in organic solvents, without damage to the graphene basal plane. Exact characterisation and quantification of grafting is complicated by the presence of solvent remaining between graphene layers, a phenomenon which is not significant in other carbon nanomaterials. Reductive alkylation was carried out on five different graphitic starting materials including two types of natural flake graphite, shear-exfoliated graphite platelets, graphite nanofibres, and few-layer graphene. The study reveals pronounced differences in the obtained grafted species with respect to the degree of functionalisation and residual solvent, exfoliation efficiency and product homogeneity. These results are shown to be dependent on the size and nature of the starting material, with few-layer graphene showing the highest grafting ratios. Few-layer graphene was also functionalised with various molecular weight poly(methyl methacrylate) (PMMA) polymers by grafting-to and grafting-from approaches; the grafting ratios were higher for the grafting-from approach and the products showed a far greater dispersibility in acetone (up to 920 µg mL^{-1}). In parallel with these direct polymer-grafting strategies on few-layer graphene, the reduction method was used to dissolve and brominate few-layer graphene sheets, achieving direct covalent attachment of bromine to the graphene framework. The brominated few-layer graphenes provide a convenient, stable, liquid-phase precursor, suitable for the synthesis of a variety of directly functionalised graphenes. As an example, the brominated species was used to initiate atom transfer radical polymerisation, to obtain PMMA-grafted graphene, which was six times more dispersible in acetone than controls. In addition, brominated graphene is active for nucleophilic substitution reactions, as illustrated by the preparation of methoxypolyethylene glycol- and hydroxyl-substituted derivatives. Grafting ratios for these polymer-functionalised materials varied between 6 and 25% and all graphene derivatives showed increased solubility in organic solvents, highlighting the potential of this route for preparing large quantities of dispersed graphene with minimal damage to the carbon framework.

Contents

List of figures

List of schemes

List of tables

List of equations

List of appendix figures

List of appendix tables

Nomenclature and abbreviations

AFM	Atomic force microscopy
AIBN	Azobisisobutyronitrile
ATRP	Atom transfer radical polymerisation
BET	Brunauer-Emmett-Teller
BPO	Benzoyl peroxide
c	Concentration
C/R	Grafting density, number of graphitic carbons per grafted moiety
CNM	Carbon nanomaterial
CNS	Carbon nanosheet
CNT	Carbon nanotube
$C_{polymer}$	Surface concentration of polymer
CVD	Chemical vapour deposition
$Đ$	Dispersity
d	Interlayer spacing
D	Separation between polymers
o-DCB	1,2-Dichlorobenzene
DMAc	N,N-Dimethylacetamide
DME	1,2-Dimethoxyethane
DMF	N,N-Dimethylformamide
EDX	Energy dispersive X-ray spectroscopy
FLG	Few-layer graphene
FWHM	Full width at half maximum
GIC	Graphite intercalation compound
GNF	Graphite nanofibre
GNP	Graphite nanoplatelet
GO	Graphite/graphene oxide
GPC	Gel permeation chromatography
GR	Grafting ratio, the mass of grafted moiety relative to the mass of graphene carbon
GRM	Graphene-related materials
HOPG	Highly-oriented pyrolytic graphite
I_c	c-axis lattice spacing
K	Dimensionless shape factor used to determine crystallite size
L_c	Crystallite size in the c-axis direction
L_D	Interdefect distance
LFG	Large flake graphite
MMA	Methyl methacrylate

M_n	Number average molar mass
M_w	Weight average molar mass
MW	Molecular weight
N_A	Avogadro's number, 6.02×10^{23} mol^{-1}
Na/np	Sodium naphthalide
n_D	Theoretical number density of grafting
NFG	Natural flake graphite
NMP	*N*-Methyl-2-pyrrolidone
NMR	Nuclear magnetic resonance
PAA	Polyacrylic acid
PAMAM	Polyamidoamine
PAN	Polyacrylonitrile
PDMAEMA	Poly(dimethylaminoethyl methacrylate)
PEG	Polyethylene glycol
PMDETA	*N,N,N',N'',N''*-Pentamethyldiethylenetriamine
PMMA	Poly(methyl methacrylate)
RAFT	Reversible addition-fragmentation chain-transfer polymerisation
R_F	Flory radius
rGO	Reduced graphite/graphene oxide
S	Sensitivity factor, for calibration of MS signals to TGA mass loss
S_{BET}	Specific surface area
SEM	Scanning electron microscopy
STM	Scanning tunnelling microscopy
TEM	Transmission electron microscopy
TFAA	Trifluoroacetic anhydride
TGA-MS	Mass spectrometry-coupled thermogravimetric analysis
THF	Tetrahydrofuran
UV-vis-nIR	Ultraviolet-visible-near infrared spectroscopy
XPS	X-ray photoelectron spectroscopy
XRD	X-ray diffraction

1. Introduction

Intrinsically, ideal graphene has exceptional properties,[1] but the true benefits of this so-called 'wonder material' are yet to be manifested in many practical applications. Generally, progress has been limited by graphene production, hampered by considerations of cost and scalability, the sheet size and quality obtainable, and difficulties in processing and stabilising bulk quantities of material that retain the properties of interest.

Some approaches, including chemical vapour deposition and micromechanical cleavage, are suitable for thin film applications, but cannot produce quantities large enough for many industrial applications, such as in energy storage devices, biomedical imaging or composite reinforcement. Bulk exfoliation processes typically achieve only a low yield of true single-layer graphene,[2, 3] and often with framework defects which result in inferior properties.[4] Whilst not all applications require single layers, increasing thickness generally reverts to conventional graphitic properties. In any case, more homogeneous materials, through controlled processing techniques or size separation, are required. In some applications, pristine graphene is not actually preferable; one field where modified graphene may perform better is as a nanofiller in composite materials.[5, 6] Increasing the interfacial interactions between filler and matrix by covalent modification can reduce the size required for effective reinforcement.[7] Covalent functionalisation of graphene has been well-explored over the past ten years, drawing extensively from reactions on fullerenes and carbon nanotubes (CNTs).[8-10] A wide range of grafting strategies have been shown to be successful, but the inherent large, flat morphology of graphene sheets results in several problems which are not applicable to fullerenes and CNTs. Isolation of single layers is less straightforward since the van der Waals forces acting over larger areas, (and natural defects, depending on the bulk starting material,) prevent easy exfoliation, and often pre-treatment steps are required to first obtain dispersions of exfoliated graphene. In addition, graphene's lack of curvature, and therefore strain, result in a much lower reactivity.[11] This lack of curvature also presents issues in processing materials after functionalisation; close restacking of graphene layers upon drying prevents complete removal of reaction by-products or residual solvent, which can complicate characterisation and potentially affect subsequent applications.

Reductive functionalisation is a versatile, and non-damaging method which has shown promise in achieving exfoliation and functionalisation without the need for preliminary pre-treatment steps. Alkali-metal graphite intercalation compounds (GICs) have long been studied, but with the discovery of graphene in 2004,[12] new interest was sparked in using them

as graphene precursors. Electrostatic repulsion provides the driving force for exfoliation, and the anionic charge facilitates functionalisation to allow modification of graphene's intrinsic properties, without additional framework damage associated with other functionalisation routes. Much research has been conducted on optimising reaction conditions for grafting,[13-15] but further study is required. Careful control of charging conditions and concentrations have been shown to be crucial factors in balancing effective exfoliation and functionalisation.[13] Furthermore, the nature of the starting material can have a significant effect on the outcome of grafting; the relative reactivities of single- and few-layer graphenes and graphite, and the influences on location, density and homogeneity of grafting, are still poorly understood.

1.1. Aims, objectives and structure

This thesis addresses the development of the reductive functionalisation strategy as a route to obtaining a range of covalently-modified graphenes from various bulk graphite precursors, with enhanced solubility to facilitate processing and potential large scale production. Chapter 2 describes the existing research on graphene production and functionalisation, and the properties and applications of these graphene derivatives, focusing particularly on liquid phase exfoliation and wet chemical functionalisation, and especially, advances in reductive chemistry applied to single-layer graphene on substrate and to bulk materials. The existing charging protocol previously developed in the group showed success in alkyl grafting of natural flake graphite;[13] one aim of this thesis is to further refine the functionalisation method, with particular emphasis on exact characterisation and quantification of functionalisation. The effect of residual solvent trapping, a topic little discussed in the literature, proved to be critical and unexpectedly large. The method was extended to other graphite starting materials to investigate the effects of flake size and morphology on the grafting outcomes; this work is discussed in Chapter 5.

Achieving greater dispersibility is vital for practical processing in large-scale industrial applications. Alkyl grafting provides a useful model system for fundamental studies, but greater improvements in solubility can be obtained by careful selection of other grafting moieties, especially polymers. In this thesis, poly(methyl methacrylate) (PMMA) was selected for polymer grafting, because it is a well-studied anionic and atom transfer radical polymerisation (ATRP) target, and is also of practical interest as a compatibiliser for epoxy resins.[16, 17] Chapter 6 compares the grafting-to and grafting-from methods by reaction of charged graphenide species with activated pre-synthesised PMMA chains, or direct reaction with methyl methacrylate (MMA) monomer for anionic polymerisation. However, many other monomers and polymers of interest contain functionalities sensitive to reducing conditions; a complementary method is presented in Chapter 7, investigating a brominated graphene

intermediate as a precursor for ATRP or nucleophilic substitution, as a means of widening the scope of reactions accessible to graphenide chemistry. The characterisation techniques and experimental methods are outlined in Chapters 3 and 4, and additional material is provided in the Appendix, where applicable. Overall conclusions drawing together the themes of this thesis are presented in Chapter 8.

2. Literature review

This chapter addresses the recent literature concerning the main advances and challenges in graphene processing and functionalisation. The structure and properties of graphene are described, and methods of synthesis are discussed, focusing on liquid phase exfoliation and the use of graphite intercalation compound precursors. The role of different types of graphene in various applications is outlined, and methods of chemical modification are critically discussed, highlighting in particular the successes and shortcomings of previous reductive functionalisation approaches.

2.1. Carbon nanomaterials

Interest in the family of carbon nanomaterials was first sparked in 1985 by the discovery of buckminsterfullerene, a spherical molecule consisting entirely of carbon atoms (C_{60}).[18] Other fullerene derivatives, such as C_{70} and C_{80},[19, 20] closely followed, and, with the discovery of multi- and single-walled carbon nanotubes,[21, 22] cemented the status of carbon nanomaterials as a significant material of interest. Graphene, the 2D allotrope of the carbon family, had been much studied theoretically, and there exists over one hundred years of graphite research, but it was not until 2004 that single-layer graphene was first isolated, by the 'Scotch tape' method employed by Novoselov and Geim.[12]

2.1.1. Structure and properties of graphene

Graphene is the structurally simplest member of the carbon family, and can be thought of as a single graphitic layer, composed of sp^2 carbons arranged in a hexagonal lattice (Figure 2.1). Multiple layers of graphene make up the 3D structure graphite, which may be classified as Bernal (or hexagonal), rhombohedral or turbostratic, depending on the exact arrangement of stacking.[23]

With such exceptional properties as its large surface area, high intrinsic carrier mobility (200,000 cm^2 V^{-1} s^{-1}), thermal conductivity (5000 W m^{-1} K^{-1}), and tensile strength (1 TPa),[1, 24] much research and speculation has been stimulated over its potential applications. Unfortunately, graphene production remains a large challenge, and due to a lack of careful nomenclature,[23, 25] many examples of 'graphene' described in the literature, or which are sold commercially, are often mixtures of few- or multi-layer graphene stacks, or else contain oxygen functionalities or defects. However, these graphene-related materials (GRMs) have also shown significant worth in numerous fields depending on the specific application, since the

number of layers, stacking arrangement, lateral size, and functionality of the graphene material all influence the material properties. Still, in many areas, the full potential of graphene is yet to be realised due to the challenges in bulk production and processing. Chemical modification of graphene has been explored as a means of overcoming these limitations, and many chemistries that have shown success for fullerene and CNT functionalisation have been extended to graphene.[9, 26, 27] Unlike other carbon nanomaterials (CNMs), however, graphene is completely flat and therefore does not exhibit any strain associated with the curvature in fullerenes and CNTs; this lack of strain results in a lower reactivity compared to other CNMs, presenting yet another challenge.[8]
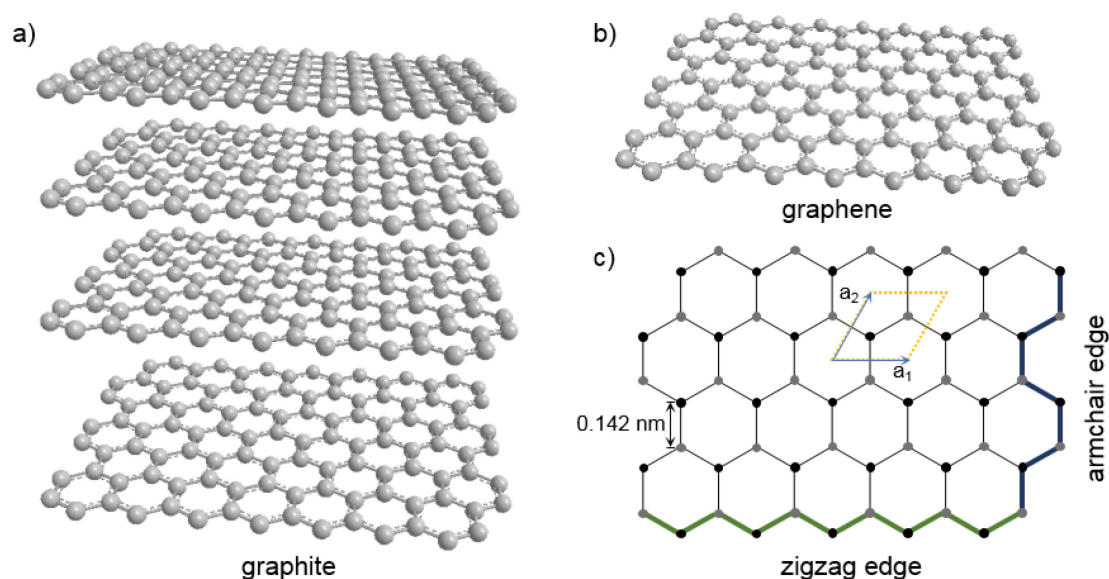
Figure 2.1. Schematic representation of a) graphite, and b) graphene; c) graphene lattice with unit cell containing inequivalent carbon atoms (black and grey) and unit vectors a_1 and a_2 indicated; armchair and zigzag edges drawn in blue and green, respectively.

2.2. Graphene synthesis

A large number of methods have been developed to produce single- and few-layer graphene, and can be categorised as either bottom-up or top-down approaches. Bottom-up techniques such as chemical vapour deposition or epitaxial growth can yield high-quality graphene, with few defects, which has potential for use in electronic devices.[28, 29] However, these substrate-based techniques are not well-suited to large-scale production, and cannot meet the demands of applications requiring large quantities of graphene. Large-scale, inexpensive production of graphene has been demonstrated using top-down approaches, where graphene is produced by direct exfoliation of graphite, by both mechanical and chemical methods.[2, 3, 30] In all fields, the method of graphene synthesis selected for a particular application must take into consideration the cost, scale, processing and quality of graphene obtainable (Figure 2.2).
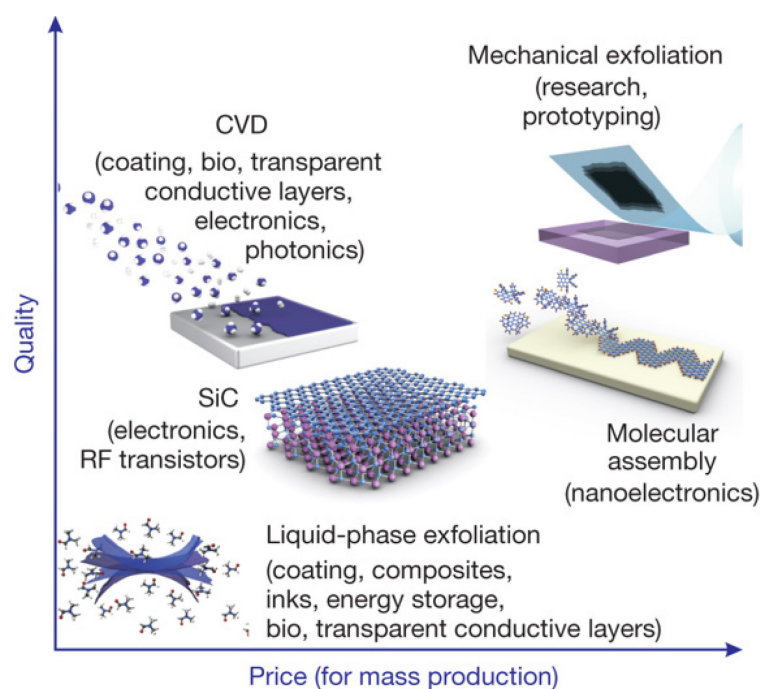
Figure 2.2. Various methods for mass production of graphene, which allow a wide choice in terms of size, quality and price for any particular application.[1]

2.2.1. Bottom-up synthesis

Chemical vapor deposition (CVD) techniques have been used to grow thin and highly crystalline graphitic layers on the surfaces of transition metal catalysts.[28, 31] At elevated temperatures, methane or other volatile hydrocarbons are decomposed on metal substrates, such as Ni or Cu, to produce graphene.[29] Large area films, up to 30 inches,[32] of single- and few-layer graphene can be achieved by this method, but uniform growth is still a challenge. Epitaxial growth of graphene on a hexagonal substrate is achieved by annealing, typically, silicon carbide at temperatures as high as 1500 °C under ultra-high vacuum, causing Si to sublime, leaving a carbon-rich surface.[33, 34] Total synthesis of atomically-precise graphene nanoribbons has also been achieved using surface-assisted coupling followed by dehydrogenation, using a gold single crystal as a template.[35] With these methods involving growth on substrates, subsequent transfer of the produced graphene to insulating surfaces typically requires first depositing a protective polymeric coating on the graphene layer, followed by etching away of the metallic substrate.[29] While these growth methods are useful for applications in high-performance graphene electronics, the generation of bulk scales of few-layered graphene for other applications remains problematic. Various modified plasma-enhanced CVD methods have been used to grow few-layer graphene nanosheets, in large quantities, from carbon precursors including methane,[36, 37] Kapton polyimide,[38] or even waste coffee grounds,[39] at relatively low temperatures compared with traditional CVD (Figure 2.3).

The resulting graphene sheets are composed of wrinkled few-layer turbostratic stacks, with a very low oxygen content; furthermore, they demonstrate good electrical conductivity and high specific capacitance, and could be useful for potential applications in electrochemical energy conversion and storage devices. Disproportionation of carbon monoxide catalysed by small iron-containing particles results in carbon filaments composed of continuously stacked graphitic layers, with the graphene layers lying perpendicular to the filament axis.[40] However, these filaments require further processing in order to isolate single layers.
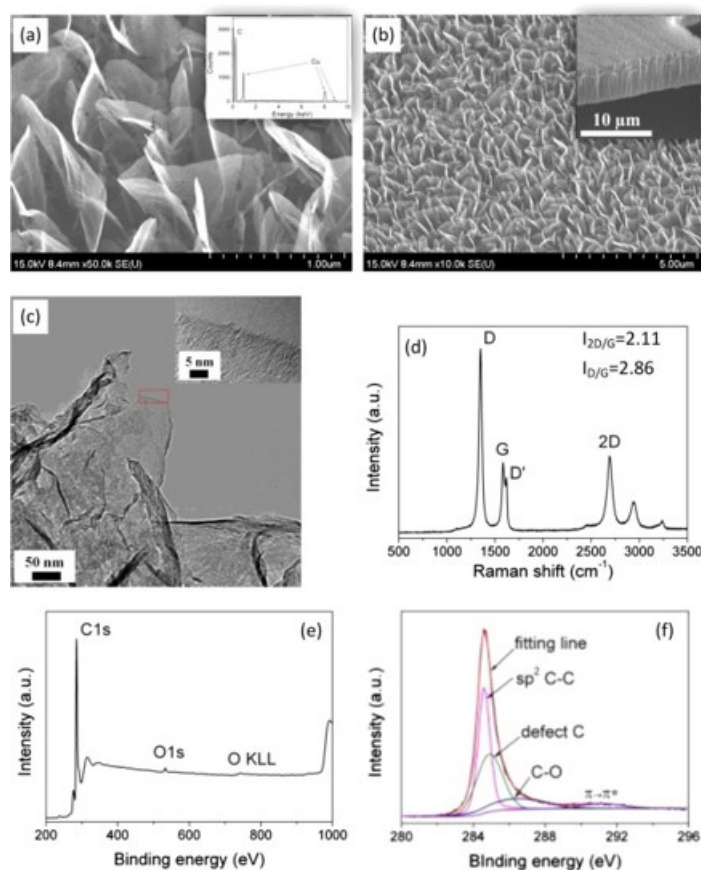
Figure 2.3. Carbon nanosheets (CNSs) grown by microwave plasma treatment. a) High- and b) low-magnification SEM images of vertically-aligned CNSs on the Cu substrate from Kapton PI film as carbon source under Ar/H$_2$ plasma irradiation. Inset in a) and b): EDX pattern and cross-sectional SEM image of vertically-aligned CNSs, respectively. c) Typical TEM image of as-synthesized CNS. Inset: TEM image of a five-layer graphene edge. d) Raman spectrum of the CNS. e) Survey scan and f) C1s curve fitting of XPS spectra of the CNSs.[38]

2.2.2. Top-down synthesis

The exfoliation of graphite to produce graphene is a far more attractive option for large-scale applications. Natural flake graphite is in plentiful supply, making it an ideal starting material for industrial processes. Many starting synthetic graphites are available for use as a precursor for exfoliated graphene, including the carbon filaments and few-layer graphene described

previously (section 2.2.1), pyrolytic graphite, formed by cracking hydrocarbons at high temperature and subsequent heat treatment, or kish graphite, obtained by the crystallisation of carbon from molten steel during the steel manufacturing process. Whilst the first isolation of graphene was achieved by micromechanical cleavage, top-down exfoliation is most commonly achieved in the liquid phase, by mechanical, chemical or electrochemical means, allowing facile subsequent processing and extension to large-scale applications.

2.2.2.1. Micromechanical cleavage

The first isolation of graphene in 2004 was achieved by the 'Scotch tape' method.[12] Repeated cleavage yields mono-, bi- and few-layer graphene flakes, which can be identified by optical microscopy on specially prepared SiO_2(300 nm)/Si substrates, and Raman spectroscopy[41] (Figure 2.4). This mechanical process results in high-quality large graphene flakes, useful for fundamental study, but the extremely labour-intensive and time-consuming process is impossible to scale up for industrial applications.
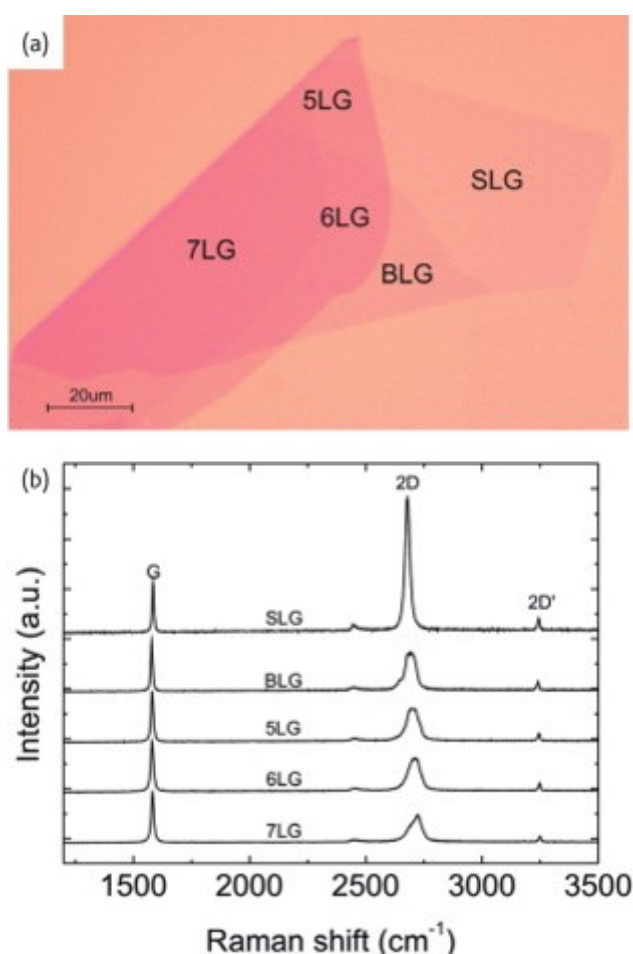
Figure 2.4. a) Optical micrograph of mechanically-cleaved flake, consisting of regions of different thicknesses; b) evolution of Raman spectra with the number of graphene layers. The spectra are normalised to the G peak intensity.[42]

2.2.2.2. Ball milling

Shear force can be exploited for the exfoliation of graphite into graphene. Ball milling is a common technique and can be conducted in wet or dry conditions.[30] In the presence of a 'good' solvent, one which has a matched surface energy with graphene flakes,[30] or surfactant in aqueous solution, a reasonable degree of exfoliation may be achieved. The addition of small aromatics as exfoliating agents, such as melamine[43] or naphthol polyoxyethylene ether,[44] can further promote exfoliation by intercalation into the graphite layers. Dry ball milling can be carried out by mixing with chemically inert, water-soluble inorganic salts,[45] which may be washed away after milling, and is often used as a means of functionalisation.[46, 47] However, ball milling typically requires long processing times, and fragmentations and defects are unavoidable. Furthermore, the resulting sheets generally require post-processing sonication steps to obtain useful graphene dispersions. The defects introduced by the high-energy collision of grinding media are not clearly defined; ball milling could be a suitable method for large-scale production of graphene, depending on the sensitivity of the subsequent application to the quality of graphene produced by these means.

2.2.2.3. Shear mixing

Based on a high-shear rotor-stator mixer, shear-assisted large-scale exfoliation of graphite was possible to produce dispersions of graphene flakes in *N*-methyl-2-pyrrolidone (NMP) and aqueous surfactant solutions,[48] or in IPA-water mixtures.[49] The graphene flakes in IPA-water had lateral sizes of 1-450 nm, with 62% of the nanosheets having a thickness of less than 1 nm.[49] The NMP or aqueous surfactant systems yielded flakes of a larger lateral size, between 300 and 800 nm, thicknesses of fewer than ten layers, and showed no evidence of oxidation.[48] The yield for this process is extremely low at <0.1%, but by recycling graphitic sediment, at least 3% of the starting graphite was transformed into graphene. A minimum shear rate was determined, below which, exfoliation to graphene could not be achieved. Cavitation and collision occurring inside the vessel also assist exfoliation, but this method is shear-force dominated, with exfoliation mainly localised in the vicinity of the rotor-stator.[30] To overcome the shortcomings of these localised high-shear regions, the method was extended to the use of a commercial kitchen blender to generate full turbulent flow. In a kitchen blender, the high-shear region is not localised in any single region of the blender.[50, 51] The exfoliation efficiency was much higher than for conventional rotor-stator systems, reaching a concentration of 0.22 mg mL^{-1} in *N*,*N*-dimethylformamide (DMF), and a yield of 7.3%,[51] in relatively short times compared to standard sonication procedures,[50] and could prove a cost-effective means of large scale graphene production.

2.2.2.4. Sonication

Sonication-assisted liquid-phase exfoliation of graphite is a very commonly-used technique to obtain graphene, with potential for large-scale production. During ultrasonication, shear forces and cavitation, the formation and collapse of micron-sized bubbles, act on the bulk material to induce exfoliation.[3] After exfoliation, the solvent-graphene interactions need to balance the van der Waals attractive forces between flakes, and therefore suitable solvents are chosen based on their ability to stabilise individualised graphene flakes. Coleman *et al.* first reported high-yield production of graphene by sonication-assisted liquid-phase exfoliation in 2008.[52] Graphite powder was dispersed in various organic solvents including DMF and NMP followed by sonication and centrifugation. Whilst an overall monolayer yield of ~1 wt% was initially obtained, repeated recycling of the sediment allowed yields of 7-12 wt% to be reached. The method is relatively simple, but hindered by the extremely low concentration of graphene (~0.01 mg mL^{-1}) which makes the approach less practical. Much research has built on this study, to achieve higher concentrations by, for example, increasing the initial graphite loading,[53] solvent exchange methods,[54] or prolonging sonication time.[55] Sonication for 460 hours resulted in concentrations of up to 1.2 mg mL^{-1} in NMP, and an overall yield of 4 wt% monolayers, but such a time-consuming process requires much energy, and the flake size was shown to reduce considerably with increasing sonication time. Successive sonication and centrifugation steps have been used as a means of flake size separation,[56] and to increase graphene yield (Figure 2.5); removal of unexfoliated material after centrifugation and redispersion of the few-layer fraction resulted in solutions of 63 mg mL^{-1}. Whilst some sedimentation occurred, an extremely high concentration of 28 mg mL^{-1} of the dispersed graphene was found to be indefinitely stable.[57] The addition of surfactants, such as sodium cholate, yielded concentrations up to 0.3 mg mL^{-1} in water, with an estimated 20% single-layer flakes.[58] Polymers are also useful for aiding graphene stabilisation in water[59, 60] and a range of organic solvents;[61, 62] in one study, graphene solutions in CHCl$_3$ and tetrahydrofuran (THF) stabilised with hyperbranched polyethylene resulted in reasonable initial concentrations (0.18 mg mL^{-1} and 0.045 mg mL^{-1}, respectively), but these dispersions could be further concentrated by solvent evaporation to give stable solutions with concentrations as high as 3.4 mg mL^{-1}.[63] Whilst the use of surfactants and polymers can significantly enhance graphite exfoliation, the main disadvantage of these additives is that they are difficult to remove, which may cause difficulties in subsequent applications, particularly in the field of electronics.
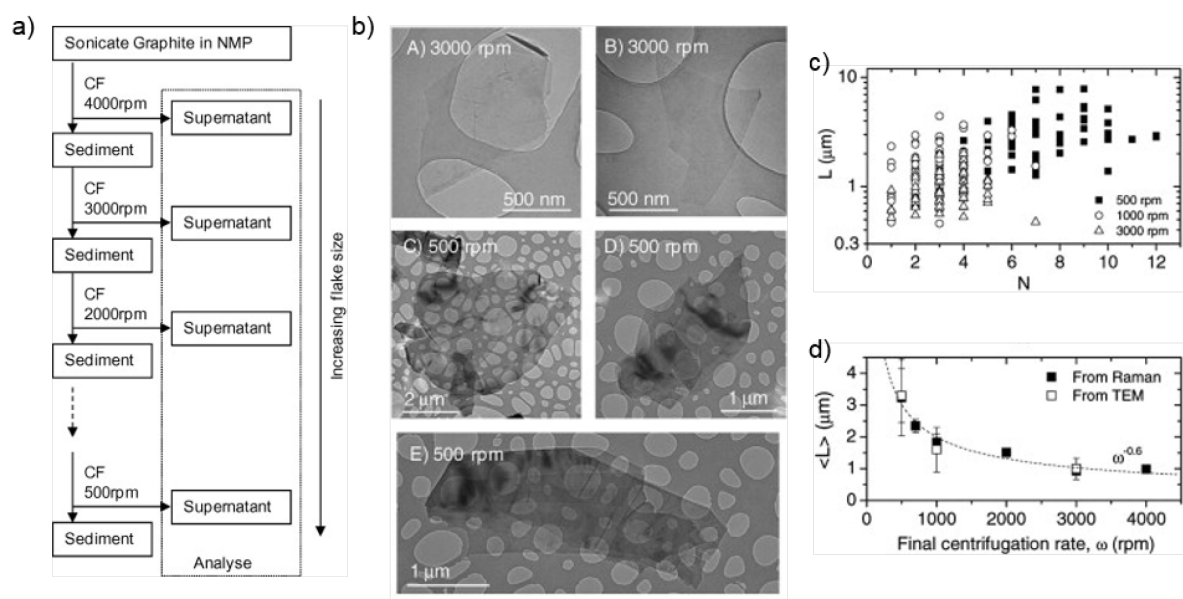
Figure 2.5. a) Schematic representation of flake separation by sonication and centrifugation; b) TEM images of flakes prepared at final centrifugation rates of 3000 rpm (A,B) and 500 rpm (C-E); c) individual flake length plotted versus estimated flake thickness (number of monolayers, N) for dispersions with final centrifugation rates of 500, 1000 and 3000 rpm; d) mean flake size as measured from TEM images, and estimated from Raman. Adapted from ref 56.

The surface energy of the solvent is an important factor when considering stable graphene dispersions. Whilst the van der Waals attraction between graphene layers is traditionally viewed as a weak force, the interaction is strong enough over a significant area to make complete exfoliation to monolayers challenging. The enthalpy of solvent and graphene mixing can be decreased by selecting solvents with surface energies similar to graphene. In graphite, the surface energy is defined as the energy per unit area required to overcome the van der Waals forces when peeling two layers apart, and has a literature value of ~70-80 mJ m^{-2}.[64-66] A study comparing the dispersibility of graphite in a wide range of solvents quantified the amount of graphite flakes dispersed as a function of solvent surface energy (calculated from surface tension), and found that the dispersed concentration showed a strong relation with solvents with a surface energy close to that of graphite, corresponding to a surface tension of 40-50 mJ m^{-2}.[52] Solvents with surface tensions close to this value were therefore predicted to be the best for dispersing graphene flakes. A subsequent study measuring the dispersibility of graphene in 40 solvents calculated the Hildebrand and Hansen solubility parameters, and found that the best dispersibility was achieved in solvents with parameters closest to these values.[67] However, these results were obtained over short sonication times and at room temperature; the surface energy and surface tension are expected to change at elevated temperatures, as prolonged or intensive sonication may induce degradation, altering the solvent's properties.[30]

As well as solvent damage, recent focus has been concentrated on the defects which are inadvertently introduced on the graphene surface. Intensive sonication at high power is a relatively harsh process and can produce areas of localised extreme temperature and pressure, which can cause significant damage to the graphene sheets. Sonication-exfoliated graphene flakes were probed by XPS, revealing a high oxygen content, comparable to that in graphene oxide (GO).[68] Strong buckling of the graphene sheets was visualised by scanning tunnelling microscopy (STM); highly disordered regions arranged in a patchwork around areas of pristine graphene were attributed to the presence of oxygen functionalities, but also contamination by adventitious species trapped between graphene layers, which prevent restored AB stacking.

The effect of sonication time and power on the oxygen content in exfoliated graphene was investigated by sonication in organic solvents NMP and 1,2-dichlorobenzene (o-DCB).[69] Defects and oxygen functionalities were found in the form of carboxylic acids and ethers/epoxides covering the graphene lattice. In contrast, a similar work which dispersed liquid-exfoliated graphene in water found that the oxygen-containing groups were mainly attached to the edges and hole-like defects in the basal plane.[70] A later study reported that the localisation of defects is strongly dependent on the sonication time;[71] for short sonication times, defects are located mainly on the sheet edges, whilst for sonication times above two hours, defects build up in the basal plane. These results contrast with other studies which assert the production of disorder-free or defect-free graphene, only characterised by non-statistical transmission electron microscopy (TEM) and Raman sampling.[72] The effects of sonication are also very specific to the particular conditions, for example, flask shape, probe depth, volume, concentration, power; a recent publication from Coleman et al.[73] aims to provide greater clarity on this liquid phase exfoliation process, to facilitate reliable reproducibility.

2.2.2.5. Graphene oxide and reduced graphene oxide

Oxidation can be achieved by various methods and is commonly used to exfoliate graphite.[74] The resulting highly-functionalised graphene sheets are defective, and therefore insulating, but the oxygen functionalities are often useful for subsequent chemical transformations. Partial recovery of the graphitic lattice may be achieved by chemical or thermal reduction. These functionalisation processes are discussed in more detail below in section 2.4.1.

2.2.2.6. Exfoliation of graphite intercalation compounds

GICs are formed by the insertion of atomic or molecular species, such as alkali metals or acid molecules, between graphene layers in a graphite host material, in a periodic arrangement.[75]

They can be classified in terms of the number of graphene layers separating two intercalant layers, known as their 'staging' index, n. For example, in a stage 1 GIC, every graphene layer is sandwiched by intercalant layers, whilst in a stage 2 GIC, there are two adjacent graphene layers between each intercalant layer, and so on (Figure 2.6). Intercalation thus results in an increase in the graphite interlayer spacing, with weakened van der Waals interactions between graphene sheets. The c-axis lattice spacing I_c depends on the staging index and is given by the following equation:

$$I_c(\text{Å}) = d_s + 3.35(n - 1) \tag{2.1}$$

where n is the stage number, and d_s is the sandwich thickness, representing the distance separating two graphene layers between which an intercalate layer is sandwiched. The effective thickness of the intercalate layer d_i is obtained by subtracting the interlayer distance of the host graphite $d_G = 3.35$ Å from d_s.[75]
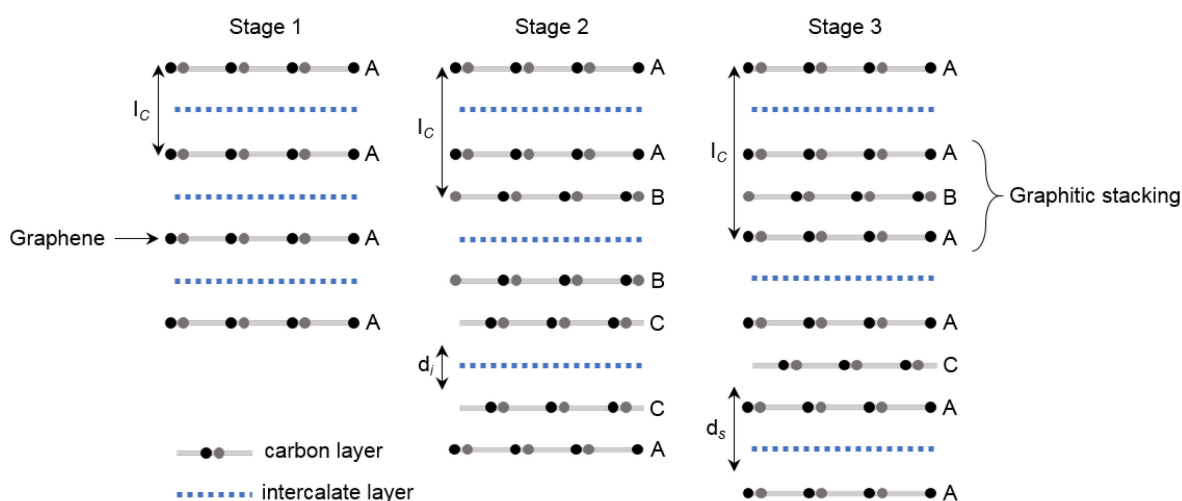
Figure 2.6. Stage structure of graphite intercalation compounds. The c-axis lattice spacing, I_c, sandwich spacing d_s, and intercalate thickness d_i, are labelled.

GICs have a long history in the literature, with the first reported synthesis of a potassium intercalation compound in 1840,[76] and the first staging classifications by X-ray diffraction in 1931.[77] There has been much interest in these materials because depending on the nature of the intercalant and staging index, GICs can exhibit a wide variety of electrical, thermal and magnetic properties.[75] Graphite can behave as both an electron donor and acceptor, as illustrated in the following reactions:

$$xC + D \rightarrow D^+ C_x^-$$

$$xC + A \rightarrow C_x^+ A^-$$
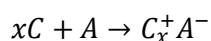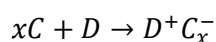
where *C*, *D*, and *A* are graphite, donor and acceptor, respectively.[78] A very large number of reagents have been intercalated into graphite, including alkali metals, alkaline earth metals, halogens, transition metal chlorides and acids; these intercalants are commonly classified according to whether they form donor or acceptor compounds.[75, 78] In general, both chemical affinities and geometric constraints associated with the intercalant size and bonding distances determine whether or not a given species will intercalate.

Synthesis of GICs is possible with solid, liquid or gaseous reagents.[42] Preparation using vapour transport with the two-zone method is the most common for obtaining well-staged specimens. Typically, the intercalant and graphite are heated at different temperatures; this temperature difference governs the staging of the resultant GIC.[79, 80] Both donor and acceptor compounds have been prepared by this method, including potassium,[79] Br_2,[81] and $FeCl_3$.[82] A modified method, involving isothermal heating of graphite and intercalant, has been used to prepare acceptor compounds intercalated with, for example, $FeCl_3$[83] or AsF_5.[84] In these procedures, the growth time is the principal parameter to control the staging. Another means of controlling the stage index is to restrict the amount of intercalant inside the reaction vessel; a number of well-staged compounds have been prepared by this method, intercalated with $AlCl_3$.[85]

Liquid intercalants are also useful for the preparation of certain intercalation compounds. For some alkali metals, direct contact with the molten metal under inert atmosphere results in well-staged GICs.[86, 87] Immersion of graphite into solutions containing reactants is used to obtain graphite-bromine compounds in CCl_4[88] and various metal chlorides in solvents such as acetone, nitromethane or $SOCl_2$.[75] One study explored the intercalation and de-intercalation of ammonium persulfate and showed that both phenomena occurred in wavefronts propagating through the flakes.[89] Raman spectroscopy and optical microscopy were used to monitor the transformation from a bright blue, characteristic of a stage 1 compound, through a range of colours to metallic grey, for stage 2, accompanied by mechanical deformation, supporting the Daumas-Herold theory of intercalant 'island' structures[90] (Figure 2.7).

In general, although liquid intercalation is convenient, it is difficult to prepare well-defined stage compounds by this technique. For donor intercalants such as the alkali metals, ternary intercalation compounds can be formed with the addition of a third, often solvent, species. Metals dissolved in liquid ammonia result in ternary intercalation compounds with ammonia co-intercalated between the graphene layers;[91-94] other organic solvents can also be incorporated into the GIC structure, including THF, 1,2-dimethoxyethane (DME), and alkyl amines.[95-99] Often a charge transfer agent such as naphthalene or anthracene is added to the reaction to facilitate the intercalation process.[13, 96, 97] The size of the coordination complexes

formed by alkali metal ions and solvent molecules results in a large expansion of the graphite layers to accommodate these species. The addition of specific chelating molecules such as crown ethers[100] or cryptands[101] can further enhance this effect.
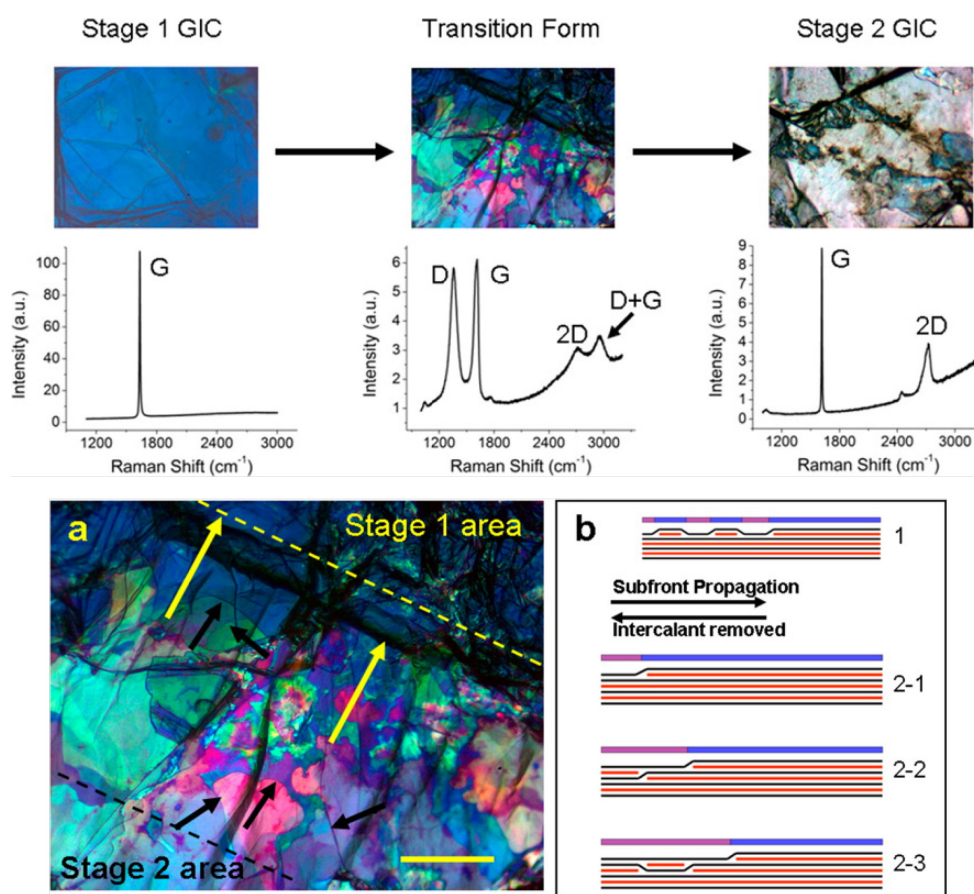
Figure 2.7. Top: study of the transition from stage 1 to stage 2 in graphite sulfate, by optical microscopy and Raman spectroscopy. Bottom: image of the transition zone (scale bar is 50 μm) and schematics of the stage transition for the subfront propagation. The black lines are the carbon layers; the red lines are the layers of intercalant. Adapted from ref 89.

Interestingly, while sodium on its own does not intercalate graphite to any great extent,[102, 103] forming only high stage compounds,[78] low and well-defined stage ternary compounds containing sodium can be readily formed, either as an alloy with Cs or K,[75] or with solvent molecules such as THF.[97] Furthermore, hydrogen, oxygen, sulfur, mercury and arsenic can be incorporated into GICs in the presence of alkali metals.[78] Similar to sodium, chlorine does not intercalate as a binary compound, but can intercalate as a mixture with bromine or iodine.[75] One explanation as to why some species cannot intercalate in low stage compounds is the in-plane lattice mismatch between the layers of graphite and the solid intercalating species; co-intercalation can improve the lattice match, thereby promoting the intercalation process.[75] Intercalation can also be achieved electrochemically, described below in section 2.2.2.7.

GICs are important and useful materials in many applications. Graphites intercalated with antimony pentafluoride or arsenic pentafluoride have shown potential as highly conductive materials, reaching higher σ (6.3×10^5 S cm^{-1}) than bulk Cu (5.9×10^5 S cm^{-1}).[104] GICs can also be superconducting,[105] whilst a large interlayer spacing is promising for hydrogen storage.[106] In commercial applications, Li-ion GICs have found particular use in batteries.[78, 107] With the sudden growth in graphene research since 2004, there has been renewed interest in GICs as possible precursors to graphene. Because the intercalation process increases the graphite interlayer spacing, especially in low stage index GICs, they are promising starting materials to produce graphene. Exfoliation of GICs can be achieved by methods such as thermal expansion, either induced by rapid heating,[108] or by microwave irradiation.[109] Heating of GICs generally causes thermal decomposition of the intercalants into gaseous species which then expand the space between the graphene sheets as they escape from the interlayer galleries (Figure 2.8). 'Expanded graphite' is used in many industrial applications, more recently as a means to produce graphene. A very common precursor for commercially available 'expanded graphite' is graphite intercalated with strong acids, usually graphite bisulfate.[110] Rapid thermal heating or microwave irradiation have been used to exfoliate a variety of other GIC precursors, including graphite intercalated with Li- or K-THF,[108, 111, 112] FeCl$_3$,[109] and strong acids.[113, 114]
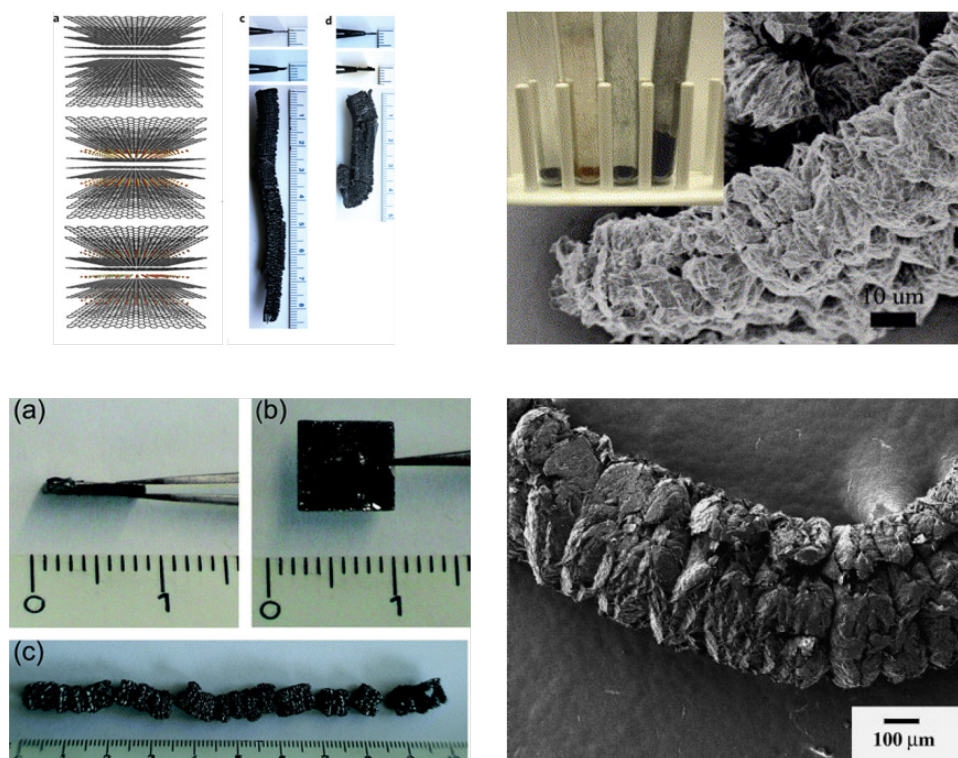
Figure 2.8. Exfoliated graphene obtained by thermal or microwave expansion of GICs. Adapted from refs 110, 112, 113, 115.

Generally these expanded materials require washing to remove intercalant residues,[108] and extra solution processing, most often sonication[109, 110] or further stabilisation with surfactant.[111] However, full characterisation of the products is either lacking, or else shows the existence of a mixture of flake thicknesses,[110, 114] and in some cases, defects introduced by oxidation.[113] One exception is the thermal expansion of stage 2 and stage 3 GICs intercalated with IBr and ICl, and subsequent dispersion, which showed a remarkable degree of layer-thickness control, with 40% bilayer and 35% 3-4 layer flakes, as determined by Raman spectroscopy.[115]

Both acceptor and donor GICs have also been directly exfoliated in solution. Graphite intercalated with sulfuric acid and ammonium persulfate does not spontaneously exfoliate,[116] but the addition of oleum results in the formation of a uniform greenish-yellow foam, containing exfoliated few-layer graphene.[117] Even after washing with water, the graphene platelets retain their expanded morphology. Direct sonication of graphite sulfate in water also yields exfoliated few-layer graphene,[118] although in both cases, the yield of single-layers is low, and the sheets are lightly oxidised. $FeCl_3$-GICs can be exfoliated by reaction with H_2O_2,[119] or heating in the presence of primary amines, although further sonication is required to form graphene dispersions, and these are composed predominantly of multi-layer graphene. A similar approach of secondary intercalation with oleyl amine was followed using a graphite precursor intercalated with sulfuric and nitric acid.[120] Large flakes of up to 300 μm^2 were obtained, of a mixture of single- and few-layer graphene. The graphene could be dispersed at concentrations of up to 0.15 mg mL^{-1}; the authors proposed that slight oxidation of the graphene sheets occurred during treatment, facilitating enhanced interactions with the long amines, which could provide stability in solution.

Solution exfoliation of alkali metal GICs is well-explored in the literature. The introduction of electrostatic repulsion and dissolution of the counter-ions provide the driving force to obtain dispersions of isolated single-layer graphene in suitable dry, aprotic solvents under inert atmosphere. Alkali metal GICs can be modelled as large polyelectrolytes in solution; for spontaneous dissolution to occur, the charge required to exfoliate and stabilise the graphenide sheets must be balanced with the enthalpy gain of charge condensation.[121, 122] Too little charge and the van der Waals energy between graphene sheets is greater than the electrostatic repulsion, whilst too much charge results in restacking and condensation of cations between graphene layers. Therefore, the metal to carbon stoichiometry, and the overall ion concentration in solution, have a significant effect on the dispersibility. With the correct conditions, spontaneous dissolution of graphenide sheets occurs, analogous to carbon nanotubide salts,[123] although to a much lesser degree. Whilst the solubility of reduced CNTs as a function of their charge has been systematically studied,[124] similar investigations on

graphene have only examined the effect of charge on subsequent functionalisation reactions, using thermogravimetric analysis coupled with mass spectrometry (TGA-MS) and Raman analysis[13, 14] (see section 2.4.6.1), and the general approach to obtaining graphenide solutions has been to use a stage 1 GIC precursor, for example KC_8, or else an excess of alkali metal in solution. Potassium GICs, obtained by treatment with liquid ammonia,[93] naphthalene and THF,[125] or in the vapour phase,[126] were dispersed in various solvents, at concentrations of up to 0.7 mg mL^{-1} in NMP[127] and 0.5 mg mL^{-1} in THF.[128] Contrary to previous reports on the decomposition of THF in the presence of KC_8,[129] these dispersions remained stable, and individualised layers were successfully imaged by TEM[127] and atomic force microscopy (AFM),[93] whilst Raman characterisation of the deposited flakes confirmed the presence of single sheets.[93] For graphenide solutions of small nanoplatelets (~100 nm), >95% of graphite was present as single-layer graphene sheets,[93] and percentage yields for the larger starting materials as high as 35% were reached,[127] although after quenching, reaggregation of the flakes is unavoidable.

Recently it has been shown that graphenide dispersions of KC_8 in THF can act as a precursor to water-soluble graphene.[130] Addition of degassed, deionised water to the quenched graphene dispersion, followed by slow evaporation of THF, resulted in a stable graphene solution, stabilised by adsorbed OH$^-$ ions, with a concentration of 0.16 mg mL^{-1}. The existence of single-layer graphene in solution was confirmed by Raman spectroscopy,[131] but the overall yield is extremely low (4%) (Figure 2.9).
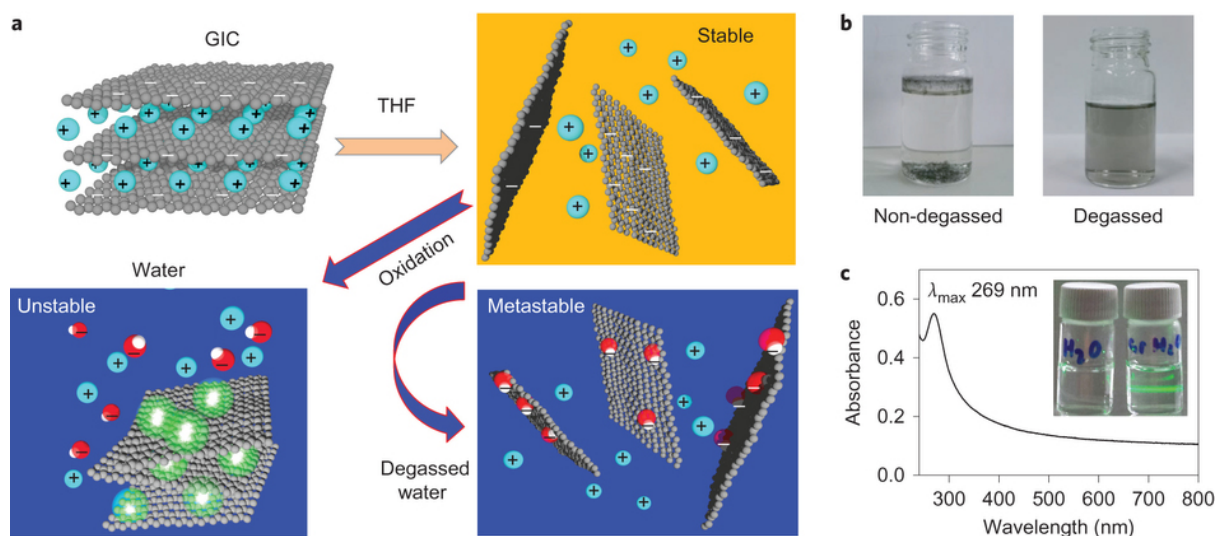
Figure 2.9. Stable dispersions of water-soluble graphene.[130]

2.2.2.7. Electrochemical exfoliation

Graphite rods have traditionally been used as electrodes in batteries and other electrochemical devices. The formation of intercalation compounds by electrochemical methods can be exploited for subsequent exfoliation to individualised graphene.[132, 133] Depending on whether an anodic or cathodic potential is applied, intercalation of anions or cations, respectively, along with any co-intercalating species in solution, causes an increase in the interlayer spacing between graphene sheets. After expansion, additional sonication is often used to further encourage exfoliation,[134] or grafting agents may be added to obtain functionalised graphene.[132] Various inorganic salt-based electrolytes have been investigated for anodic exfoliation, reaching yields of 85% of graphene sheets containing fewer than three layers, and more than 80% with a lateral size larger than 5 µm.[135] The intercalation of Li cations and propylene carbonate, in a cathodic process, resulted in a yield of over 70% of few-layer graphene (<5 layers), with about 50% of these sheets having 2-3 layers. An average lateral size of 1-2 µm was obtained, and a low defect concentration was observed by Raman spectroscopy.[134] Electrochemical processing is a relatively clean technique and is simple to carry out. However, the exfoliation process is not fully optimised or controllable, evident by the production of solutions of few-layer graphene; full exfoliation to single-layer graphene remains a challenge.

2.2.2.8. Summary of exfoliation methods

For large-scale processing, micromechanical cleavage is an unsuitable method of graphene production. Ball milling can be scalable but introduces defects onto the graphene lattice, and generally requires post-processing, for most applications. Of the liquid-phase approaches, the main difficulties arise from the ability to first isolate, and then stabilise, individual graphene flakes. Shear mixing and sonication both rely on mechanical driving forces to exfoliate graphite, and have a reasonable yield, making them applicable on a large-scale, but these methods can cause inadvertent damage without careful tuning of the processing conditions. In addition, 'good' solvents required for suitable stabilisation, such as NMP or DMF, can be toxic and difficult to remove. GO relies on the introduction of defects for increased dispersibility, but the properties are detrimentally affected by the oxidation process. Electrostatic repulsion provides the driving force for exfoliation of GICs, and individualised sheets are stable in solution, but the inert conditions required can complicate processing. For both electrochemical and GIC exfoliation, the bulk product is composed of a mixture of single- and few-layer graphene. The relatively low concentrations achievable require large amounts of solvent, which can affect cost and feasibility of scaling. For all applications, the choice of

exfoliation method is a compromise between the scale required, the cost, the obtainable yield, and the quality of the graphene flakes.

2.3. Graphene applications

Graphene has found applications in many fields, including electronics, sensors, energy generation and storage, biomedicine, and composites and coatings.[1] The quantity and quality of graphene required varies according to the intended use; some applications such as transparent electrodes and sensors require thin films of graphene, other applications including batteries and supercapacitors, or polymer composites require relatively large amounts of graphene nanosheets and platelets.

As graphene is a zero-bandgap semiconductor, opening up a bandgap is critical to achieve the switchable states required for digital electronics. It is possible to create a bandgap by confining the lateral dimensions of the graphene layer, or by electrical or chemical doping.[4] Printing of graphene inks is a viable method for large-scale fabrication of graphene devices. Graphene produced by liquid-phase exfoliation has been used to produce thin-film transistors, as well as transparent and conductive patterns.[136-138] Graphene shows promise as an electrode material due to its large surface area which facilitates electron transport along the surface; highly conductive transparent electrodes for applications in displays and OLEDs have been fabricated from various graphenes,[4, 136-138] whilst in the field of energy storage and conversion, graphene nanosheets have shown potential in devices such as rechargeable lithium ion batteries, supercapacitors and solar cells.[24] Graphene's large surface area can also be exploited in other fields; graphene can serve as a host material for metal nanoparticles and easy charge transfer facilitates catalysis of oxidation and reduction reactions, as well as a multitude of synthetic coupling reactions.[24] Solution-exfoliated graphene modified with fluorophores such as pyrene have found applications in sensing. π-π stacking causes quenching of the pyrene's fluorescence, but when binding to a specific molecule occurs, this π-π stacking is disrupted, thus recovering fluorescence and emitting a detectable signal.[139] In biomedical applications, graphene quantum dots and functionalised GO have been used for bio-imaging and enhanced phototherapy in cancer treatment, and have shown potential for drug delivery systems.[10]

The quality, size and distribution of the flakes, the yield of monolayers, and the quantity required are all important considerations when deciding which type of graphene to select. For example, in some of the applications listed above, pristine graphene may not necessarily offer the best performance enhancements, and modification by functionalisation could improve performance of the produced material.

2.3.1. Composites and coatings

One particular area where modified graphene may be preferential to pristine graphene is as a nanocomposite filler.[6, 140] The interphase between the nanoparticle and the matrix phase plays a central role in the overall performance of a composite material, as this is where the load, thermal energy, electrons and phonons are transferred.[141] True graphene-based composites have been difficult to manifest due to difficulties in processing large amounts of single-layer graphene. Furthermore, pristine graphene is a poor filler, lacking in functional groups to interact with a polymer matrix; the interfacial interactions within a composite rely on van der Waals forces, or π–π stacking, and the graphene flakes would need to be >30 µm in lateral size, and remain flat over tens of microns for efficient mechanical reinforcement.[142, 143] In addition, the distribution of graphene within the matrix phase has a significant impact on the nanocomposite's performance,[144] and agglomerates may act as defects in the material, with detrimental effects. Functionalised graphene therefore offers a possible solution to these problems: grafted addends prevent aggregation of graphene layers, and can increase compatibility with a polymer matrix, allowing a homogeneous dispersion to form. The chemical interaction is maximised to avoid de-bonding and delamination, resulting in a stronger interface,[141, 145] which reduces the critical size of flakes.

Many examples of previous graphene-based composites have used graphene oxide, where defects enable the polymer and filler to interact;[146-148] a study comparing effects of the addition of single-walled carbon nanotubes (SWCNTs), expanded graphite, and expanded GO to polar polymers such as PMMA, polyacrylonitrile (PAN) and polyacrylic acid (PAA), found that expanded GO performed better than SWCNTs and expanded graphite, and could significantly enhance the mechanical and thermal properties of the composite, at loadings as low as 0.05 wt% in the case of PMMA.[148] The improvement in reinforcement was attributed to the wrinkled sheet morphology and surface functionalities, which afforded a better interaction with the host polymer compared to unmodified SWCNTs and expanded graphite. A different approach exploits the oxygen groups on GO to introduce further matrix-compatible or cross-linking functionalities, which could help improve dispersion and prevent phase segregation upon curing;[149-152] modification is often preceded or followed by chemical reduction to partially recover the carbon framework. Amine-containing polymers have been introduced in this way as a method to covalently graft to epoxy resins, resulting in an increase in Young's modulus and glass transition temperature.[153, 154] Ultimately, however, GO and reduced GO (rGO) are still defective, resulting in inferior properties,[155] and so the composite material does not benefit from the intrinsic properties of graphene. GIC precursors[156] or microwave plasma-grown graphene,[157] as well as solution-exfoliated graphene nanoplatelets, have also been explored

as nanofillers for various polymer matrices.[158-160] One study compared the effect of covalent modification on interface strength and found that whilst the surface-modified graphene platelets formed clusters, a higher degree of dispersion and exfoliation was achieved, compared with unmodified graphene, and reported an enhanced glass transition temperature, and higher fracture energy release rate.[161] A similar approach exploiting covalent interactions with the epoxy matrix also reported an increase in fracture energy release rate, and improved modulus, compared with the epoxy/unmodified graphene composite.[141] In many cases, the subsequent modification procedures are often complicated and require many grafting steps, which can limit the scalability of these methods.

Overall, comparisons of the enhancements that graphene derivatives can afford polymer composites have shown that modified graphene can outperform unfunctionalised exfoliated few-layer graphene. A report describing the reinforcement of polypropylene and PMMA with electrochemically-exfoliated few-layer graphene (<5 layers) of two different lateral sizes confirmed that the larger flakes had a greater reinforcing effect on the composite, but interestingly, GO flakes with smaller lateral sizes could achieve similar improvements for PMMA at low loadings.[7] The effects of functionalisation on the composite performance, then, are a compromise between improving the graphene-polymer interface and introducing defects onto the graphene sheet. Depending on the properties required, and the corresponding loadings, the requirements on flake size may therefore be less stringent, if careful functionalisation regimes are applied.

2.4. Graphene functionalisation

In many bulk applications, the low solubility of graphene in common organic solvents often prevents straightforward processing. Functionalisation can introduce useful surface groups, enabling better dispersion and compatibility with solvents and polymer matrices. Chemical functionalisation can also allow doping, and introduce a bandgap into graphene, thereby providing control of its electronic properties, depending on the nature of the functional group. Modification can be achieved by non-covalent or covalent interactions. Graphene's extended aromatic framework enables easy interaction with other molecules *via* π-π stacking, van der Waals interactions, hydrophobic interactions and electrostatic interactions.[10] Non-covalent modification of graphene has been extensively explored and can be useful since the sp^2 carbon lattice is preserved, retaining graphene's intrinsic properties.[162] Examples such as surfactant-assisted exfoliation or polymer wrapping have been discussed in section 2.2.2.4; large molecules with aromatic components, such as porphyrins,[163] naphthalene,[164] naphthalene diimide,[165] and pyrene,[166] with modified side chains, have exploited the π-π interactions to stabilise graphene sheets in solution. The drawbacks of non-covalent

functionalisation are that the systems produced are generally metastable, relying only on relatively weak interactions, and often the intended applications require graphene without contaminants, which may have adverse effects on the materials' properties.

Covalent functionalisation can be achieved by gas- or liquid-phase methods. Gas-phase methods are much less developed than wet chemical techniques, but generally have the advantage of avoiding the vast amount of solvent waste, and accompanying costs, associated with liquid-phase routes, and can preserve the morphology and structure of individualised CNMs or hierarchical structures. However, grafting usually occurs at high temperature causing degradation of the carbon structure, is limited in terms of functionalities and grafting control, and can generally achieve a lower grafting density than wet chemical approaches.[167]

Wet chemical covalent functionalisation has been extensively explored and reviewed[8-10, 24, 168] in the literature, and offers a versatile and potentially scalable means of modifying graphene. The majority of graphene functionalisation methods have been developed from strategies first employed on CNTs and fullerenes. In general, however, whilst graphene has a higher exposed surface for reaction, bulk functionalisation of graphene is less straightforward than for fullerenes and nanotubes since the starting materials is rarely true single-layers, but multi-layer aggregates, or bulk graphite. Furthermore, graphene lacks the reactivity induced by curvature strain which is present in the 0D and 1D analogues.[11] Nonetheless, many of these techniques have been successfully extended to graphene functionalisation.

2.4.1. Oxidation

First prepared in the nineteenth century,[155] graphite oxide is produced by oxidation in the presence of strong acids and oxidants, most commonly by the Hummers method using sulfuric acid, sodium nitrate and potassium permanganate.[169] The level of oxidation can be varied based on the method, reaction conditions and precursor graphite used. Whilst the exact structure is still highly debated, the favoured Lerf-Klinowski model[170] (Figure 2.10) proposes a highly disrupted sp^2 carbon network where a significant fraction of the carbon is bonded to hydroxyl addends or participates in epoxide groups. Edges are thought to be populated with carboxylic or carbonyl groups. These oxygen-containing groups afford significant solubility, and dispersions of individualised graphene oxide sheets can be obtained by stirring or shaking,[2] sonication,[171] or thermal expansion[172] in a wide range of solvents, including water, DMF, NMP, and THF.[173] However, whilst the obtained flakes can be up to hundreds of microns in lateral size,[174] the oxygen functionalities which impart solubility are intrinsically defects interrupting the graphitic network,[74] and the sheets are therefore electrically insulating.[74]
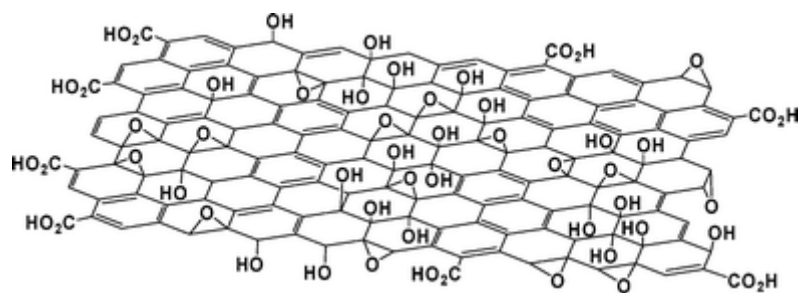
Figure 2.10. Proposed structure of GO, containing reactive epoxide, hydroxyl, and carboxylic acid functionalities.[175]

The electrical and thermal properties may be partially recovered by restoring the sp^2 carbon network through chemical reduction with, for example, hydrazine,[176] sodium borohydride,[177] or hydroquinone;[178] rGO may also be obtained by thermal treatment.[179] Whilst removal of some oxygen functionalities is possible, full recovery of electrical conductivity is rarely achieved.[42] However, these oxygen-containing moieties afford significant chemical reactivity, and functionalisation of GO is often based on reactions at these activated sites.[74] Chemical modification has been achieved at the carboxylic acid sites by reaction with amine-terminated moieties,[180, 181] whilst hydroxyl groups on the surface have been shown to react with acyl bromide ATRP initiators, allowing subsequent polymerisation of styrene and MMA.[181, 182] These oxygen-functionalised sites also play a useful role in improving the interface between nanofiller and matrix in GO-based composites[141, 149] (discussed above in section 2.3.1).

A more recent, and milder, approach to introducing oxygen functionalities was explored exploiting the reactivity of graphite sulfate.[118] Sonication in water afforded hydroxyl-functionalised graphene, with an estimated degree of functionalisation of 4%. Reduction of the sheets with hydroiodic acid and trifluoroacetic acid recovered high quality micron-sized graphene sheets with a density of defects of 0.06%, indicating that little lattice damage occurred over the oxidation process. A similar study first exfoliated graphite sulfate with the addition of oleum; subsequent washing with water resulted in the addition of a low degree of oxygen functionalities.[117] However, the overall yield is low for these processes, compared with typical approaches to obtaining GO.

2.4.2. Radical grafting

Highly reactive radical species are useful for graphene functionalisation and successful grafting of various moieties has been achieved. Well-known radical precursor molecules such as benzoyl peroxide (BPO) have been attached to supported single-layer graphene following thermal activation or laser irradiation,[183, 184] whilst azobisisobutyronitrile (AIBN) functionalisation of bulk graphite was achieved by stirring in NMP at elevated temperatures.[185]

AIBN is also useful for initiating other radical reactions; thiols have been converted to the reactive thiyl species, allowing grafting of polymer brushes on bulk graphene.[159, 186] Carbene addition has been used to introduce bromine onto the graphene surface, by sonication in bromoform,[187] achieving a grafting density as high as one dibromocarbene unit per thirty-seven basal carbons. Supported single-layer graphene was also chlorinated by reaction with chlorine gas, initiated by UV irradiation.[184, 188]

Reactions with aryl diazonium salts are a large and well-explored class within graphene functionalisation chemistry.[8] The reaction is versatile, allowing the preparation of tailored functional materials with improved dispersibility in a wide range of solvents, by simply altering the substituents on the benzene ring. Common substituents include nitro[189-192] or alkoxy[193] groups, bromine,[194, 195] or alkynes.[196, 197] Aryl diazonium salts with different para-substituents, -Cl, -NO$_2$, -OCH$_3$ and -Br, were attached to surfactant-wrapped rGO in solution.[194] The presence of these different groups allowed easy detection by XPS, providing a quantification of 4.6 at% in the case of -Cl and 3.2 at% for -Br. Solubilities were also shown to improve, reaching up to 0.5 mg mL^{-1} in DMF. In a study on single- and few-layer graphene obtained by micromechanical cleavage, the addition of surfactant was found to facilitate reaction.[190] Hemicylindrical surfactant structures on the graphene surface, with the polar head group free to interact with the diazonium reagent, were proposed to enable a higher concentration of diazonium reagent near the carbon plane. Single-layer graphene proved to be far more reactive to diazonium addition than bi- or multi-layer graphene, whilst edges also showed a higher reactivity, by at least two times, than the bulk sample, characterised by Raman spectroscopy. This trend in edge reactivity was also reported by other groups carrying out functionalisation of both single- and bi-layer graphene,[191] and bulk expanded graphite.[195] The location of grafted sites of bulk graphite functionalised with 4-bromobenzene was illustrated by EFTEM elemental mapping, where edge grafting in the bulk was explained by the relative availabilities of edge and inner basal planes to reagents[195] (Figure 2.11).

In the case of single- and bi-layer graphene, where grafting location was mapped by Raman spectroscopy (Figure 2.12), the preference for edge functionalisation was attributed to the higher degree of disorder at the flake edges, which enhances the decay of the adsorbed diazonium ion to the covalently bound reagent, since the energy of distorting the graphene lattice here is less than that inside the basal plane.[191]
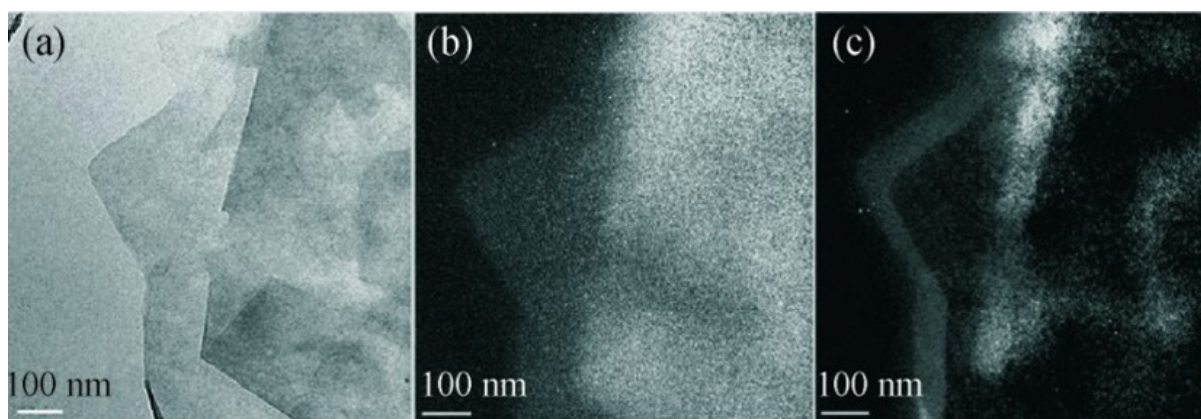
Figure 2.11. EFTEM of bromophenyl-functionalised expanded graphite; a) zero-loss image, b) C mapping, and c) Br mapping; Br is only observed within ~70 nm of the flake edge.[195]
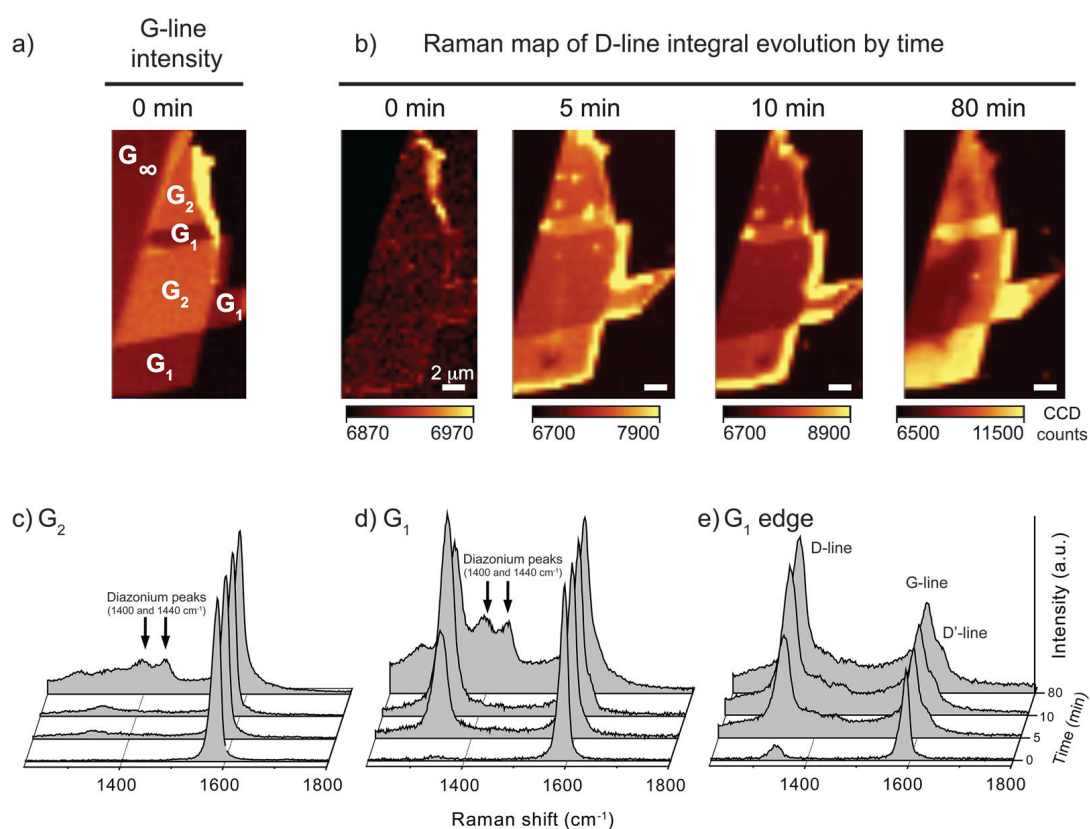
Figure 2.12. Raman analysis of a graphene flake with single- (G_1) and bi-layer (G_2) regions, during aryl diazonium functionalisation; a) overview of the flake with G_1 and G_2 regions; b) mapping of the evolution of the D peak during functionalisation, and the point spectra corresponding to the regions c) G_2, d) G_1 and e) G_1 edge.[198]

The diazonium salts involved in grafting often contain latent substituents which are used as a means of introducing further functionality to the graphene layers. Alkyne-containing diazonium groups have been frequently used for subsequent cycloaddition reactions, to introduce polymers such as polyethylene glycol (PEG) or PMMA, and further improve solubility.[196, 197] In

addition, polystyrene was introduced to rGO by first reacting with a hydroxyl-containing diazonium, followed by grafting of an initiator molecule, and then ATRP of styrene.[199]

Radical reactions are a powerful tool for graphene functionalisation. In general, however, these reactions have been carried out on supported single-layer graphene or on pre-exfoliated graphene or rGO dispersions. Functionalisation of single-layer graphene on substrate is useful for fundamental study, but cannot be scaled for industrial applications. Pre-exfoliating graphene is usually achieved by extensive sonication and centrifugation cycles, and therefore requires much additional processing and can be damaging, whilst the rGO carbon lattice is already inferior to pristine graphene. Furthermore, many of the systems above contain, or require, surfactant which can cause additional problems during post-processing.

2.4.3. Cycloaddition reactions

Cycloadditions are a versatile class of reaction, useful for the covalent modification of CNMs because they can be well-controlled and are clean reactions. A process that has been extensively used for chemical modification of fullerenes[200] and carbon nanotubes,[201] is the 'Prato reaction': the cycloaddition of azomethine ylides generated *in situ* by condensation of aldehydes and α-amino acids. Addition of an amine-terminated PEG[202] or a polyamidoamine (PAMAM) dendrimer[203] to sonication-dispersed graphene allowed quantification of functionalisation by the Kaiser test; subsequent coordination of gold nanoparticles enabled spatial mapping of grafted locations, illustrating that cycloaddition occurred all over the basal plane, with no preference for edge sites (Figure 2.13). This all-over grafting afforded an increase in solubility of 0.52 mg mL^{-1} in DMF.[203]
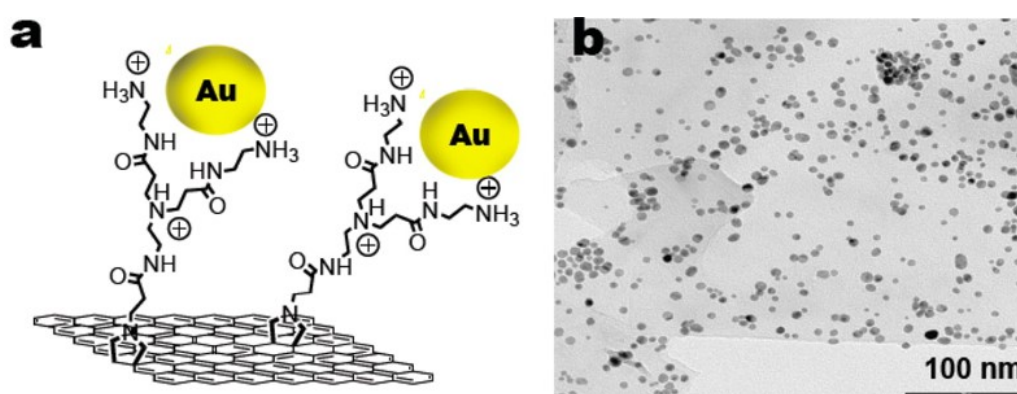
Figure 2.13. a) Schematic, and b) TEM image of graphene layer functionalised with Au nanoparticles. Adapted from ref 204.

The Diels-Alder reaction has also been employed for covalent modification of graphene. One study by Haddon *et al.*[205] illustrated the versatility of graphene as a Diels-Alder substrate, and its ability to function as either the diene or the dienophile. Various types of graphene and

graphite, with different dienes (9-methylanthracene and 2,3-dimethoxy-1,3-butadiene) and dienophiles (tetracyanoethylene and maleic anhydride) were used to prove the efficiency of this reaction.

Reaction of bulk exfoliated graphene with several acetylene dicarboxylates *via* a zwitterionic intermediate achieved grafting densities of between 10 and 50 graphene carbons per addend, depending on the size of the grafting moiety.[206] The products were soluble in chloroform, water and DMF at concentrations up to 0.28 mg mL^{-1}. Graphene can also undergo [2+1] cycloadditions, such as the reaction of azido-phenylalanine with sonication-exfoliated micro-crystalline graphite, resulting in a highly-functionalised material with one phenylalanine substituent per 13 carbons,[207] or the photo- or thermally-initiated reaction with substituted perfluorophenylazides (PFPA) which imparted solubility in common organic solvents or water, depending on the nature of the functional group on the PFPA.[208]

Cycloadditions are useful for introducing a wide range of functionalities on graphene. However, as for radical reactions, despite the efficiency of functionalisation by cycloaddition, pre-treatment to obtain solutions of exfoliated single- and few-layer graphene is required prior to reaction.

2.4.4. Halogenation

Halogenation of CNMs[209-211] is a useful route to obtain highly reactive species which may be used in further reactions. Fluorination has been carried out on single- and few-layer graphene on silicon substrates by treatment with aqueous solutions of HF,[212] or on CVD graphene by exposure to XeF$_2$ gas;[210, 213] an extremely high grafting density was achieved (C$_2$F), resulting in an insulating material. Further, the fluorinated sites were substituted with a series of nucleophiles, illustrating the potential for introducing a variety of functional groups, although in some cases the substitution efficiency was very low.[213] Single-layer graphene has also been functionalised with chlorine by UV-initiated radical grafting, achieving a uniform coverage of 8 at% chlorine on the sample.[188] A higher degree of functionalisation was obtained by microwave irradiation of expanded graphite in liquid chlorine, reaching 21 at% Cl, and a solubility of 0.5 mg mL^{-1} in DMF, of mostly monolayer graphene.[209] In the analogous bromination case, only 4 at% bromine was introduced, and a yield of 5% monolayers was obtained. The chlorinated graphene derivative also underwent substitution with lauryl amine, providing a useful precursor for subsequent functionalisations.

Bromine grafting has also been well-explored, although intercalation or adsorption of molecular bromine is common.[214] Bromine has been introduced onto various CNMs by several methods, including exposure to bromine vapour,[215] long sonication[216] or microwave

irradiation[209] in bromine liquid, reaction with dibromocarbene,[187] and photocatalytic addition using *N*-bromosuccinimide as a bromine precursor.[217] However, direct covalent attachment of bromine to graphene is rare and usually achieved by harsh methods such as plasma treatment[218] or at high temperature and pressure.[219] These approaches have achieved a high coverage of bromine on the graphene surface, 20% Br/C on highly-oriented pyrolytic graphite (HOPG), 40% Br/C on natural graphite,[218] and 26 wt% Br on GO;[219] but this level of functionalisation severely reduces the conductivity of the graphene lattice. Furthermore, as for the other functionalisation methods described above, bromination is frequently carried out on pre-exfoliated materials,[209, 216, 219, 220] requiring extra processing steps. Nevertheless, similar to fluorinated and chlorinated CNMs, bromine-activated carbon species can be used in subsequent nucleophilic substitution reactions, as reported for brominated HOPG and multi-walled carbon nanotubes (MWCNTs); for example, following plasma-chemical bromination, the C-Br bonds underwent hydrolysis, or further grafting with 1,6-diaminohexane and (3-aminopropyl)triethoxysilane.[218] Bromination of SWCNTs by reductive functionalisation also showed that nucleophilic substitution of sidewall bromine addends was possible, introducing 2,2,2-trifluoroethanolate and hydroxyl groups at the brominated sites.[221] Bromine addends have also been used for Suzuki coupling reactions, allowing the introduction of polythiophene onto rGO.[220]

2.4.5. Polymer grafting

Polymer grafting can greatly improve the solubility of CNMs, additionally limiting their restacking and agglomeration on drying. Generally, there are two approaches: using polymers with well-defined molar mass and an activated end group, in a 'grafting-to' approach, allows control of polymer properties,[197] but the large steric bulk of the chains tends to limit grafting density; conversely, direct growth of polymers from the CNM surface, by 'grafting-from', can achieve dense coverage,[222] but molar mass and dispersity (*Đ*) can be affected by the heterogeneity of the substrate. As discussed in the previous sections, many examples of polymer attachment to graphene are carried out *via* intermediate steps where some form of initiator or modifier is first grafted to the graphene sheets, before a subsequent graft-to or graft-from reaction to introduce the polymer. Large PAMAM dendrons,[203] PEG,[180, 196, 223, 224] polyethylene,[225] PMMA and copolymers of PMMA and 2-(acetylthio)-ethyl methacrylate[186] have been attached to pre-modified exfoliated graphene, GO or rGO starting materials by the various approaches outlined above. Polymers including PMMA, PAN, polythiophene, poly(dimethylaminoethyl methacrylate) (PDMAEMA), and polystyrene have been grown by grafting-from techniques such as ATRP,[181, 182, 199, 226, 227] free radical polymerisation,[228] reversible addition-fragmentation chain-transfer (RAFT) polymerisation[197] or Suzuki

coupling,[220] from pre-attached initiators on the graphene or GO surface. Anionic polymerisation can be carried out directly from the surface but has so far only been applied to the growth of polystyrene on graphene nanoribbons formed by unzipping MWCNTs;[229] this approach is further limited to monomers with side groups which are stable to reducing conditions. In addition, other studies suggest that whilst polymerisation is initiated by GIC species, no covalent attachment is formed with the graphene sheets, reported for the polymerisation of both styrene[230] and isoprene.[231]

These grafting approaches have also been successfully applied to other CNM starting materials.[232] Pre-synthesised polystyrene of varying molecular weights was introduced to SWCNT surfaces by sequential grafting, first of an alkyne-terminated group, which could then undergo cycloaddition with azide-terminated polymer chains.[233] Azide-terminated polystyrene was also used to directly graft polymer onto the CNT sidewall by aziridine ring formation.[234] Grafting-from of PMMA and polystyrene on SWCNTs and MWCNTs has been achieved by ATRP;[234-236] this approach can also be extended to the surface of BNNTs with the polymerisation of glycidyl methacrylate and styrene.[237] In all cases, an initiator was first attached to the CNM surface, usually by multi-step reactions, before polymerisation. In both the graft-to and graft-from methods, since most of the approaches involve the grafting of a modifying group prior to polymerisation, the amount of polymer introduced during reaction is fundamentally limited by this initial surface concentration.

Polymer-grafted graphenes have particular importance for applications as nanofillers in composite materials. The variety of polymers that may be introduced on the graphene surface provide an easy means of tuning the compatibility with a range of matrix materials, and thereby enabling the production of composites with tailorable properties.[5]

2.4.6. Reductive chemistry

As discussed above in section 2.2.2.6, alkali metal GICs are a useful precursor to dispersions of negatively-charged graphene sheets which are individualised in solution. The negative charges on the graphenide sheets may also be exploited for reaction with suitable electrophiles; these side-chains prevent re-aggregation of the individualised sheets, thereby improving solubility. Grafting by this method results in small defects at the grafting site where an sp^3 carbon is introduced into the sp^2 network, but the grafting ratio may be controlled by varying the initial charge stoichiometry, and therefore the intrinsic properties of graphene should be carefully tunable. In general, reductive functionalisation is a versatile route which has been applied extensively to other CNMs to obtain materials grafted with a wide variety of moieties.[87, 238, 239] For graphene, in particular, common charging methodologies for

functionalisation include metal-ammonia solutions,[240] potassium GICs produced by vapour transport or direct metal contact, dispersed in solvents such as THF or DME,[241] or direct formation of ternary compounds in those solvents, often with the addition of a charge transfer agent[13, 242] (refer to section 2.2.2.6 for more details). An overview of the modifications achieved by reductive functionalisation of graphene is provided in Figure 2.14.
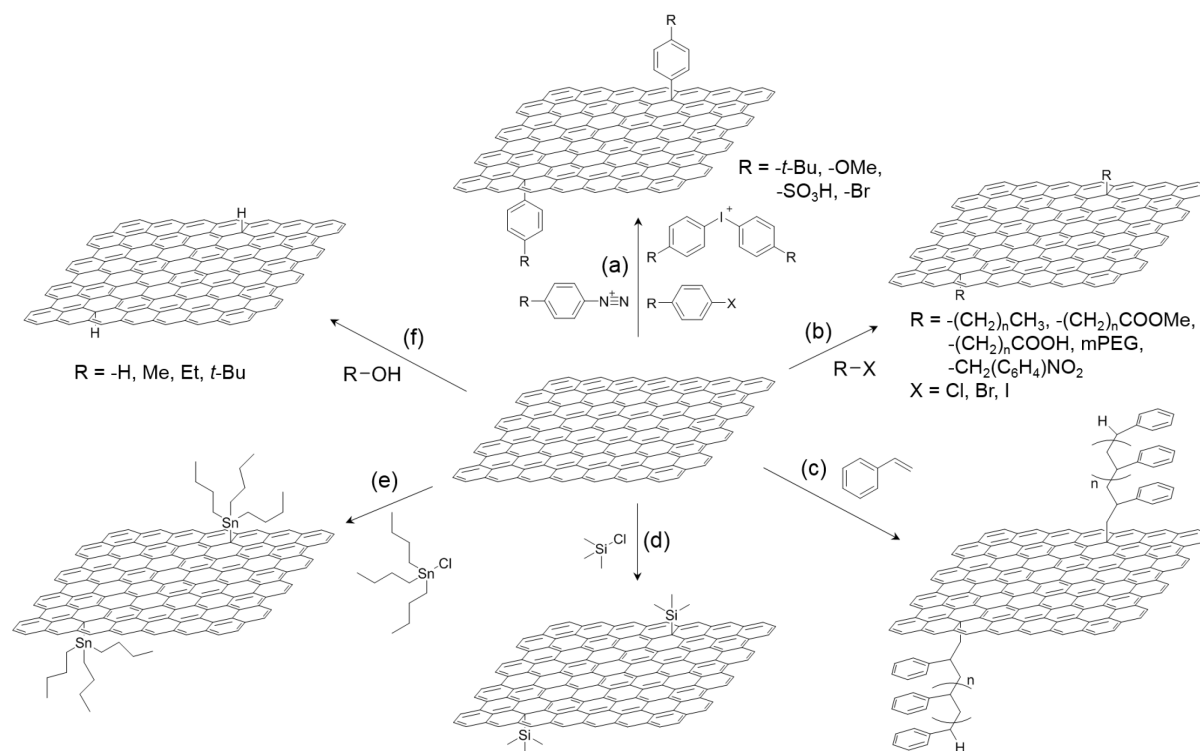
Figure 2.14. Schematic of literature examples of reductive functionalisation products. a) Aryl grafting from diazonium salts,[242] iodonium salts,[241] aryl halides;[243] b) alkyl,[13] alkyl ester,[244] alkyl acid[87] and mPEG grafting;[245] c) vinyl monomers such as styrene;[230] d) trimethylsilyl chloride;[246] e) tributyltin chloride;[247] and f) hydrogenation from proton sources water, methanol, ethanol, *t*-butanol.[14]

2.4.6.1. Reductive functionalisation

Stabilisation of graphenide dispersions is only possible so long as a dry, air-free environment can be maintained. Upon contact with ambient conditions, the Coulombic repulsion is lost when negative charges are quenched, and restacking and aggregation are once more energetically favourable compared with solvent interactions. Functionalisation can impart solubility to isolated graphene layers, and provide steric stabilisation against restacking during processing. In principle, with moderate and controllable grafting densities, the connectivity of the carbon lattice is retained, thereby reducing the detrimental effects that covalent grafting and exfoliation can have on graphene's intrinsic mechanical and electrical properties. With careful choice, solubility may be tailored to suit a wide range of solvents. As a direct extension of the Birch reduction, successful hydrogenation of bulk graphite,[92, 94] as well as single-layer

graphene supported on Si/SiO_2,[247, 248] has been carried out using excess lithium in liquid ammonia, followed by quenching with proton donors *tert*-butyl alcohol[92] ethanol,[247] methanol,[249] or water.[94] A recent in-depth study, on the efficiency of various proton donors with a series of potassium GICs from different graphite starting materials, illustrated that a tunable degree of functionalisation could be achieved by varying the initial charge ratio and proton donor.[14] A very high degree of hydrogenation has been achieved in these studies (($C_1H_{0.7})_n$,[14] ($C_1H_{0.8})_n$,[92] ($C_1H_{0.2})_n$[247]), but no reports of solubility were mentioned, likely because proton addends are small and do not significantly aid graphene dispersion. These studies are in contrast to previous reports describing the formation of highly exfoliated graphite and graphene nanoscrolls, as a result of vigorous hydrogen evolution on addition of water or ethanol to potassium and caesium GICs.[250, 251] The competition between hydrogenation, by simple H^+ abstraction from the proton source, or hydrogen formation, by single-electron transfer, is governed by the size of the proton donor, the relative amount of edge sites, the solvent choice, and the amount of charge.[14, 252]

A range of grafting moieties have been explored (Figure 2.14), including aryl diazonium salts,[242, 253] diaryliodonium compounds,[241, 254] various length bromine-terminated carboxylic acids[87, 244] and reactions with aryl halides.[111, 243, 255] These studies report grafting densities from as low as one grafted moiety per 10000 basal carbons[241] up to around one group in fifty,[244] much lower than the densities achieved with hydrogenation; these grafting densities are likely a result of the larger grafting groups. However, despite a lower degree of functionalisation, improved dispersibility of these graphene derivatives in water[87] and chloroform[244] was reported, with 4-*tert*-butylphenyl-functionalised graphene reaching a solubility of 27 µg mL^{-1} in chloroform.[242] More recently, direct formation of a C-Si bond, with comparable grafting density to aryl-functionalised graphene, was achieved by reaction of potassium GICs dissolved in DME with trimethylsilyl chloride;[246] formation of a C-Sn bond was also achieved on single-layer graphene, by reaction with tributyltin chloride.[247]

Alkylation is a useful and extensively studied model reaction system, and has been achieved *via* several reduction routes and subsequent reaction with different alkyl halides; Billups *et al.* reported a traditional Birch reduction, followed by reaction with dodecyliodide,[240] whilst more recently the Hirsch group achieved functionalisation with varying length alkyl chains of different graphitic materials by reduction with Na/K alloy in DME.[15, 256] Different alkylated graphenes were produced by reaction of graphite reduced by sodium naphthalide in THF, changing alkyl length, halide, and stoichiometry, with optimal conditions yielding solubilities of up to 37 µg mL^{-1} in *o*-DCB and 20 µg mL^{-1} in $CHCl_3$.[13] High degrees of edge functionalisation were achieved for alkyl-modified graphene nanoribbons formed by unzipping MWCNTs with Na/K

in DME.[257] Even so, despite successful identification of exfoliated single layers by TEM and AFM,[242] characterisation by these methods is not representative of the bulk product, which invariably remains a mixture of both functionalised graphene and starting graphite material. More recently, scanning Raman spectroscopy[255] has become a useful technique for bulk characterisation, enabling a spatial and statistical overview of grafting (Figure 2.15). Solubility measurements can also give some indication of the bulk degree of modification, with higher solubility generally implying greater functionalisation, by a particular moiety. However, even with C/alkyl ratios of ~21-340, the alkyl-modified graphenes are still only sparingly soluble in most organic solvents, ranging between 2.05 and 32.9 µg mL^{-1}, limiting the scalability of this method.
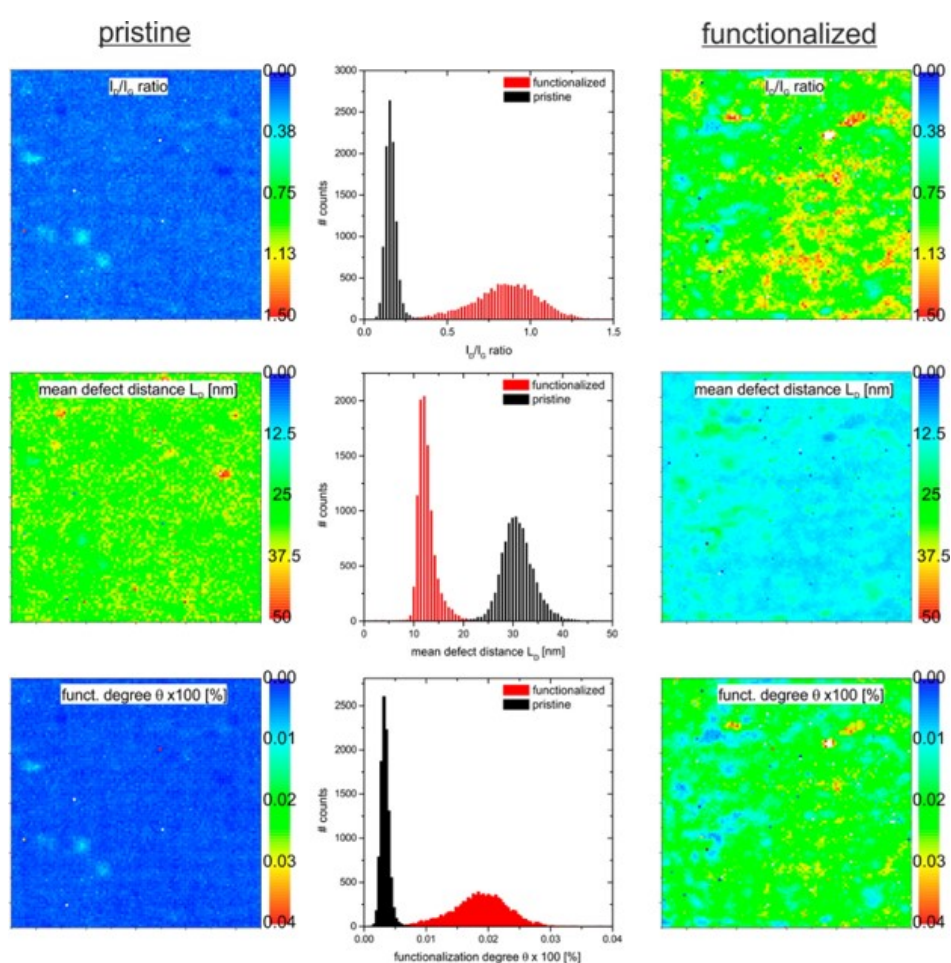
Figure 2.15. Spatial and histogram representations of grafting in phenyl-modified graphene. (Top) I_D/I_G ratio, (middle) mean defect distance L_D, and (bottom) functionalisation degree in pristine (left) and functionalised (right) graphene.[255]

Grafting of polymeric species can impart a higher degree of solubility. In a 'grafting-to' approach, brominated polyethylene glycol was reacted with graphite and exfoliated graphite nanoplatelets; these functionalised materials found stable dispersions in water at up to 200 µg mL^{-1}.[245] The 'grafting-from' approach has also been explored, by anionic

polymerisation of styrene initiated by reduced graphene nanoribbons[229] or graphite,[230] analogous to reactions with methyl methacrylate on SWCNTs.[222, 258]

2.4.6.2. Charge quenching

An ongoing issue concerns whether the amount of charge can be fully controlled or completely removed during these reactions.[259] Typically, additional quenching of residual charges after functionalisation is achieved by exposure to ambient conditions or addition of cyclohexane and water,[15] ethanol[240] or bubbling through dry oxygen.[13] For reactions with CNTs, it was reported that complete discharging does not occur, resulting in inadvertent functionalisation on exposure to air.[260] Two very recent works explore various chemical discharging agents, offering alternative non-destructive quenching procedures[261, 262] (Figure 2.16). Incomplete discharging of graphenide solutions can also affect solvent removal after processing, another area requiring further investigation. In CNTs and fullerenes, residual solvent is much less problematic, since their inherent curvatures prevent such close restacking, preserving open channels through which solvent may escape. The presence of solvent remaining between graphene layers, especially for the larger graphite materials, can affect the apparent grafting ratios obtained from TGA data.[241]
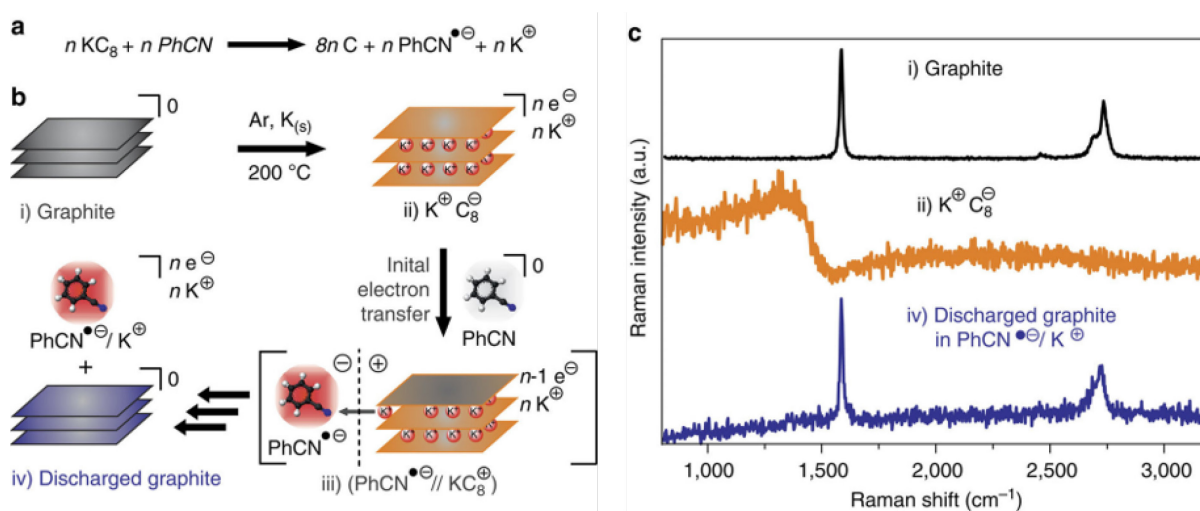
Figure 2.16. Quantitative discharging of potassium GICs with benzonitrile. a) Reaction scheme for discharging with benzonitrile; b) after graphite and potassium and combined to form KC_8, the addition of benzonitrile leads to initial electron transfer, followed by de-intercalation of K^+. After subsequent oxidation and K^+ migration, fully discharged graphite is obtained. c) Raman spectra (λ_{exc} = 532 nm) of the respective species in the GIC/benzonitrile cell. Adapted from ref 262.

2.4.6.3. Graphite starting material

The quality of the graphite starting material has been shown to have a strong influence on the outcome of grafting; under identical conditions, powdered graphite achieved the best degree

of functionalisation and solubility, compared to flake and spherical forms.[15] Whilst the majority of studies report homogeneous functionalisation across the whole graphene basal plane,[255] others propose grafting propagating from edges or defects.[111, 244, 248] In particular, one recent study investigated the spatial evolution of hydrogenated sites on single- and bi-layer graphene (Figure 2.17); by covering the edges of a few-layer flake, it was shown that grafting occurred by an intercalation process, and could only proceed through available edges.[248] An early study on potassium graphite proposed different reactivity types in edge and bulk carbon atoms, with edge atoms undergoing a two-electron Birch-type reaction, whilst bulk carbons give up only one electron potentially acting as a catalyst for Wurtz-type coupling.[252] The differences in reported functionalisation homogeneity and efficiency may well result from the size and morphology of the starting graphite flakes, and their intrinsic defect concentration, as well as the reactive nature of the grafting reagent.
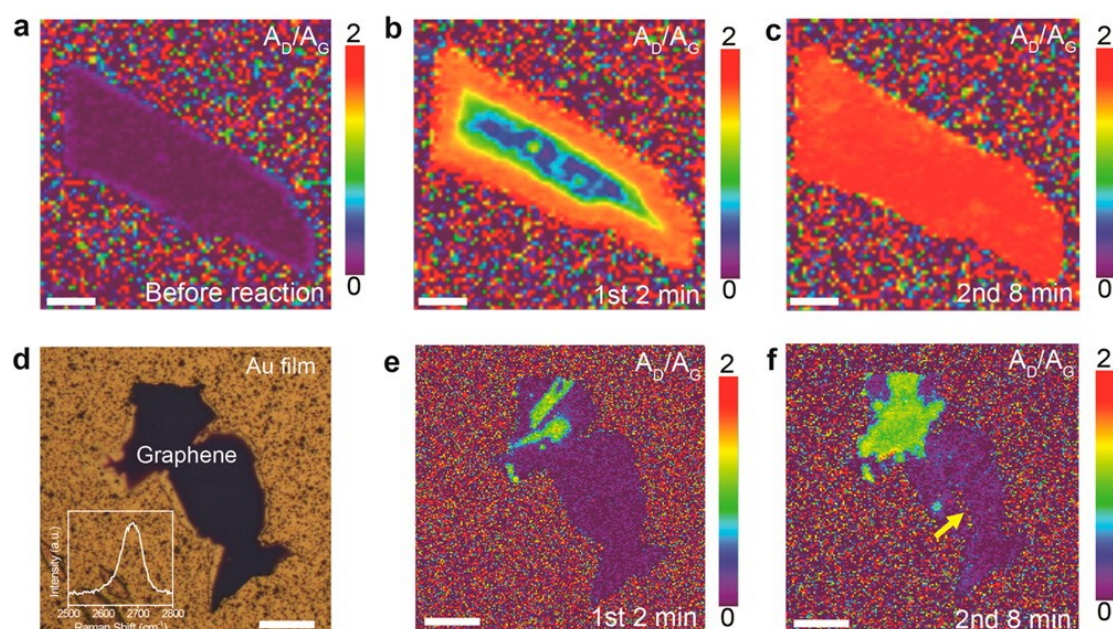
Figure 2.17. Structural evolution of bi-layer and edge-covered few-layer graphene during a Birch-type reduction. a–c) Evolution of the Raman A_D/A_G map for AB-bi-layer during Birch-type reduction with Li in liquid NH_3; d) optical image of the edge-covered few-layer graphene, the 2D peak is shown as inset image; Raman A_D/A_G map of the edge-covered flake e) after exposure for 2 min to a solution of Li in liquid NH_3 and f) after further exposure for 8 min. The scale bars in parts a–c and d–f are 3 and 20 μm, respectively.[248]

Strong van der Waals interactions in the layered structure of the starting graphite render many parts of the sample inaccessible for easy grafting. Even though a range of graphene modifications by reductive functionalisation have been reported, this inaccessibility, and the relative unreactivity of the lattice could explain why analogous grafting reactions on CNTs achieve a higher grafting density,[241, 263] and why many reactions that are accessible to CNTs[264] have not yet been reported for graphene.

2.4.7. Summary of covalent functionalisation methods

Covalent functionalisation requires the rehybridisation of carbons from sp^2 to sp^3; inevitably, even at low levels of grafting (<5 at%), some of graphene's intrinsic properties will be lost.[265] This effect can be overcome by careful control over functionalisation degree; further, some reactions which occur preferentially at edges may be beneficial for particular applications. In many cases though, reactions require handling of difficult reagents, or dry, inert conditions, and the low scalability and air sensitivity may prevent wider industrial use. The majority of these functionalisation approaches require pre-dispersion by intensive sonication, pre-treatment by oxidation, or else involve lengthy work up procedures. Unfortunately, solubility remains extremely low, and is a significant limitation to the large-scale processing of modified graphene.

2.5. Summary and outlook

This chapter has highlighted the main methods of producing graphene from bulk graphite starting materials. There have been many developments in liquid-phase exfoliation to obtain processable dispersions of graphene, but several challenges remain: the dispersions are inevitably a mixture of single- and few-layer graphene, requiring additives for stabilisation; in addition, the yield and solubilities of these dispersions are still low, and therefore unsuitable for large-scale processing. Some techniques which recycle the starting material can increase the overall amount of graphene obtained, but exfoliation methods with higher yields are still of critical interest.

In many applications, a mixture of single- and few-layer sheets may not intrinsically be a problem; but careful characterisation of the bulk product is needed. This issue has been addressed to some degree using methods such as scanning Raman spectroscopy or TGA, but many traditional layer identification methods, such as AFM and TEM, are limited in their ability to provide a statistically relevant analysis.

Functionalisation can significantly improve the dispersibility of these single- and few-layer materials, and many approaches (often extensions of CNT and fullerene chemistry) have been successfully applied to graphene. However, often the same reaction conducted as a fundamental study on single-layer graphene can have entirely different results when applied to a bulk material, largely due to the inhomogeneity of the starting graphite. Furthermore, many different types of graphite and graphene starting materials are commercially available, with different properties, and this can significantly affect the outcomes of the reaction.

3. Characterisation techniques

In all areas of chemistry, characterisation is essential to understanding a material's structure and properties. Carbon nanomaterials, in particular, present a challenge since the heterogeneity of the bulk sample and often poor solubility mean that traditional techniques such as nuclear magnetic resonance (NMR) and mass spectrometry (MS) are inaccessible. For graphite and graphene, bulk characterisation methods such as thermogravimetric analysis (TGA), Raman spectroscopy and X-ray diffraction (XRD) can provide a statistical overview of sample characteristics including grafted functionalities, graphitic quality, and degree of exfoliation. Individual sheets can be probed by transmission electron microscopy or atomic force microscopy; in these techniques, assignments of layer thickness and structural integrity are possible locally. However, sample preparation remains challenging, and the results can be biased by artefacts introduced during sample preparation. Statistically, conclusions from microscopy techniques concerning the bulk sample should be regarded with some degree of caution. A combination of methods probing at the bulk and molecular levels is therefore required to provide a comprehensive characterisation of graphene and its derivatives. In the following sections, the main characterisation techniques employed in this thesis, and their application to graphite and graphene, are discussed.

3.1. Thermogravimetric analysis

TGA measures the changes in mass occurring in a sample as a function of increasing temperature under a controlled atmosphere, and can provide information regarding the material's thermal stability and the organic and inorganic components which are present. The measurement is usually carried out with a linear heating rate, in an oxidative (air) or inert (nitrogen or argon) atmosphere.

Measurements under oxidative atmosphere are useful for determining the content of inorganic residue in a sample. In CNTs or graphene materials obtained from 'bottom-up' syntheses, this char is usually residual catalyst particles; in donor graphite intercalation compounds, metal salts remain after combustion. Various oxidative reactions are possible during heat treatment which may lead to a gain in mass. These processes must be taken into account when calculating the carbon:inorganic ratio.

Given the much greater thermal stability of graphite and its related materials than of small organic moieties, TGA is used extensively to quantify the degree of grafting in functionalised

derivatives; adsorbed species, such as intercalated solvent, may also be identified. Analysis is typically carried out under inert atmosphere: the underlying graphitic carbon structure is retained during the heating process, whilst organic addends decompose at characteristic temperatures. Quantification of functional groups is straightforward by comparing the total mass loss to the mass of material remaining, if complete pyrolysis of the organic moieties occurs before any damage to the graphitic framework. However, some functional groups may not pyrolyse fully in inert atmosphere, and as-received materials may also exhibit some weight loss; it is therefore important to measure against these controls in order to obtain a baseline from which to accurately evaluate the degree of grafting.

Further evolved gas analysis (EGA) of the volatile species generated from TGA decomposition may be carried out in real time to confirm the identity of these moieties. Most commonly, the TGA may be coupled with a MS or a Fourier Transform Infrared spectrometer (FT-IR). Due to the low sensitivity of FT-IR, relatively large amounts of sample are required for effective detection; for CNMs with low degrees of grafting, FT-IR may not be a suitable method of analysis. Conversely, MS can detect very low levels of material, and this increased sensitivity makes it a valuable technique for further characterisation, although the range of detectable fragment sizes is limited.

Decomposition processes are dependent on TGA parameters, such as heating rate and gas flow, and the sample conditions, including initial mass and morphology. Often, the onset of decomposition occurs gradually, due to the heterogeneity of the material; therefore, a temperature range, or the temperature corresponding to the maximum weight loss rate, is reported. For consistent, comparable data, parameters should be kept constant between samples to improve reproducibility and accuracy of analysis, and experiments should be repeated to minimise the effect of sample inhomogeneity.

3.1.1. Mass spectrometry-coupled thermogravimetric analysis

In mass spectrometry-coupled thermogravimetric analysis (TGA-MS), the volatile species evolved during TGA are transferred to a MS where they are subsequently ionised and deflected through a magnetic field. Greater deflection occurs when the ion is light, or has greater charge. The resulting ions are detected according to their mass-to-charge (m/z) ratio, and the abundance counted. These ion fragments may be characteristic of individual organic moieties, so MS can provide useful confirmation of what addends are present in the sample. The intensity of these signals with time can be correlated to temperature, and careful consideration of both the temperature of decomposition and the mass fragments observed in those intervals can enable differentiation between covalently-grafted and physisorbed

species. Since spectra are taken real time during a TGA measurement, there is a compromise between the range of masses to be detected and the resolution of spectra against time that can be achieved.

3.2. Raman spectroscopy

When a sample is illuminated by a monochromatic light source, electrons may be excited into higher virtual energy states; following excitation, the electrons relax back, emitting a photon in the process. The majority of electrons scatter elastically, emitting a photon of the same frequency as the incident radiation; this process is known as Rayleigh scattering. A small fraction ($\sim10^{-5}\%$) of electrons undergo Raman scattering and return to either a higher or lower level than their original state, resulting in the emission of a photon with correspondingly lower (Stokes) or higher (anti-Stokes) energy (Figure 3.1). The Raman spectrometer measures only Raman scattering, filtering out the dominant Rayleigh signal. Anti-Stokes scattering is much less intense than Stokes since a molecule must already be in an excited state, and at room temperature, the ground state will be the most populated. Thus, Raman spectroscopy principally detects photons emitted by Stokes scattering. The change in energy of the emitted photon corresponds to the difference between vibrational energy levels in a molecule; Raman spectroscopy therefore provides valuable information regarding molecular vibrations and bonds. Raman scattering is governed by different selection rules to infrared absorption; for a vibration to be Raman active, there must be a change of polarisability in the normal mode. Peaks in the spectrum arise from specific molecular bond vibrations for individual or groups of bonds and vibrations. In crystalline solids, the Raman spectrum corresponds to collective vibrational modes, or phonons.
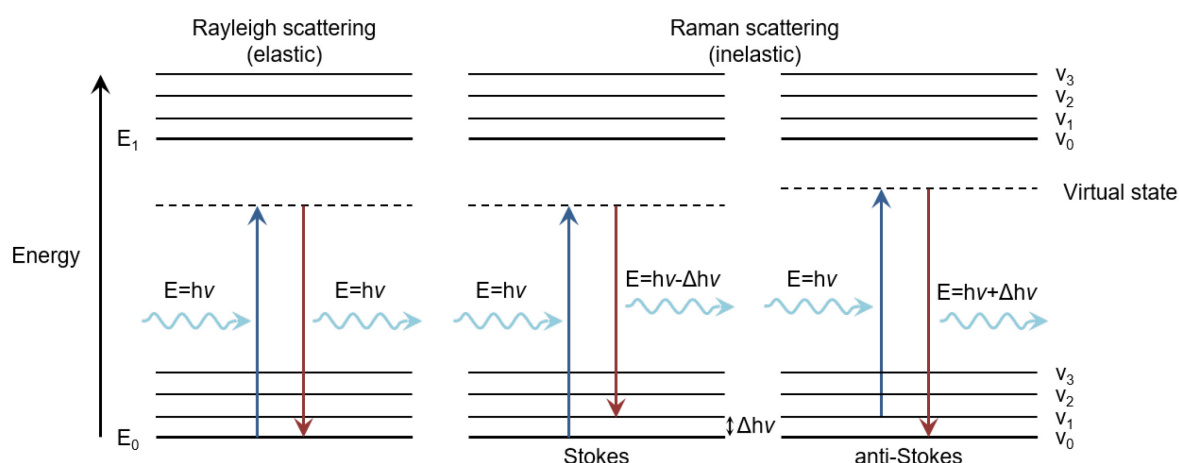
Figure 3.1. Schematic energy diagram of Rayleigh and Raman Stokes and anti-Stokes scattering modes. E_n and v_n represent the electronic and vibrational levels, respectively.

3.2.1. Raman spectra of graphite and graphene

Raman spectroscopy is an important method of graphene characterisation. The position, full width at half maximum (FWHM, Γ) and relative intensities of the main excitations can provide information regarding graphitic nature, the number and orientation of layers, the quality and types of edges, and the effects of perturbations arising from electric or magnetic fields, strain, doping, disorder and functional groups.[266] Graphitic materials typically exhibit four characteristic bands, arising from in-plane vibrations in the carbon lattice (Figure 3.2).
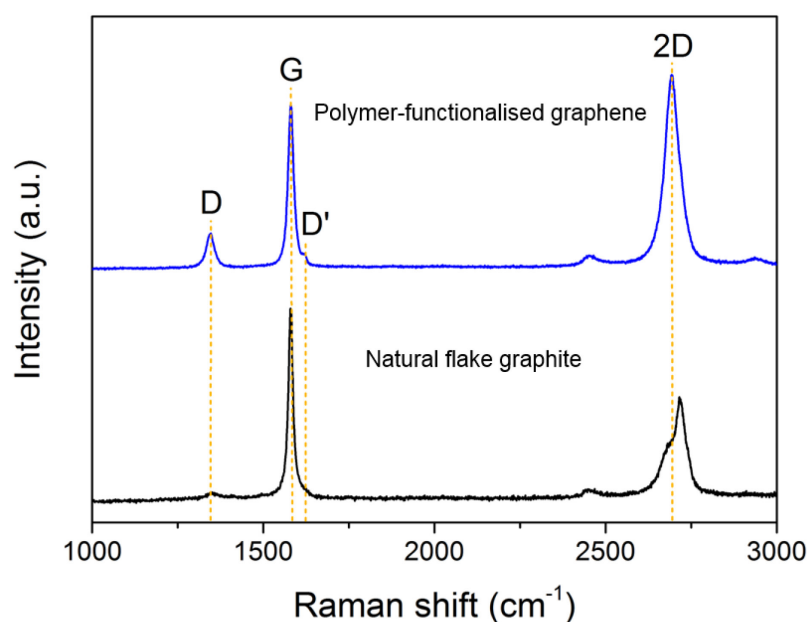
Figure 3.2. Raman spectra of natural flake graphite and polymer-functionalised graphene. The D, G, D' and 2D bands are highlighted.

The G band, appearing at ~1580 cm^{-1}, is due to bond stretching of sp^2 carbon pairs in both rings and chains, and can be taken as a measure of graphitic nature. The G peak is not dispersive (its frequency does not depend on the laser excitation energy), but the position is very sensitive to effects of external applied fields, strain or doping. This mode can therefore be used to probe modifications of the graphitic structure.

The D band, at ~1350 cm^{-1}, is a dispersive mode arising from breathing modes of sp^2 carbon rings, and requires a defect for its activation. In general, the D band intensity is a measure of the disorder within a sample, whether from sp^3 sites, lattice vacancies, or layer and crystallite edges; by comparing the relative intensities of the defect and graphitic bands, I_D/I_G (occasionally the relative areas, A_D/A_G, are considered instead), an estimate of the degree of disorder can be made. In particular, I_D/I_G is commonly used to quantify the number of defects

introduced by covalent grafting, discussed by several models in the literature.[255, 267, 268] Generally, according to the Tuinstra-Koenig relation,[269] at low defect concentrations, I_D/I_G increases linearly with the defect density, but at a critical concentration, the relationship breaks down and the trend is reversed, with an increasing I_D/I_G actually indicating a return to order (Figure 3.3). Examination of the peak shapes and FWHM allows identification of which regime is applicable. Still, general caution should be exercised when interpreting the I_D/I_G ratio as a measure of functionalisation, since many other factors can contribute to the signal intensity. The D' band at ~1620 cm^{-1} can also be useful for investigating the types of disorder present on the graphene lattice. This peak is similarly defect activated, in an intravalley scattering process, and comparison of the intensity relative to the D peak ($I_D/I_{D'}$) can give a useful indication of whether defects arise from boundaries, vacancies, or sp^3 sites.[270]
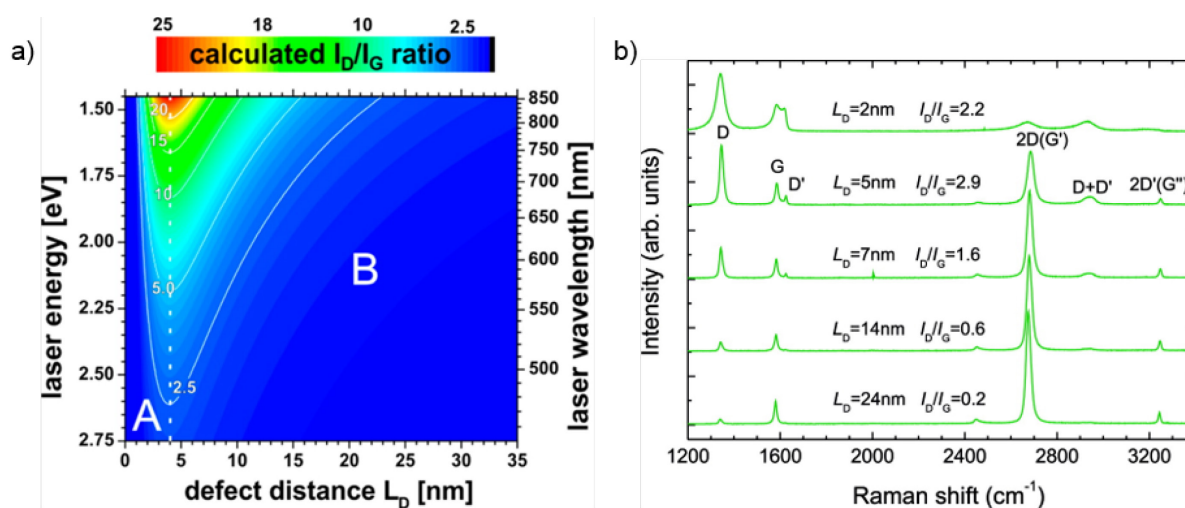
Figure 3.3. a) Generalised correlation between calculated I_D/I_G ratio, mean defect distance L_D and laser energy or wavelength. The region marked 'A' is designated as the region with a high density of defects, while the region marked 'B' is referred to as the low defect density region.[255] b) Raman spectra of five ion-bombarded SLG measured at E_L = 2.41 eV (λ_L = 5.14 nm); the respective I_D/I_G values are indicated for each spectrum.[267]

The peak at ~2700 cm^{-1}, designated the 2D band (or G' in older literature), originates from a double resonance process,[266] and provides information about the number of layers and stacking order. In pristine single-layer graphene, this peak has a sharp symmetrical Lorentzian lineshape, with linewidth ~25 cm^{-1}, and a greater intensity than the corresponding G band. The shape and intensity change significantly when moving from SLG to graphite, with interactions between AB-stacked graphene layers resulting in splitting of the 2D band into several components whose relative contributions can affect the peak shape, position and intensity (Figure 3.4). The relative intensities of the 2D and G bands (I_{2D}/I_G) is often used as a measure of exfoliation, along with analysis of peak shape. Turbostratic graphite also exhibits a

symmetrical Lorentzian lineshape, but with a much wider FWHM of ~50 cm^{-1} (refer to Figure 3.2, Raman spectrum of polymer-functionalised graphene).
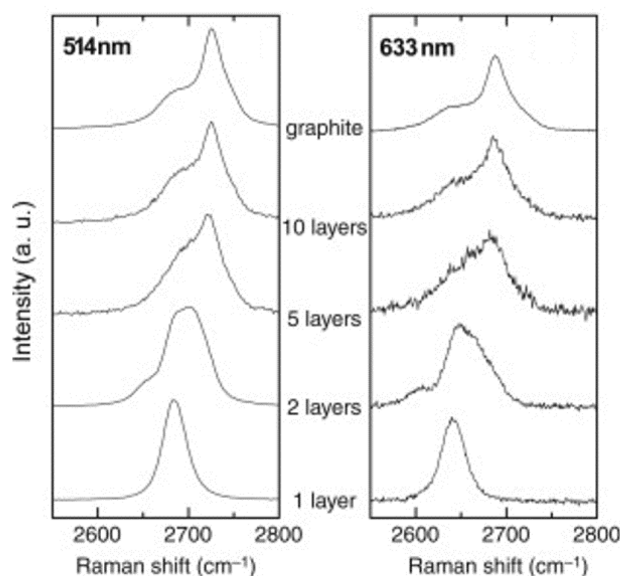
Figure 3.4. Evolution of the 2D peak as a function of number of layers for 514 and 633 nm excitations.[271]

Raman spectroscopy is a useful technique for the characterisation of carbon nanomaterials in general as it is fast, high resolution, and typically the samples (which may be solids, liquids and gases) require little or no special preparation. Raman is a non-destructive technique, providing suitable measurement parameters, including excitation wavelength, laser intensity, acquisition time and number of cycles, are considered. To obtain a good quality spectrum, a short excitation wavelength and higher power source are desirable, but in many cases, fluorescence may dominate the spectrum; instead, using a laser of a different wavelength and reduced power, but with increased acquisition time and collection cycles, can overcome this problem.

3.2.2. Statistical/scanning Raman

Due to the heterogeneous nature of bulk graphite samples, Raman mapping is necessary in order to obtain statistically relevant conclusions regarding functionalisation and exfoliation. Typically, over 500 independent sites are probed and the spectra averaged to give representative data reflecting the degree of grafting and the nature of stacking within the bulk material. In addition, spatial mapping of, for example, the I_D/I_G and I_{2D}/I_G ratios, can provide information on the distribution and homogeneity of functionalisation and exfoliation processes.

3.3. Ultraviolet-visible-near infrared absorption spectroscopy

When light shines on a material, an electron can absorb energy and be promoted to a higher electronic level if the energy of the incident light corresponds to the energy of that transition. Ultraviolet-visible-near infrared (UV-vis-nIR) absorption spectroscopy measures how much radiation is absorbed as a function of wavelength. The absorbance (A) of a material is related to the ratio of transmitted (I) to incident (I_0) radiation by:

$$A = \log_{10}\left(\frac{I}{I_0}\right) \tag{3.1}$$

At low concentrations, the Beer-Lambert law states that the absorbance at a specific wavelength is directly proportional to the concentration of a substance in solution (c):

$$A = \varepsilon c l \tag{3.2}$$

Where ε is the material's extinction coefficient at that wavelength and l is the pathlength. Since the extinction coefficient is an intrinsic property inherent to the sample and the pathlength is fixed experimentally, UV-vis-nIR absorbance is routinely used to determine the concentration of materials in solution.

However, signal intensity may be lost not only from sample absorbance but from scattering, reflections, or fluorescence. The usual protocol for compounds in solution is to subtract a background of solvent in an identical environment, which can minimise these effects. For suspensions with larger particles that have sizes similar to the wavelength of incident light, significant scattering, known as Tyndall scattering, may occur leading to a large loss of intensity, resulting in a higher perceived concentration. This effect is particularly significant in CNM dispersions due to the size of aggregates, and therefore careful sample preparation, typically involving extensive ultrasonication and centrifugation, is required to ensure that measurements are carried out on true solutions of individualised CNM species. Additionally, since low wavelength light undergoes more scattering (the intensity of scattered light depends on the fourth power of frequency), when determining the concentration of CNMs, absorptions at relatively high wavelengths are used.[52] For graphene, the absorption at 660 nm is taken as the reference. The typical value quoted in the literature for the extinction coefficient of graphene is ε_{660} = 2460 L g^{-1} m^{-1}, based on measurements obtained from natural flake graphite.[52] In principle, the extinction coefficient should vary according to the nature of the

graphitic starting material; however, the quoted number is often used as a standard in the literature from which to compare solubilities.

3.4. X-Ray diffraction

XRD is a commonly used technique to determine the structural arrangement of atoms or molecules in a crystalline material. X-rays typically have wavelengths between 0.1 Å and 100 Å, the same order of magnitude as interatomic distances in a crystal, resulting in significant diffraction. Several target materials are available for X-ray generation, but copper is the most widely used target metal, generating CuK_α radiation of 0.154 nm. Monochromatic X-rays striking a sample may be scattered by electrons surrounding the atoms, through different angles. In the case where diffracted waves are in-phase, constructive interference occurs, as determined by Bragg's law:

$$n\lambda = 2d \sin\theta \tag{3.3}$$

where n is any integer, λ is the wavelength of the X-ray (nm), d is the spacing between diffracting planes (nm) and θ is the incident angle (°). By varying the angle of incident radiation, all possible reflections from different planes may be identified; the intensity of the detected photons in relation to the scattering angle (commonly plotted as 2θ) gives the diffractogram pattern, specific to a certain crystal. Using Bragg's law, positions of diffraction peaks may be converted to d-spacings to allow identification of a crystal. Peak intensities provide information about how much scattering contributes to that reflection, or how much of a particular phase is present in the sample. The width of the signal, β (rad), is inversely proportional to the crystallite size, L_{hkl}, which can be calculated using the Scherrer equation:

$$L = \frac{K\lambda}{\beta \cos\theta} \tag{3.4}$$

where λ and θ are defined as before, and K is a dimensionless shape factor,[272] often taken as 1, but varies with the actual shape of the crystallite. For calculations of the crystallite size in graphite along the c-axis, a value of 0.91 is commonly used.[273] Corrections for instrumental line broadening may be performed by substituting an alternative value of β:

$$\beta^2 = B^2 - b^2 \tag{3.5}$$

where B is defined as the broadening of the diffraction peak, and b is the linewidth of a standard material with an essentially infinite crystallite size (typically Si) at approximately the same 2θ as the experimental line of interest in the sample. Since many different factors, in addition to instrumental line broadening, contribute to the width of the diffraction peak, such as lattice strain and imperfections, the value obtained from the Scherrer equation is the lower bound on the particle size.

Powder XRD has been routinely used to investigate the crystalline structure of graphite and related carbon materials. The average in-plane crystallite width can be obtained, as well as the crystallite height in the c-axis direction. When combined with calculations of interplanar spacings, the number of coherent graphene layers may be estimated, and therefore provide an indication of the degree of exfoliation. In particular, XRD has been used in the identification of stage structures in various GICs. XRD is a fast, non-destructive technique, and can often provide unambiguous sample determination. However, for graphite and its derivatives, the high aspect ratio of the flakes induces preferential orientation in the sample, and comparisons between reflections arising from different crystallographic planes should be made with care. Furthermore, measurements often require a large amount (~100 mg), which may be a limitation to the analysis of CNMs produced on a small scale.

3.5. X-Ray photoelectron spectroscopy

X-ray photoelectron spectroscopy (XPS) is a technique used to investigate the surface chemistry of solid materials. The elemental composition, chemical environment and electronic state of the surface constituents can all be determined by XPS. Spectra are obtained by irradiating a solid surface with a low-energy, monochromatic X-ray source; the incident rays cause the ejection of core-level electrons from atoms at the sample surface. The kinetic energy of a photoemitted electron is dependent on the incident photon energy, and on the binding energy of the electron, and is characteristic of the element, orbital and chemical environment from which the electron originated. Electrons are detected and their energies determined as a function of their velocity entering the detector. By measuring over a range of electron kinetic energies, it is possible to determine which elements are present near the surface of a sample and their chemical state.

The area under a peak in the XPS spectrum gives a measure of the relative amount of that element in the sample; the shape and precise position indicate the chemical state. XPS therefore allows quantification and identification of all elements, except hydrogen (in any compound, hydrogen does not have a core electron to be emitted). XPS is a surface sensitive technique because, while X-rays may penetrate deep into the sample, only electrons

generated near the surface (~10 nm depth) have sufficient energy to escape, and be detected. Due to inelastic collisions within the sample's atomic structure, ejected electrons from depths greater than a few nanometres lose energy and contribute only to the background signal, or are undetected.

XPS can be an extremely valuable method to investigate changes in atomic composition and structure of CNMs following functionalisation. The introduction of different atomic species can be monitored, and analysis of high resolution core level spectra allows differentiation between various chemical environments, and therefore chemical bonds. For CNMs in particular, the various sp^2 and sp^3 carbon environments (for example, C-C, C=C, C-O, C=O, COOR) may be differentiated within the C1s peak by their different binding energies; further cross-referencing with the O1s peak may provide confirmation of these bonds. Deconvolution of these peaks often proves challenging, however, due to small shift differences and the effects of line broadening arising from surface charging, sample contamination, overlapping signals, and resolution limits for weak signals. Quantification of surface modifications is possible, although some degree of caution must be exercised (the typical error quoted is 10%): because XPS primarily characterises the surface, any conclusions drawn regarding the bulk sample should be considered carefully. Only small amounts of sample are required for analysis, but care should be taken during preparation to avoid contamination from adsorbed atmospheric species (such as H_2O and CO_2), which can affect quantification results. The detection limit is typically around 0.1 at%, so for CNMs with very low degrees of functionalisation or doping, quantification may not be applicable.

3.6. Microscopy

3.6.1. Scanning electron microscopy

Scanning electron microscopy (SEM) produces images by raster-scanning the sample with a focused high-energy beam of electrons. The electrons can penetrate to a depth of a few microns, depending on the accelerating voltage and the density of the sample. As electrons interact with the sample, backscattered (BSE) and secondary electrons (SE) are produced, as well as characteristic X-rays, which are then collected by a detector. Typically, topographical SEM images are formed from collected low-energy SE, which originate from approximately the top 15 nm of the sample surface. These images are useful for showing the morphology and topography of the samples. The maximum resolution obtained in an SEM depends on several factors, such as the electron spot size and interaction volume of the electron beam with the sample, but typically, resolution is on the order of 1-20 nm; therefore, whilst SEM is a useful technique for imaging the size and overall morphology of flakes, single-layer graphene

cannot be distinguished from a multi-layer stack. In addition to imaging, energy dispersive X-ray spectra (EDX or EDS) can provide elemental analysis by detecting emitted X-rays characteristic of the elements present. SEM imaging relies on the conductivity of samples, to dissipate the build-up of electrostatic charge; bulk graphite and graphene therefore present few problems although highly-functionalised samples may require coating with a thin layer of metal nanoparticles, usually Au or Cr. Generally, graphite powder samples can be mounted onto an aluminium stub by double-sided carbon tape or silver paint, or dispersions can be drop-cast directly onto the stubs; all samples must be thoroughly dried before imaging.

3.6.2. Transmission electron microscopy

Imaging by TEM is achieved by focusing a high-energy electron beam onto a thin sample and detecting the intensity of the transmitted electrons; with particular imaging conditions, atomic resolution can be achieved. Most commonly, images are generated in bright field mode, which measures the intensity of unscattered electrons; thicker areas of the sample scatter or absorb more electrons and appear darker, whilst thinner areas transmit electrons and therefore appear brighter. Dark field images are produced by collecting only scattered electrons, which may be useful for studying crystal defects and specific crystallographic phases. TEM can also detect other scattering events, such as Bragg scattering, X-ray scattering and inelastic scattering, providing useful complementary characterisation methods including selected area electron diffraction (SAED), EDX or electron energy loss spectroscopy (EELS). Electron diffraction in graphite/graphene typically shows a pattern of concentric hexagons with six-fold symmetry (Figure 3.5c); analysis of the relative intensities of the inner and outer spots can provide unambiguous proof of single-layer graphene.[52] The combination of high resolution TEM and electron diffraction is therefore invaluable for the characterisation of single- and multi-layer graphene (Figure 3.5). Despite the very high energy of the electron beam, CNMs are generally stable for relatively long periods at typical operating voltages (200 keV), although imaging at lower voltages (80 keV) can prevent specimen damage in more sensitive samples. Imaging is limited to very small areas within the specimen, so care should be exercised when drawing conclusions regarding the bulk sample.
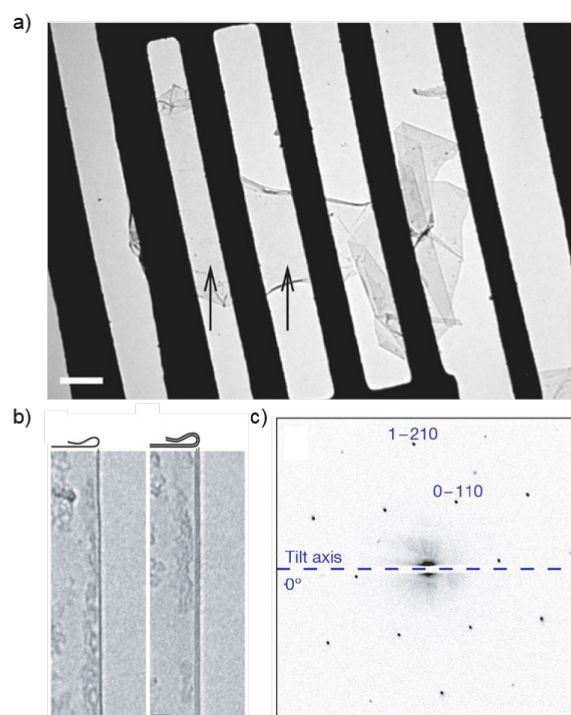
Figure 3.5. a) Bright-field TEM image of a suspended graphene membrane; the arrows indicate monolayer regions; scale bar, 500 nm. b) TEM images of folded edges for monolayer and bilayer graphene, respectively; scale bars, 2 nm. c) Electron diffraction pattern from a graphene monolayer, with Bragg reflections labelled. Adapted from ref 274.

3.6.3. Atomic force microscopy

AFM is used to image surface topographies with a resolution down to the nanometre level. The AFM probe, a sharp tip typically made of silicon or silicon nitride at the end of a flexible cantilever, is raster-scanned across a surface; the interaction between the tip and surface causes deflection of the tip which allows measurement of the sample height to generate a mapped image. AFM is frequently used for imaging CNMs, and is useful for measuring the lateral size, number of layers and thicknesses of isolated graphene sheets and stacks. However, sample preparation can be difficult; very dilute graphene dispersions are usually drop-cast, spin-coated, or spray-coated onto cleaned silica or freshly-cleaved mica substrates, and thoroughly dried under vacuum before imaging. AFM is time consuming and usually can only image extremely small areas; as with TEM, sufficient measurements should be taken to ensure a representative picture of the bulk sample. Furthermore, identification of graphene monolayers in the presence of other impurities is often non-trivial, but comparison of observed flake sizes and shapes with those obtained by TEM, as well as cross-characterisation with Raman spectroscopy, can enable identification of graphene sheets, residual solvent or other monolayer impurities in the sample.

3.7. Brunauer-Emmett-Teller surface area analysis

The specific surface area of a sample may be determined by measuring the volume of gas, typically nitrogen, physisorbed onto the surface across a range of pressures at constant temperature, usually -196 °C (liquid nitrogen). The Brunauer-Emmett-Teller (BET) adsorption isotherm equation can be applied to calculate the adsorbed gas monolayer capacity, v_m:

$$\frac{1}{v[(p_0/p) - 1]} = \frac{c - 1}{v_m c}\left(\frac{p}{p_0}\right) + \frac{1}{v_m c} \tag{3.6}$$

where p is the partial vapour pressure of adsorbate gas in equilibrium with the surface at the temperature of adsorption, p_0 is the saturation pressure, v is the volume of gas adsorbed, and c is an empirical dimensionless constant related to the enthalpy of adsorption. A plot of $1/v[(p_0/p)-1]$ against the relative pressure, p/p_0, yields a straight line from which the value of v_m may be obtained. In general, this relation is only applicable in the range $0.05<p/p_0<0.3$. The amount of adsorbed gas can then be correlated to the specific surface area (S_{BET}) of the material using:

$$S_{BET} = \frac{v_m N_A a_{ads}}{Vm} \tag{3.7}$$

where N_A is Avogadro's number, a_{ads} is the adsorption cross-section of the adsorbing species (for N_2, a_{ads} is 0.162 nm^2), V is the molar volume of the adsorbate gas, and m is the mass of the solid sample. BET measurements are useful to characterise the surface area of CNMs; however, a relatively large amount of sample is required for analysis (generally, at least 50 mg).

3.8. Nuclear magnetic resonance spectroscopy

NMR spectroscopy is one of the dominant methods of analysis in organic chemistry because it can often provide detailed structural information on the compounds of interest. The nucleus of an atom has a characteristic nuclear spin (I); isotopes of particular interest for NMR spectroscopy such as ^{1}H, ^{13}C, ^{19}F and ^{31}P all have $I = ½$. Under the influence of an external magnetic field, the nucleus can be aligned either with the field (lower energy state) or against it (higher energy). When radiation of a resonant frequency is applied, nuclei in the lower energy state are excited to the higher state; the absorption of energy, or the subsequent relaxation can be observed either by scanning through a range of radio frequencies, or more commonly nowadays, by the Fourier Transform method which subjects the sample to one broad pulse of

radio waves used to excite all nuclei, and subsequent results are later deconvoluted. In a real molecule, the effective magnetic field 'felt' by a particular nucleus depends on the magnetic effect of nearby nuclei and electrons, which causes the excitations to occur at slightly different frequencies, depending on whether a stronger or weaker effective magnetic field is felt. These differences are plotted as chemical shifts (δ, in parts per million, ppm) relative to a reference zero point (in proton NMR this is usually tetramethylsilane). The larger the shift from the zero point, typically the more deshielded the nucleus environment. The chemical environments of different nuclei can therefore be probed to allow effective characterisation of the whole molecule.

3.9. Gel permeation chromatography

Gel permeation chromatography (GPC) is commonly used to characterise polymer molar mass and dispersity. Separation of a mixture of polymers with different molecular weights within a gel column is based on the size of the analytes. Small analytes can enter pores more easily, and therefore are retained for longer and eluted last. Conversely, larger polymers are less easily trapped within the pores and are eluted quickly. The retention time therefore provides information regarding the polymer size, and requires calibrating against a polymer standard to obtain the molar mass and dispersity.

4. Materials and methods

4.1. Graphite

Natural flake graphite, was obtained from Graphexel Ltd. (grade: 2369). Large flake natural graphite ('Natural Graphite') was purchased from NGS Naturgraphit GmbH with a purity of 99.9% C and flake size of 2-5 mm, stated by the manufacturer. Graphite nanoplatelets (Elicarb Materials Grade Graphene Powder SP8082) were supplied by Thomas Swan, with a typical lateral size of 1-5 μm, I_D/I_G 0.07-0.1, surface area 30-50 m^2 g^{-1}, and an sp^2 carbon content of 98%w/w, as stated by the manufacturer. Graphite nanofibres were obtained from FutureCarbonGmbH (batch no. A09-122.123). Few-layer graphene (FLG) was supplied by Cambridge Nanosystems. Flakes have a thickness of <1 nm, an average diameter of 0.5 μm (from 0.25 μm to 1 μm), and a carbon purity >99.5%, as stated by the manufacturer.

4.2. Materials

4.2.1. List of chemicals

Table 4.1. List of chemicals and solvents used in this thesis.

Chemical	Formula	Grade (%)	Supplier
1-Bromododecane	$C_{12}H_{25}Br$	97	Sigma-Aldrich
(1-Bromoethyl)benzene	C_8H_9Br	97	Sigma-Aldrich
Bromine	Br_2	99.99	Sigma-Aldrich
Copper(I) bromide	CuBr	98	Sigma-Aldrich
Copper(II) bromide	$CuBr_2$	99	Sigma-Aldrich
Dodecane	$C_{12}H_{26}$	99	Sigma-Aldrich
Methyl methacrylate	$C_5H_8O_2$	99	Sigma-Aldrich
N,N,N',N'',N''-Pentamethyldiethylenetriamine (PMDETA)	$C_9H_{23}N_3$	99	Sigma-Aldrich
Naphthalene	$C_{10}H_8$	99	Sigma-Aldrich
Poly(ethylene glycol) methyl ether (mPEG, M_w 2000 g mol^{-1})	$CH_3(C_2H_4O)_nOH$	-	Sigma-Aldrich
Sodium	Na	99.95, ingot	Sigma-Aldrich
Trifluoroacetic anhydride	$C_4F_6O_3$	99	Sigma-Aldrich
1,2-Dimethoxyethane	$C_4H_{10}O_2$	99.5, anhydrous	Sigma-Aldrich
2-Propanol	C_3H_8O	99	VWR
Acetone	C_3H_6O	99.9	Sigma-Aldrich
Deuterated chloroform	$CDCl_3$	99.8	Sigma-Aldrich
Dichloromethane	CH_2Cl_2	99.8	VWR
Diethyl ether	$C_4H_{10}O$	99.5	VWR
Ethanol	C_2H_6O	99.9	VWR
Glacial acetic acid	$C_2H_4O_2$	99.85	Sigma-Aldrich

Chemical	Formula	Grade (%)	Supplier
n-Hexane	C_6H_{14}	97	VWR
N,N-Dimethylacetamide	C_4H_9NO	99.8, anhydrous	Sigma-Aldrich
N,N-Dimethylformamide	C_3H_7NO	99.9	VWR
Tetrahydrofuran	C_4H_8O	99, anhydrous	In house
Tetrahydrofuran (washing)	C_4H_8O	99.8	VWR
Water	H_2O	99.99	VWR
Triethylamine	$C_6H_{15}N$	99	Sigma-Aldrich
Phosphorus pentoxide	P_2O_5	98	Sigma-Aldrich
Calcium hydride	CaH_2	99.99	Sigma-Aldrich
Oxygen/Nitrogen (20/80%)	O_2/N_2	-	BOC

4.2.2. List of other materials

Aluminium oxide 90 active neutral was obtained from Merck UK. Molecular sieves were purchased from Sigma-Aldrich and activated by microwaving (800 W, 90 s) and heating at 250 °C for 3 h under vacuum, before keeping under vacuum for a further 16 h at room temperature. Holey carbon films on 300 mesh copper grids for TEM experiments were purchased from Elektron Technology UK Ltd. For AFM imaging, silicon wafers with a 300 nm SiO_2 coating were used to enable easy identification of single- and few-layer graphene and were obtained from PI-KEM Ltd.

4.2.3. Materials preparation

THF, dried in-house in a solvent-drying tower packed with alumina, and anhydrous DME were degassed *via* a freeze-pump-thaw method then further dried over 20 vol% 4 Å activated molecular sieves. *N,N*-dimethylacetamide (DMAc) was dried over 20 vol% 4 Å activated molecular sieves. 1-bromododecane, dodecane and trifluoroacetic anhydride were degassed *via* a freeze-pump-thaw method and dried over 10 vol% 4 Å activated molecular sieves. Naphthalene and mPEG were dried overnight under vacuum in the presence of phosphorus pentoxide before use. Sodium, bromine, (1-bromoethyl)benzene, PMDETA, and copper(II) bromide were used as received. Methyl methacrylate was passed through an alumina column to remove stabilisers, before degassing *via* freeze-pump-thaw and drying over 20 vol% 4 Å activated molecular sieves. Prior to ATRP reactions, acetone was distilled over CaH_2 and stored under nitrogen. Immediately before use, both monomer and solvent were purged with nitrogen for 30 min. Copper(I) bromide was purified by washing with glacial acetic acid, followed by 2-propanol, and then dried under vacuum.[275]

4.3. Experimental procedures

All work involving group 1 metals and reduced graphites was performed in an mBraun Labmaster glove box under nitrogen atmosphere with water and oxygen levels <0.1 ppm, unless otherwise stated. All glassware used, including glass stirrer bars, was dried at 150 °C in a drying oven for 24 h, prior to use.

4.3.1. Preparation of sodium naphthalide solution

A stock sodium naphthalide solution was prepared to allow for accurate, simple addition of sodium to the dried graphite. In a typical experiment, 23 mg (1 mmol) sodium and 128 mg (1 mmol) dried naphthalene were dissolved in 10 mL degassed anhydrous THF in a nitrogen-filled glove box, and stirred with a glass stirrer bar for 1 day until all sodium had dissolved, forming a dark-green solution. The solution remained stable for up to one week, slowly turning brown.

Identical procedures were followed for the preparation of DME and DMAc solutions of sodium naphthalide. The dark green DME solution did not remain stable for more than two days, turning a red-brown colour, so was added to graphite as soon as all sodium had dissolved (typically after 1 day). DMAc was stable for much longer, only producing a white precipitate after one week.

4.3.2. Dodecyl-functionalised graphites

Synthesis of C$_{12}$H$_{25}$-NFG. A Young's tube containing graphite (15 mg, 1.25 mmol carbon) and a magnetic stirrer bar was heated at 400 °C for 1 h under vacuum, and then kept under vacuum for 16 h at room temperature, before placing in a glove box. 1.04 mL (C/Na = 12) of the sodium naphthalide solution was added to the Young's tube and the concentration of graphite in THF adjusted to 0.1 M by addition of 11.46 mL degassed anhydrous THF ([Na] = 0.008 M). The suspension was stirred for 1 day, after which time the graphite turned a shiny blue colour. The mixture was bath ultrasonicated for 5 min before 0.076 mL (0.313 mmol, 3 eq. per sodium) 1-bromododecane was added dropwise to the tube. Upon addition, the graphite sedimented immediately, leaving a cloudy grey supernatant. The reaction was stirred at room temperature for 1 day under N$_2$. After bubbling dry O$_2$/N$_2$ (20/80%, ~1 L) into the solution for 15 min, the solution was stirred overnight under dry O$_2$/N$_2$ to quench any remaining charges on the functionalised graphene. The mixture was filtered through a 0.1 μm PTFE membrane (Millipore), and washed thoroughly with hexane, THF, ethanol and water to remove any residual naphthalene, alkyl by-products and sodium salts formed during

the reaction. The product was obtained as a dark grey powder after washing with ethanol and drying overnight under vacuum at 80 °C.

Synthesis of $C_{12}H_{25}$-(graphite). An identical procedure to above was followed with different starting graphites to obtain dodecyl-grafted products $C_{12}H_{25}$-LFG, $C_{12}H_{25}$-GP, $C_{12}H_{25}$-GNF and $C_{12}H_{25}$-FLG.

Synthesis of $C_{12}H_{25}$-(solvent)-NFG. The procedure described above using DME or DMAc in place of THF was used to obtain the products $C_{12}H_{25}$-DME-NFG and $C_{12}H_{25}$-DMAc-NFG.

Quenched controls, Na-(solvent)-(graphite). A control experiment excluding the addition of 1-bromododecane was conducted as above, varying the starting graphite and solvent as appropriate. The quenched products were washed and dried thoroughly, prior to characterisation, to obtain Na-DME-NFG, Na-DMAc-NFG, Na-THF-LFG, Na-THF-GP, Na-DMAc-GP, Na-THF-GNF and Na-THF-FLG.

Dodecane adsorption control, $C_{12}H_{26}$+NFG. In an identical procedure to above, dried and degassed dodecane (0.071 mL, 0.313 mmol), in place of 1-bromododecane, was added dropwise to the graphenide dispersion. After stirring at room temperature for 1 day under nitrogen, the reaction was quenched with dry O_2/N_2, and washed and dried as before, to yield the product $C_{12}H_{26}$+NFG.

4.3.3. PMMA grafting

4.3.3.1. Grafting-to approach

Synthesis of different molar mass PMMA by ATRP. In a typical experiment, CuBr (156.06 mg, 1.09 mmol) and $CuBr_2$ (12.14 mg, 0.054 mmol) were placed in a Schlenk flask equipped with a stirrer bar, which was previously evacuated and flushed with nitrogen. The flask was evacuated and filled with nitrogen three times and then left under nitrogen. Subsequently, methyl methacrylate (6 mL, 54.26 mmol) and acetone (3.12 mL) were added to the flask. The complexing agent, PMDETA (238.8 µL, 1.14 mmol) was added, and the solution was stirred until a blue-green colour developed, indicating the formation of the Cu complex. The mixture was degassed using three freeze-pump-thaw cycles. The initiator (1-bromoethyl)benzene (149.4 µL, 1.05 mmol) was introduced and the flask was placed in an oil bath and stirred at 50 °C for different periods of time (30 min, 1 h and 2 h) to obtain different molecular weight polymers. The flask was removed from the oil bath and the reaction stopped by exposing to air and dilution with THF. The solution was filtered through a column filled with neutral alumina washing with THF to remove side products. The solvent was evaporated under

reduced pressure and the polymer was precipitated in dichloromethane/diethyl ether (35.7%, 56.3%, 68.2% conversion for 30 min, 1 h and 2 h, respectively). GPC (DMF): M_n = 4980 g mol^{-1} ($Đ$ = 1.56), M_n = 8040 g mol^{-1} ($Đ$ = 1.62), and M_n = 9980 g mol^{-1} ($Đ$ = 1.65) for 30 minutes, 1 hour and 2 hours reaction time, respectively. ^{1}H NMR (CDCl$_3$) for M_n ~5000 g mol^{-1}: δ 0.85-1.03 (m, 3H, -CH$_3$), 1.82-1.95 (m, 2H, -CH$_2$-), 3.61 (m, 3H, -COOCH$_3$) ppm.

The polymers were dried for 24 hours under vacuum prior to subsequent reaction.

Synthesis of FLG-g-t-(n). In a typical experiment, a Young's tube containing FLG (15 mg, 1.25 mmol carbon) and a magnetic stirrer bar was heated at 400 °C for 1 h under vacuum, and then kept under vacuum for 16 h at room temperature, before placing in a glove box. 1.04 mL (C/Na = 12) of sodium naphthalide solution was added to the Young's tube followed by 11.46 mL degassed anhydrous THF. The black suspension was stirred for 1 day, before varying amounts of brominated PMMA (520 mg (M_n = 5000 g mol^{-1}), 832 mg (M_n = 8000 g mol^{-1}), 1.04 g (M_n = 10000 g mol^{-1}); all 0.104 mmol) were added to the reaction mixture. The reaction was stirred at room temperature for 1 day under N$_2$. After bubbling dry O$_2$/N$_2$ into the solution for 15 min, the solution was stirred overnight under dry O$_2$/N$_2$. The mixture was filtered through a 0.1 μm PTFE membrane, and washed thoroughly with THF, acetone, water and ethanol, before drying under vacuum at 80 °C.

Na-THF-FLG+PMMA-Br control. Quenched and dried Na-THF-FLG (15 mg) was stirred with 520 mg PMMA-Br (M_n = 5000 g mol^{-1}) in THF (12.5 mL). After stirring for 1 day at room temperature, the reaction was washed with THF, acetone, water and ethanol, before drying under vacuum at 80 °C.

4.3.3.2. Grafting-from approach

Functionalisation of graphene with trifluoroacetic anhydride (TFAA). A Young's tube containing FLG (15 mg, 1.25 mmol carbon) and a magnetic stirrer bar was heated at 400 °C for 1 h under vacuum, and then kept under vacuum for 16 h at room temperature, before placing in a glove box. 1.04 mL (C/Na = 12) of sodium naphthalide solution was added to the Young's tube followed by 11.46 mL degassed anhydrous THF. The suspension was stirred for 1 day, before sealing and transferring to a Schlenk line outside the glove box. Dried and degassed TFAA (44.07 μL 0.313 mmol) was added slowly to the reaction mixture and the solution was allowed to stir for 1 day under N$_2$. After bubbling dry O$_2$/N$_2$ into the solution for 15 min, the solution was stirred overnight under dry O$_2$/N$_2$. The mixture was filtered through a 0.1 μm PTFE membrane, and washed thoroughly with THF, water and ethanol, before drying under vacuum at 80 °C.

FLG+TFAA control. Dried FLG (15 mg) was stirred with 44.07 µL dried and degassed TFAA in THF (12.5 mL). After stirring for 1 day at room temperature, the reaction was washed with THF, water and ethanol, before drying under vacuum at 80 °C.

Synthesis of FLG-g-f-(n). In a typical experiment, a Young's tube containing FLG (15 mg, 1.25 mmol carbon) and a magnetic stirrer bar was heated at 400 °C for 1 h under vacuum, and then kept under vacuum for 16 h at room temperature, before placing in a glove box. 1.04 mL (C/Na = 12) of sodium naphthalide solution was added to the Young's tube followed by 11.46 mL degassed anhydrous THF. The suspension was stirred for 1 day, then sealed and transferred to a Schlenk line outside the glove box. After cooling to 0 °C, different amounts of previously degassed methyl methacrylate (162 µL, 1.56 mmol, (M_n = 800 g mol^{-1}); 337 µL, 3.12 mmol, (M_n = 1000 g mol^{-1}); 674 µL, 6.24 mmol, (M_n = 1400 g mol^{-1}); 1.04 mL, 9.36 mmol, (M_n = 2300 g mol^{-1})) were added slowly to the reaction mixture. The reaction was stirred at room temperature for 1 day under N_2, becoming increasingly viscous. After bubbling dry O_2/N_2 into the solution for 15 min, the solution was stirred overnight under dry O_2/N_2. The mixture was filtered through a 0.1 µm PTFE membrane, and washed thoroughly with THF, acetone, water and ethanol, before drying under vacuum at 80 °C.

FLG+MMA control. Quenched and dried Na-THF-FLG (15 mg) was stirred with 162 µL MMA in THF (12.5 mL). After stirring for 1 day at room temperature, the reaction was washed with THF, acetone, water and ethanol, before drying under vacuum at 80 °C.

4.3.3.3. Graft-to and graft-from on natural flake graphite

Synthesis of NFG-g-t. An identical procedure to the synthesis of FLG-*g-t*-(n) was followed, using 15 mg NFG in place of FLG, and 520 mg PMMA-Br (M_n = 5000 g mol^{-1}).

Synthesis of NFG-g-f. An identical procedure to the synthesis of FLG-*g-f*-(n) was followed, using 15 mg NFG in place of FLG, and 337 µL (3.12 mmol) MMA.

4.3.4. Bromination and polymerisation

4.3.4.1. Bromination

Synthesis of FLG2-Br. A Young's tube containing FLG2 (60 mg, 5 mmol carbon) and a glass stirrer bar was heated at 400 °C for 1 h under vacuum, and then kept under vacuum for 16 h at room temperature, before placing in a glove box. 4.16 mL of the sodium-naphthalide solution was added to the Young's tube and the concentration of FLG2 in THF adjusted to 0.1 M by addition of 45.84 mL degassed anhydrous THF (C/Na = 12, [Na] = 0.008 M). The suspension was stirred for 1 day, then bath ultrasonicated for 5 min, before connecting to an

Ar-filled Schlenk line and purging 3 times. After cooling to 0 °C, 1 mL (19.4 mmol) liquid bromine was added dropwise slowly, under positive pressure of argon. The reaction was allowed to reach room temperature and stirred for 1 day, after which time the FLG sedimented leaving a brown supernatant. After bubbling dry O_2/N_2 through the solution for 15 min, the solution was stirred overnight under dry O_2/N_2 to quench any remaining charges on the functionalised graphene. The mixture was filtered through a 0.1 µm PTFE membrane, and washed thoroughly with DMAc and THF to remove any residual sodium, naphthalene and bromine by-products. The product FLG2-Br was obtained as a black powder after drying overnight under vacuum.

Quenched control, Na-THF-FLG2. A control experiment excluding the addition of bromine was conducted in the same way as before. The quenched product was washed and dried thoroughly, prior to characterisation.

Bromine adsorption control, FLG2+Br$_2$. A Young's tube containing FLG2 (15 mg, 1.25 mmol carbon) and a glass stirrer bar was heated at 400 °C for 1 h under vacuum, and then kept under vacuum for 16 h at room temperature, before placing in a glove box. 12.5 mL degassed anhydrous THF was added and the suspension was stirred for 1 day. Following ultrasonication for 5 min, the flask was connected to an Ar-filled Schlenk line and purged three times. After cooling to 0 °C, 0.25 mL (4.85 mmol) liquid bromine was added dropwise under positive pressure of argon. The reaction was allowed to reach room temperature and stirred for 1 day. After bubbling dry O_2/N_2 through the solution for 15 min, the solution was stirred overnight under dry O_2/N_2. The mixture was filtered through a 0.1 µm PTFE membrane, and washed thoroughly with DMAc and THF. The product was obtained after drying overnight under vacuum.

4.3.4.2. Atom transfer radical polymerisation

Synthesis of FLG2-PMMA via ATRP. A Schlenk flask containing FLG2-Br (20 mg, 0.02 mmol -Br) and a stirrer bar was heated at 80 °C under vacuum for 2 h. 20 mL dry acetone was added, and the mixture ultrasonicated for 10 min to disperse the FLG2-Br. The suspension was degassed by three freeze-pump-thaw cycles. Separately, CuBr (8 mg, 0.056 mmol) and $CuBr_2$ (1.26 mg, 0.0056 mmol) were added to a Schlenk flask equipped with a stirrer bar, which was previously evacuated and flushed with nitrogen. The flask was degassed and filled with nitrogen three times and then left under nitrogen. Subsequently, methyl methacrylate (1 mL, 9.36 mmol) and PMDETA (0.012 mL, 0.057 mmol) were added and the solution was stirred until the Cu complex had formed, turning a blue-green colour. The mixture was degassed by three freeze-pump-thaw cycles, then introduced to the FLG2-Br

solution using a dry, air-free syringe, and the flask placed in an oil bath and stirred at 50 °C for 2 h. The flask was then removed from the oil bath and the reaction stopped by exposing to air and dilution with THF. The mixture was filtered through a 0.1 μm PTFE membrane and washed with copious amounts of acetone and THF, then dried under vacuum.

ATRP control, FLG2+MMA. In a similar reaction and washing sequence to before, as-received FLG2 (20 mg), rather than FLG2-Br, was used as the initiator in a polymerisation control reaction.

4.3.4.3. Nucleophilic substitution

Synthesis of FLG2-PEG. A round-bottomed flask containing FLG2-Br (20 mg, 0.02 mmol -Br) and a stirrer bar was heated at 80 °C under vacuum for 2 h. 15 mL dry THF and 5 mL dichloromethane were added and the mixture ultrasonicated for 10 min to disperse the FLG2-Br. mPEG (100 mg, 0.05 mmol) was added then the reaction mixture was stirred at 40 °C for 2.5 h. The black suspension was filtered through a 0.1 μm PTFE membrane and washed with copious amounts of THF, water and ethanol. The product FLG2-PEG was obtained after drying under vacuum.

Substitution control, FLG2+PEG. In a similar reaction and washing sequence to before, as-received FLG2 (20 mg), rather than FLG2-Br, was stirred with mPEG in a control reaction.

Synthesis of FLG2-OH. FLG2-OH was obtained by an identical procedure using water (3 mL) as the hydroxyl source, instead of mPEG. The product was washed and dried as before, prior to characterisation.

4.4. Equipment and characterisation

4.4.1. TGA-MS

TGA-MS was performed using a Mettler Toledo TGA/DSC 1 instrument integrated with a Hiden HPR-20 QIC EGA mass spectrometer, with lidded 70 μL alumina pans. For a typical measurement, ~1 mg sample was heated to 100 °C under nitrogen atmosphere (60 mL min^{-1}) at a rate of 35 °C min^{-1} and held isothermally for 28 min, to purge the system and remove residual water or volatile solvent. The temperature was then increased from 100 °C to 850 °C at 10 °C min^{-1} under nitrogen or air atmosphere (60 mL min^{-1}). A background of the pan only was performed and manually subtracted from each sample measurement. Mass spectrometry analysis was run at a pressure in the range of 10^{-6} mbar, operating in multiple ion detection (MID) mode with a 200 mA filament current. No more than 16 *m/z* values up to 200 amu were

selected with a lowest detectable pressure range of 10^{-13} Torr using the secondary electron multiplier (SEM) detector. For specific fragments (*m/z* 28, 44) the Faraday cup detector was used. All samples were dried at 80 °C under vacuum for 1 h before measurement. For MS data, spectra measurement times (*t*) were converted to TGA temperatures (*T*) by:

$$T = 100 + \frac{(t - 1801)}{6} \tag{4.1}$$

based on the isotherm and heating ramp parameters given above.

4.4.1.1. Calculation of grafting ratio

The presence of trapped solvent between the graphene layers after exfoliation may lead to an overestimate of the functional groups introduced on the sheets, from TGA measurements alone. In order to provide a more accurate quantification of these functional groups, the relative peak areas of different MS fragments evolved during TGA were analysed to determine the relative quantities of trapped solvent and grafted moieties. In these calculations, it is assumed that the grafted moiety leaves negligible residue after pyrolysis (reasonable for PMMA-Br (Figure 4.1b) and 1-bromododecane (Appendix I, Figure I.5)), and that the residual weight is graphene carbon. The method is explained below, using grafting of PMMA on FLG as an example.
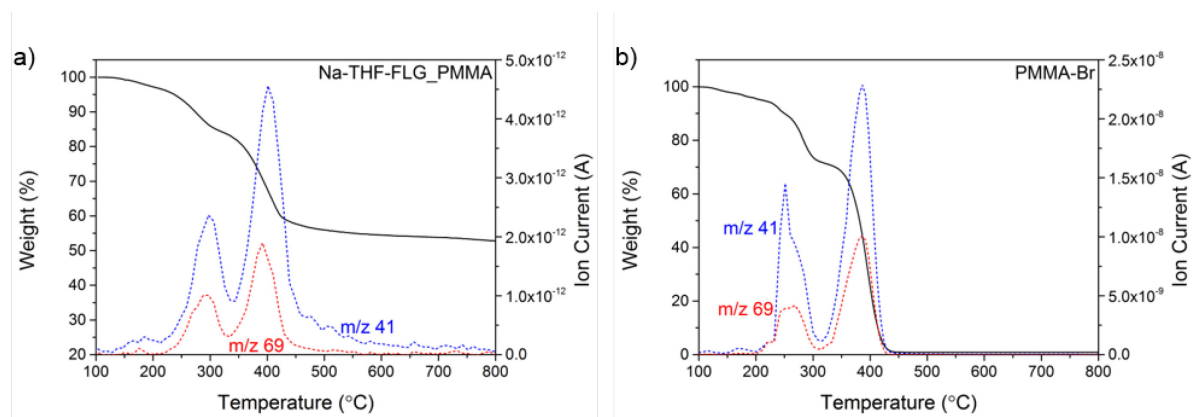
Figure 4.1. TGA-MS profiles of a) Na-THF-FLG_PMMA, and b) PMMA-Br, and accompanying mass fragments *m/z* 41 (PMMA and THF) and 69 (PMMA only).

TGA-MS data of a control mixture of Na-THF-FLG and PMMA (Na-THF-FLG_PMMA) in a known ratio was studied to determine the sensitivity of detection of THF species relative to PMMA (Figure 4.1a). Two mass fragments were selected, one which is present in both THF and PMMA (e.g. *m/z* = 41) and one which arises from PMMA alone (e.g. *m/z* = 69), to relate the intensities of the MS signals to the quantities of each species. As a first approximation, it

was assumed that the decomposition of mixed PMMA would follow a similar pathway to covalently-grafted PMMA. The amount of THF in Na-THF-FLG is known (see Chapter 6, Figure 6.2b). Therefore, in Na-THF-FLG_PMMA, the relative masses of each species are known.

The TGA-MS of PMMA alone shows typical signals $m/z = 41$ (found also in THF, Chapter 6, Figure 6.2b) and $m/z = 69$ (found only in PMMA) (Figure 4.1b). Whilst the absolute areas of these two signals fluctuates with the pressure inside the MS, and with other external factors, the *relative* areas remain constant and afford the relation $A_{41} = (1.8\pm0.3)\times A_{69}$ (average of three measurements). OriginPro 9.0.0 was used to integrate peak areas, using a straight-line baseline function.

In the control sample Na-THF-FLG_PMMA, the signal from $m/z = 41$ arises from PMMA and THF. The area of $m/z = 41$ can be split into its contributions from PMMA (A_{41}(PMMA)) and THF (A_{41}(THF)). Since m/z 69 arises from PMMA only, A_{41}(PMMA) can be calculated using the relation above:

$$A_{41}(PMMA) = 1.8 \times A_{69} \tag{4.2}$$

The THF contribution to the peak area is given by:

$$A_{41}(THF) = A_{41}(total) - A_{41}(PMMA) \tag{4.3}$$

The ratio of these two areas, A_{41}(THF) and A_{41}(PMMA), can be compared to the ratio of the known masses of PMMA and THF, and used to derive a sensitivity factor, S, relating the relative sensitivities of fragment detection to the relative masses:

$$S = \frac{A_{41}(PMMA)}{A_{41}(THF)} \times \frac{Mass\%(THF)}{Mass\%(PMMA)} \tag{4.4}$$

A sensitivity factor of $S = 2.2\pm0.5$ was calculated (average of 3 measurements) for PMMA and THF (i.e. for a given amount of sample, the same amount of PMMA is detected at an intensity 2.2 times weaker than that amount of THF) and applied to all TGA-MS calculations to obtain the relative quantities of PMMA and THF in the PMMA-grafted samples.

In the grafted samples, the fractional contributions of PMMA (f_{PMMA}) and THF (f_{THF}) to each weight loss are given by:

$$f_{PMMA} = \frac{S \times A_{41}(PMMA)}{S \times A_{41}(PMMA) + A_{41}(THF)} \qquad (4.5)$$

and:

$$f_{THF} = \frac{A_{41}(THF)}{S \times A_{41}(PMMA) + A_{41}(THF)} \qquad (4.6)$$

The individual mass loss attributed to PMMA can be calculated by multiplying f_{PMMA} by the observed weight loss, and similarly for the mass attributed to THF.

$$wt\%_{PMMA} = wt\%_{total} \times f_{PMMA} \qquad (4.7)$$

The same method was applied to calculate the degree of dodecyl grafting, in this case using the mass fragments m/z 43 (from dodecyl and solvent) and 57 (from dodecyl alone). Sensitivity factors of 3.5±0.3, 1.1±0.5, and 0.8±0.5 were obtained for the systems in THF, DME and DMAc, respectively, and were used to calculate the grafting ratios and grafting density values.

The grafting ratio (GR), defined as the mass fraction of grafted material, R, relative to the carbon framework, C, was obtained by taking the weight loss attributed to R ($wt\%_R$, calculated by the method above) and the residual weight as remaining graphite starting material ($wt\%_C$):

$$GR = \frac{wt\%_R}{wt\%_C} \times 100 \qquad (4.8)$$

The as-received graphites provided a baseline for TGA analysis, unless otherwise stated. For grafted species with no common m/z fragments with the solvent, or for which TGA measurement was impractical (Br_2 and TFAA), the GR was obtained taking the total mass loss from TGA, and was taken as the upper estimate of grafting.

4.4.1.2. Calculation of grafting density

The C/R ratio (the grafting density, or number of graphitic carbons per grafted moiety) was calculated from:

$$C/R = \frac{MW_R}{wt\%_R} \times \frac{wt\%_C}{A_{rC}} \qquad (4.9)$$

where MW_R and A_{rC} are the molecular weight of the grafted moiety and the atomic weight of carbon, respectively.

The theoretical number density of grafting per cm², n_D, assuming perfect exfoliation, was obtained using the relation:

$$n_D \ (cm^{-2}) = \frac{10^{14}}{0.0262 \ C/R} \tag{4.10}$$

where the denominator is the area of the graphene lattice per grafted moiety, calculated by multiplying the area occupied by one carbon atom (0.0262 nm²) by C/R.

4.4.1.3. Surface concentration and polymer separation

The surface concentration of PMMA, C_{PMMA} (μmol m⁻²) (Chapter 6), is calculated from the mass of PMMA in the sample ($wt\%_{PMMA}$), determined by TGA-MS, and the specific surface area, S_{BET} (m² g⁻¹), from BET measurements (section 4.4.8):

$$C_{PMMA} = \frac{wt\%_{PMMA} \times 10^4}{M_n(PMMA) \times S_{BET}} \tag{4.11}$$

where M_n(PMMA) is the molar mass of PMMA.

The separation between polymers, D, is given by:

$$D \ (nm) = \frac{2 \times 10^{12}}{\sqrt{\pi \times C_{PMMA} \times N_A}} \tag{4.12}$$

where N_A is Avogadro's number. For derivations of these equations, see Appendix II.

4.4.2. Raman spectroscopy

Raman spectra were collected on a Renishaw inVia micro-Raman spectrometer using a 50 mW 532 nm laser calibrated to silicon prior to measurement. The laser power and scan duration were varied between samples to avoid damage, but typically point spectra measurements were carried out over 2×20 s scans at 10% laser power with a 2400 l/mm diffraction grating from 1000-3000 cm⁻¹. Statistical Raman data were typically collected at 1×30 s scan, 10% laser power over the range ca.1270-2800 cm⁻¹ in Streamline acquisition mode using a 1800 l/mm grating, in at least 500 areas per sample. The laser spot size is a

function of the objective magnification and laser wavelength but typically for these measurements was ~1 µm. WiRe 4.1 software was used for cosmic ray removal, background correction, fitting of the D, G, D' and 2D peaks, image mapping and all analysis of peak data. Averaged values and standard deviations were calculated from the full range of data. All point spectra were normalised to the G peak at ~1580 cm^{-1} for comparison. For peak ratios, intensity, rather than area, was used to reduce errors resulting from low signal intensity. Samples were prepared by drop casting ethanol dispersions onto a glass slide or silicon wafer.

Raman I_D/I_G ratios were used to calculate number density of grafting, n_D, assuming a low density of defects below the Tuinstra-Koenig limit.[269] The original conversion from interdefect distance, L_D, to n_D uses L_D as the radius of the circle surrounding one defect;[267] in this thesis, a modified equation replacing L_D with half the value has been used instead:

$$n_D(cm^{-2}) = 2.92{\times}10^{10}E_L^4(eV^4)\frac{I_D}{I_G} \tag{4.13}$$

$E_L{}^4$ is the energy of the green laser (2.33 eV). n_D may then be related to C/R using Equation (4.10).

4.4.3. UV-vis spectroscopy

UV-vis-NIR absorption spectra were measured with a Perkin Elmer Lambda 950 UV/Vis spectrophotometer, typically between 200 and 1400 nm (1 nm intervals), using a quartz cuvette with 1 cm pathlength, and run against an air background. Blank solvent backgrounds were subtracted manually for concentration determination. Graphite samples were prepared by bath sonication (45 kHz, VWR USC300T) in the relevant solvent for 15 minutes and allowed to sediment for two days, to remove non-dispersed particles. The supernatant was carefully decanted and the concentration determined by the Beer-Lambert law (Equation (3.2)), using the extinction coefficient for dispersed graphene in solution, ε_{660} = 2460 L g^{-1} m^{-1}.[52] If necessary, samples were diluted so that the maximum absorption value was less than 2. For graphene, the absorbance at 660 nm was taken, in a relatively featureless part of the spectrum, to avoid the Tyndall effect and solvent absorptions.

4.4.4. NMR spectroscopy

^{1}H NMR measurements were performed on a Bruker 400 MHz NMR spectrometer operating at 9.4 T. Samples were dissolved in deuterated chloroform (CDCl$_3$) and all spectra were recorded with 16 scans. Measurements were run from δ 0-13 and all chemical shifts (δ) are

given in ppm, where the residual $CHCl_3$ peak was used as an internal reference (δ = 7.28 ppm). Spectra were analysed using MestReNova software. NMR was performed by Noelia Rubio-Carrero.

4.4.5. GPC

Polymer M_n and dispersity were determined using a Polymer Labs GPC 50 system with two PL-gel 5 µm columns and a refractive index detector. Samples were eluted with DMF with 1% triethylamine (TEA) and 1% acetic acid. The instrument was calibrated to PMMA standards (M_n 1000–200000 g mol^{-1}, Sigma-Aldrich). Data were processed using Polymer Labs Cirrus software. GPC was performed by Noelia Rubio-Carrero.

4.4.6. XRD

XRD data was recorded on a PANalytical X'Pert PRO diffractometer operating at 40 kV and 40 mA, with CuK_α (λ = 1.542 Å) radiation, at a scan rate of 0.085° s^{-1}, step size of 0.0334°, and 2θ varying between 5° and 60°. Dried powder samples (5-10 mg) were mounted onto a zero-background Si sample holder (PANalytical Ltd., UK) and levelled to the height of the top of the holder using a glass slide.

4.4.6.1. Non-ambient XRD

Non-ambient XRD measurements were acquired on a PANalytical X'Pert PRO MPD diffractometer equipped with monochromated cobalt radiation ($CoK_{\alpha1}$, λ = 1.789 Å), operating at 40 kV and 30 mA. The diffractometer was fitted with an Anton Paar HTK 1200N sample stage allowing operation from room temperature to 1200 °C. The sample was prepared by spreading a thick slurry of the graphite material in ethanol onto a thin silica glass disk, ensuring a uniform flat surface after evaporation of the solvent. The silica disk was then secured onto the alumina sample carrier and mounted within the heating chamber. The heating and data acquisition programs were controlled using X'pert Data Collector software. Heating of the sample was conducted in an air environment. The temperature was increased at 10 °C min^{-1} between measurements and held isothermally during data acquisition. Measurements were taken at 25 °C, and thereafter from 100 °C to 700 °C in 20 °C intervals. Scans were taken from 5-40° with a step size of 0.0167° and a scan rate of 0.0167° s^{-1}. Ian Wood (UCL) and David Buckley are acknowledged for their help in obtaining these measurements.

Peak deconvolution and curve fitting was performed in OriginPro 9.0.0 using Voigt lineshapes to account for natural and instrumental line broadening. A peak broadening of 0.12° was obtained from a standard Si sample and used to calculate the crystallite size in the c-axis

direction, L_c, using the Scherrer equation (Equation (3.4)). The number of layers, n, was calculated from the crystallite size using:

$$n = \frac{L_c}{d} + 1 \qquad (4.14)$$

where d is the interlayer spacing, which is calculated from Bragg's law (Equation (3.3)).

4.4.7. XPS

XP spectra were recorded using a K-alpha$^+$ XPS spectrometer equipped with an MXR3 AlK$_\alpha$ monochromated X-ray source (hv = 1486.6 eV). X-ray gun power was set to 72 W (6 mA and 12 kV); with these X-ray settings, the intensity of the Ag 3d$_{5/2}$ photoemission peak for an atomically clean Ag sample, recorded at 20 eV pass energy (PE), was 5×10^6 counts s^{-1} and the FWHM was 0.58 eV. Binding energy calibration was made using Au 4f$_{7/2}$ (84.01 eV), Ag 3d$_{5/2}$ (368.20 eV) and Cu 2p$_{3/2}$ (932.55 eV). Charge compensation was achieved using the FG03 flood gun using a combination of low energy electrons and the ion flood source. Survey scans were acquired using 200 eV pass energy, 1 eV step size and 100 ms (50 ms $\times$ 2 scans) dwell times. All high-resolution spectra were acquired using 20 eV pass energy, 0.1 eV step size and 1 s (50 ms $\times$ 20 scans) dwell times. Samples were prepared by pressing the sample onto carbon-based double-sided tape. Pressure during measurement acquisition was $\leq 1 \times 10^{-8}$ mbar. CasaXPS (v2.3.16) was used for data interpretation. CasaXPS relative sensitivity factors (RSF) based on Scofield cross-sections were used for atomic percentage quantification analysis (where RSF of C1s = 1.000). Shirley background subtractions were employed and peaks were fitted using GL(30) lineshapes (a combination of Gaussian (70%) and Lorentzian (30%)). All XP spectra were charge corrected by referencing the fitted contribution of C-C graphitic-like carbon in the C1s signal to 285 eV.

XPS atomic composition data was used to determine C/R for some functionalised graphenes. GR was obtained from C/R using:

$$GR = \frac{MW_R}{A_{rC}} \times \frac{1}{C/R} \times 100 \qquad (4.15)$$

Number density of grafting from XPS was calculated using Equation (4.10) given above.

4.4.8. BET

The adsorption and desorption isotherms of nitrogen at -196 °C were carried out on 20-50 mg of sample using a Micromeritics Tristar 3000. Specific surface areas were calculated according to the BET equation from the adsorption isotherms. Prior to analysis, the samples were degassed with continuous N_2 flow at 100 °C for 12 hours. BET measurements were obtained by Cynthia Hu.

4.4.9. SEM

SEM images were taken using a Leo Gemini 1525 field emission gun scanning electron microscope (FEGSEM) with SmartSEM software, at an accelerating voltage of 5 keV, working distance of ~7 mm and a 30 μm aperture. Statistical analysis of flake/particle dimensions was established by measuring the diameters and thicknesses with ImageJ software. At least 50 measurements (over different points in the sample) were taken to calculate the average value and standard deviation. Powder samples were fixed onto aluminium stubs using carbon tabs (Agar Scientific Ltd.); SEM images were obtained by Hannah Leese.

4.4.10. TEM

Bright-field TEM (BF-TEM) was carried out using a JEOL JEM-2000 or a JEOL JEM-2100Plus TEM at 200 kV operating voltage. Samples were prepared on 300 copper mesh holey carbon grids by drop-casting dilute graphene dispersions (<10 μg mL^{-1}) in absolute ethanol onto a grid supported by filter paper and drying under vacuum. Dark-field TEM (DF-TEM) and EDX mapping were performed on a Cs-aberration-corrected FEI Titan 80/300 TEM/STEM with an accelerating voltage of 80 kV. DF-TEM experiments were performed by Edward White.

4.4.11. AFM

Samples for atomic force microscopy were typically prepared by drop-casting a dilute dispersion of the graphene material (<10 μg mL^{-1}) in absolute ethanol or chloroform on a clean silicon wafer and allowed to dry before soaking in water and ethanol, then drying under vacuum for 16 h. AFM measurements were carried out in tapping mode using a Nanoscope IV Digital Instruments AFM (Veeco), with Nanosensor tapping mode probes supplied by Windsor Scientific. Scans were performed from 1×1 μm to 10×10 μm at 512 line resolution, scan frequency of 1 Hz, with the scan rate dependent on the number of lines and scan area. AFM micrographs were processed in NanoScope Analysis (v1.40, Bruker). AFM images were collected by Noelia Rubio Carrero and Hannah Leese.

5. Variables affecting the exfoliation and functionalisation of graphite intercalation compounds

Modification of graphene by covalent grafting is important for many applications and reductive functionalisation is a powerful, non-destructive method to obtaining individualised single- and few-layer graphene sheets. Reductive exfoliation requires the formation of alkali-metal graphite intercalation compounds, which, depending on the graphitic starting material and charging conditions, can spontaneously disperse to form graphenide-containing solutions. Upon quenching and processing, however, solvent can remain trapped between the large, flat graphene sheets, even after extensive drying. The presence of uncontrolled amounts of solvent complicates the characterisation of these functionalised materials, and quantification of grafting by the usual methods can often lead to contradictory and misleading conclusions. This phenomenon is much less significant in CNTs and fullerenes, due to their curved morphologies, but it is a prominent problem within the graphene community, although there is little discussion in the literature addressing the issue.

In this chapter, the reductive functionalisation method will be discussed in detail, exploring whether solvent trapping is dependent on the solvent medium, and how grafting efficiency is affected. Functionalisation of five different graphitic starting materials, with a range of lateral sizes and thicknesses, is studied, to investigate how grafting density is affected by flake size and morphology. In these experiments, dodecyl addends provide a well-defined model system, widely studied in the literature, for ease of comparison.

5.1. Functionalisation of natural flake graphite

Natural flake graphite (NFG) was used as the starting point for this study. It is naturally abundant and inexpensive, with a high crystallinity, although the existence of some natural defects in the material[276] prevent full exfoliation to single-layer graphene without mechanical input. Due to the relative inaccessibility of the basal planes of inner graphene layers, it is expected that there would be a difference in reactivity between these sites and the less sterically hindered edges and outer surfaces of each flake. With a naturally occurring starting material, the inhomogeneity in flake size and thickness must be considered when evaluating functionalisation. The main challenges in grafting to NFG lie in the large, flat, pristine nature of the material, since its intrinsic lack of strain and existing defects give rise to a lack of reactivity, in comparison to fullerenes and CNTs.

5.1.1. Characterisation of natural flake graphite

Photographic and SEM images of as-received NFG (ar-NFG) clearly show the flake structure of this material (Figure 5.1a and b). The flakes range from 200-800 μm in lateral size with thicknesses of up to 15 μm, and show smooth flat surfaces, covered with smaller fragments of <5 μm lateral size (Figure 5.1b inset top). Thick stacks are evident from the flake edges, which also show wrinkling and folding (Figure 5.1b inset bottom). The XRD pattern (Figure 5.1c) shows the characteristic interlayer (002) peak at $2\theta = 26.6°$, which corresponds to an interlayer distance of 3.35 Å (incident X-ray CuK_α 1.542 Å). This strong sharp peak and the presence of a well-defined higher order (004) peak indicate a high degree of crystallinity. Furthermore, the absence of a significant D peak (average peak intensity I_D/I_G ratio of 0.05±0.05) in a typical Raman spectrum is evidence of the lack of defects arising from functional groups, grain boundaries and flake edges (Figure 5.1d). The very low standard deviation in I_D/I_G is a consequence of the homogeneity of the pristine material. The 2D peak has an asymmetric shape, showing a shoulder characteristic of graphite,[41] and centred around 2715 cm^{-1}. NFG has excellent thermal stability, losing only 0.3 wt% when heated to 800 °C under nitrogen (Figure 5.2a).
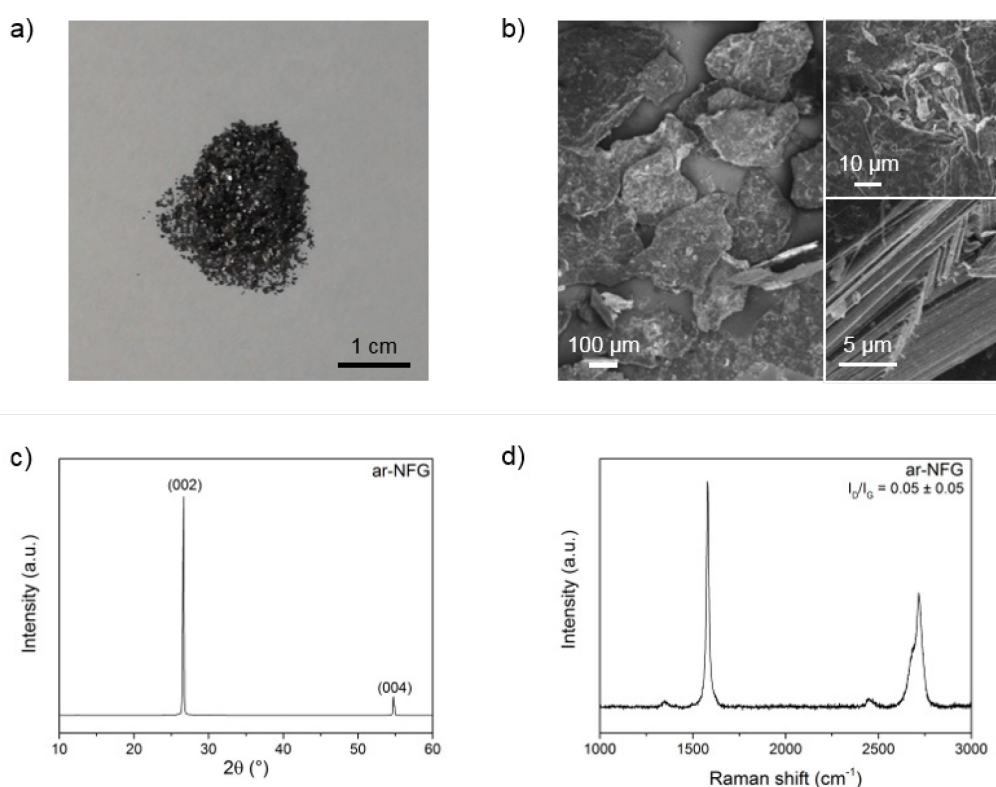
Figure 5.1. a) Photograph, b) SEM image, c) XRD pattern, and d) Raman spectrum of ar-NFG.

5.1.2. Reductive treatment of natural flake graphite

Graphite was heated at 400 °C under vacuum for one hour and then kept under vacuum for a further sixteen hours at room temperature, to remove water and other impurities. Reduced graphite was prepared by treatment with sodium naphthalide in THF (Scheme 5.1a (A)). Naphthalene was selected as the transfer agent, whilst sodium, as the electron source, together with THF were used due to their ability to form the ternary stage-1 Na-THF-GIC.[78, 98] Naphthalide solutions of Li, Na and K are often used interchangeably, but in principle lithium naphthalide is expected to be the strongest reducing agent of the three because there exists only weak ion pairing between the naphthalide anion and the metal cation.[277] However, practical limitations prevent the use of lithium metal inside the nitrogen-filled glovebox, due to reaction between lithium and nitrogen. Alkali metal naphthalides have a high reduction potential[277] and are commonly used in the reduction of SWCNTs.[238, 258, 278-281] The presence of coordinated THF increases the interlayer spacing more effectively for sodium than potassium[98] in this process, potentially enabling more extensive exfoliation of the graphene layers, providing motivation for using sodium naphthalide. A pre-made solution was added to the graphite for ease of handling, and glass stirrer bars were used for all charging reactions since PTFE is unstable to naphthalide/graphenide conditions. A charging ratio (number of framework carbon atoms per sodium atom, C/Na, assuming graphite molecular weight of 12 Da) of 12 and an absolute sodium concentration of 0.01 M was used, as these have previously been shown to optimise exfoliation/functionalisation for the same graphite material.[13] The graphite transformed from a grey colour to a shiny blue, characteristic of graphite intercalation compounds. Following brief and mild bath sonication to encourage exfoliation, a brownish, graphenide-containing dispersion was generated.

5.1.3. Dodecyl functionalisation as a model reaction

The resulting charged graphene sheets were functionalised by slow addition of a three-times excess of 1-bromododecane while stirring, to yield dodecyl-functionalised graphene ($C_{12}H_{25}$-NFG, Scheme 5.1a (B)). After functionalisation, the graphene dropped out of solution and the supernatant became a cloudy grey colour. Reactions of alkyl halides with negatively-charged carbon allotropes have been widely explored in the literature;[13, 239, 240, 256, 263, 281, 282] in particular, grafting of dodecyl addends, providing a well-defined model system with which to examine solvent trapping and functionalisation. Therefore, the reaction with 1-bromododecane was explored for this study. Functionalisation is thought to proceed *via* a free-radical mechanism[238] (Scheme 5.1b), and slow addition was carried out to prevent loss of charge through Wurtz-type homocoupling of alkyl radicals formed *in situ*;[283] whilst previous work on

the analogous CNT reaction has shown that the amount of dimer produced is small,[238] similar studies on potassium GICs suggest that very slow or dilute addition is essential to prevent this unwanted side reaction.[111, 252] Any residual charge on the graphene sheets was removed by quenching with dry oxygen/nitrogen (20%/80%). $C_{12}H_{25}$-NFG was obtained after extensive washing, and dried under vacuum prior to any characterisation. A control reaction was also carried out, omitting the addition of the electrophile, to investigate whether the charging and quenching procedures were damaging to the carbon framework (Na-THF-NFG, Scheme 5.1a (C)).
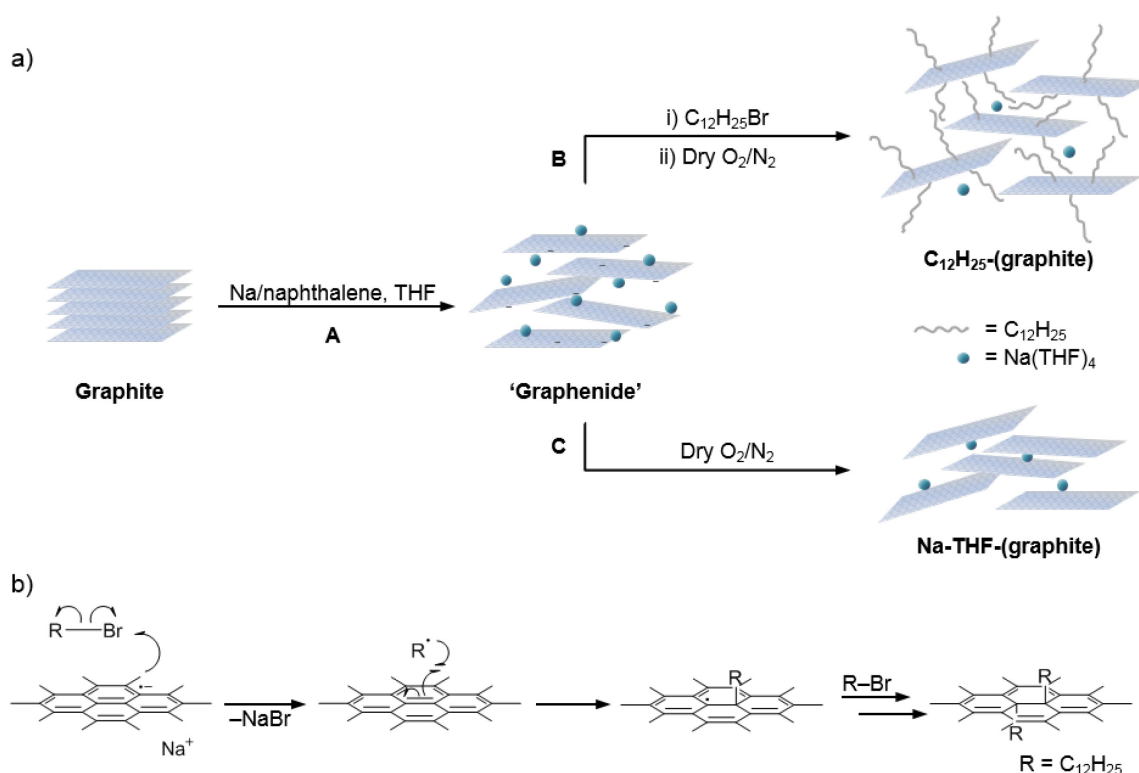
Scheme 5.1. a) Generalised reaction scheme for dodecyl functionalisation of graphite. Reductive exfoliation (step A) followed by reaction with 1-bromododecane to yield dodecyl-functionalised graphite, $C_{12}H_{25}$-(graphite) (route B); or direct quenching with dry O_2/N_2 to yield Na-THF-(graphite) (route C); b) proposed radical mechanism for alkyl bromide reaction with reduced graphite.

The TGA-MS for $C_{12}H_{25}$-NFG shows two distinct weight losses at around 150-250 °C (17.0 wt%) and 400-600 °C (7.5 wt%) (Figure 5.2). Corresponding alkyl mass fragments m/z 43 ($-C_3H_7^+$), 57 ($-C_4H_9^+$) are seen in these temperature ranges, suggesting that alkyl species are present in the sample. However, there is also a significant amount of THF present, which can be seen from mass fragments m/z 43 ($-CHCH_2O^+$), 72 ($C_4H_8O^+$); the m/z 57 fragment arises from the dodecyl chains only, and is not present in Na-THF-NFG (Figure 5.2b), whereas m/z 43 is common to both dodecane and THF. The TGA-MS provides evidence of alkyl residues on the surface; pure dodecane decomposes predominantly around 200 °C

(Appendix I, Figure I.1), suggesting that alkyl groups are present as covalently-bound species, or at least, a strong interaction exists between the alkyl chain and the graphene layers.
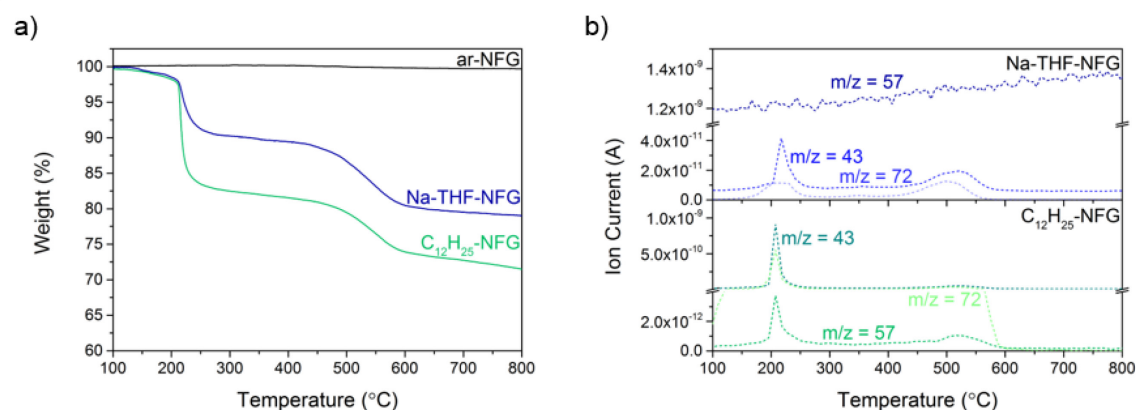
Figure 5.2. a) TGA profiles of ar-NFG, Na-THF-NFG and $C_{12}H_{25}$-NFG, and b) corresponding MS signals for Na-THF-NFG and $C_{12}H_{25}$-NFG; m/z 43 (-$C_3H_7^+$) or (-$CHCH_2O^+$), 57 (-$C_4H_9^+$), 72 ($C_4H_8O^+$).

Further evidence to support this assertion was provided by a control experiment ($C_{12}H_{26}$+NFG) with non-electrophilic dodecane in place of 1-bromododecane. Dodecane was expected to be unreactive to graphenide, but would be able to diffuse through the graphene interlayers in a similar way to 1-bromododecane. Following an identical work up procedure, no alkyl fragments were detected by TGA-MS (Figure 5.3), confirming that any physisorbed alkyl species, either unreacted 1-bromododecane or products of coupling reactions, were successfully removed during washing and therefore suggesting that in $C_{12}H_{25}$-NFG, dodecyl residues are covalently bound.
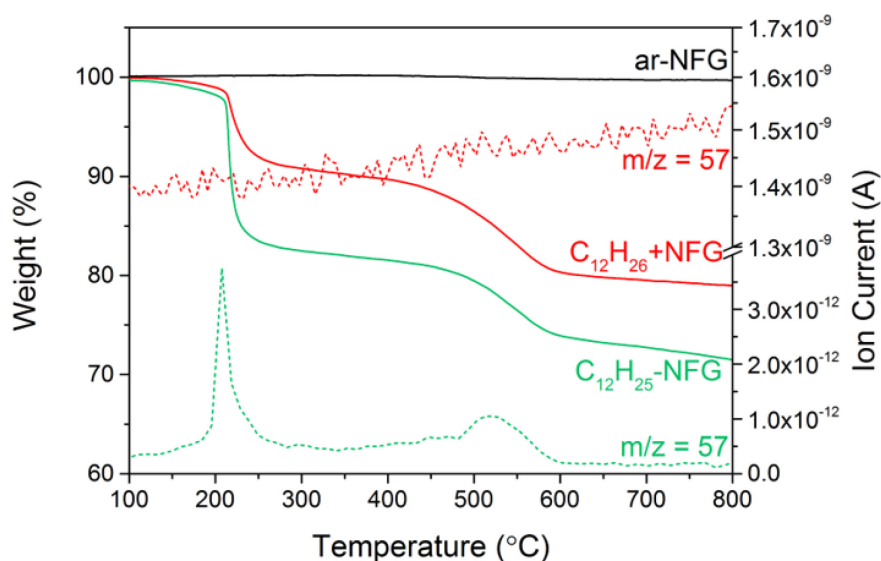
Figure 5.3. TGA-MS profile of ar-NFG, $C_{12}H_{26}$+NFG and $C_{12}H_{25}$-NFG, and corresponding m/z 57 (-$C_4H_9^+$) for $C_{12}H_{26}$+NFG and $C_{12}H_{25}$-NFG.

Previous grafting studies have attributed early weight loss as physisorption of alkyl groups, and decomposition at higher temperatures to covalently grafted species;[256] here, the control reaction indicates that both are likely to relate to grafted species. Interestingly, the temperature of alkyl decomposition is concurrent with solvent loss, discussed below.

Naphthalene can adsorb to the graphene layers, due to π-π interactions; however, no mass fragments for $m/z = 128$, attributed to $C_{10}H_8^+$, ionised naphthalene, were detected by MS, suggesting that it is washed out during the work up procedure (Figure 5.4).
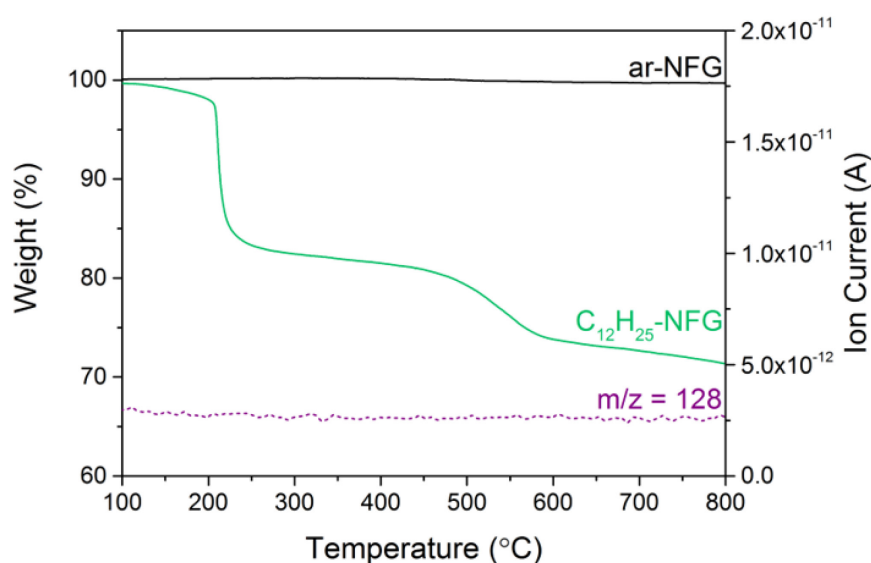
Figure 5.4. TGA-MS profile of $C_{12}H_{25}$-NFG and absence of naphthalene ion m/z 128 ($C_{10}H_8^+$).

Whilst adsorbed alkyl and naphthalene species are successfully removed during washing, residual THF remains even at high temperatures, complicating the determination of grafting ratio; the TGA-MS for Na-THF-NFG shows a similar two-step weight loss (5.6 wt% at 150-250 °C and 14.6 wt% 400-600 °C) with similar mass fragments arising from THF (Figure 5.2). The mass fragment m/z 57 is notably absent, so may be attributed to alkyl chains alone, in the grafted $C_{12}H_{25}$-NFG sample. Both grafted and control samples were visibly expanded following TGA under nitrogen; a similar expansion can be seen in other 'expandable graphites' following heat treatment,[110, 111, 114, 115] supporting the observation that there is still a significant amount of volatile intercalated species. Even after additional bath sonication washing steps and drying under vacuum, solvent remained trapped inside the graphene layers (Appendix I, Figure I.2).

The dodecylated graphene flakes were dispersed in THF, deposited onto holey carbon film and imaged by TEM (Figure 5.5). The few-layer stacks illustrate that significant exfoliation has occurred. As highlighted in the images (arrows marked (i)), solvent pockets are visible

between the graphene sheets. Wrinkling and folding of the sheets are evident (arrows marked (ii)), but with no visible evidence of large-scale defects.
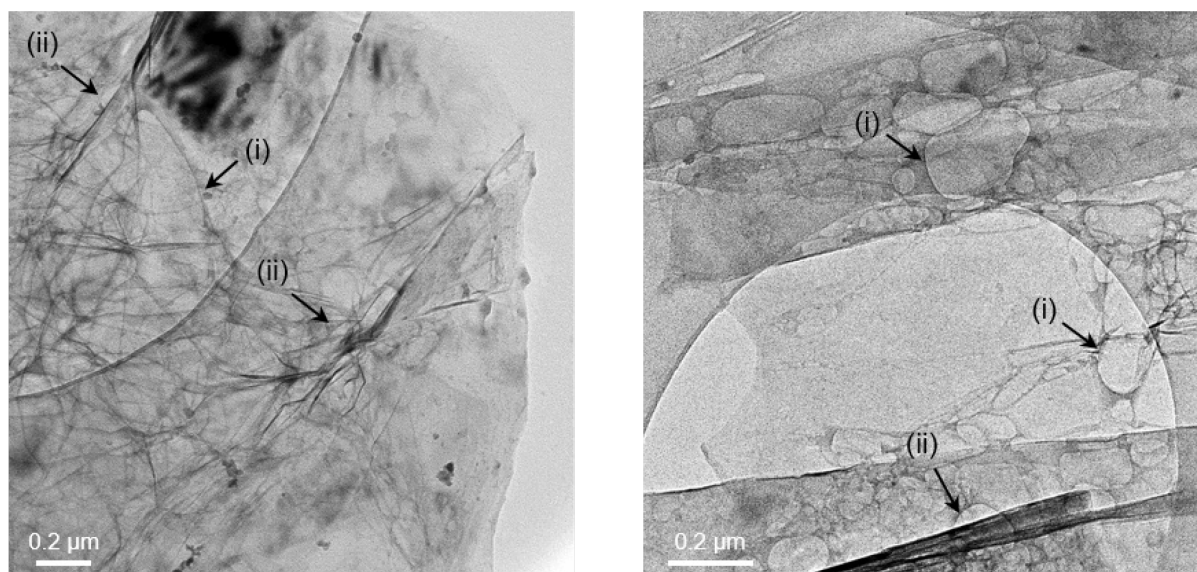
Figure 5.5. TEM images of $C_{12}H_{25}$-NFG showing regions of single- and few-layer graphene. Pockets of trapped solvent (i) and wrinkles and folds (ii) are indicated by the arrows.

XRD patterns for $C_{12}H_{25}$-NFG and Na-THF-NFG show a significant weakening and slight broadening of the graphite interlayer (002) peak at $2\theta = 26.6°$ (Figure 5.6a). The greatly reduced intensity of this peak in $C_{12}H_{25}$-NFG and Na-THF-NFG relative to peaks arising from the same crystallographic plane (see below) imply that long-range stacking was disrupted during the reaction, and that considerable exfoliation was achieved. Graphitic areas remain even after reductive treatment; an estimate, using the Scherrer equation, of the average number of layers in these coherent graphitic domains is ~80 layers for both $C_{12}H_{25}$-NFG and Na-THF-NFG, decreased from ~200 in ar-NFG. After reduction, small peaks between 5° and 25°, characteristic of the (001), (002) and (003) reflections of a stage-1 Na-THF-GIC,[97] provide confirmation that residual THF remains in the sample, coordinated to sodium cations (Figure 5.6b). Stage-1 Na-THF-GICs can exist in two forms: phase A, where the sodium cations are coordinated by four THF molecules, or phase B, where each sodium cation is two-coordinate. Phase A gives rise to peaks at 8°, 16° and 24.1°, corresponding to an interlayer distance of 11.1 Å and a resulting intercalate thickness (by subtracting the thickness of a graphene layer, 3.35 Å) of 7.75 Å, close to the literature reported value.[97] Similarly, a very small peak at 12.4° arising from the phase B structure is detected, with a calculated interlayer distance of 7.1 Å corresponding to an intercalate thickness of 3.79 Å, the height of two THF molecules 'lying down' around a sodium cation. A further large peak at 25.3° is attributed to the presence of a so-called 'random stage' structure,[284] where the stacking of hexagonal carbon layers and Na-THF layers is so disordered that all 00*l* diffraction lines, except the line due to the most

probable spacing of 3.52 Å, are broadened to the extent of being undetectable. This peak has also been attributed to turbostratic graphite[285] suggesting extensive exfoliation followed by imperfect restacking on drying. Exposure to ambient conditions and the work up procedure were intended to fully remove all remaining sodium and THF; therefore, the partial removal of some of these species and the handling process are likely to induce some phase change and movement of the intercalant within the graphene layers. Phase A is known to convert to phase B or the random stage phase on exposure to air;[97] $C_{12}H_{25}$-NFG shows a decrease in the phase A structure from Na-THF-NFG and contains Na-THF with a predominantly random stage structure, suggesting that the presence of alkyl chains helps to keep the interlayer galleries open allowing some diffusion of THF from the structure. However, dodecyl chains are not sufficiently large to allow full deintercalation, and after preferential deintercalation of the sheet edges, layers may seal up again trapping a proportion of the stage-1 structure. The presence of dodecyl chains does not significantly alter the interlayer spacings; a hypothetical dodecane chain at full extension measures 1.38 nm, but in reality the chains are most likely adsorbed flat across the graphene sheet. The presence of Na-THF implies an incomplete quenching of charge and that washing procedures are not sufficient to completely remove intercalated sodium species.
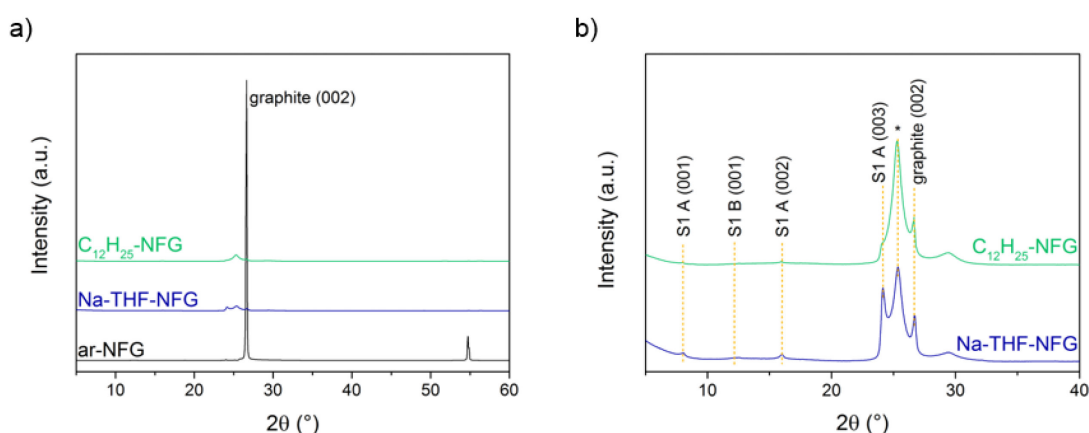
Figure 5.6. a) XRD patterns for ar-NFG, Na-THF-NFG and $C_{12}H_{25}$-NFG; and b) magnified XRD patterns of Na-THF-NFG and $C_{12}H_{25}$-NFG; stage 1 phase A and B structures correspond to interlayer spacings of 11.1 and 7.1 Å, respectively. The starred peak is attributed to the 'random stage' phase or turbostratic graphite.

An estimate of the amount of residual sodium inside the sample was obtained by TGA of Na-THF-NFG in air (Figure 5.7). After combustion a white solid remained, so assuming all sodium converted to sodium oxide after 800 °C, and graphite left no remaining char, the residual mass gives a sodium oxide content of 2.8 wt% of the total sample and therefore a sodium content of 2.0 wt%. Taking the total amount of THF from the mass losses around 170-260 °C (THF-I) and 370-520 °C (THF-II) (Table 5.1), and attributing the remaining weight

loss to combustion of graphitic carbon, a ratio of THF/Na = 3.1 was obtained, suggesting that THF exists coordinated to sodium in a mixture of phase A and phase B regions, and that any free uncoordinated solvent is likely lost during initial drying. A C/Na = 71.2 indicates that most of the original sodium was removed with around one sixth remaining after the work up procedure.
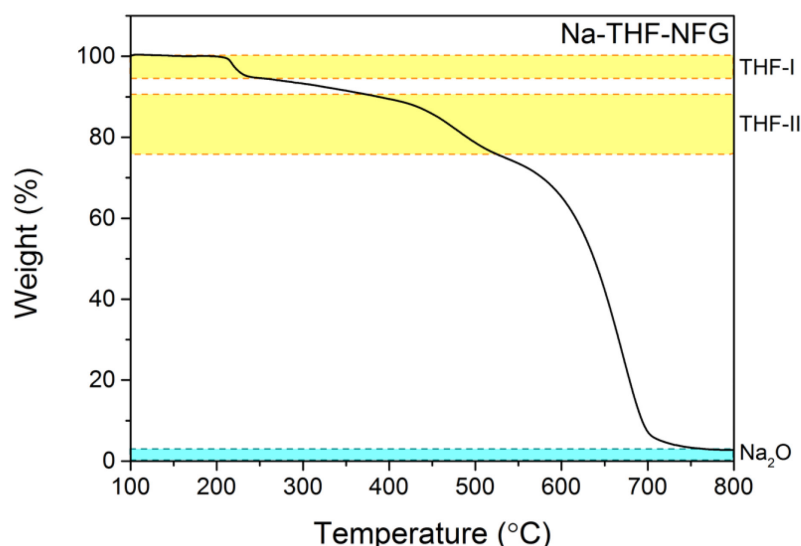
Figure 5.7. TGA of Na-THF-NFG under air atmosphere. The regions marked THF-I, THF-II and Na$_2$O were used to determine the amount of residual Na-THF.

XPS data confirm the presence of sodium, with analysis of high resolution spectra indicating an atomic composition of 0.6 at% Na, 88.9 at% C and 10.5 at% O. The sodium content detected by XPS is similar to the value obtained by TGA, within error; XPS is a highly surface sensitive technique, and it may be that sodium species inside the layers remain undetected.

Table 5.1. Summary of Na content in ar-NFG and Na-THF-NFG obtained by TGA and XPS.

Sample	THF-I (wt%)*	THF-II (wt%)*	Na$_2$O (wt%)*	Na (wt%)*	at% C[†]	at% O[†]	at% Na[†]	wt% Na[†]
ar-NFG	-	-	-	-	95.0	5.0	0	0
Na-THF-NFG	5.6	14.6	2.8	2.0	88.9	10.5	0.6	1.1

*Calculated from TGA measurements; [†]obtained from XPS; high resolution data provided in Appendix I, Figure I.3.

The presence of sodium, as well as THF, confirmed by XRD, TGA in air and XPS, implies that incomplete quenching of the charges occurs after reaction. Residual charge on the graphene sheets could result in inadvertent functionalisation upon exposure to air or water, but grafting is very dependent on charge stoichiometry[259] and at this low residual charge ratio, the TGA-MS of Na-THF-NFG confirms the absence of hydroxyl peaks (Figure 5.8), with only peaks attributed to THF present (Appendix I, Figure I.4).
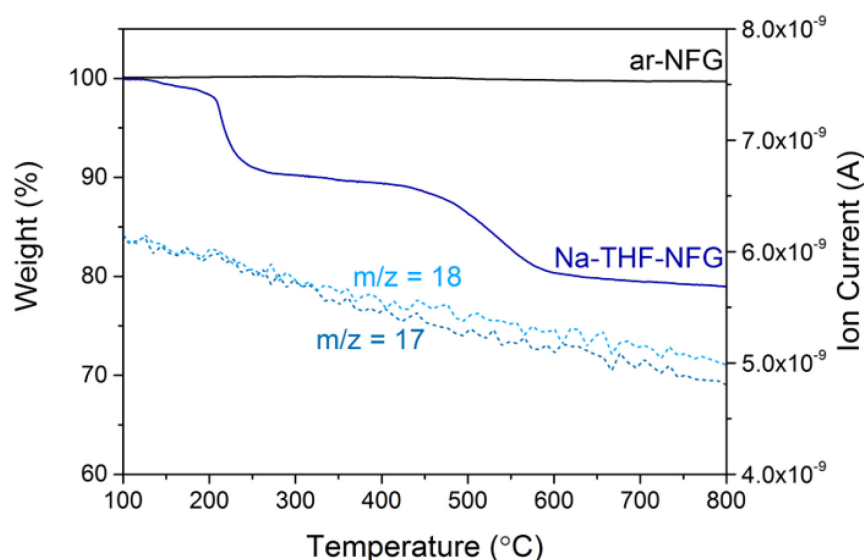
Figure 5.8. TGA-MS profile of Na-THF-NFG and absence of hydroxyl ions, m/z 17 (-OH⁺), 18 (H₂O⁺).

Further verification of the undamaging nature of the charging and quenching procedure is obtained by Raman spectroscopy of Na-THF-NFG (Figure 5.9). There is no significant change in I_D/I_G for Na-THF-NFG (0.06±0.08) compared with ar-NFG (0.05±0.05), confirming that inadvertent functionalisation of the carbon framework does not take place during reduction, or upon quenching, unlike other studies based on KC_8 in NMP[261] (Figure 5.9b), possibly because Na-THF-NFG has a lower reduction potential relative to KC_8. It appears then that any remaining charge on the graphene is insufficient to react with other species, or that it is localised around sodium cations and is inaccessible for further functionalisation. In contrast, the Raman spectra for $C_{12}H_{25}$-NFG show a small increase in the D peak with an I_D/I_G of 0.18±0.18, suggesting that grafting has occurred with the introduction of sp^3 defects on the carbon lattice. Both $C_{12}H_{25}$-NFG and Na-THF-NFG show a greater degree of exfoliation than the graphite starting material (Figure 5.9c); I_{2D}/I_G increases from 0.47±0.04 in ar-NFG to 0.49±0.13 in Na-THF-NFG, and more significantly to 0.6±0.2 in $C_{12}H_{25}$-NFG. In both cases, the 2D peak is shifted to lower wavenumbers (by ~15 cm⁻¹ in Na-THF-NFG and ~35 cm⁻¹ in $C_{12}H_{25}$-NFG) and there is a change to a more symmetric line shape, reflecting the loss of long-range graphitic stacking,[41] showing that this reductive procedure can effectively exfoliate graphene sheets in solution. A slight splitting of the G peak can be seen for both $C_{12}H_{25}$-NFG and Na-THF-NFG which can be an indication of mixed stage intercalation or doping:[286, 287] in this case, the presence of Na-THF between the graphene layers. The averaged spectra reflect a mixture of areas with significant intercalation and no intercalation, manifested as a broadened G peak (Figure 5.9a). Using a modified version of the model proposed by Cançado

et al.,[267] the number density of grafting per unit area, n_D, may be calculated from the I_D/I_G ratio (see Chapter 4, section 4.4.2). The number density of alkyl groups in $C_{12}H_{25}$-NFG is 1.6×10^{11} cm^{-2}; determination of n_D was carried out assuming that the sample falls within the low defect density regime, where I_D/I_G increases with increasing functionalisation, since the shape and FWHM (Γ_{2D}) of the peaks remained well-defined and narrow. This density of grafting corresponds to a C/R of 2418; the initial charging ratio was C/Na 12, suggesting that only ~1 in 200 charges have been utilised, for successful grafting. However, these values are expected to underestimate the degree of grafting, because the calculations are based on evenly-spaced defects; the broadened I_D/I_G histogram indicates the presence of a mixture of regions with high and low grafting density and, therefore, some degree of heterogeneity in functionalisation.

Figure 5.9. a) Averaged Raman spectra, and Raman histograms of b) I_D/I_G and c) I_{2D}/I_G ratio of ar-NFG, Na-THF-NFG and $C_{12}H_{25}$-NFG; point spectra normalised to the G peak intensity and offset for clarity.

Quantification of grafting from TGA-MS is less straightforward than subtracting the as-received material or quenched control as a baseline; the amount of residual THF may be affected by the introduction of alkyl groups. Instead, examination of the mass fragment ratios in $C_{12}H_{25}$-NFG, 1-bromododecane and a control sample with known amounts of Na-THF-NFG and 1-bromododecane (Na-THF-NFG_$C_{12}H_{25}$Br) allows a more accurate determination of the grafting ratio and C/R. Due to pressure fluctuations in the mass spectrometer, the integrated area underneath the mass fragment signal can only be directly related to the absolute amount of a certain species for that particular measurement. The relative areas of two *m/z* signals arising from the same species should, however, remain constant; for example, in 1-bromododecane, two major alkyl fragments *m/z* 43 and 57 appear in the ratio $A_{43}/A_{57} = 1.8$ (Appendix I, Figure I.5). TGA measurement of the control sample Na-THF-NFG_$C_{12}H_{25}$Br, with known quantities of $C_{12}H_{25}$Br, THF and graphene carbon, allows calibration of the relative intensities of the MS signals with the relative amounts of dodecyl addends and THF. A detailed explanation of the method is provided in Chapter 4, section 4.4.1.1. A sensitivity factor, *S*, of 3.5 (i.e. for a given amount of sample, the same amount of $C_{12}H_{25}$Br is detected at an intensity 3.5 times weaker than that amount of THF) was derived from these calculations, and was used

to determine the dodecyl and THF contributions to each weight loss step in $C_{12}H_{25}$-NFG (Figure 5.10). A value of 852 graphene carbons per dodecyl addend was determined, a higher grafting density than predicted by Raman; a corresponding GR of 1.7% and a C/THF of 18 was also obtained. A C/THF ratio of 26 was calculated for unfunctionalised Na-THF-NFG straightforwardly from TGA mass loss.
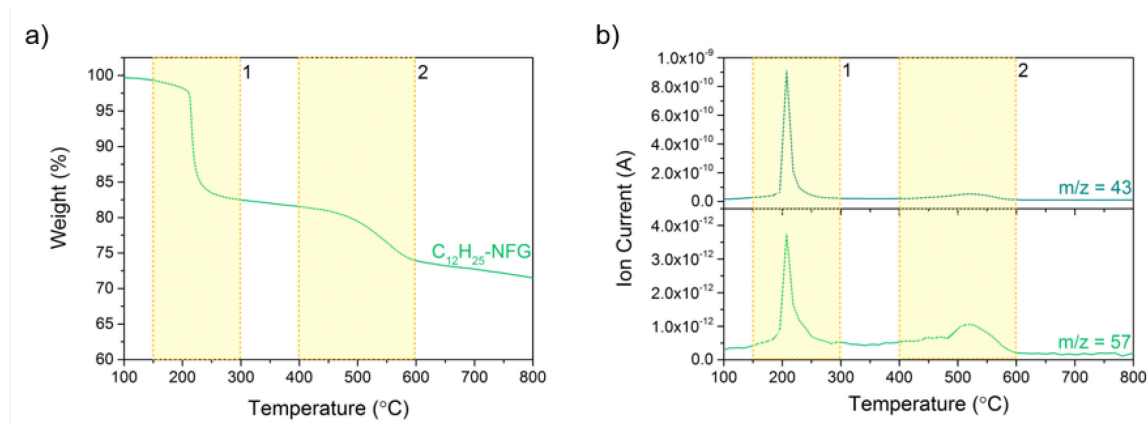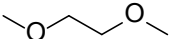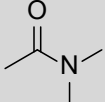
Figure 5.10. a) TGA profile and b) mass fragments m/z 43 ($C_3H_7^+$) and 57 ($C_4H_9^+$) of $C_{12}H_{25}$-NFG; GR and C/R were obtained by taking the mass losses and mass fragment areas in the highlighted regions.

Overall, the evidence demonstrates that dodecyl chains were successfully grafted; analysis of the Raman I_D/I_G ratio offers insight into the introduction of grafted groups in $C_{12}H_{25}$-NFG, and functionalisation is further corroborated by the presence of alkyl fragments in the TGA-MS. Quantification by Raman spectroscopy underestimates the number of grafted sites compared with the value obtained from TGA-MS calculations; this discrepancy is attributed to the heterogeneity in functionalisation. The presence of residual Na-THF, implied by XRD and confirmed by XPS data, shows that only partial quenching occurs, although it was confirmed that the residual charge is unreactive to ambient species. At such high temperatures, far exceeding the boiling point of THF, solvent appears to remain stable between the graphene interlayer galleries; the persistence of solvent may introduce complications in subsequent applications of this functionalised material. The solvent trapping may occur as a result of preferential removal of charge from edge sites, resulting in a sealing up of the graphene layers preventing diffusion of oxygen further into the structure; at these low degrees of grafting, even the presence of dodecyl addends does not sufficiently prevent the closing up of interlayer galleries. Grafting of different addends should provide more stability to exfoliated graphene, reducing restacking and the amount of solvent remaining in the sample. A more extensive discussion regarding functionalisation with PMMA will follow in Chapter 6, but the remainder of this chapter focuses on alternative solvents and graphite starting materials.

5.2. Alternative solvents

The low degree of grafting and large amount of trapped solvent are undesirable for applications requiring good solubility or which are sensitive to contaminants. Furthermore, the TGA-MS of $C_{12}H_{25}$-NFG shows that the loss of dodecyl addends occurs at the same two temperatures as the removal of THF, suggesting two different grafting environments, and an interdependence between solvent volatilisation and alkyl combustion. Therefore, two alternative aprotic solvents were explored to investigate whether an improvement in solvent trapping and functionalisation could be achieved (Table 5.2). 1,2-dimethoxyethane has been extensively used for coordination of alkali metals for graphite intercalation,[95, 242, 284] whilst *N,N*-dimethylacetamide has been shown to be successful at stabilising nanotubide dispersions,[281] and therefore, by extension, might enable formation of graphenide solutions.

Table 5.2. Summary of the three solvents used in this study.

Solvent	Structure	Boiling point (°C)	Dielectric constant
Tetrahydrofuran (THF)		66	7.6
1,2-dimethoxyethane (DME)		85	7.2
N,N-dimethylacetamide (DMAc)		165	37.8

5.2.1. Synthesis and functionalisation of Na-solvent-GICs

The DME and DMAc sodium naphthalide solutions were prepared in an analogous way to the THF solution and ar-NFG was charged under the same conditions. The dark green DME solution did not remain stable for more than two days, turning a red-brown colour, suggesting that solvent degradation occurred; the solution was therefore added to graphite as soon as the sodium had fully dissolved, generally, after one day. The dark green DMAc solution remained stable for much longer, only producing a white precipitate after one week. The graphites turned a metallic blue colour after charging, suggesting that successful intercalation occurred in solution. The samples underwent an identical functionalisation, quenching and work up procedure as before, to yield the functionalised products $C_{12}H_{25}$-DME-NFG and $C_{12}H_{25}$-DMAc-NFG, and the quenched GICs Na-DME-NFG and Na-DMAc-NFG.

5.2.2. Characterisation of Na-solvent-GICs and $C_{12}H_{25}$-solvent-GICs

TGA analysis under nitrogen shows different decomposition pathways between the Na-solvent-GICs and functionalised materials (Figure 5.11). Na-DME-NFG shows a minimal

weight loss of around 5 wt% between 100 °C and 800 °C (Figure 5.11b) suggesting that quenching and washing removed most of the sodium and DME, although there are still two distinct temperature regions where loss occurs, at 150-300 °C and 400-550 °C, even with this small amount of solvent. Fragments m/z 43 (CH_3OC-$^+$) and 45 (CH_3OCH_2-$^+$) detected by MS in these temperature ranges are attributed to DME (Figure 5.11e). After functionalisation, a greatly increased weight loss can be seen, with the first step occurring at a lower temperature of 100-250 °C (8.3 wt%) and the second step in the range 420-590 °C (12.3 wt%) (Figure 5.11b). MS data for $C_{12}H_{25}$-DME-NFG indicates that mostly DME is lost in the first step (m/z 45), whilst the second weight loss is due to the pyrolysis of alkyl chains (m/z 57 and 43) and solvent (m/z 43 and 45) (Figure 5.11e). As for Na-THF-NFG (Figure 5.11a and d), no m/z 57 fragment is detected in Na-DME-NFG, so this feature may be assigned solely to the dodecyl chains.
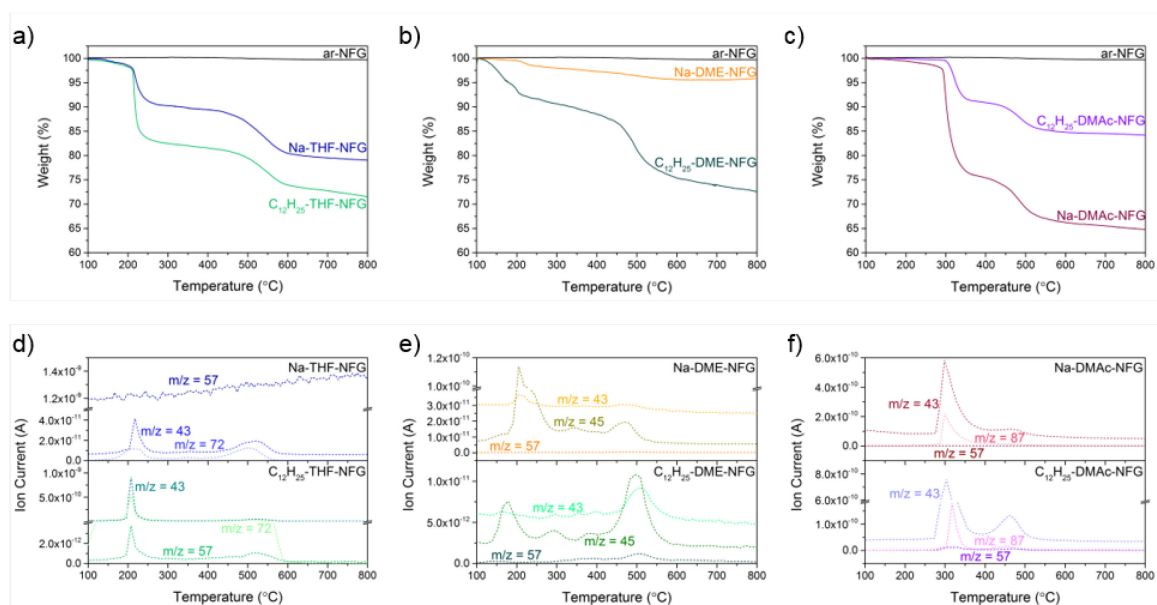
Figure 5.11. TGA (top) and MS (bottom) data for a,d) Na-THF-NFG and $C_{12}H_{25}$-THF-NFG; m/z 43 (-$C_3H_7$$^+$) or (-$CHCH_2O^+$), 72 ($C_4H_8O^+$); b,e) Na-DME-NFG and $C_{12}H_{25}$-DME-NFG; m/z 43 (-$C_3H_7$$^+$) or ($CH_3OC$-$^+$), 45 ($CH_3OCH_2$-$^+$); and c,f) Na-DMAc-NFG and $C_{12}H_{25}$-DMAc-NFG; m/z 43 (CH_3CO-$^+$), 87 ($CH_3CON(CH_3)_2$$^+$); in all samples, m/z 57 (-$C_4H_9$$^+$).

Na-DMAc-NFG shows a sharper and higher temperature first weight loss step than Na-THF-NFG or Na-DME-NFG, between 270 and 380 °C (22.7 wt%), possibly due to its higher boiling point (Figure 5.11c). The second weight loss at 420-550 °C (7.8 wt%) is in a similar temperature range to Na-THF-NFG and Na-DME-NFG, suggesting that solvent escape at this temperature is not dependent on the solvent type. Accompanying mass fragments m/z 43 (CH_3CO-$^+$), and 87 ($CH_3CON(CH_3)_2$$^+$) confirm that DMAc is lost during pyrolysis (Figure 5.11f). The functionalised sample $C_{12}H_{25}$-DMAc-NFG surprisingly shows a smaller apparent weight loss over the whole temperature range (Figure 5.11c), demonstrating how variable the

degree of solvent trapping is, and why grafting ratio cannot be calculated from TGA measurements alone. As before, the mass fragment *m/z* 57 confirms the presence of alkyl species, absent in Na-DMAc-NFG; but DMAc also remains in the sample (Figure 5.11f). Quantification of functionalisation was possible by applying the method detailed in section 5.1.3. Calculations resulted in a GR of 6.7% and C/R of 209 for $C_{12}H_{25}$-DME-NFG and GR 1.0% and C/R 1389 for $C_{12}H_{25}$-DMAc-NFG. Interestingly, the decomposition of alkyl fragments is coincidental with the volatilisation of solvent, regardless of the solvent boiling point (Appendix I, Figure I.6 and Figure I.7); similar simultaneous desorption of H_2O, CO and CO_2 has also been observed in GO.[288]

The amount of solvent remaining in the functionalised and control graphites was also extremely variable. In the materials prepared in THF and DME, a smaller amount of solvent remained in the unfunctionalised sample, compared to the grafted counterpart (Table 5.3), which is surprising since it might be expected that alkyl chains would prevent close restacking of layers, thus allowing solvent to diffuse out of the layers. Conversely, Na-DMAc-NFG contains more residual DMAc than $C_{12}H_{25}$-DMAc-NFG; this higher stability may be in part due to the preference of amide solvents for carbon, the higher dielectric constant or the lower volatility of DMAc relative to THF or DME (Table 5.2).

Table 5.3. Summary of grafting data and residual solvent content obtained by TGA for Na-solvent- and $C_{12}H_{25}$-solvent-NFG samples.

Solvent	$C_{12}H_{25}$-solvent-NFG GR (%)	$C_{12}H_{25}$-solvent-NFG C/R	$C_{12}H_{25}$-solvent-NFG C/solvent	Na-solvent-NFG C/solvent
THF	1.7	852	18	26
DME	6.7	209	28	165
DMAc	1.0	1389	36	15

As for Na-THF-NFG, the amount of residual sodium was calculated for Na-DMAc-NFG from TGA measurements conducted in air (Figure 5.12c). A similar white solid remained after combustion, and the residual mass gave a sodium oxide content of 5.7 wt%. The total amount of solvent from mass losses around 270-350 °C (DMAc-I) and 360-490 °C (DMAc-II) (Table 5.4) was correlated to the remaining sodium and graphitic carbon, obtaining a ratio of 2.3 DMAc/Na. Coordination of DMAc to sodium is not widely discussed in the literature, and the coordination number and structure is unknown; however, this number suggests that a similar coordination pattern to Na-THF occurs here with DMAc. A C/Na of 27.5 indicates that sodium-DMAc was much harder to remove than sodium-THF, and just under half of the original sodium could not be removed during the work up procedure.
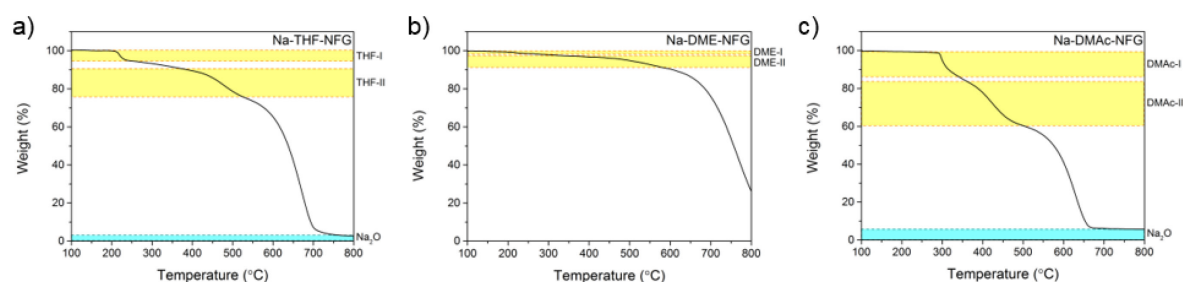
Figure 5.12. TGA of a) Na-THF-NFG, b) Na-DME-NFG, and c) Na-DMAc-NFG under air atmosphere. For Na-THF-NFG and Na-DMAc-NFG, the regions marked solvent-I, solvent-II and Na$_2$O were used to determine the amount of residual Na-solvent; Na-DME-NFG did not fully combust by 850 °C, so XPS measurements were used to calculate sodium content.

The presence of sodium-DMAc is confirmed by XPS, with a composition of 86.2 at% C, 11.6 at% O, 0.5 at% Na and 1.7 at% N (from 95.0 at% C and 5.0 at% O in ar-NFG). Based on sodium and nitrogen contents alone, a DMAc/Na ratio of 3.4 can be deduced (Table 5.4).

Table 5.4. Summary of solvent content in ar-NFG and Na-solvent-NFG, by TGA and XPS.

Sample	solv-I (wt%)*	solv-II (wt%)*	Na$_2$O (wt%)*	solv/Na*	at% C[†]	at% O[†]	at% Na[†]	at% N[†]	solv/Na[†]
ar-NFG	-	-	-	-	95.0	5.0	0	-	-
Na-THF-NFG	5.6	14.6	2.8	3.1	88.9	10.5	0.6	-	-
Na-DME-NFG	1.9	1.6	-	-	95.5	4.31	0.2	-	2.0
Na-DMAc-NFG	14.0	22.6	5.7	2.3	86.2	11.6	0.5	1.7	3.4

*Calculated from TGA measurements; [†]obtained from XPS; high resolution data provided in Appendix I, Figure I.3.

Na-DME-NFG contains 95.5 at% C, 4.31 at% O and 0.2 at% Na, from XPS analysis (Table 5.4); these values are consistent with ~4 wt% solvent obtained by TGA measurement, assuming that each sodium cation is coordinated to two DME molecules. The sodium content was not calculated by TGA under air because complete combustion did not occur by 850 °C (Figure 5.12b).

The Raman spectra for Na-DMAc-NFG show significant intercalation has occurred (Figure 5.13); the G band intensity is strongly enhanced and the 2D peak signal weakens significantly (I_{2D}/I_G 0.13±0.12) in many regions across the flakes.[116] The bulk of the sample shows no increase in I_D/I_G (0.05±0.14) confirming that no functionalisation from solvent occurs. In the functionalised C$_{12}$H$_{25}$-DMAc-NFG, the D band increases only slightly (0.1±0.3) suggesting that little functionalisation occurs; calculations indicate a n_D of 8.6×10^{10} cm^{-2} and a C/R of 4435 (Table 5.5). A corresponding small increase in $I_D/I_{D'}$ is seen in C$_{12}$H$_{25}$-DMAc-NFG (2.2±3.4 from 1.3±1.5) which is not seen in Na-DMAc-NFG (1.6±1.4) suggesting an increased contribution from sp^3 defects compared to edge sites.[270] A distinct bimodal trend is seen in the I_{2D}/I_G ratio of C$_{12}$H$_{25}$-DMAc-NFG, reflecting areas of intercalated and non-intercalated regions; after

grafting, the dodecyl chain may act as a spacer between graphene sheets, allowing diffusion of DMAc and sodium out of the layers.
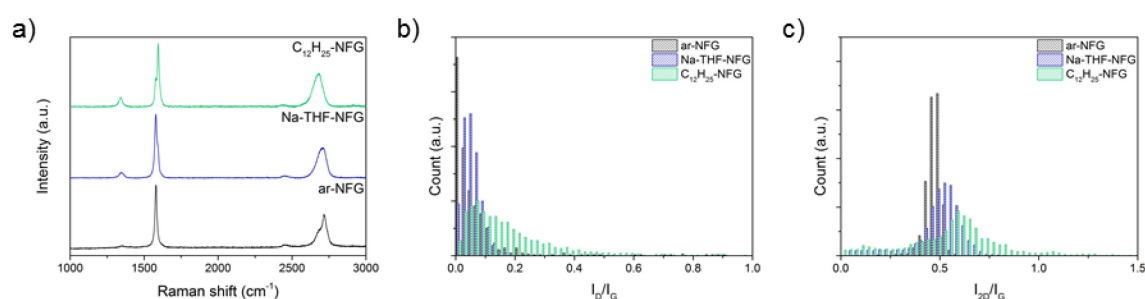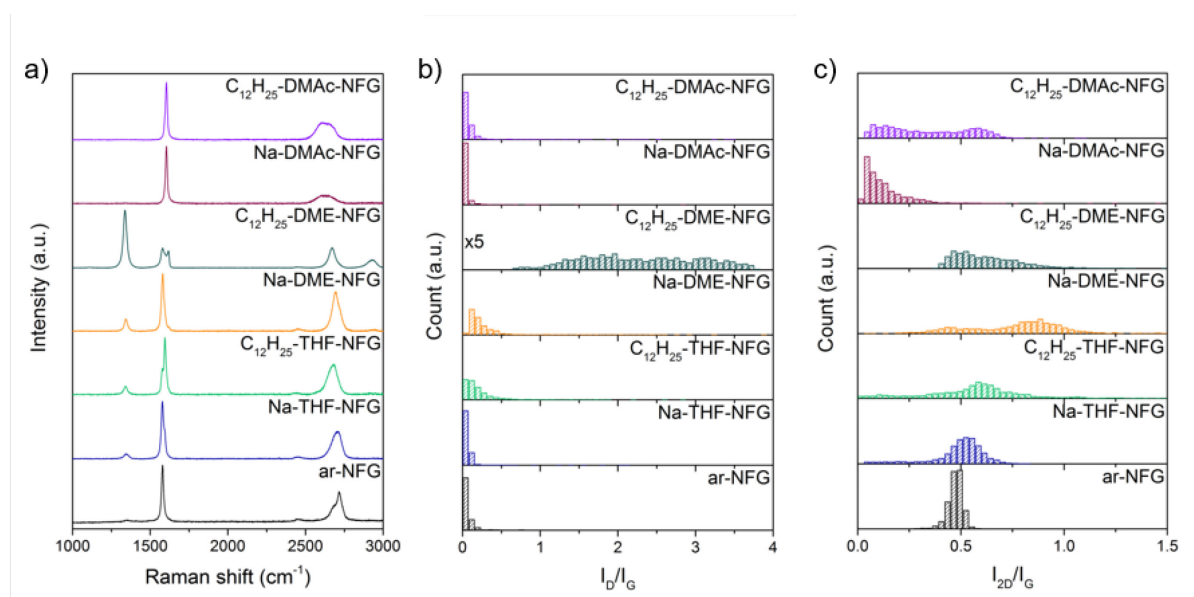

Figure 5.13. a) Averaged Raman spectra, and Raman histograms of b) I_D/I_G and c) I_{2D}/I_G ratio of ar-NFG, Na-THF-NFG, $C_{12}H_{25}$-THF-NFG, Na-DME-NFG, $C_{12}H_{25}$-DME-NFG, Na-DMAc-NFG, and $C_{12}H_{25}$-DMAc-NFG; point spectra normalised to highest peak signal and offset for clarity.

Unlike the DMAc-prepared materials, the samples reduced in DME show a significant change in the D band intensity. The I_D/I_G ratio in $C_{12}H_{25}$-DME-NFG is hugely increased to 2.3±0.8, indicative of successful grafting, and a large D' peak ($I_D/I_{D'}$ 5.2±1.2) can be seen overlapping with the G band. The calculated n_D of 2.0×10^{12} cm^{-2}, and C/R of 193 are in excellent agreement with calculations from TGA-MS. However, the unfunctionalised sample Na-DME-NFG also shows an increase in the I_D/I_G (0.3±0.3) and $I_D/I_{D'}$ ratio (2.2±2.6) suggesting that some degree of inadvertent functionalisation occurs in this case.

Table 5.5. Summary of Raman data for ar-, Na-solvent- and $C_{12}H_{25}$-solvent-graphite.

Sample	I_D/I_G	I_{2D}/I_G	$I_D/I_{D'}$	n_D (cm^{-2})	C/R
ar-NFG	0.05±0.05	0.47±0.04	1.3±1.5	-	-
Na-THF-NFG	0.06±0.08	0.49±0.13	1.4±2.2	-	-
$C_{12}H_{25}$-THF-NFG	0.2±0.2	0.6±0.2	3±3	1.6×10^{11}	2418
Na-DME-NFG	0.3±0.3	0.8±0.2	2±3	-	-
$C_{12}H_{25}$-DME-NFG	2.3±0.8	0.62±0.16	5.2±1.2	2.0×10^{12}	193
Na-DMAc-NFG	0.05±0.14	0.13±0.12	1.6±1.4	-	-
$C_{12}H_{25}$-DMAc-NFG	0.1±0.3	0.3±0.2	2±3	8.6×10^{10}	4435

There is also a large degree of exfoliation in both cases, reflected in the I_{2D}/I_G of 0.62±0.16 for $C_{12}H_{25}$-DME-NFG and 0.8±0.2 for Na-DME-NFG. Whilst the evidence shows that Na-DME proved effective at exfoliating the graphite starting material, the broad histograms reflect the

inhomogeneity of the samples containing a mixture of graphite, intercalated and exfoliated sheets.

In contrast to previous XRD studies of Na-GICs, the intercalated graphite samples were thoroughly washed, and studied under ambient conditions, to see how much solvent remained even after processing. XRD patterns show the presence of an intercalation compound for Na-DMAc-NFG (Figure 5.14), with slightly different interlayer spacings to the THF sample, suggesting that DMAc does successfully coordinate to sodium cations. The different spacing arises from the different molecule size, although the conformation of DMAc molecules around the sodium cation is unknown. Peaks at 2θ = 12.5° and 25.1° (CuK$_\alpha$ = 1.542 Å) correspond to an interlayer spacing of 7.1 Å, matching the stage 1B structure in Na-THF-NFG. With the similar intercalate thickness of 3.75 Å, it is assumed that the DMAc molecules adopt a lying down arrangement around each sodium cation; TGA and XPS analyses suggest a bi- or tri-coordinate structure. A peak at 25.6°, showing no higher or lower stage reflections and corresponding to a layer thickness of 3.5 Å, is assigned as areas of random staging, or turbostratically stacked graphite.[285] No clearly defined peak at 26.6° can be seen, although there is a broad tail, suggesting that the majority of the sample is fully intercalated or else, lacks coherent long-range stacking structure to be detected by XRD. The XRD pattern for C$_{12}$H$_{25}$-DMAc-NFG also contains peaks at 12.6° and 25.6°. The peak intensity of 25.1° has decreased, and is no longer distinct from the signal attributed to random staging, indicating a reduced long-range order in the stage 1 intercalation structure. These results suggest that alkylation prevents layers from closing fully, allowing the diffusion of some solvent from the structure. As for Na-DMAc-NFG, no apparent graphite (002) peak remains. For Na-DME-NFG, no defined peaks at low angle can be seen, but a broadening of the graphite (002) occurs, supporting the results obtained from TGA and Raman that some degree of exfoliation occurs, with only a small amount of intercalant remaining. The pattern for C$_{12}$H$_{25}$-DME-NFG is dramatically different again, exhibiting broad peaks at 12.3° and between 24.1 and 25.1°. These lines may be indexed using an interlayer spacing of 7.3 Å and suggest a stage 1 structure, likely with a mixture of DME in a 'lying down' phase B conformation, and grafted dodecyl chains. A small graphite (002) indicates that incomplete exfoliation occurred. The peak at 25.1° is assigned as the random stage phase. Another broad peak at 28.1° corresponding to an interlayer spacing of 3.17 Å could not be identified, but may also be a larger angle reflection of a poorly-defined stage structure which shows no other strong signals. A similar peak is apparent in the THF-prepared samples.
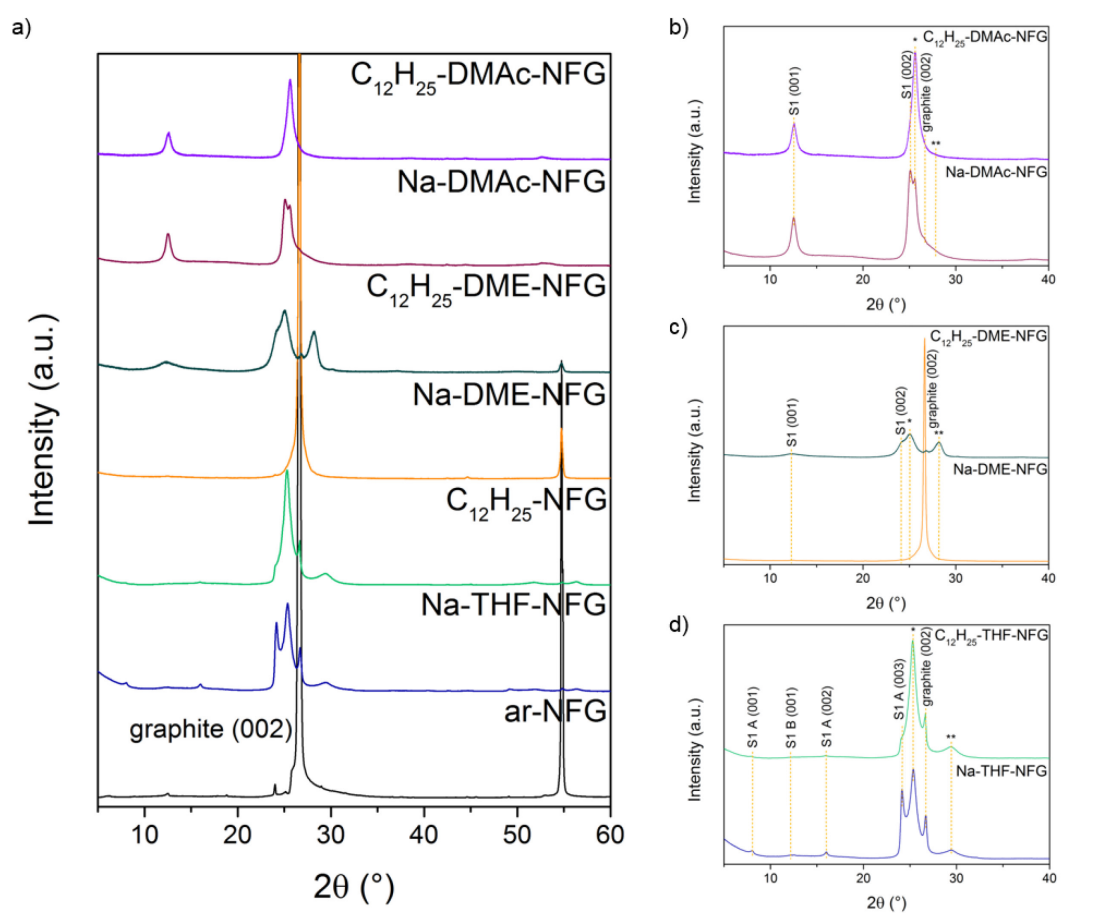
Figure 5.14. a) XRD patterns for ar-, Na-solvent- and $C_{12}H_{25}$-solvent-NFG; and magnified XRD patterns of b) Na-DMAc-NFG and $C_{12}H_{25}$-DMAc-NFG, c) Na-DME-NFG and $C_{12}H_{25}$-DME-NFG, and d) Na-THF-NFG and $C_{12}H_{25}$-THF-NFG. The peak labelled * is attributed to the 'random stage' phase or turbostratic graphite; the peak labelled ** arises from an unknown phase.

5.2.2.1. Summary of solvent effects on grafting

Overall, the highest grafting ratio (6.7%) was achieved by functionalisation in DME (Table 5.6). However, Raman analysis of the unfunctionalised control suggests that some inadvertent grafting may occur; degradation of solvent in the pure sodium naphthalide (Na/np) solution was observed after one day, which may result in reactive radical species which can attack the carbon framework, possibly activating further sites for reaction. This inadvertent functionalisation was also useful to prevent restacking, resulting in a highly-exfoliated material. A similar degree of exfoliation was achieved by functionalisation in THF, but graphenide dispersions prepared in DMAc did not exfoliate to any significant degree, due to the stability of the Na-DMAc-GIC structure formed; the resulting unavailability of grafting sites resulted in a lower GR than achieved in THF. In all cases, solvent remained trapped; interestingly, for THF and DME, alkyl grafting actually increased the amount of residual solvent, whilst in DMAc,

the opposite was observed, likely due to the heterogeneity in the starting material (discussed below in section 5.3).

Table 5.6. Summary of grafting and solvent data for different solvent systems.

Sample	GR (TGA)	C/R (TGA)	C/R (Raman)	C/solvent (TGA)	Na-solvent-NFG C/solvent (TGA)	Raman I_{2D}/I_G
$C_{12}H_{25}$-THF-NFG	1.7	852	2418	18	26	0.6±0.2
$C_{12}H_{25}$-DME-NFG	6.7	209	193	28	165	0.62±0.16
$C_{12}H_{25}$-DMAc-NFG	1.0	1389	4435	36	15	0.3±0.2

5.2.3. Na-solvent-GIC solvent deintercalation

5.2.3.1. XRD monitoring of solvent deintercalation

To better understand in what form solvent remained in the samples, and how the detachment of alkyl addends is affected, the behaviour of the Na-solvent-NFGs upon heating was investigated by XRD. The Na-solvent-NFGs and ar-NFG were heated in air to 700 °C and X-ray diffraction patterns were collected at 20 °C intervals from 100 °C.
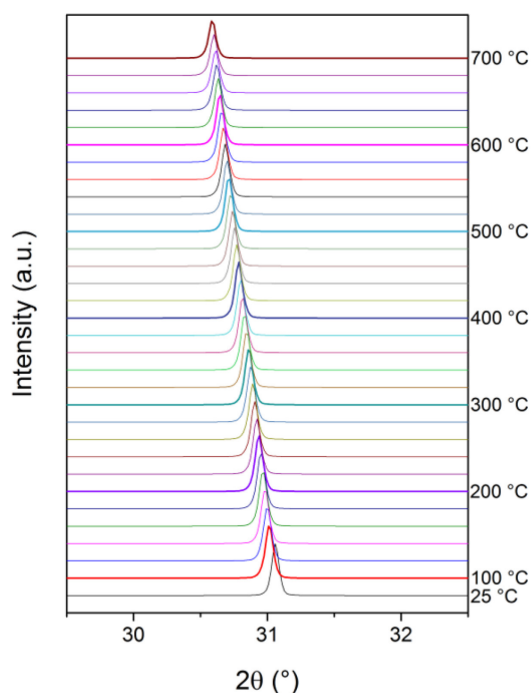
Figure 5.15. XRD patterns of ar-NFG at 25 °C, then from 100-700 °C in 20 °C intervals; CoK$_{\alpha1}$ 1.789 Å.

XRD of ar-NFG using CoK$_{\alpha1}$ radiation (1.789 Å) at 25 °C shows the graphite (002) peak $2\theta = 31.1°$, corresponding to an interlayer spacing of 3.34 Å (Figure 5.15). The XRD patterns indicate some degree of thermal expansion with increasing temperature, ending with an

interlayer spacing of 3.39 Å at 700 °C. Loss of adsorbed species such as atmospheric moisture and hydrocarbons may also contribute to layer expansion; the 0.2 wt% TGA weight loss of ar-NFG supports this assertion. The persistence of the (002) peak at 700 °C shows that ar-NFG is stable in air, confirmed by TGA.

Under the same heat treatment, Na-THF-NFG gave rise to dramatically different behaviour (Figure 5.16). At 25 °C, the characteristic stage 1 A peaks can be seen; with CoK$_{\alpha 1}$ radiation, these peaks appear at 9.3° (001), 18.5° (002) and 28.0° (003). The random stage structure peak is shifted with cobalt radiation to 29.5°. The graphite (002) peak is also present at 31.1°, but at a much-reduced intensity compared to ar-NFG. The broad peak at 8.1° is present in all scans, and blank scans of silica glass (Appendix I, Figure I.8), so is not attributed to the sample.
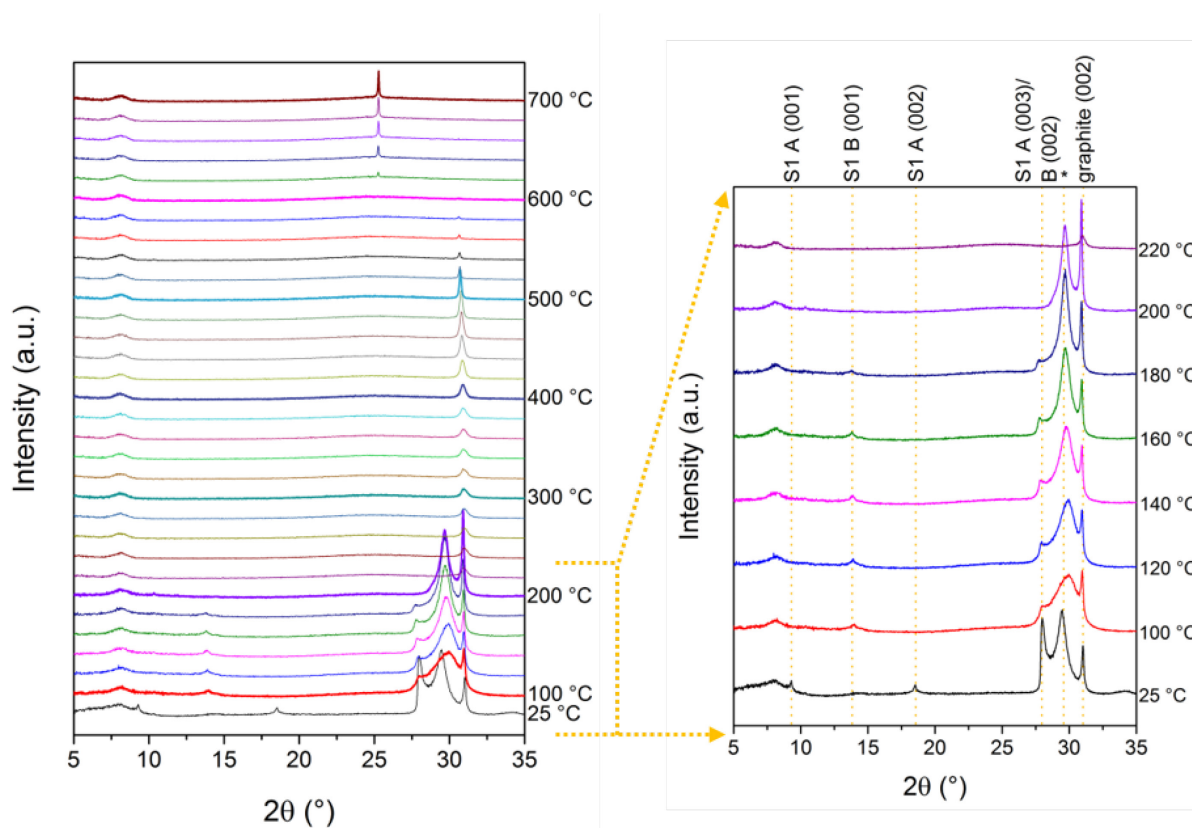
Figure 5.16. XRD patterns of Na-THF-NFG at 25 °C, then from 100-700 °C in 20 °C intervals, and magnified diffractograms; CoK$_{\alpha 1}$ 1.789 Å. Stage 1 phase A and B structures correspond to interlayer spacings of 11.1 and 7.1 Å, respectively. The starred peak is attributed to the 'random stage' phase or turbostratic graphite. The broad peak at 8.1° is present in the blank scan of silica glass and is not attributed to the sample.

At 100 °C, a conversion of stage 1A to 1B was observed from the complete loss of the A(001) and A(002) peaks; the loss of the A(003) reflection is masked by the appearance of the (002) peak for phase B at the same value of 2θ, accompanied by the B(001) peak at 14.1°. The

random stage phase became less ordered with a lower d-spacing, indicated by a broadening of the peak and a shift to a higher angle (29.9°). These shifts suggest that significant reordering occurred within the temperature range. As the temperature was increased to 200 °C, eventually all remaining phase B Na-THF converted to the random stage or turbostratic phase, reflected in the decreasing 2θ position of B(002) indicating slight layer expansion from rearrangement/solvent loss, along with a steady decrease in peak intensity and eventual total loss of the peak by 200 °C (Figure 5.16). Concurrently, the random stage/turbostratic graphite peak sharpens and intensifies, also with a slight downshift in 2θ, whilst the graphite (002) peak becomes stronger, suggesting the recovery of some graphitic domains, presumably from the 'closing up' of layers as solvent pockets coalesce and travel outwards towards the edges of the flakes. Between 200 °C and 220 °C, two things occurred: all well-defined GIC stage structuring was lost from the sample, coinciding with the first temperature step in the TGA showing the loss of THF; and the graphite peak loses significant intensity and broadens, suggesting that ordered areas of graphite were expanded during this solvent loss, with graphene layers being forced apart to allow THF molecules to escape.

Upon further heating, the sample showed a slow recovery of graphitic domains, with assumed sliding of intercalant solvent pockets between the layers towards flake edges following the Daumas-Herold model,[90] with an acceleration around 400 °C; this temperature coincides with the second step loss of THF in the TGA. As the THF molecules are escaping from disordered pockets, gradually the graphene layers reorder, regaining graphitic AB stacking. After 520 °C, it can be seen from the decrease and then disappearance of the graphite (002) peak that further solvent escape occurred resulting in layer expansion, after which the sample gradually combusted, and eventually all carbon material disappeared. The remaining white solid on the disc showed a distinct peak at 25.3° and is thought to be some sort of sodium silicate, a result of reaction of residual sodium with the silica plate (Figure 5.17).
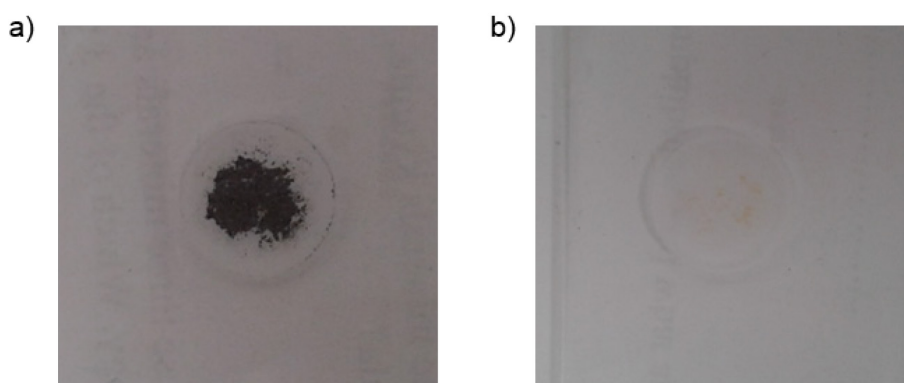
Figure 5.17. Photographs of Na-THF-NFG a) before, and b) after heating to 700 °C.

The trend seen by XRD is corroborated by the Raman I_{2D}/I_G ratios of samples taken at 100 °C intervals (Figure 5.18). At 200 °C and below, the I_{2D}/I_G ratio of Na-THF-NFG is upshifted with a broad distribution, reflecting the more exfoliated nature and existence of different environments in the sample. Γ_{2D} is also broad and shows a bimodal distribution, again indicative of different graphitic environments. Above 200 °C, however, the histograms narrow and decrease, suggesting a recovery of graphitic stacking after solvent escape, supporting the results obtained from XRD. Unlike in the XRD measurements, where total combustion occurred by 600 °C, graphite remained in the sample examined by Raman; this discrepancy is attributed to the different temperature ramps and heating environments.
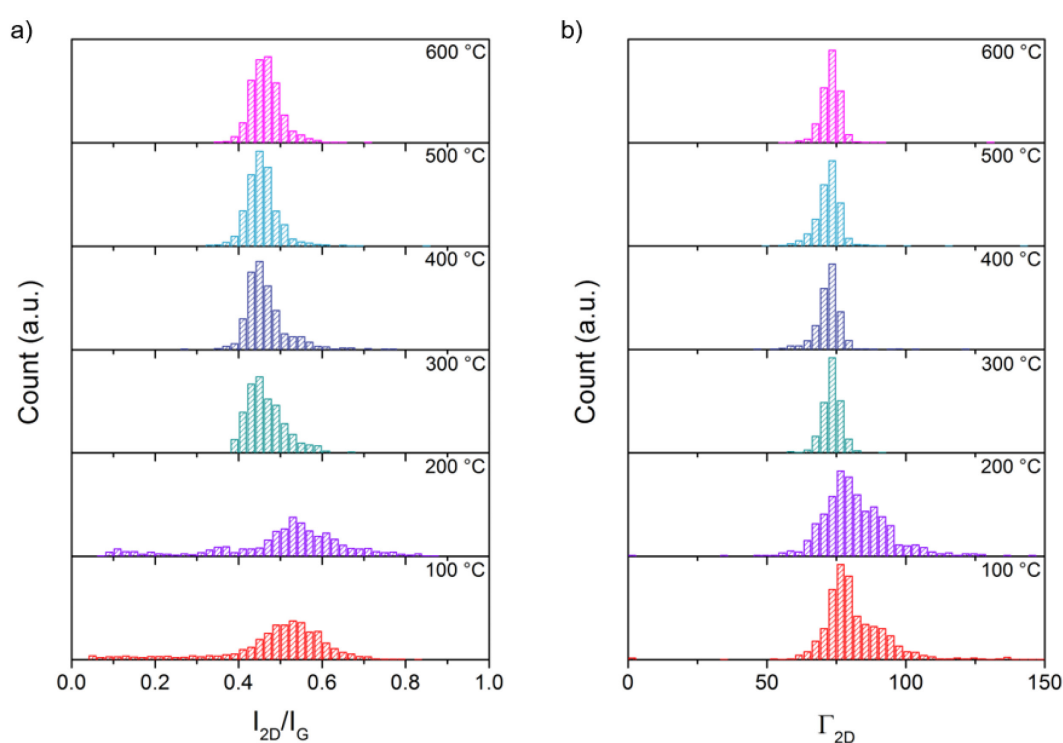
Figure 5.18. Raman histograms of b) I_{2D}/I_G ratio and c) Γ_{2D} of Na-THF-NFG, at 100 °C intervals.

Overall, a striking correlation can be seen between the graphite (002) peak intensity and the TGA profile of Na-THF-NFG (Figure 5.19). In the temperature range where solvent loss is detected by TGA, there is a concomitant decrease in the (002) peak, signalling the expansion of graphene layers. Leading up to these regions, there is a slow increase, suggesting that intercalant rearrangement occurs with increasing temperature, where the driving force is the restacking of graphitic layers, with increasing van der Waals energy. In the first step, solvent from the large, ordered GIC domains is lost; the second step presumably arises from solvent lost from less well-defined, smaller domains, which show no long-range order in XRD.
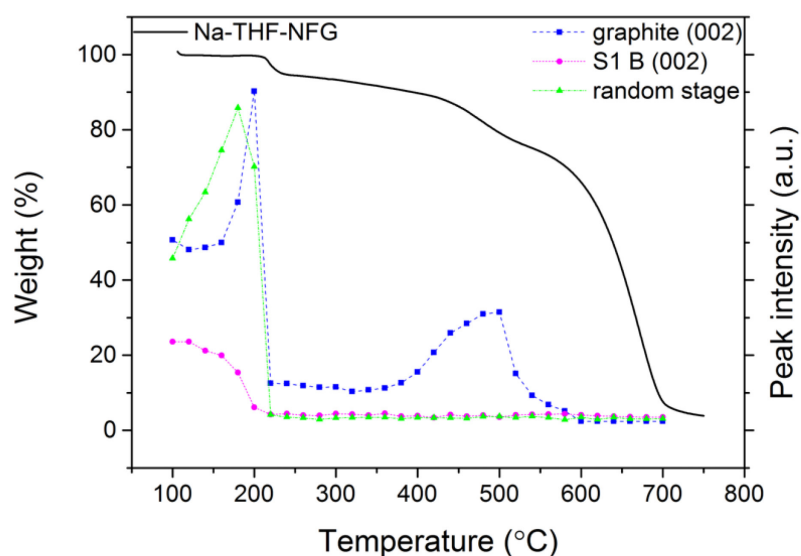
Figure 5.19. XRD peak intensity of graphite (002), S1 B (002) and random stage structure in Na-THF-NFG against temperature, with TGA shown for comparison.

In an analogous experiment, Na-DME-NFG shows the characteristic graphite (002) peak at 31.1° at 25 °C (Figure 5.20a); the intensity is significantly weaker than in ar-NFG, for a similarly prepared sample, indicating that some degree of exfoliation occurred during the reductive process. As the temperature increased, the graphene layer spacing increased, indicated by the decreasing 2θ position, following a similar trend to ar-NFG. A plot of the graphite (002) peak intensity against temperature shows the reordering of graphitic domains up to ~250 °C, followed by disordering and layer expansion, presumably after solvent loss (Figure 5.20b). The graphite domains grow again between 450 and 600 °C where more DME is lost from the sample, before gradually disappearing due to combustion. Complete combustion of the sample occurred by 680 °C, earlier than results obtained from TGA, due to the difference in temperature ramp.

Na-DMAc-NFG behaves in a similar way to Na-THF-NFG under the same heat treatment (Figure 5.21a). With CoK$_{\alpha 1}$ radiation, the intercalate peaks appear at 14.5° and 29.1° at 25 °C. The signal attributed to random staging or turbostratic graphite is also present at 29.8°, overlapping with the S1(002) peak. The graphite (002) peak is barely visible above the background, indicating very few remaining domains with coherent graphitic stacking. As the temperature increases, the intercalate (001) gradually decreases, whilst the (002) briefly increases before decreasing, gradually merging with the random stage peak; concurrently, the random stage peak increases in intensity up to 240 °C before gradually disappearing (Figure 5.21b).
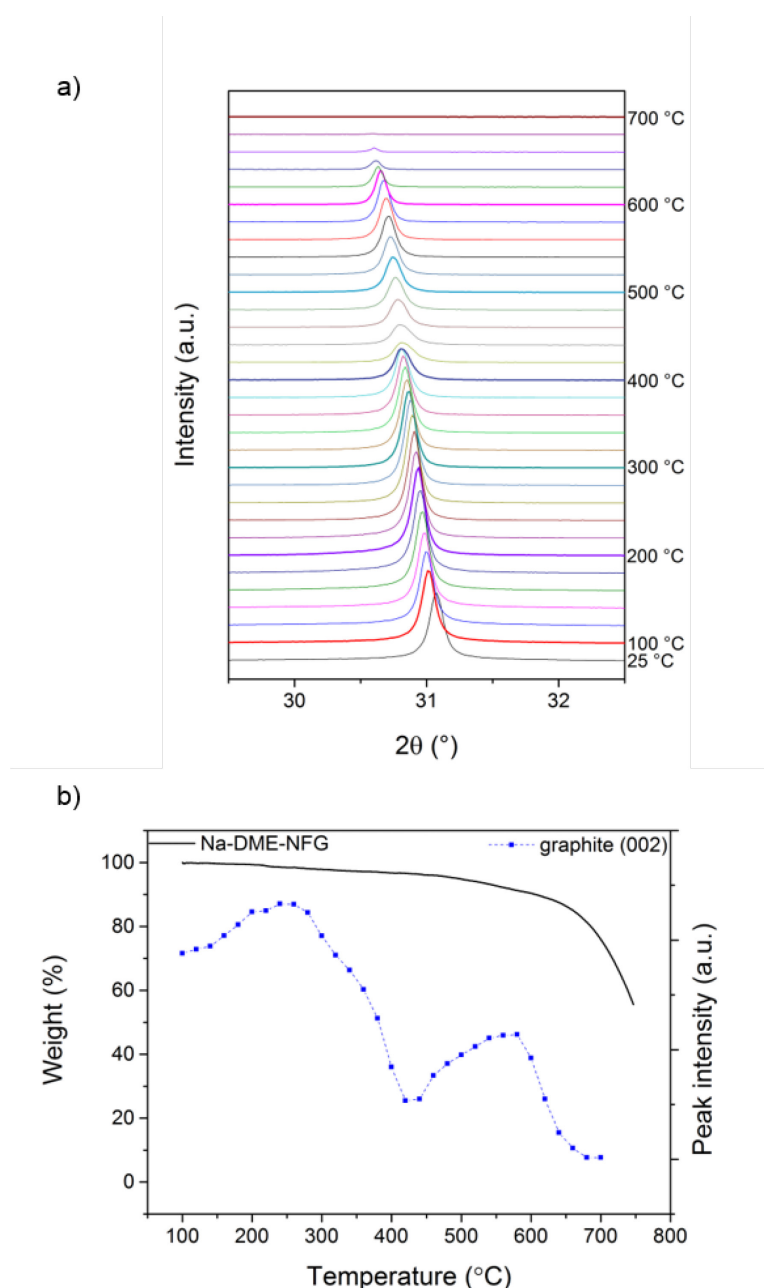
Figure 5.20. a) XRD patterns of Na-DME-NFG at 25 °C, then from 100-700 °C in 20 °C intervals; CoKα1 1.789 Å; and b) XRD peak intensity of graphite (002) in Na-DME-NFG against temperature, with TGA shown for comparison.

By 280 °C, all trace of defined GIC structure is lost and the graphite peak weakens and broadens, coinciding with the first solvent loss step, where DMAc molecules are escaping from flake edges. A gradual increase in the graphite (002) intensity follows around the second loss of DMAc from the sample; from 460 °C onwards, the peak signal decreases due to combustion of the sample. A similar residue remained after combustion to that in Na-THF-NFG, supposed to be sodium silicate. The same trend in the graphite (002) peak intensity with temperature can be seen (Figure 5.21c), although in a much less defined way, which is attributed to the

fact that the (002) peak signal was extremely weak, appearing over a broad background, resulting in much less reliable curve fitting data.
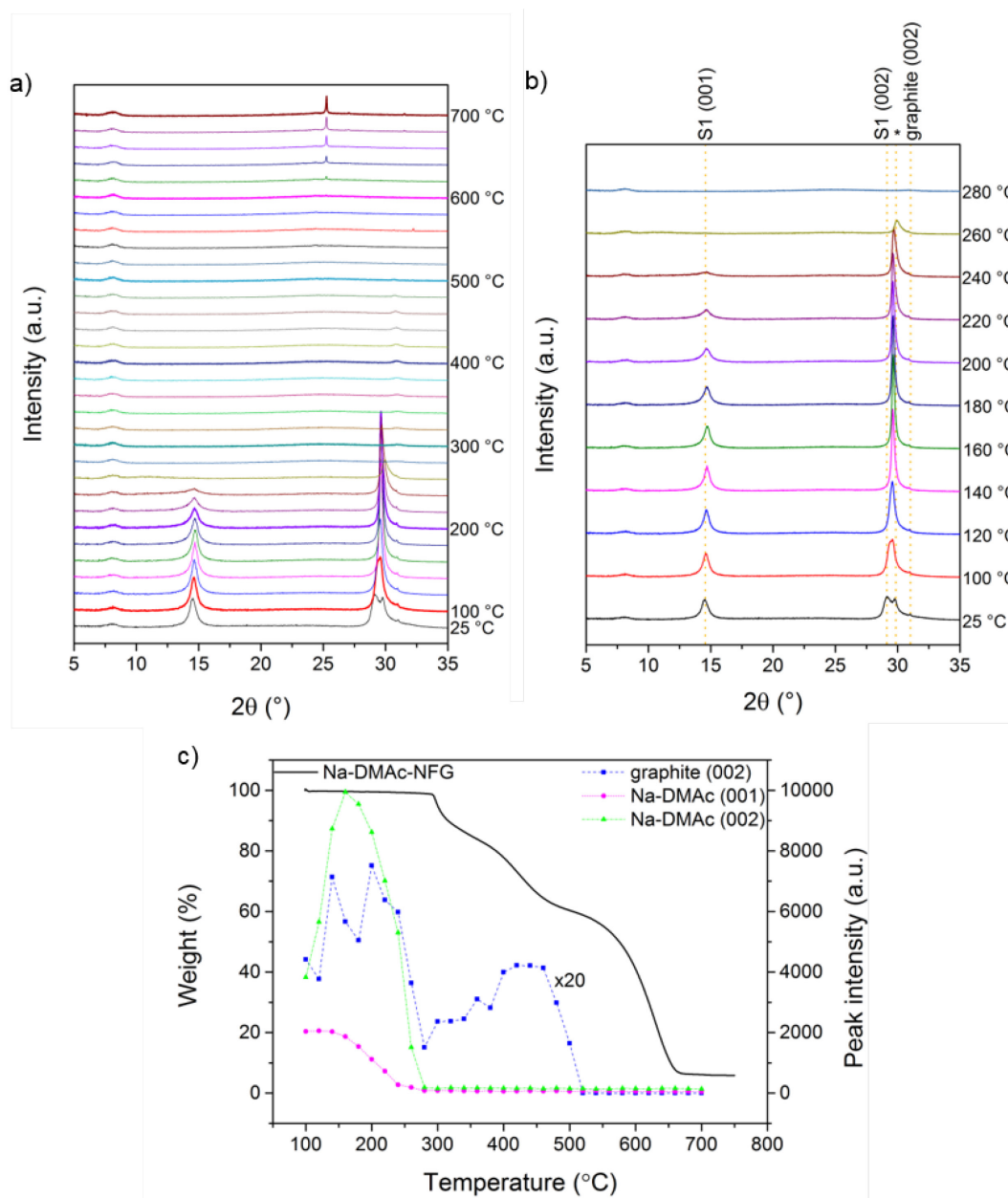
Figure 5.21. a) XRD patterns of Na-DMAc-NFG at 25 °C, then from 100-700 °C in 20 °C intervals; b) magnified X-ray diffractograms between 25-220 °C; CoKα1 1.789 Å; stage 1 structure corresponds to an interlayer spacing of 7.1 Å; the starred peak is attributed to the 'random stage' phase or turbostratic graphite; c) XRD peak intensity of graphite (002) in Na-DMAc-NFG against temperature, with TGA shown for comparison.

Overall, these XRD measurements during heating indicate that the Na-solvent-GICs are extremely stable in ambient conditions at room temperature. Gradual rearrangement of the staging structure occurs up until the first exfoliation step (generally around 200-300 °C), where solvent is lost from the sample, and all distinct staging is lost. Interestingly, rearrangement

during these temperatures does not proceed *via* other higher stage intercalation compounds, since no peaks were detected for these structures. Following the first exfoliation step, there is a gradual annealing of the remaining graphite, reflected in the increase in the graphite (002) peak, proceeding until the second loss of residual solvent, which causes further exfoliation. In such large, flat sheets, it might be expected that sealing up of layers causes solvent trapping, and that the effect might be mitigated with the use of different graphite starting materials (see section 5.3).

5.2.3.2. TEM imaging of solvent deintercalation

Illumination of the solvent-intercalated samples under an electron beam illustrates the movement of solvent domains. To image these areas, a smaller graphite platelet (GP) with an average lateral size of ~5 µm was used, to be able to track movement across whole flakes. Characterisation of the starting material is given in Section 5.3.1.2. An identical charging procedure was applied to GP in THF and DMAc to yield Na-THF-GP and Na-DMAc-GP. EDX mapping of Na-THF-GP indicates that in fact THF and sodium are clustered around pocket edges (Figure 5.22), where dense areas of oxygen and sodium correspond to the brighter regions of the dark field TEM image.
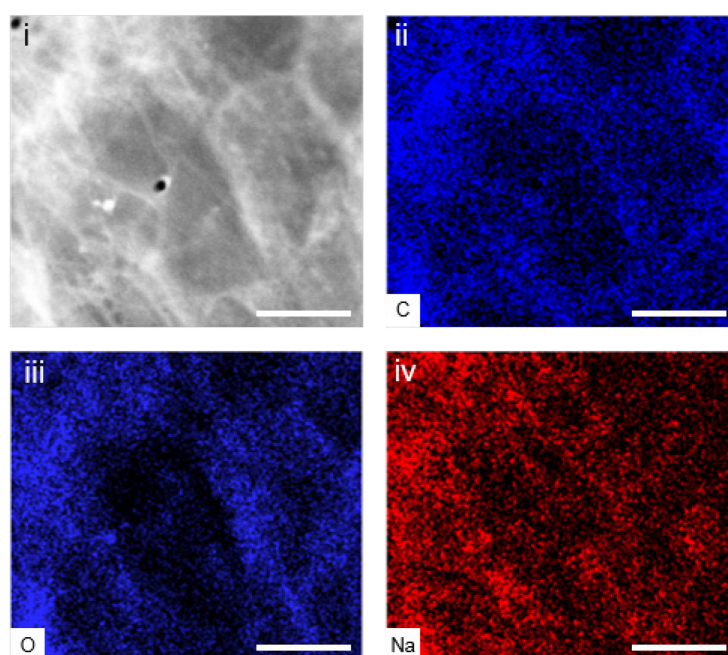
Figure 5.22. EDX mapping of solvent pockets in Na-THF-GP: i) dark field TEM image, and corresponding maps of ii) C, iii) O and iv) Na content; scale bar is 200 nm.

The presence of sodium and oxygen clusters could be ambiguously attributed to sodium oxide, or sodium-THF. However, analysis of Na-DMAc-GP mapping indicates that similar areas also

contain nitrogen, confirming that there is solvent in these regions (Figure 5.23), and that it is coordinated to sodium.
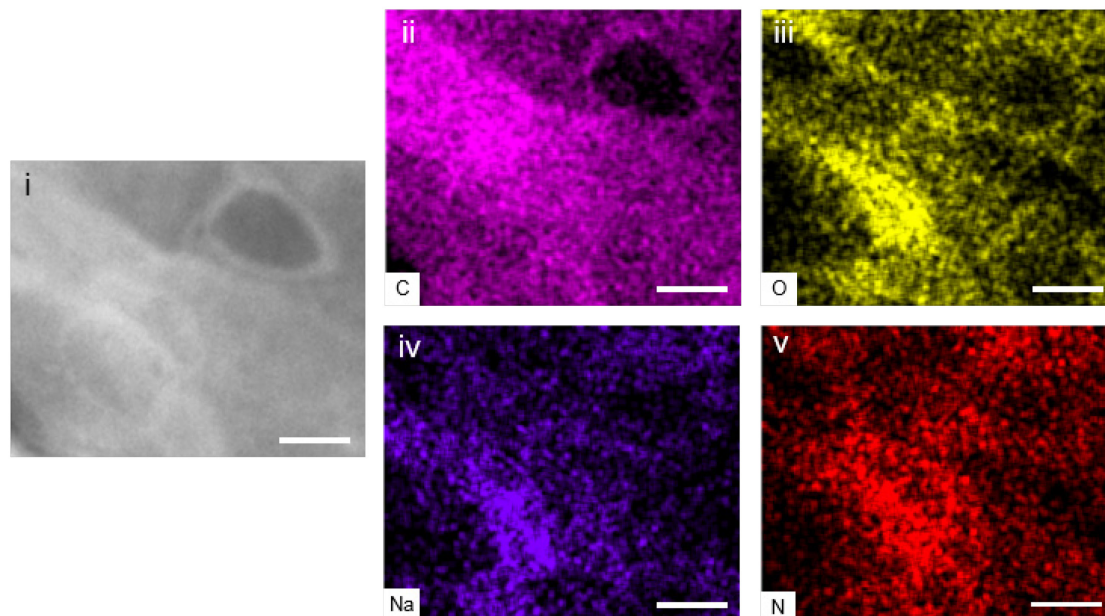
Figure 5.23. EDX mapping of solvent pockets in Na-DMAc-GP: i) dark field TEM image, and corresponding maps of ii) C, iii) O, iv) Na and v) N content; scale bar is 100 nm.
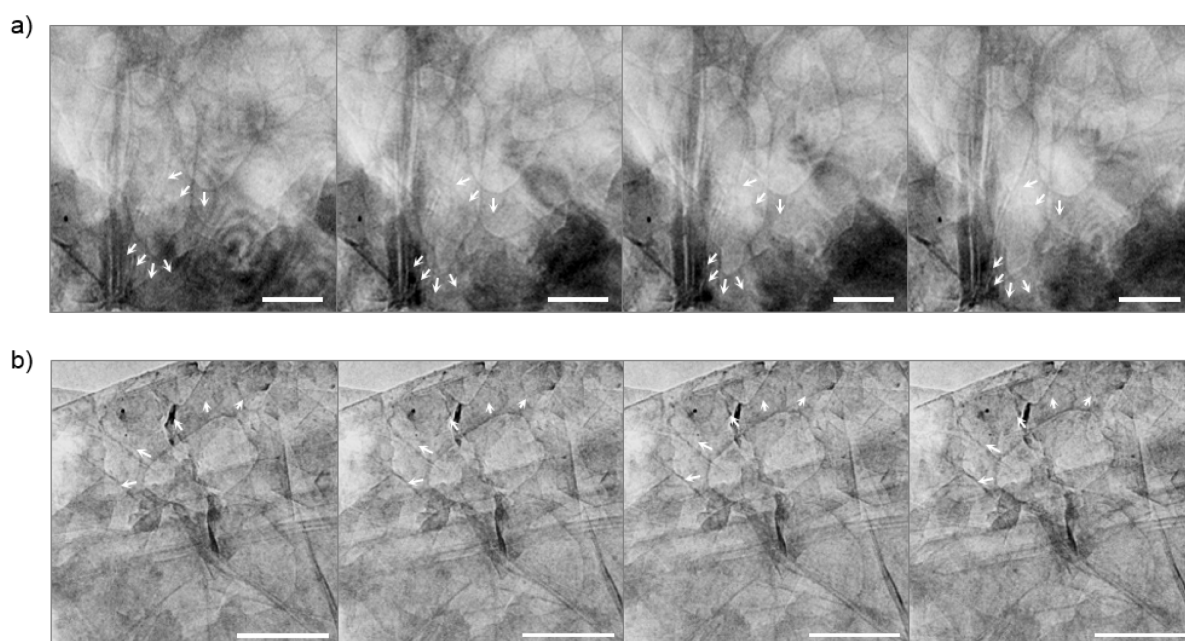
Figure 5.24. Time-lapse TEM images of pocket areas growing and travelling under the electron beam, in two different regions shown in a) and b); scale bar is 100 nm.

Over the whole sample, the pocket areas, ranging from ~10-300 nm, appear less dense than the surrounding regions, and show no Moiré patterns or wrinkling. Under the electron beam, bubbling and shifting of layers was observed through the movement of waves of these Moiré

patterns. The growth and movement of these graphitic 'pocket' domains can be seen, with solvent being pushed towards the edges (Figure 5.24), consistent with XRD patterns showing rearrangement in the staging structure; it seems that the driving force for this mechanism is the restacking of graphene layers. Even after prolonged exposure to the electron beam, these pockets can still be imaged, confirming the high stability of these Na-solvent-GICs.

5.2.4. Summary of alternative solvent systems

In natural flake graphite, regardless of the medium, solvent remains trapped in the final product, coordinated to sodium, and is extremely difficult to remove; TGA, XRD and TEM illustrate the stability of these GIC structures. Even at high temperature when any ordered GIC structure is disrupted, graphite pockets still trap residual solvent. Despite the suitability of amidic solvents for stabilising CNMs, graphenide solutions in DMAc do not exfoliate to any significant degree, due to the stability of the Na-DMAc-GIC structure formed; the resulting unavailability of grafting sites results in a lower GR than achieved in THF. DME results in a large degree of exfoliation, but Raman data suggests that this phenomenon may be due to inadvertent functionalisation. In other applications, this could be advantageous, but for the systematic functionalisation study, a stable system is required which can effectively exfoliate without inadvertently damaging the carbon framework. In the following work, a THF solution of sodium naphthalide is therefore used for the reductive process.

5.3. Alternative graphite starting materials

Natural flake graphite contains large, flat graphene layers, within which it is easy to trap solvent. Furthermore, naturally occurring defects[276] could prevent full exfoliation to single-layer graphene. In this section, different graphite starting materials are explored to see how the grafting and amount of trapped solvent vary with the flake size and morphology. Five starting graphite materials are examined: two naturally occurring flake graphites of different lateral flake size, shear-exfoliated graphite platelets, and two artificially grown graphene products, graphite nanofibres and few-layer graphene. Natural flake graphite (NFG) has been characterised above (Section 5.1.1), details of the remaining materials are provided in the following section.

5.3.1. Characterisation of graphite starting materials

5.3.1.1. Large flake graphite

This large flake graphite (LFG) is naturally occurring, showing a similar high crystallinity to NFG. The as-received flakes (ar-LFG) have an average lateral size of 5 mm and thickness of

500 µm with smooth, flat surfaces (Figure 5.25). The characteristic graphite (002) peak at $2\theta = 26.6°$ can be seen in the XRD pattern and the presence of the higher order (004) peak indicates high crystallinity, with an estimated 200 layers per stack (Figure 5.25c). In the Raman spectrum the 2D peak at ~2720 cm^{-1} shows a strong asymmetric shoulder, characteristic of graphite, and the absence of a D peak ($I_D/I_G = 0.06±0.05$) indicates a lack of defects from grain boundaries, flake edges or functionalities (Figure 5.25d).
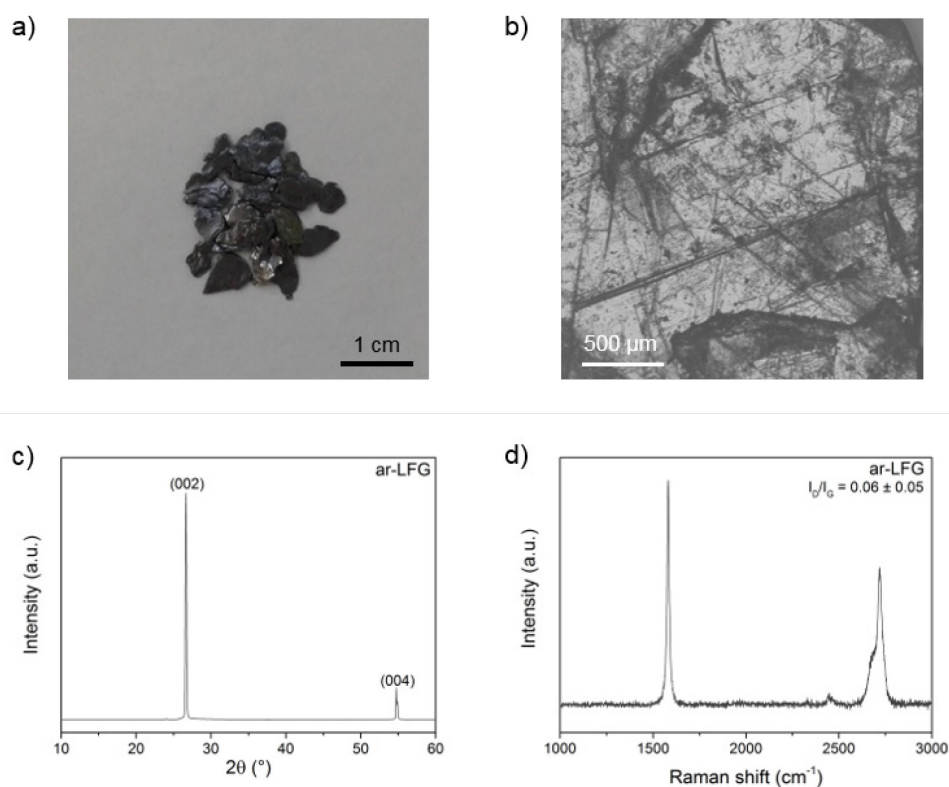
Figure 5.25. a) Photograph, b) optical micrograph, c) XRD pattern, and d) Raman spectrum of ar-LFG.

5.3.1.2. Graphite platelets

These graphite platelets are obtained from shear exfoliation of natural graphite and consist of smaller, more exfoliated flakes. The SEM image of as-received GP (ar-GP) shows partially exfoliated flakes of around 5 µm in size, with thicknesses of around 500 nm (Figure 5.26b). The flakes generally have smooth flat surfaces but show some crumpling at flake edges, presumably introduced during the shear exfoliation procedure. The XRD pattern shows the interlayer (002) peak, and a small (004) reflection; these peaks have a much lower intensity than for a similarly prepared sample of ar-NFG, suggesting smaller stacked domains (Figure 5.26c). Analysis of the peak width provides an estimate of ~150 graphene layers. An I_D/I_G ratio of 0.12±0.02 implies the presence of some defects which may arise from the edges or may be introduced during the exfoliation process (Figure 5.26d). The 2D peak, centred at 2690 cm^{-1},

is asymmetric, but with a less pronounced graphitic shoulder indicating that this material has a greater degree of exfoliation than NFG. XPS compositional analysis reveals the presence of sodium in the as-received material (0.1 at%), likely from residual surfactant from the exfoliation step; the composition is taken into account when considering grafting and the amount of solvent and sodium trapped.
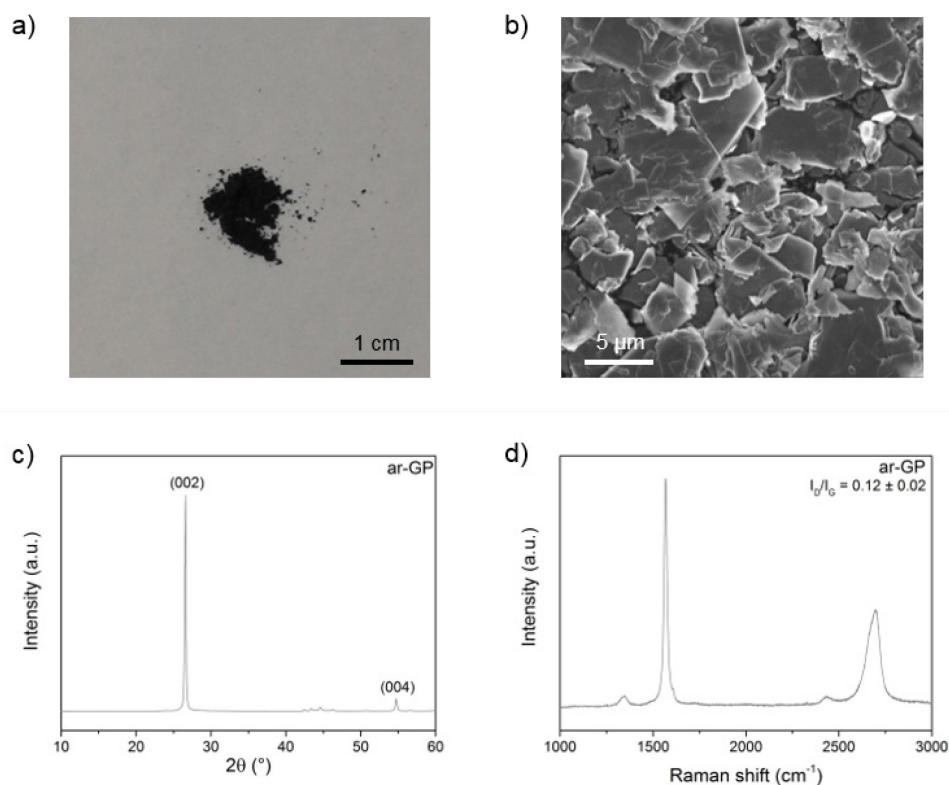
Figure 5.26. a) Photograph, b) SEM image, c) XRD pattern, and d) Raman spectrum of ar-GP.

5.3.1.3. Graphite nanofibres

Graphite nanofibres (GNF) consist of graphene platelets with diameters in the range 80-150 nm stacked in a highly-ordered layered structure, with the graphitic c-axis parallel to the length of the fibre. Average fibre lengths range from 1 to 5 μm (Figure 5.27b). The high crystalline quality in the direction of the nanofibre axis can lead to easy shear distortions, and therefore platelet exfoliation. A large D peak (I_D/I_G = 1.6±0.1) can be seen in the Raman spectrum of the as-received material (ar-GNF) (Figure 5.27d), arising from edge scattering of the graphene platelets.[266] The graphitic shoulder is notably absent in the 2D peak, showing less coherence between graphene layers and therefore less ordered stacking, and the peak is downshifted to 2680 cm^{-1}, relative to graphite. In the XRD pattern, the (002) peak is broadened and the (004) is greatly reduced in intensity, suggesting low stacking order; the Scherrer equation provides an estimate of ~60 coherent graphene layers (Figure 5.27c).

Broad overlapping signals between 42° and 46° arise from (101) and (100) plane contributions;[289] these are increased in intensity compared to the two natural flake materials, since less preferential sample alignment occurs for GNF during measurement.
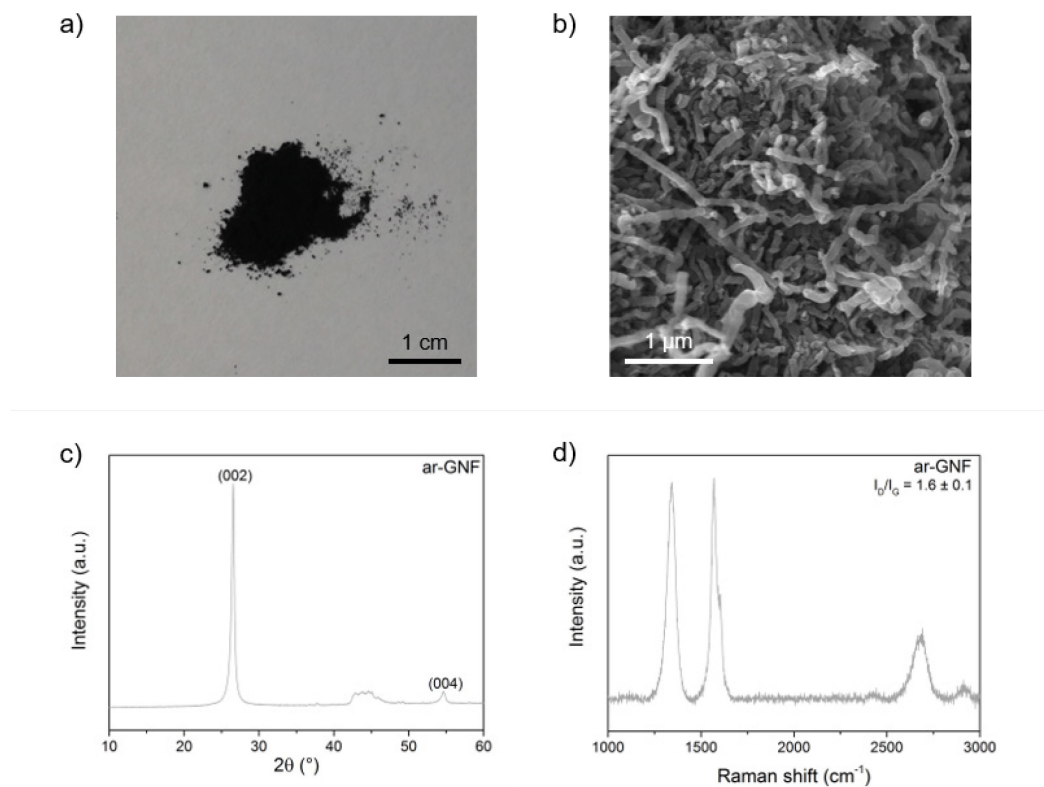
Figure 5.27. a) Photograph, b) SEM image, c) XRD pattern, and d) Raman spectrum of ar-GNF.

5.3.1.4. Few-layer graphene

This few-layer graphene (FLG) is grown by microwave plasma treatment, yielding small wrinkled flakes (Figure 5.28a) with a slightly crumpled morphology which prevents restacking; the starting material is therefore already reasonably exfoliated (~13 layers, estimated by XRD), and the flake surfaces and edges are accessible for functionalisation. It is also less likely that solvent remains trapped between graphene layers after processing, compared to larger, flatter sheets. Lateral flake size lies in the range 0.25 to 1.5 µm (Figure 5.28b) although they appear smaller by TEM, due to wrinkling and folding. The XRD pattern for as-received FLG (ar-FLG) shows a low degree of c-axis coherence, with a weak and broad (002) peak; the (004) peak is notably absent (Figure 5.28c). The slight downshift of the (002) corresponds to a slightly expanded d-spacing of 3.37 Å. A large D peak ($I_D/I_G = 0.31\pm0.04$) can be seen in the Raman spectrum, arising from edge scattering,[266] because many flakes are smaller than the laser spot size (Figure 5.28d). The 2D peak centred at 2683±3 cm^{-1} is highly symmetrical and

downshifted slightly, reflecting the significantly exfoliated nature of the material. The well-defined G band at ~1580 cm^{-1} indicates a high degree of graphitisation in the flakes.
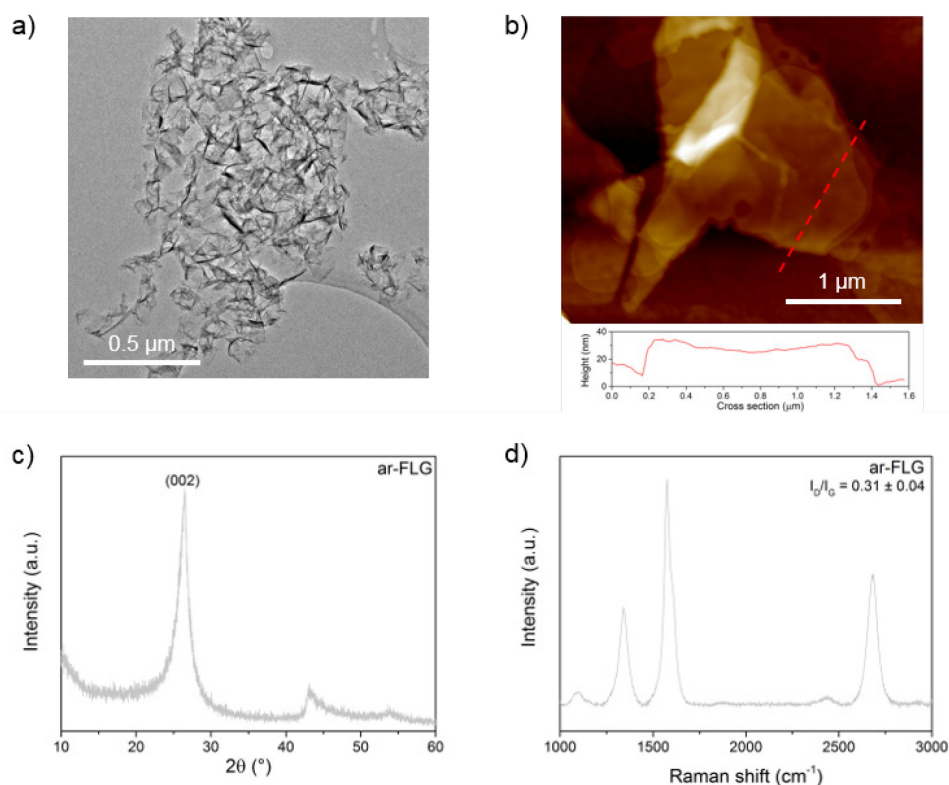
Figure 5.28. a) TEM image, b) AFM image and height contour, c) XRD pattern, and d) Raman spectrum of ar-FLG.

5.3.1.5. Summary of graphite starting materials

The LFG, NFG, GP and GNF materials all show long-range order and a strong degree of stacking with estimated layer numbers in the range 61-212 (Table 5.7); FLG shows a far higher degree of exfoliation in the as-received material, due to the crumpled morphology which prevents close restacking of graphene layers, compared with the flatter flakes observed in the other graphite samples.

Table 5.7. Summary of Raman, TGA and XRD data for graphite starting materials.

Sample	Lateral flake size (μm)	Flake thickness (μm)	Raman I_D/I_G average	TGA mass loss (%)*	XRD layer number†
ar-LFG	5000	500	0.06±0.05	0	212
ar-NFG	500	10	0.05±0.05	0.3	205
ar-GP	5	0.5	0.12±0.02	2.1	156
ar-GNF	0.1	3‡	1.6±0.1	1.5	61
ar-FLG	1.2§	0.02§	0.31±0.04	3.6	13

*At 800 °C. †Estimated using the Scherrer equation with $K = 0.91$ and taking instrumental line broadening as 0.12°. ‡Fibre length. §Estimated by AFM.

5.3.2. Preparation of $C_{12}H_{25}$-(graphite) and Na-THF-(graphite)

Reductive functionalisation with 1-bromododecane was carried out on large flake graphite, natural flake graphite, graphite platelets, graphite nanofibres and few-layer graphene. For the two flake graphites, LFG and NFG, upon treatment with sodium naphthalide a characteristic metallic blue colour was observed, indicating successful formation of a Na-THF-GIC. For the smaller materials, a black dispersion formed; graphenide solutions of FLG and GNF remained stable after several days, although charged GP sedimented after leaving to settle for several hours without stirring. Following functionalisation with 1-bromododecane, each graphite material dropped out of solution, and the supernatant became a cloudy grey colour. These dispersions were removed from the glovebox, quenched and washed, as detailed previously, to yield dodecyl-functionalised graphites ($C_{12}H_{25}$-(graphite)). Charged solutions were also directly quenched with dry O_2/N_2 without the addition of an electrophile, as solvent controls (Na-THF-(graphite)).

5.3.3. Characterisation of $C_{12}H_{25}$-(graphite) and Na-THF-(graphite)

Following reductive treatment, a greater degree of exfoliation can be observed in the functionalised LFG, NFG and GP, compared to the respective starting materials (Figure 5.29). Loosely stacked, smaller flakes are apparent, with some sheets appearing folded and crumpled, especially at flake edges (Figure 5.29 insets). The individual flake sizes for $C_{12}H_{25}$-LFG average ~61 μm and for functionalised NFG the average lateral size is ~35 μm; no significant reduction is observed for the three smaller graphites (Figure 5.31). In $C_{12}H_{25}$-GNF (Figure 5.29d), the fibres are shortened and there is greater disorder along the *c*-axis, likely due to intercalation and deintercalation resulting in slippage between graphene layers, as well as mechanical exfoliation from stirring. $C_{12}H_{25}$-FLG remains very similar in appearance to ar-FLG; the starting material is already very exfoliated, so reductive treatment was not expected to have a significant effect.
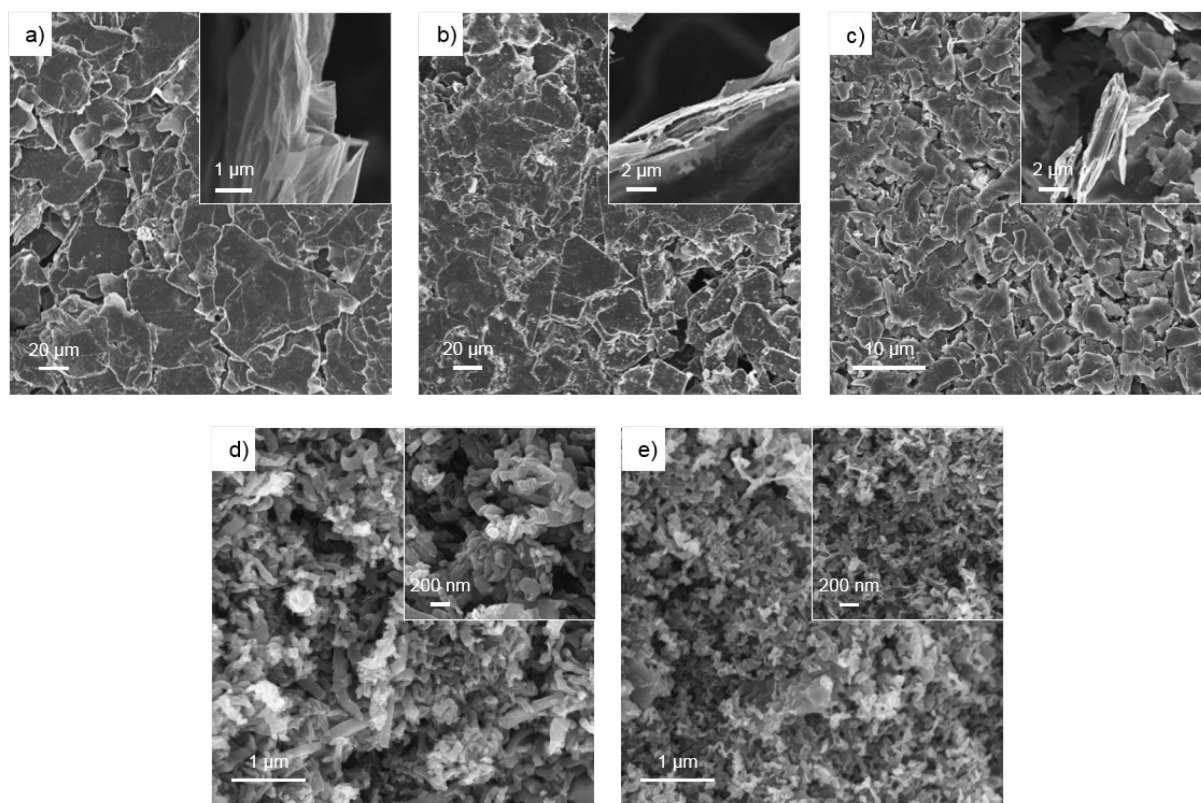
Figure 5.29. SEM images of a) $C_{12}H_{25}$-LFG, b) $C_{12}H_{25}$-NFG, c) $C_{12}H_{25}$-GP, d) $C_{12}H_{25}$-GNF, and e) $C_{12}H_{25}$-FLG.

Single- and few-layers are also evident by TEM (Figure 5.30). The larger sheets show wrinkled restacked flakes, with traces of solvent visible between the layers. In $C_{12}H_{25}$-GNF, some small individual platelets can be seen, but mostly GNF exfoliated to shortened fibres. $C_{12}H_{25}$-FLG does not show much discernible difference from the starting material, which is unsurprising since ar-FLG is already reasonably well exfoliated. However, by AFM, images obtained of Na-THF-FLG (Figure 5.30f) reveal flakes of around 4 nm thick, reduced from 20 nm in ar-FLG (Table 5.7). This thickness corresponds to ~12 layers, the size of the coherently-stacked domains observed in ar-FLG (Table 5.7). Reductive treatment therefore resulted in exfoliation of aggregates to these few-layer stacks, but with no further exfoliation beyond this point. The average lateral size of the flakes was reduced to 640 nm (Figure 5.31).
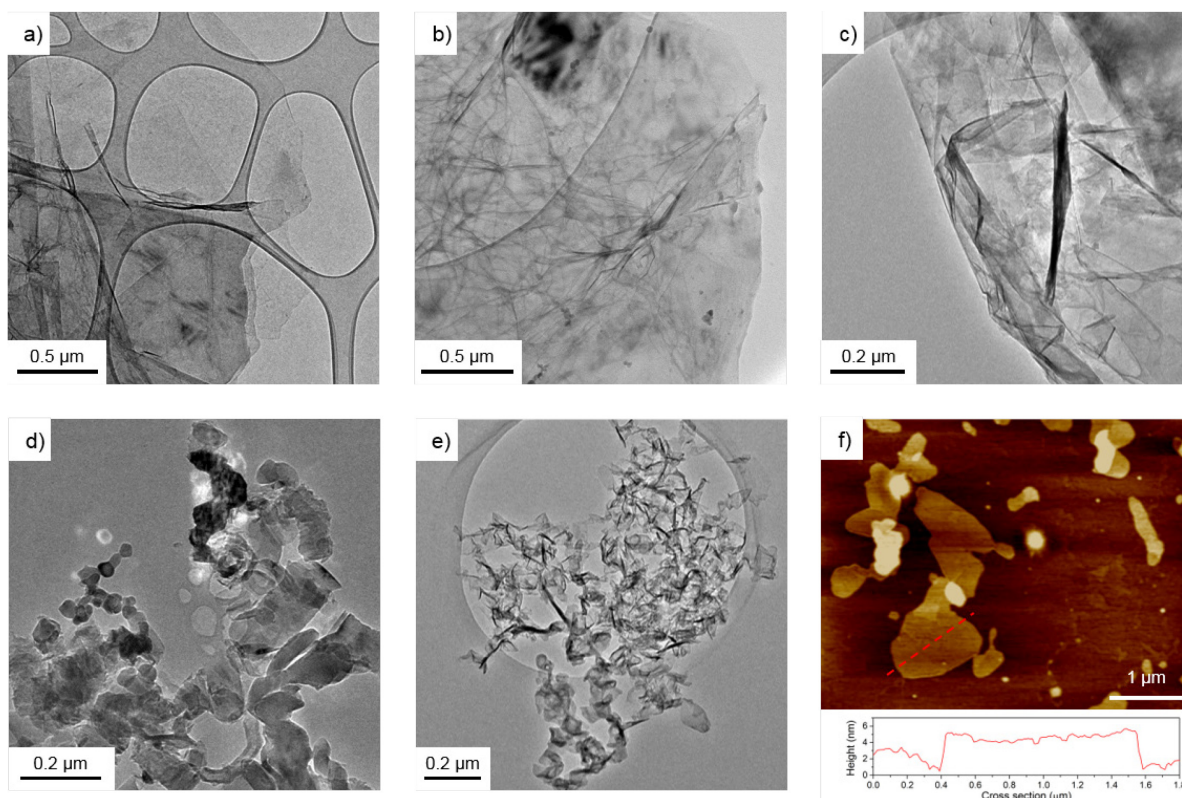
Figure 5.30. TEM images of a) $C_{12}H_{25}$-LFG, b) $C_{12}H_{25}$-NFG, c) $C_{12}H_{25}$-GP, d) $C_{12}H_{25}$-GNF, e) $C_{12}H_{25}$-FLG; and f) AFM image of Na-THF-FLG with height contour.
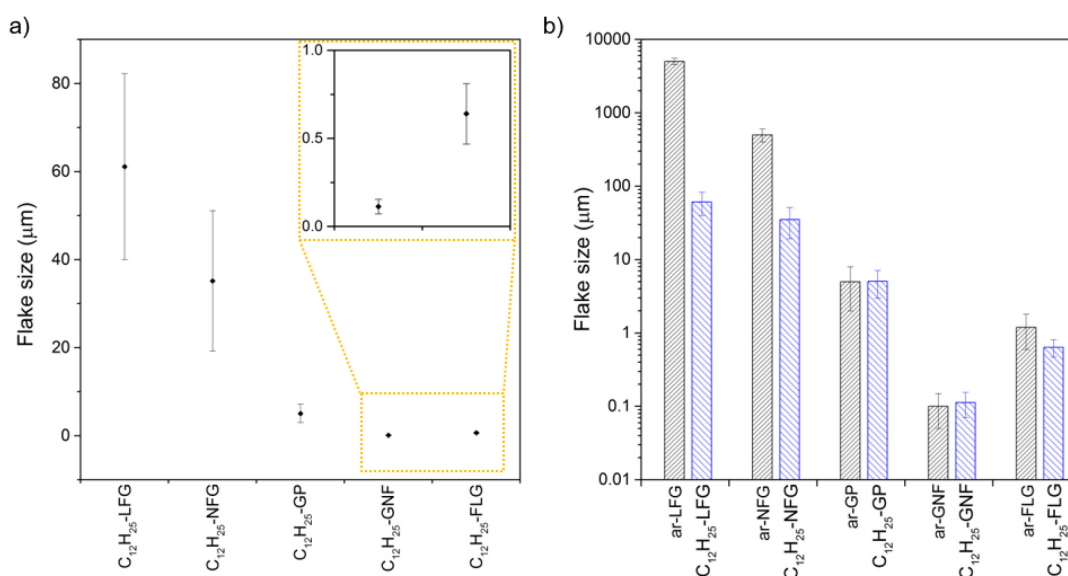
Figure 5.31. a) Average flake size and standard deviation for functionalised graphites. Values for $C_{12}H_{25}$-LFG, $C_{12}H_{25}$-NFG, and $C_{12}H_{25}$-GP obtained by SEM, $C_{12}H_{25}$-GNF by TEM and $C_{12}H_{25}$-FLG assumed to be the same as Na-THF-FLG by AFM. b) Comparison of average flake size in as-received material and after functionalisation. The larger flakes show a much greater reduction in size after reductive treatment.

XRD patterns confirm that exfoliation does indeed occur for most samples (Figure 5.32 i). For identically prepared samples, a large decrease in intensity of the graphite (002) at ~26.6° is seen in both the exfoliated Na-THF-(graphite) and $C_{12}H_{25}$-(graphite) materials. LFG and its derivatives show very similar diffraction patterns to NFG (discussed in Section 5.1.3), with the (003) peak of a stage 1A Na-THF-GIC, and the so-called random stage phase peak present in the reductively exfoliated samples. However, the relative intensities of these peaks compared to the graphite (002) peak suggest that these treated LFG materials are less effectively exfoliated than NFG, likely due to the larger flake size. $C_{12}H_{25}$-LFG has a greatly reduced stage 1A (003) signal, and an increased random stage phase in relation to the graphite (002) peak, suggesting that alkyl chains prevent graphene sheets from fully restacking and closing, allowing some diffusion of solvent molecules between the layers. For the smaller GP material, reductive exfoliation results in a slight weakening of the graphite (002) peak, along with the appearance of a shoulder at ~25.5°, attributed to the random stage phase, or regions of turbostratic stacking where the interlayer spacing is expanded relative to hexagonal graphite.[285, 289] In $C_{12}H_{25}$-GP, the graphite (002) further decreases in intensity, and the random stage peak is seen only as a broad tail. In the GNF materials, a weakened graphite (002) signal in Na-THF-GNF indicates slight exfoliation; after functionalisation, however, the intensity further reduces, and a large broad peak at ~25.0° appears, corresponding to an interlayer spacing of 3.6 Å, which can be attributed to either a random stage phase, or else the functionalised, imperfectly restacked graphene layers. The ar-FLG material shows a broad weak signal at 26.5°, corresponding to a layer spacing of 3.4 Å. Interestingly, after reductive exfoliation, a very sharp peak appears, over the original broad signal, indicating that some degree of restacking of graphene layers has occurred during the charging or drying process. In an identically prepared sample of the functionalised material, however, very weak signals between 25° and 27° suggest that a great degree of exfoliation has occurred, and therefore that dodecyl chains are preventing restacking from occurring.

Further evidence of exfoliation of all starting materials was obtained by analysis of the Raman spectra. A general increase in I_{2D}/I_G can be seen in the reductively treated and functionalised graphites, indicating the presence of exfoliated layers (Figure 5.32 ii). Little difference is seen in Na-THF-FLG and $C_{12}H_{25}$-FLG, since ar-FLG is already reasonably well exfoliated. Γ_{2D} remains the same after dodecyl grafting, but decreases slightly in Na-THF-FLG to 54 ± 2 cm^{-1} (Figure 5.32 iii). In LFG, NFG and GP after processing, the 2D peak loses its graphitic shoulder and becomes sharper and more symmetrical, confirming that c-axis disorder is introduced. Additionally, an increase in Γ_{2D} indicates that graphene layers are turbostratically stacked.[271] $C_{12}H_{25}$-GNF shows only a small increase in I_{2D}/I_G, and a small decrease in Γ_{2D}, indicative of some degree of exfoliation. In all cases, greater exfoliation is seen in the dodecyl-grafted

material compared to the unfunctionalised control, supporting the assertion that alkyl chains help prevent perfect restacking of graphene layers after drying.
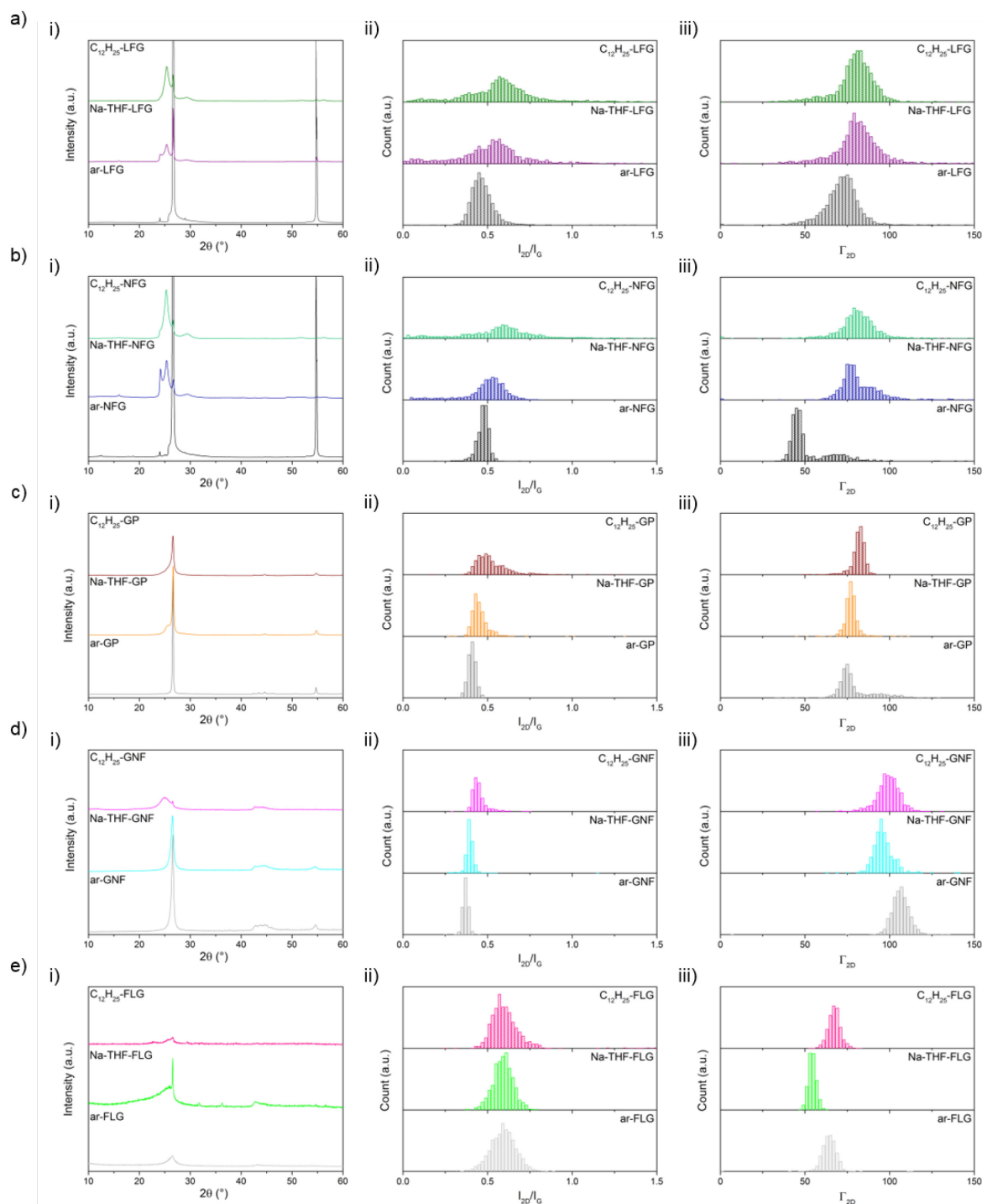
Figure 5.32. XRD (i) and Raman histograms of I_{2D}/I_G ratio (ii) and Γ_{2D} (iii) for ar-, Na-THF-, and $C_{12}H_{25}$- a) LFG, b) NFG, c) GP, d) GNF, and e) FLG.

Raman spectroscopy additionally provides information regarding the degree of grafting (Figure 5.33 and Table 5.8). A general increase in I_D/I_G ratio after reaction with 1-bromododecane was observed, compared with the as-received and quenched samples, for all starting materials

(Figure 5.33 ii), indicating that successful functionalisation occurred;[13, 15] this increase is most dramatically seen for the three smaller flake sizes. Furthermore, the I_D/I_G distributions broaden following grafting, suggesting that functionalisation occurs in an inhomogeneous way. In the unfunctionalised, exfoliated Na-THF-(graphite) experiments, no samples show any significant increase in I_D/I_G ratio, confirming that the charging and quenching procedures result in no additional damage or inadvertent grafting. In LFG, little change in the D peak is observed, with I_D/I_G increasing slightly from 0.06±0.05 in ar-LFG to 0.08±0.12 in Na-THF-LFG and 0.13±0.17 for $C_{12}H_{25}$-LFG. Similarly, as mentioned previously for natural flake graphite, the initial I_D/I_G ratio of 0.05±0.05 in ar-NFG does not change significantly on exfoliation (0.06±0.08) but following grafting increases to 0.20±0.18, reflecting the introduction of sp^3 defects onto the graphene layers. The I_D/I_G ratio for GP increases after functionalisation (0.12±0.18 in ar-GP to 0.48±0.14 in $C_{12}H_{25}$-GP) clearly indicating that sp^3 grafting sites are being introduced onto the carbon lattice. This effect is also seen in GNF and FLG; despite the large initial D peak in ar-GNF (1.56±0.07), I_D/I_G increases further with functionalisation (1.7±0.2), whilst in FLG, this value varies from 0.31±0.04 in ar-FLG to 0.6±0.2 in $C_{12}H_{25}$-FLG.

The I_D/I_G ratio can be used to calculate the interdefect distance and number density of grafted sites per unit area.[267] The spectra for each graphitic material show well-defined D, G and 2D bands, allowing the classification of these materials in the 'low defect density regime',[290] where the defect density does not exceed the Tuinstra-Koenig limit;[255, 267] the observed general trend of increasing I_D/I_G with increasing disorder is consistent with a large distance between grafted sites. The broadened histograms in the functionalised materials suggest that grafting may not occur uniformly; therefore the number density of grafted sites, n_D, rather than interdefect distance, L_D, is provided as the measure of grafting. A modified calculation of the conversion from L_D to n_D provided by Cançado et al.[267] was used and is explained in the experimental methods section, along with details of C/R calculations. The values for density of grafting per unit area are detailed in Table 5.9 where a general trend of increasing number density and decreasing C/R can be seen with decreasing flake size. The values obtained from these calculations are expected to overestimate the degree of grafting, with a more pronounced effect in the smaller flakes, since the initial I_D/I_G ratio is not accounted for. The effect of the initial D band is most pronounced in GNF due to the small flake size. Straightforward subtraction of the starting I_D/I_G ratio is not possible, however, because the sp^3 sites are not evenly distributed. Nonetheless, the observed trend does not just reflect the underlying flake size and contributions to the D peak from edge scattering.
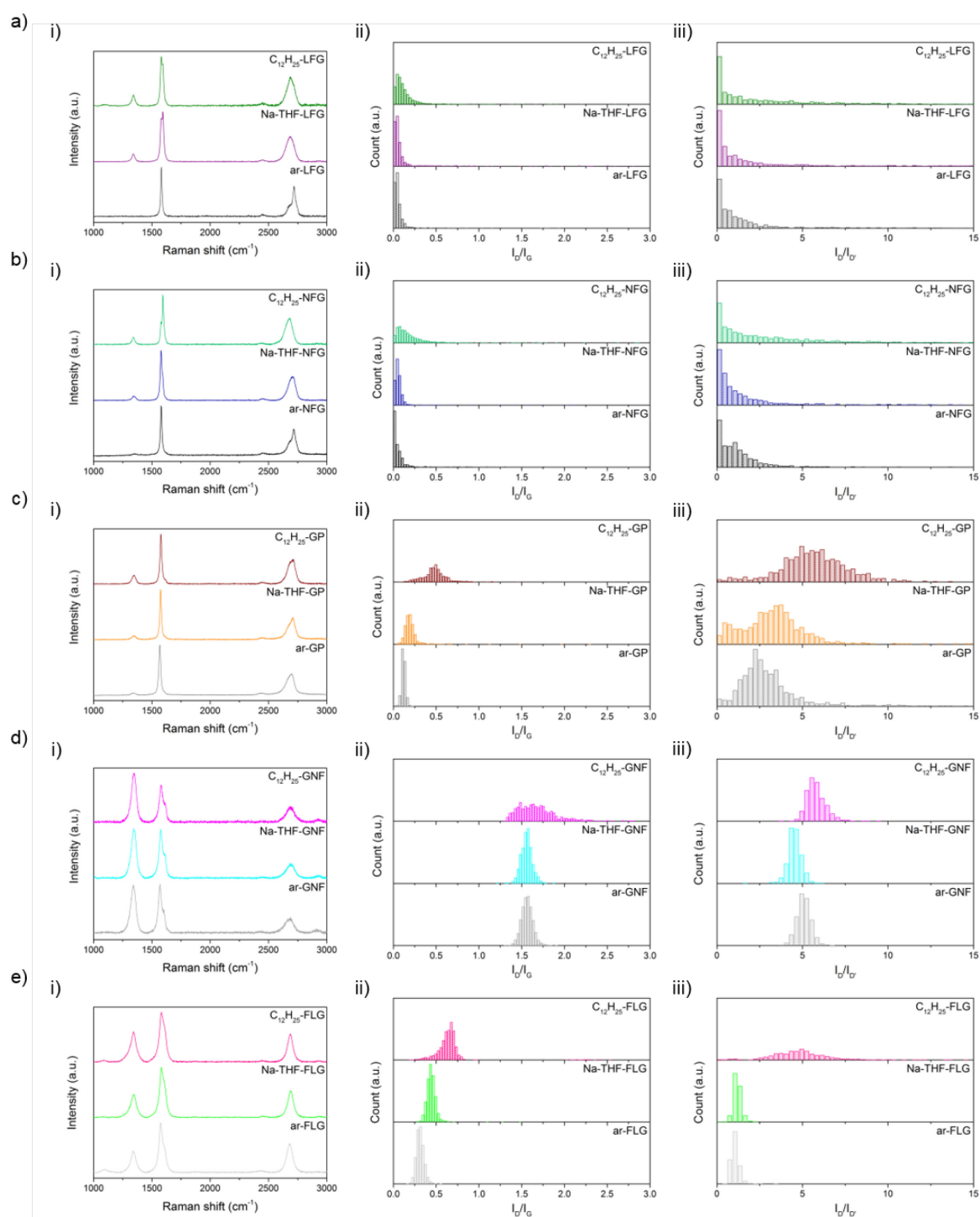
Figure 5.33. Averaged Raman spectra (i) and Raman histograms of I_D/I_G (ii) and $I_D/I_{D'}$ (iii) ratio for ar-, Na-THF-, and $C_{12}H_{25}$- a) LFG, b) NFG, c) GP, d) GNF, and e) FLG.

Additional analysis of the D' band shows an increase in $I_D/I_{D'}$ after functionalisation for all $C_{12}H_{25}$-(graphite) samples (Figure 5.33 iii) which is consistent with an increase in the ratio of sp^3 defects to edge-type defects,[131] and therefore indicates that covalent grafting occurs, with retention of lattice connectivity. The $I_D/I_{D'}$ growth is more marked in the smaller flakes GP, GNF and FLG; in the larger flakes NFG and LFG, the increase is reflected in a broadening of the

histogram. It is also worth mentioning that curve fitting of the D' peak at extremely low intensities is much less reliable, and values should be taken only as an indication. The slight increase in I_D/I_G for Na-THF-(graphite) samples likely arises because exfoliation results in smaller flakes (Figure 5.31) and therefore a higher proportion of edges; little change in $I_D/I_{D'}$ for these unfunctionalised materials confirms that the increased D band signal arises only from edges.[270]

Table 5.8. Summary of Raman data* for ar-, Na-THF-, and $C_{12}H_{25}$-(graphite).

Sample	I_D/I_G	$I_D/I_{D'}$	I_{2D}/I_G	Γ_{2D} (cm^{-1})	2D position (cm^{-1})
ar-LFG	0.06±0.05	1±2	0.47±0.07	72±12	2714±3
Na-THF-LFG	0.08±0.12	2±3	0.50±0.18	81±14	2690±18
$C_{12}H_{25}$-LFG	0.13±0.17	2±3	0.55±0.18	80±12	2687±12
ar-NFG	0.05±0.05	1.3±1.5	0.47±0.04	52±14	2712±16
Na-THF-NFG	0.06±0.08	1±2	0.49±0.13	82±12	2694±13
$C_{12}H_{25}$-NFG	0.18±0.18	3±3	0.6±0.2	81±13	2686±15
ar-GP	0.12±0.02	3.0±1.9	0.41±0.02	79±11	2707±2
Na-THF-GP	0.21±0.19	3.2±1.8	0.45±0.06	77±4	2703±3
$C_{12}H_{25}$-GP	0.48±0.14	5.6±1.9	0.5±0.1	81±4	2695±4
ar-GNF	1.56±0.07	5.1±0.4	0.37±0.02	107±6	2687±3
Na-THF-GNF	1.56±0.07	4.5±0.4	0.40±0.04	96±6	2688±1
$C_{12}H_{25}$-GNF	1.7±0.2	5.8±0.6	0.45±0.04	99±7	2697±2
ar-FLG	0.31±0.04	1.1±0.2	0.59±0.07	64±4	2683±3
Na-THF-FLG	0.43±0.05	1.2±0.2	0.59±0.06	54±2	2688±1
$C_{12}H_{25}$-FLG	0.6±0.2	4.8±1.6	0.6±0.1	67±4	2685±2

*Mean values and standard deviation calculated from at least 500 spectra.

Table 5.9. Number density and C/R obtained from Raman data.

Sample	Flake size (µm)	Number density (cm^{-2})	C/R*
$C_{12}H_{25}$-LFG	61±21	1.1×10^{11}	3418
$C_{12}H_{25}$-NFG	35±16	1.6×10^{11}	2418
$C_{12}H_{25}$-GP	5±2	4.2×10^{11}	919
$C_{12}H_{25}$-GNF	0.11±0.04	14.4×10^{11}	265
$C_{12}H_{25}$-FLG	0.64±0.17	5.5×10^{11}	688

*Number of graphene carbons per grafting moiety.

Improved solubility of these functionalised graphites in common organic solvents also provides confirmation of successful grafting. Previous alkyl-grafted graphites have shown reasonable solubility in chloroform;[13, 240] therefore, absorbance measurements were conducted on chloroform dispersions (Table 5.10).

Table 5.10. Calculated concentrations of ar-(graphite) and $C_{12}H_{25}$-(graphite) in chloroform, obtained from UV/vis absorption spectra.

	ar-(graphite) concentration (µg mL^{-1})	Na-THF-(graphite) concentration (µg mL^{-1})	$C_{12}H_{25}$-(graphite) concentration (µg mL^{-1})
LFG	1.61	2.23	4.67
NFG	7.04	6.35	19.2
GP	8.54	43.1	275
GNF	156	360	692
FLG	4.20	550	660

The absorption at 660 nm and the extinction coefficient for dispersed graphene in solution (ε_{660} = 2460 L g^{-1} m^{-1})[52] were used to estimate the concentrations of the different solutions using the Beer-Lambert law.

The smaller flake sizes show the largest increase in solubility. However, alkyl chains are not an ideal candidate for increasing solubility; instead polymer grafting would be expected to have a large influence on dispersibility and will be discussed in Chapters 7 and 8.

Further evidence for covalent functionalisation in all graphite materials was obtained by TGA-MS under nitrogen (Figure 5.34). In the two functionalised natural graphites, $C_{12}H_{25}$-LFG and $C_{12}H_{25}$-NFG (Figure 5.34a and b), two defined weight losses are observed, between 200 and 300 °C (11.3 wt% and 17.0 wt% respectively), and from 450 to 650 °C (6.7 wt% and 7.5 wt% respectively).
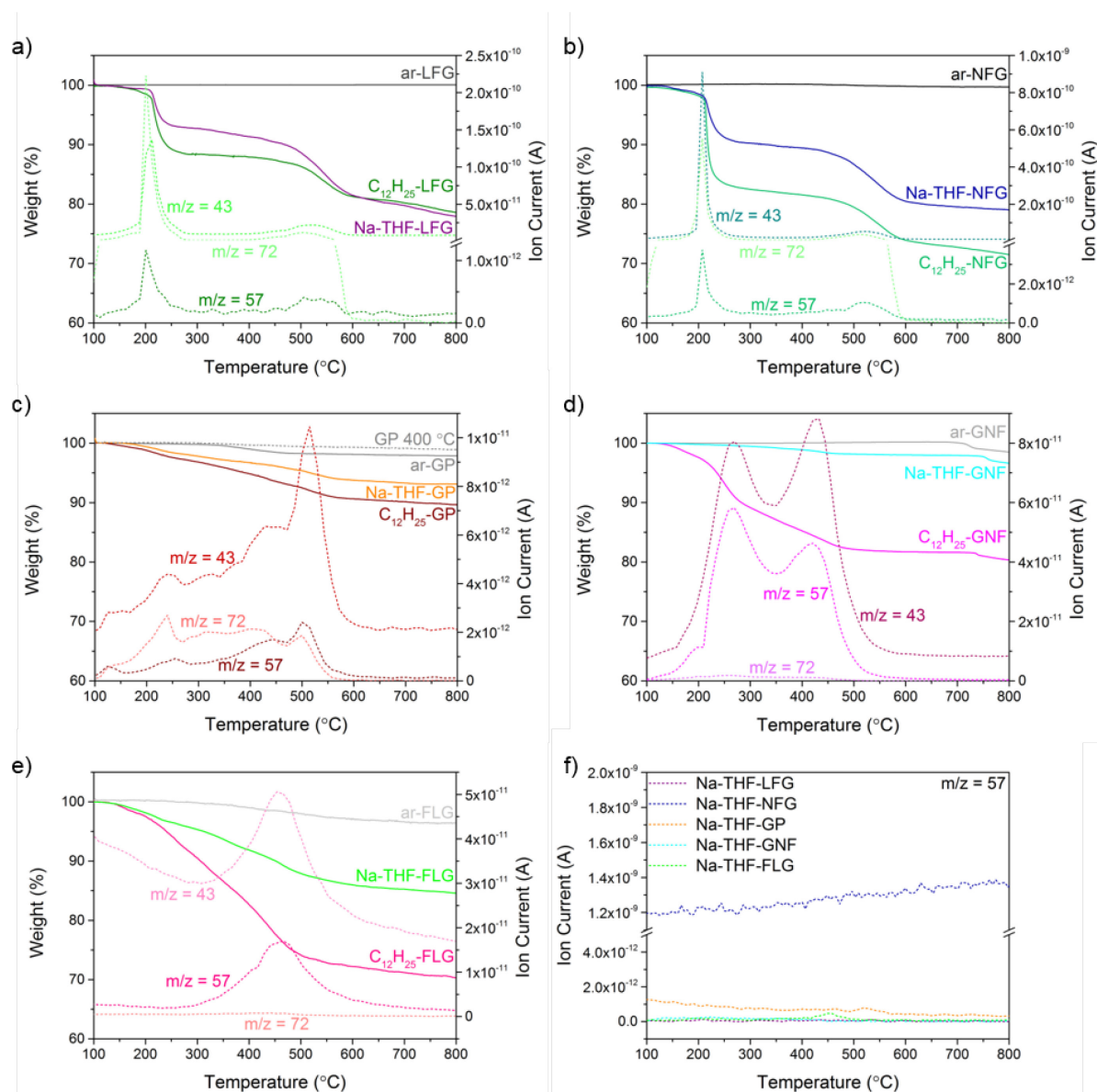
Figure 5.34. TGA-MS profiles of ar-, Na-THF-, and $C_{12}H_{25}$- a) LFG, b) NFG, c) GP, and GP 400 °C, d) GNF, and e) FLG; dodecyl and THF fragments m/z 57 ($C_4H_9^+$), 43 ($C_3H_7^+$/-CHCH$_2$O-$^+$), 72(C_4H_8O); f) m/z 57 for each Na-THF-(graphite).

Whilst remaining intercalated solvent contributes to these weight loss steps, the mass fragment arising from dodecyl chains (*m/z* 57) can clearly be seen in each step. Since the dodecane control shows no remaining alkyl traces, the presence of this fragment may be taken as evidence that dodecyl chains are covalently grafted. In $C_{12}H_{25}$-GP, a more gradual weight loss was observed, starting around 150 °C and stabilising after 600 °C (Figure 5.34c); fragments in the mass spectrum attributed to THF and dodecyl addends are also detected in this temperature range, with the alkyl fragment giving the strongest signal at 350-600 °C, corresponding to a total 8.1% weight loss. $C_{12}H_{25}$-GNF and $C_{12}H_{25}$-FLG show gradual weight losses (18.1 wt% and 19.4 wt% respectively) in a similar temperature range to GP (Figure 5.34d and e). In all cases except FLG, the mass spectrum shows a double peak profile, suggesting that alkyl chains and solvent molecules are escaping at two discrete temperatures; however, these steps are particularly well-defined in the larger, flatter flakes. Regardless of flake size and morphology, solvent trapping happens to a certain extent in each graphite; however, the grafted graphenes show a consistently higher weight loss than their corresponding ungrafted samples apart from in the largest, LFG, which showed no significant change. Furthermore, the dodecyl fragment (*m/z* 57) is seen in each functionalised case, but is absent in the quenched controls, where the mass loss arises from solvent alone (Figure 5.34f).

The grafting ratios and C/R were obtained from analysis of *m/z* 43 and 57 fragments and the accompanying mass loss in the corresponding temperature range (see section 5.1.3). For GP, the as-received material shows a defined weight loss at 330-480 °C, but this material is removed during the heating at 400 °C under vacuum, prior to reaction. Therefore, the TGA of this heat-treated GP (GP 400 °C), rather than ar-GP, was taken as a baseline from which to calculate mass loss (Figure 5.34c). Since the difference in TGA traces between the other as-received and heat-treated graphites is insignificant, the TGA profiles of the as-received samples were used for calculations. A general increase in grafting ratio, and corresponding decrease in C/R can be seen with decreasing flake size (Table 5.11). These values are in reasonable agreement with values obtained from Raman data (Table 5.9), although they diverge for smaller flake sizes, discussed further below.

Table 5.11. Grafting ratio and C/R obtained from TGA-MS data.

Sample	GR (%)*	C/R[†]	C/THF[‡]
$C_{12}H_{25}$-LFG	1.1	1246	27
$C_{12}H_{25}$-NFG	1.7	852	18
$C_{12}H_{25}$-GP	7.3	193	349
$C_{12}H_{25}$-GNF	21.0	67	405
$C_{12}H_{25}$-FLG	25.7	55	309

*Grafting moiety/graphite mass ratios, in wt%. For details of these calculations, see Chapter 4, section 4.4.1.1. [†]Number of graphene carbons per grafting moiety. [‡]Number of graphene carbons per THF molecule.

5.3.4. Investigation of the functionalisation pattern in graphite

The grafting location on graphene sheets can have a significant effect on the flake's subsequent properties. Many previous discussions regarding reductive functionalisation have assumed homogeneous grafting across the flake,[15, 92, 255] with only a handful concluding that functionalisation is initiated by, and directed to, the edges.[111, 248] In the case of homogeneous grafting across the basal surface of the graphene layer, the grafting ratio and C/R would be expected to remain constant as a function of flake size (between comparable starting graphites). In this grafting study, the trend suggests that in fact functionalisation does not occur evenly on the basal plane. Instead, the grafting ratio obtained from TGA measurements and the number density of grafting per unit area calculated from Raman I_D/I_G vary inversely with flake radius (Figure 5.35). The C/R ratios obtained from analysis of both sets of data are in reasonable agreement, and a general correlation with flake size can be seen with grafting sites apparently scaling in relation to the available edges of each graphene layer, rather than the basal area. Edge-initiated grafting is therefore proposed as a model of functionalisation, consistent with C/R varying with the flake radius.
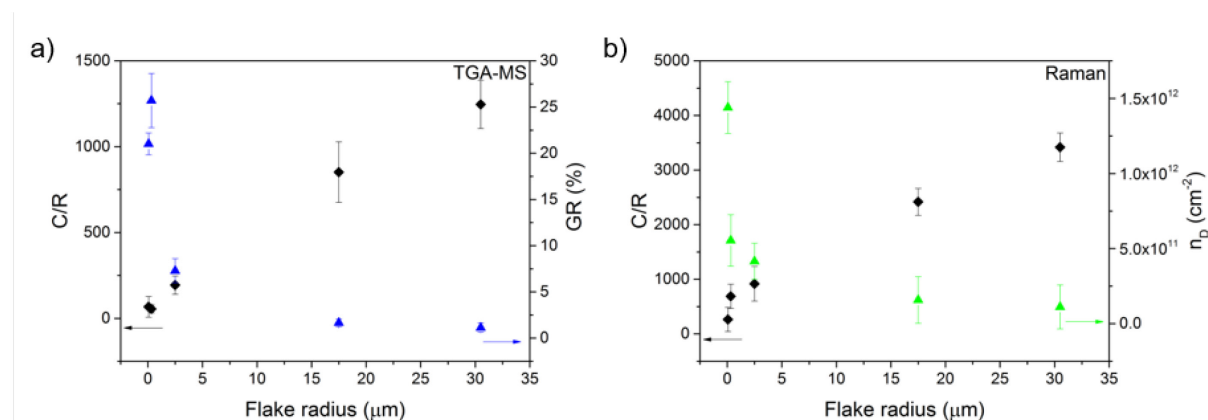
Figure 5.35. a) C/R (black) and GR (blue) obtained from TGA-MS data. C/R data points for the smallest flakes, GNF and FLG, overlap; b) C/R (black) and n_D (green) obtained from Raman data.

In the case of fully exfoliated single-layer graphene, all carbon sites, edge and basal, are accessible to alkyl grafting; uniform functionalisation might therefore be expected. In intercalated graphite stacks where full exfoliation has not occurred, the inner basal planes are no longer as easily accessible, requiring diffusion of reactive moieties into the interlayer galleries, before grafting can occur. Edges, then, are more likely to react, before the inner sites. In addition, grafted groups at flake edges may further inhibit functionalisation inside the flakes, due to the steric bulk of the chains; larger moieties would therefore be expected to enhance this effect, resulting in a functionalisation gradient, with a higher density of grafted sites near flake edges (Figure 5.36).
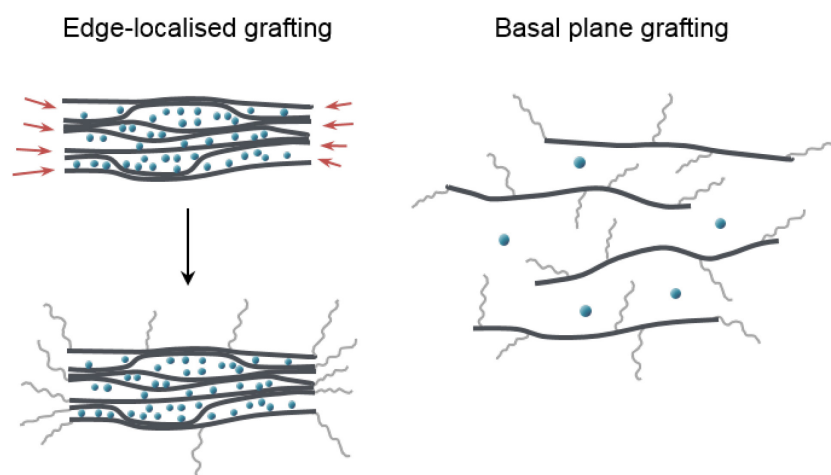
Figure 5.36. Edge-localised versus basal plane grafting.

The divergence of the C/R ratios obtained by TGA and Raman (Figure 5.35) with decreasing flake size is consistent with the proposed model. In the Raman spectra for the smaller flakes sizes, a lower apparent I_D/I_G ratio will be obtained for edge-functionalised flakes, compared to uniformly functionalised graphene layers, since more of the carbon lattice remains intact, resulting in little change in the G band intensity with relation to the D. The effect is much less pronounced in the larger graphites since the flakes are far larger than the laser spot. The C/R ratios of the smaller flakes are therefore expected to be an underestimate of grafting, when compared to values obtained by TGA analysis.

Further examination of Raman data, in particular the D and D' bands, can provide additional support for proposed edge-initiated grafting (Figure 5.33 iii and Table 5.8). In GNF and FLG, since the laser spot is larger than the flakes, every spectrum is an average of all edge and sp^3 contributions, and therefore the increase in $I_D/I_{D'}$, or sp^3 to edge sites, can be straightforwardly taken as an indication of grafting. For GP, where typical flakes are not significantly larger than the laser spot, a similar argument applies. NFG and LFG flakes are significantly larger than the laser spot and therefore measurements of two distinct environments, edge and basal carbons, are obtained. In the as-received materials, the larger ratio of basal to edge carbon sites results in a very low, practically zero, D band intensity, and a correspondingly low $I_D/I_{D'}$. The tail of the histogram to higher $I_D/I_{D'}$ presumably is from edge contributions. Following supposed edge grafting, the $I_D/I_{D'}$ from the centre of the graphene flakes would remain unchanged, whilst the $I_D/I_{D'}$ at the edges would be expected to increase and is reflected in a lengthening of the tail of the histogram, seen in $C_{12}H_{25}$-LFG and $C_{12}H_{25}$-NFG, and absent in their as-received counterparts. On the other hand, if grafting were to occur uniformly across the flake, the whole histogram would be expected to shift to higher $I_D/I_{D'}$ values, reflecting the

introduction of sp^3 sites all over the flake. Since this overall increase is not seen, $I_D/I_{D'}$ data can therefore be taken as further proof of edge grafting.

The proposed reaction of edge-initiated grafting, rather than random coverage of the basal plane, is generally in contrast to the grafting seen in CNTs and fullerenes.[238, 291] This phenomenon may be attributed to the fact that there is less strain in a flat graphene sheet than in its curved allotropes, resulting in a less reactive starting material. Interestingly, preferential edge grafting may also arise from another effect. A previous study of Birch-type reduction of CNTs showed that successive charging and functionalisation of tubes resulted in a propagative functionalisation mechanism where functionalised sites spread in bands over the tubes from previously grafted sites;[292] a similar phenomenon was seen in one study of propagative exfoliation of graphene.[244] By regarding the edges of the graphene sheets as defects, it may be reasonable to assume that grafting occurs preferentially at these sites before propagating inwards. In the larger, thicker natural graphites, this mechanism would be further favoured, where exfoliation is already energetically more difficult, and easy intercalation and diffusion of reactants inside the graphite is prevented,[248] limiting reaction at those inner sites. Further, natural defects may pin sheets together, meaning that only the outer surfaces and edges of the graphene layers are accessible for functionalisation.

Of the two smaller flakes sizes, $C_{12}H_{25}$-FLG has a higher GR than $C_{12}H_{25}$-GNF (25.7% compared with 21.0%). FLG has a larger lateral flake size, but is significantly more exfoliated than GNF, and this increased functionalisation occurs because more flake edges and surfaces are exposed, allowing easy diffusion of the electrophile to reactive sites.

Raman mapping provides further evidence of edge-localised functionalisation (Figure 5.37). NFG was bath sonicated in ethanol to obtain small flakes with accessible edges (Figure 5.37a-c), and compared with functionalised $C_{12}H_{25}$-NFG (Figure 5.37d-f). In bath-sonicated NFG, the map of I_D/I_G ratio clearly illustrates the presence of a D peak around the edge of the flake, and at defect sites visible in the optical image. Example spectra taken at the points marked in (a) show a small D peak at edges, and none in the centre of the flake, as expected. In the functionalised graphite, $C_{12}H_{25}$-NFG, generally a much greater I_D/I_G ratio can be seen (Figure 5.37e), again concentrated around the edges of the flake. The more pronounced D peak can be seen in the point spectra taken at different areas across the flake.
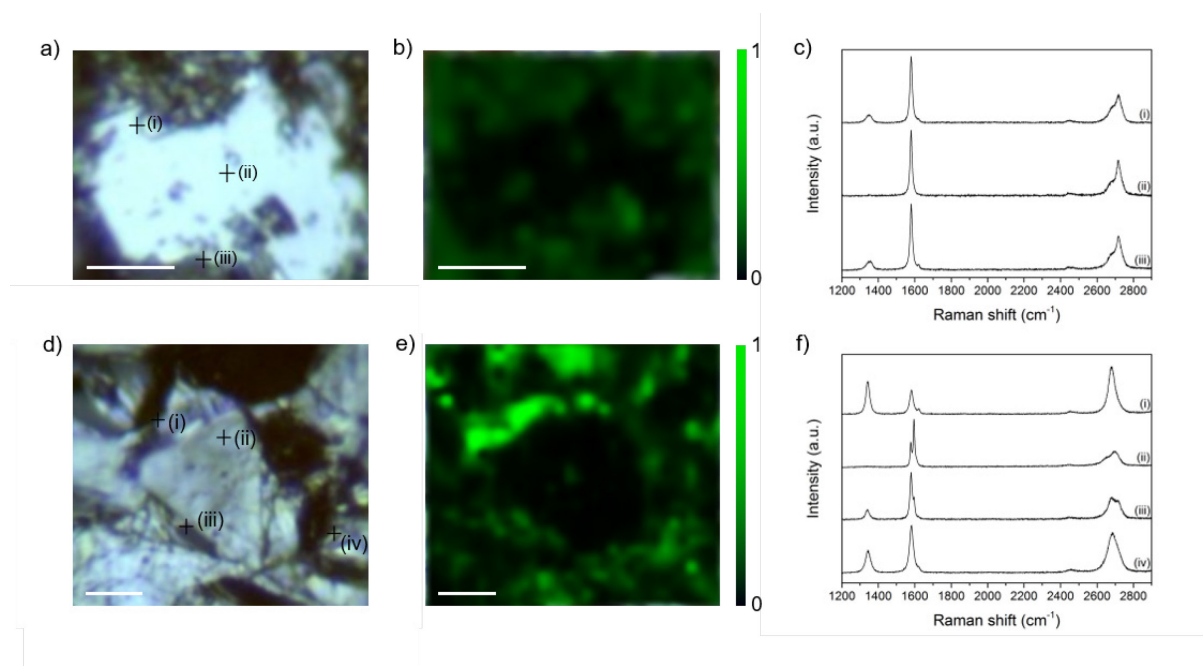
Figure 5.37. Comparison of flake edges in bath-sonicated NFG (top) and $C_{12}H_{25}$-NFG (bottom). a,d) Optical micrographs, b,e) Raman map of I_D/I_G, and c,f) Raman spectra acquired at the positions marked in a and d. Scale bar 10 μm.

$I_D/I_{D'}$ obtained from the representative spectra shown in Figure 5.37c and f show a marked difference before and after functionalisation. In NFG, from the spectra taken at the edges of the flake, the $I_D/I_{D'}$ is ~4 (Table 5.12), characteristic of edge-type defects; this value increases significantly to ~10 in spectra taken from the edges of $C_{12}H_{25}$-NFG flakes, reflective of the sp^3 defects introduced during grafting.[270] Even in the area where only a small increase in the D band was observed (area (iii) in Figure 5.37f), the $I_D/I_{D'}$ ratio indicates that covalent grafting did occur. Overall, the Raman maps show that the increase in I_D/I_G is not just from additional exposure of flake edges following reductive treatment, but from the introduction of sp^3 defects, providing valuable evidence for localisation of grafting at flake edges.

Table 5.12. Summary of I_D/I_G and $I_D/I_{D'}$ values of the spectra obtained in Figure 5.37.

Spectrum	I_D/I_G	$I_D/I_{D'}$
NFG (i)	0.12	5.04
NFG (ii)	0	-
NFG (iii)	0.13	2.98
$C_{12}H_{25}$-NFG (i)	1.37	9.67
$C_{12}H_{25}$-NFG (ii)	0	-
$C_{12}H_{25}$-NFG (iii)	0.21	10.38
$C_{12}H_{25}$-NFG (iv)	0.47	9.43

These conclusions regarding higher edge/basal functionalisation are in line with previous findings of bulk reduced graphite,[111] and most recently, reductive hydrogenation studies conducted on single- and few-layer graphene,[248] as well as diazonium radical grafting of aryl groups.[191, 195] The amount of residual solvent shows the opposite trend, with the C/THF ratio

generally varying inversely with the C/R ratio, over the range of flake sizes (Table 5.13). Surprisingly, Na-THF-FLG contains more residual solvent than even Na-THF-GP, after processing. In the three smaller flakes, grafting of alkyl chains helps reduce the amount of residual solvent; the chains prevent close restacking and allow diffusion of the solvent through the interlayer galleries. In the much larger flakes, the presence of alkyl chains is much less significant, and the amount of THF remains approximately the same as in the unfunctionalised samples.

Table 5.13. Comparison of residual THF in Na-THF- and $C_{12}H_{25}$-(graphite) samples, by TGA.

Graphite	Na-THF-(graphite) C/THF	$C_{12}H_{25}$-(graphite) C/THF
LFG	27	27
NFG	26	18
GP	102	348
GNF	276	405
FLG	45	309

The two smallest flake sizes yield much higher grafting ratios than the larger graphites, due to the accessibility of exposed edges. In all cases, solvent persists despite grafting and extensive washing; surprisingly FLG holds more residual solvent than GNF or GP, perhaps due to better intercalation initially. Grafting of larger addends might be expected to increase exfoliation and prevent the trapping of residual solvent.

5.4. Summary

Reductive treatment with sodium naphthalide in THF was shown to effectively exfoliate natural flake graphite, and facilitated functionalisation with dodecyl addends. Whilst successful grafting was confirmed by TGA-MS and Raman data, a significant amount of residual THF remained after processing, complicating the characterisation of the modified graphite. Solvent remains in a coordinated structure with sodium, indicating that only partial quenching of residual charges occurs, although the charge left on the graphite sheets is insufficient to react further with any ambient species, for example, water, confirmed by Raman analysis.

Grafting showed different efficiency in different solvent systems. DMAc was selected for its suitability in dissolving CNTs; however, the achieved GR was lower than that in THF, and the formation of extremely stable Na-DMAc-GICs precluded the isolation of any significant amount of exfoliated graphene. The reaction of graphite with 1-bromododecane in DME resulted in a large degree of exfoliation, and grafting ratio of 6.7%, but Raman spectra of the unfunctionalised control suggests that inadvertent grafting occurs in the system. Whilst these side reactions may not matter in some applications, for systematic studies of grafting, these species can complicate grafting analysis, as well as potentially disrupt properties of interest. THF coordinates to sodium to form large, stable cation complexes which increase the graphite

interlayer spacing effectively, and, therefore, represents a compromise between degree of exfoliation and grafting available using this system.

Reductive treatment with sodium naphthalide in THF was then applied to a range of graphite materials with varying sizes and morphologies, to successfully covalently graft dodecyl addends, which can be seen in the TGA-MS, Raman data and increased solubility. Analysis of the Raman D and D' bands confirms that the reductive process alone does not cause additional damage to the carbon framework, in any of the graphite materials. Furthermore, charging of the graphene sheets allows exfoliation to few-layers in solution; these layers were stabilised by attachment of dodecyl addends, which is reflected in the XRD and Raman data for the Na-THF-(graphite) and $C_{12}H_{25}$-(graphite) materials, although thicker flakes do remain in the larger graphite samples.

The flake size and morphology of the starting material were shown to affect the degree of grafting and the amount of residual solvent. The C/R ratios are proportional to lateral flake size, suggesting that grafting is localised near the edges of the flakes. Further mapping of functionalised NFG illustrates that grafting is directed towards flake edges. This mechanism of grafting is believed to arise from the relative inaccessibility of the inner basal plane to reactive moieties, resulting in preferential grafting at flake edges; this grafting mechanism may have implications on the properties of these materials. These functionalised graphites may find use in a wide range of applications, depending on the particular properties required. However, even with the small, exfoliated flakes, residual solvent and sodium species could complicate the direct application of these modified materials. Grafting of dodecyl addends provides a useful model system with which to study functionalisation parameters, and although the solubility was increased with grafting, the enhancement was not significant, especially in the larger flakes. Alternative functional groups, which could impart better solubility to the graphene sheets, might prevent complete restacking, and allow more complete removal of sodium and solvent from the system. Smaller monomers may be of particular interest, to better access the graphene basal plane and improve grafting density. This approach is investigated further in the following chapters.

6. Grafting-to versus grafting-from approaches for poly(methyl methacrylate) functionalisation of graphene

Graphene could offer many functional benefits to polymer-based composites due to its exceptional intrinsic properties, but pristine graphene itself has a low solubility in common solvents, preventing bulk processing in many applications. One of the primary purposes of covalent grafting is to enable better dispersion of single- and few-layer graphene for subsequent applications. Whilst grafting of short, defined-length alkyl chains is useful to facilitate understanding of the functionalisation process in graphene, the solubility of these modified materials is not greatly increased. In contrast, functionalisation with matrix-compatible moieties could allow easier dissolution, additionally limiting their restacking and agglomeration on drying, and therefore improve handling in bulk applications. Longer chains offer the possibility of steric stabilisation in solution and diffusion into polymer matrices to form strong interfaces. Reductive functionalisation has already shown versatility in the range of electrophiles that may be used.[13, 14, 111, 242, 245] Whilst care must be taken that labile protons or groups susceptible to reduction are protected, a variety of grafting moieties can be added.

In this chapter, the grafting of poly(methyl methacrylate) to few-layer graphene is explored by the grafting-to and grafting-from approaches. PMMA was selected both as a classic anionic model system, and because it is a potentially relevant system in composite applications. Comparison of the grafting-to and grafting-from routes allows an optimisation of the degree of exfoliation and dispersibility, with respect to molar mass. In the grafting-to approach, different molecular weights of PMMA-Br were reacted directly with graphenide, whilst the grafting-from method exploits the graphenide species as an initiator of anionic polymerisation.

The two methods were also extended to larger natural flake graphite to investigate whether solvent trapping could be mitigated and whether a greater degree of exfoliation could be achieved with larger grafting moieties.

6.1. Grafting-to and grafting-from polymerisation on FLG

The grafting study in the previous chapter concluded that FLG achieved the best compromise in terms of exfoliation, grafting and solubility. FLG was therefore used for the polymer functionalisation reactions discussed in this section. Characterisation of the starting material can be found in Chapter 5, section 5.3.1.4.

PMMA is readily miscible with epoxy[293] and is commonly used as a compatibiliser for nanofillers in epoxy resin;[16, 17] the monomer MMA is commercially available, and inexpensive. Furthermore, it is a standard anionic and ATRP target, with many well-used literature precedents to follow. Anionic polymerisation from charged CNTs has been previously explored resulting in CNTs grafted with PMMA,[222] poly(methyl *N*-acetamidoacrylate)[258] and polystyrene.[294] Examples of anionic polymerisation of MMA suggest that the ester groups are stable to graphenide conditions, and can therefore be added straightforwardly to the graphenide solution without the risk of side reactions.
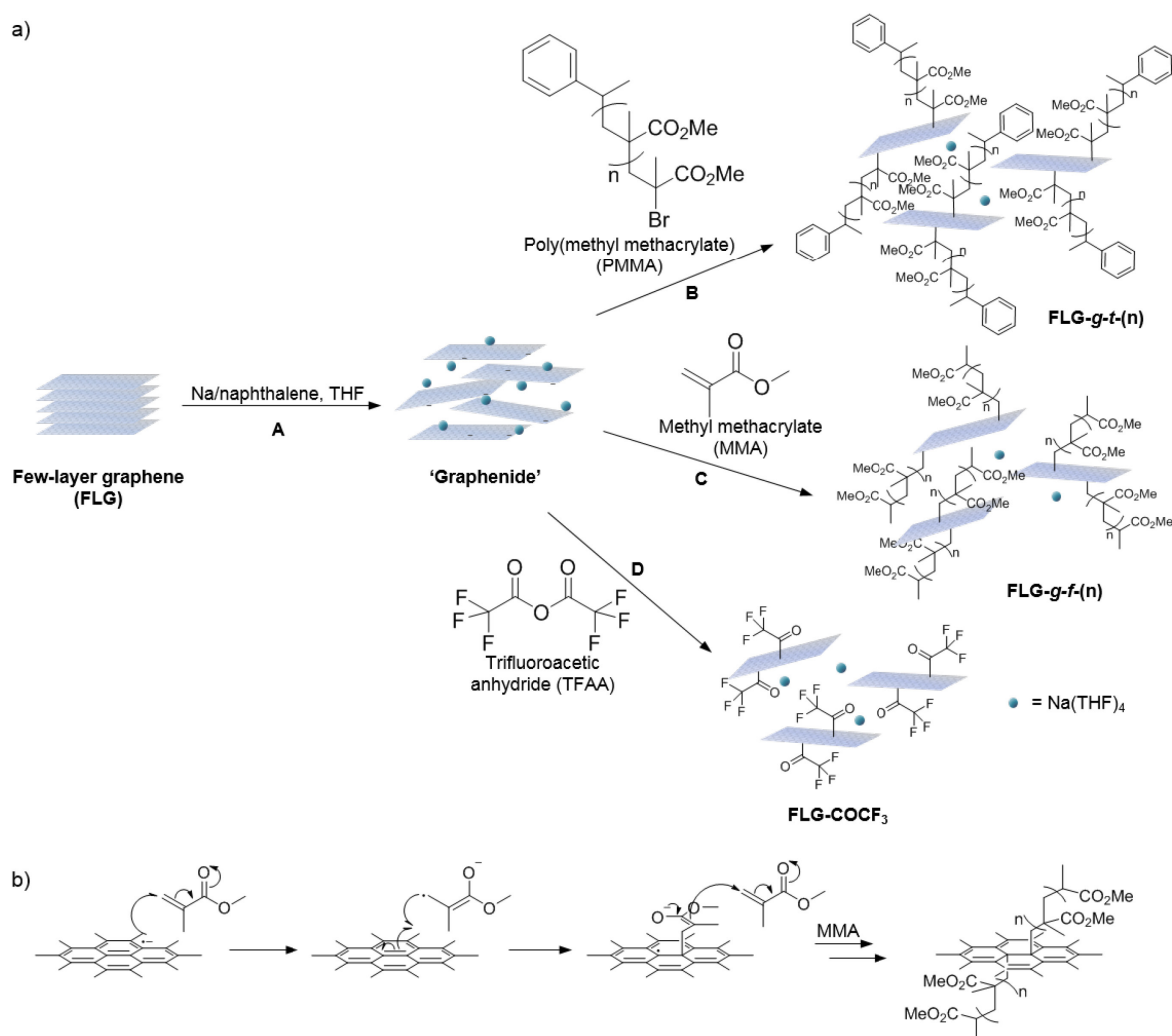
Scheme 6.1. a) Grafting approaches used for the functionalisation of FLG with PMMA. Reductive exfoliation (step A) followed by reaction with bromine-terminated PMMA (route B) to yield the grafting-to products FLG-*g-t*-(n); or with MMA (route C) to yield grafting-from products FLG-*g-f*-(n); the number of active initiation sites was determined by reaction with TFAA (route D), to yield FLG-COCF3; b) proposed mechanism for reaction of reduced FLG with MMA.

Generally, using polymers with defined molecular weight and a reactive end group, in a grafting-to approach, allows control of the polymer properties; however, grafting density tends

to be limited by the large steric bulk of the chains. Conversely, in a grafting-from approach, *in situ* anionic polymerisation from the graphene lattice can achieve densely-grown polymers,[222] but with less control over molar mass and greater dispersity due to the inhomogeneity of the initiator surface. Comparison of the two approaches, exploring PMMA grafting on FLG (Scheme 6.1a) is useful to understand how the molar mass can affect exfoliation efficiency and dispersion.

6.1.1. Grafting-to approach to PMMA-FLG

6.1.1.1. Synthesis of PMMA-Br

Bromine-terminated PMMA polymers with different M_n were prepared for the grafting-to approach, using ATRP, following a previously described procedure.[275] (1-Bromoethyl)benzene was used as the initiator. The reaction times were varied for each polymerisation process in order to obtain polymers with a range of M_n between 5000 and 10000 g mol^{-1}. A typical TGA-MS trace shows that full decomposition occurs before 450 °C, with the characteristic mass fragments arising from the polymer (Figure 6.1). The polymers were thoroughly dried under vacuum prior to reaction with FLG.
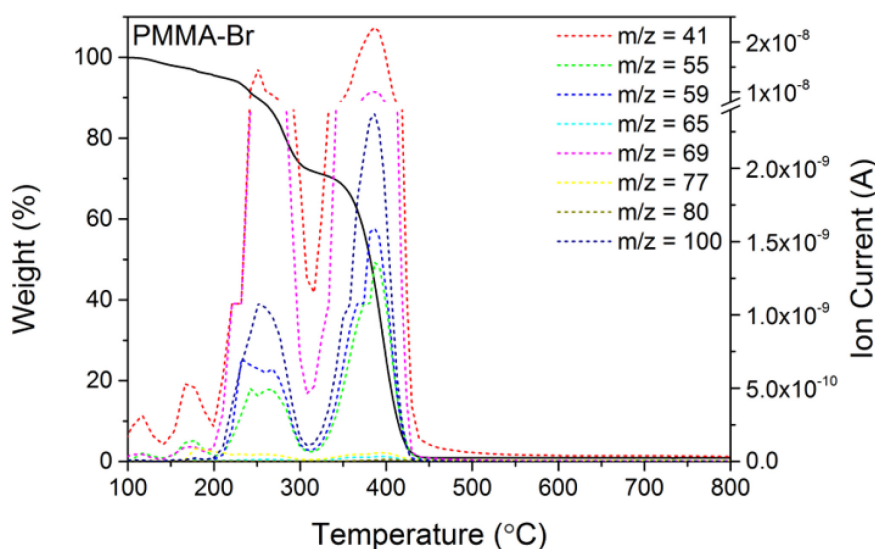
Figure 6.1. TGA-MS profile of PMMA-Br (M_n 5000 g mol^{-1}) and its associated mass fragments.

6.1.1.2. Reaction of PMMA-Br with FLG

A charged FLG solution (with the same C/Na 12, and [Na] of 0.008 M) was reacted with PMMA-Br of different molar masses (Scheme 6.1a (B)); the mixture was quenched with dry O_2/N_2 and extensively washed with acetone, THF and water, to obtain the products

FLG-*g-t*-5000, FLG-*g-t*-8000 and FLG-*g-t*-10000. A control reaction mixing quenched Na-THF-FLG with PMMA-Br (M_n 5000 g mol^{-1}) precludes the possibility of physisorption, with the TGA-MS showing no additional weight loss or any peaks attributed to PMMA (Figure 6.2a). The peak *m/z* 41 is attributable to residual solvent remaining inside the sample, also seen in Na-THF-FLG (Figure 6.2b).
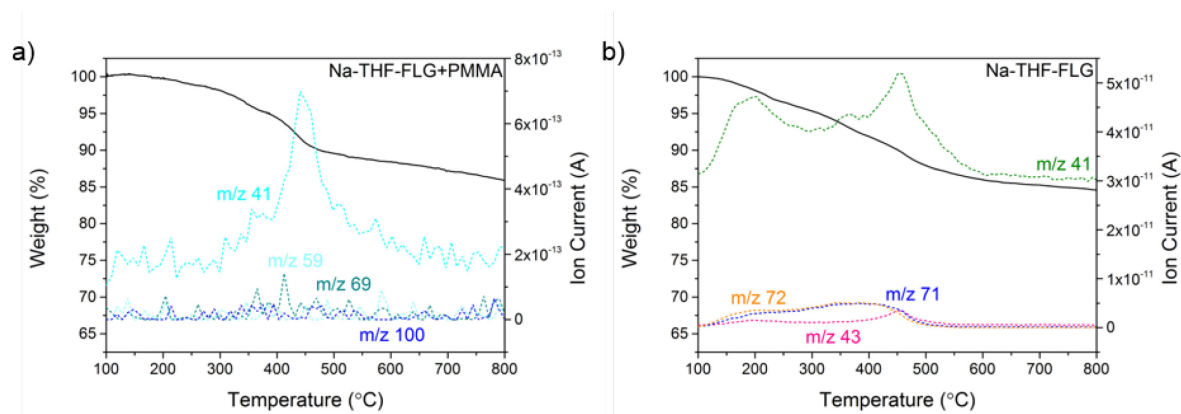
Figure 6.2. TGA-MS profiles of a) Na-THF-FLG+PMMA and b) Na-THF-FLG. No PMMA fragments (*m/z* 59, 69, 100) are seen in Na-THF-FLG+PMMA, only *m/z* 41 which is attributed to THF, also present in Na-THF-FLG.

TGA-MS data confirms that all FLG-*g-t*-(n) show a similar weight loss in the region 250-600 °C (Figure 6.3), consistent with the decomposition temperature of pure PMMA (refer to Figure 6.1). Typical PMMA fragments (*m/z* 41 (-CH$_2$C(CH$_3$)-$^+$), 69 (-CH$_2$C(CH$_3$)(CO)-$^+$), and 100 (-CH$_2$C(CH$_3$)(COOCH$_3$)-$^+$)) are detected in the same temperature range. The *m/z* fragment 77 corresponds to the phenyl end group of the initiator molecule, whilst the signal from *m/z* 41 has contributions from both THF (-CHCH$_2$CH$_2$-$^+$) and PMMA. Since physisorbed polymer is removed by the washing step (Figure 6.2a), it is expected that PMMA is covalently attached to the FLG surface. The fragment *m/z* 41 is common to both PMMA and THF; to calculate the amount of PMMA and trapped THF, a control TGA-MS measurement of known quantities of Na-THF-FLG and PMMA (M_n 5000 g mol^{-1}) was analysed to calibrate the relative intensities of the MS signals with the relative amounts of THF and PMMA (Chapter 4, section 4.4.1.1). A sensitivity factor, *S*, of 2.2 (i.e. for a given amount of sample, the same amount of PMMA is detected at an intensity 2.2 times weaker than that amount of THF) was obtained by these calculations, and was used to calculate PMMA and solvent amounts in all the following samples (full TGA-MS are provided in Appendix II, Figure II.1). Whilst the decomposition of PMMA is expected to be altered somewhat by its covalent interaction with the FLG layers, this method gives a reasonable estimate of the degree of grafting.
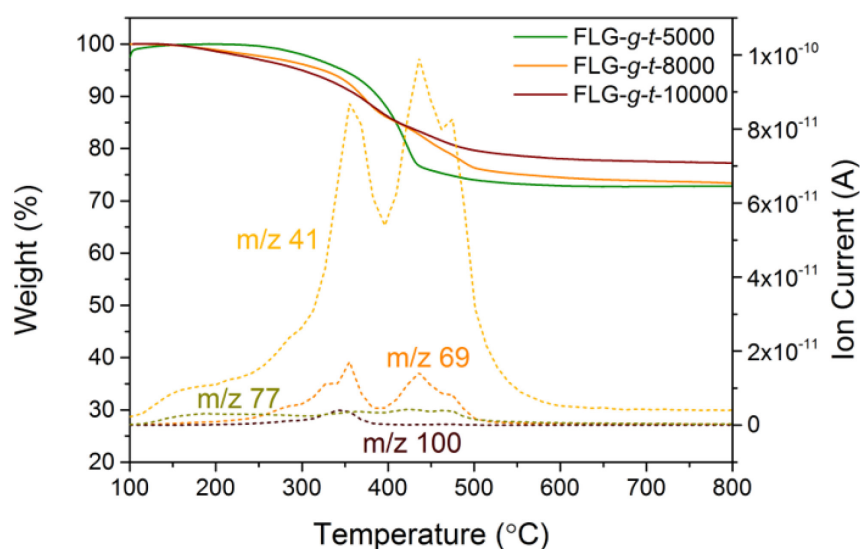
Figure 6.3. TGA profiles of FLG-*g-t*-5000, FLG-*g-t*-8000 and FLG-*g-t*-10000, and corresponding MS trace of FLG-*g-t*-8000; *m/z* 41 (-CH$_2$C(CH$_3$)-$^+$) or (-CHCH$_2$CH$_2$-$^+$), 69 (-CH$_2$C(CH$_3$)(CO)-$^+$), 77 (C$_6$H$_5$-$^+$) and 100 (-CH$_2$C(CH$_3$)(COOCH$_3$)-$^+$).

Grafting ratios decrease as the polymer weight increases (from 20.3% in FLG-*g-t*-5000 to 12.6% in FLG-*g-t*-10000) (Table 6.1); the increased steric bulk of the larger polymers occludes a greater number of neighbouring carbon sites, limiting the grafting density. The grafting ratios correspond to C/PMMA values between 2055 to 6615, far lower than that achieved by reaction with dodecyl bromide (Chapter 5, section 5.3.4), attributed to the much larger polymer size. The amount of solvent remaining was similar between the different samples and, in fact, greater than the residual amount in the alkyl-grafted sample, suggesting that grafting of large polymers at flake edges does not significantly aid solvent diffusion, and may even cause trapping.

Table 6.1. Summary of grafting data for grafting-to products.

Sample	Polymer M$_n$ (g mol^{-1})	GR (%)	C/PMMA	C/THF
FLG-*g-t*-5000	4980	20.3	2055	36
FLG-*g-t*-8000	8040	15.1	4421	31
FLG-*g-t*-10000	9980	12.6	6615	38

6.1.2. Grafting-from approach to PMMA-FLG

Dried and degassed MMA monomer was added slowly to the charged FLG dispersion (Scheme 6.1a (C)), cooled at 0 °C, to prevent possible side reactions resulting in chain transfer and termination.[295] Because of the volatility of MMA, the charged graphenide dispersion was removed from the glovebox and connected to a nitrogen Schlenk line, before addition of MMA, to prevent contamination. Polymerisation is thought to initiate with electron transfer from the

graphenide surface to the monomer to form a radical anion (Scheme 6.1b). The free radical can react with the carbon lattice, whilst the polymer grows by anionic propagation. The solution quickly increased in viscosity, indicating that the polymerisation reaction was successful. The reaction was stirred for 24 hours before quenching and washing thoroughly with acetone, THF and water to remove unreacted MMA, ungrafted PMMA and sodium. MMA/Na ratios were varied (15, 30, 60, 90) in order to grow polymers of different molar masses.

6.1.2.1. Determination of the number of initiation sites

The previous chapter showed that grafting does not fully utilise the initial charging ratio of one sodium to twelve framework carbons. Therefore, to obtain an estimate for the number of active sites initiating polymerisation, reduced FLG was functionalised with trifluoroacetic anhydride (Scheme 6.1a (D)). TFAA is a similar size to MMA monomer, and contains a trifluoromethyl group which can be detected by both TGA-MS (Figure 6.4) and XPS (Table 6.2). After confirming that physisorbed TFAA was fully removed in the control reaction FLG+TFAA (Figure 6.4), quantitative analysis regarding the number of fluorine-containing groups attached to each graphene layer ($C/COCF_3$ = 149 from XPS, and 171 from TGA) gives an idea of grafting efficiency, and allows the M_n of the grown polymers to be estimated. This grafting density is surprisingly low compared with that achieved for alkyl grafting on FLG (C/R = 55), perhaps due to the lower reactivity of TFAA compared with alkyl halides.
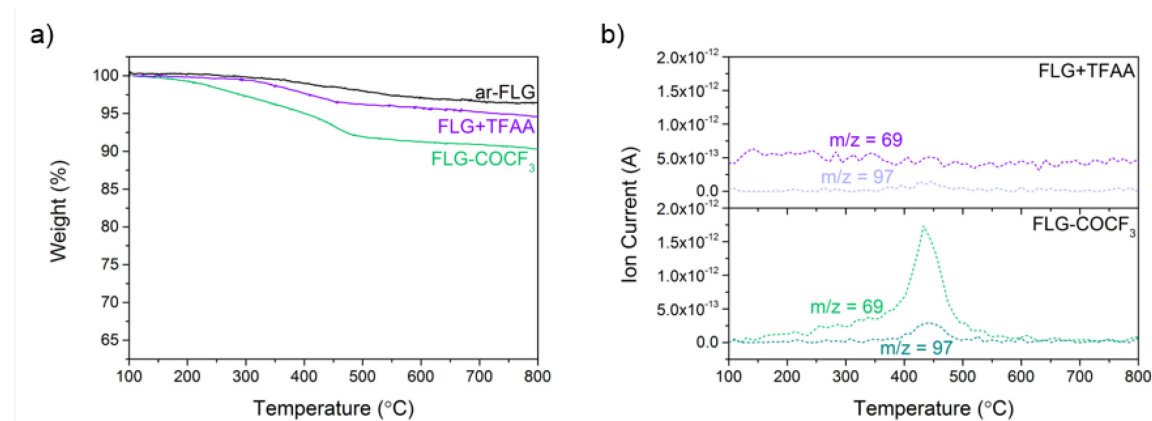
Figure 6.4. a) TGA data for ar-FLG, physisorption control FLG+TFAA, and FLG-COCF₃; b) corresponding MS profiles of FLG+TFAA and FLG-COCF₃, *m/z* 69 (-CF₃⁺), 97 (-COCF₃⁺).

Table 6.2. Characterisation data of FLG-COCF₃.

Sample	GR (%) (TGA)	$C/COCF_3$ (TGA)	$C/COCF_3$ (XPS)	at% C (XPS)	at% O (XPS)	at% F (XPS)
ar-FLG	-	-	-	95.9	4.1	-
FLG-COCF₃	4.7	171	149	92.1	6.2	1.7

6.1.2.2. Characterisation of FLG-g-f-(n)

A control experiment mixing exfoliated Na-THF-FLG and MMA monomer, and washing (following the same procedure), showed no residual MMA fragments by TGA-MS (Figure 6.5), suggesting that all adsorbed species could be successfully removed.
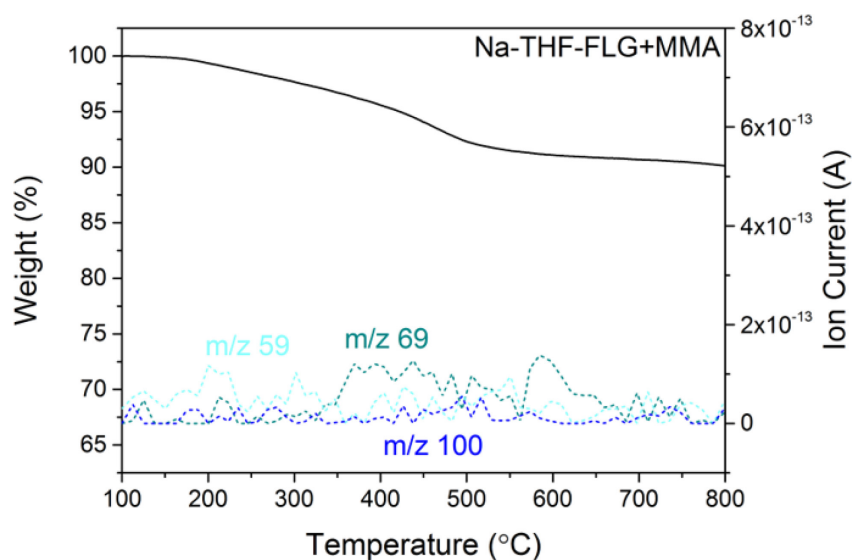
Figure 6.5. TGA-MS profile of Na-THF-FLG+MMA control; m/z 59 (-COOCH$_3^+$), 69 (-CH$_2$C(CH$_3$)(CO)-$^+$), and 100 (-CH$_2$C(CH$_3$)(COOCH$_3$)-$^+$).

The TGA-MS profiles of the grafting-from products show weight losses of between 35.3 wt% and 56.8 wt% in the range 200-500 °C, consistent with PMMA decomposition (Figure 6.6); the corresponding PMMA fragments, m/z 41, 59, 69 and 100, were detected by MS in the same temperature range (full TGA-MS provided in Appendix II, Figure II.2).

High grafting ratios of ~45-127% were achieved by the grafting-from approach, increasing with larger MMA/Na ratio, as expected (Table 6.3). However, the increase is not directly proportional to the amount of monomer introduced in the reaction, indicating that not all the monomer was consumed, and that termination of the polymer occurred before the reaction could go to completion. The molecular weight of the polymers was estimated from the grafting ratio by assuming the same density of active sites determined by reaction with TFAA; the values varied from 800 to 2300 g mol^{-1} (Table 6.3). The amount of solvent remaining in the grafting-from samples shows an erratic trend, but overall is similar to the amount remaining in the grafting-to products.
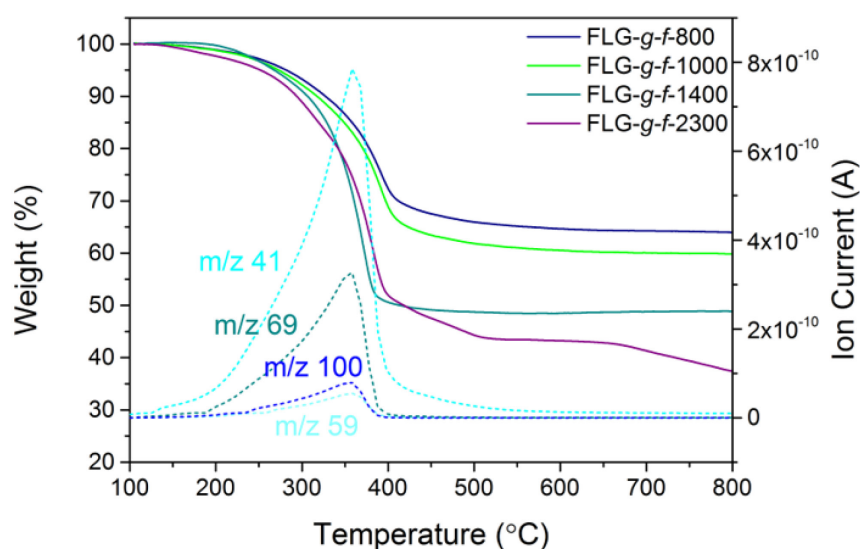
Figure 6.6. TGA profiles of FLG-*g-f*-800, FLG-*g-f*-1000, FLG-*g-f*-1400 and FLG-*g-f*-2300, and corresponding MS trace of FLG-*g-f*-1400; *m/z* 41 ($-CH_2C(CH_3)-^+$) or ($-CHCH_2CH_2-^+$), 59 ($-COOCH_3^+$), 69 ($-CH_2C(CH_3)(CO)-^+$), and 100 ($-CH_2C(CH_3)(COOCH_3)-^+$).

Table 6.3. Summary of grafting data for grafting-from products.

Sample	MMA/Na	GR (%)	M_n (g mol^{-1})*	C/THF
FLG-*g-f*-800	15	44.6	798	56
FLG-*g-f*-1000	30	55.6	995	58
FLG-*g-f*-1400	60	79.1	1415	23
FLG-*g-f*-2300	90	126.5	2265	24

*M_n calculated based on GR and an assumed C/PMMA of 149, for all cases.

NMR analysis of the products shows typical signals attributable to PMMA polymer (Figure 6.7). In the ^{1}H NMR spectrum of PMMA-Br, the peak at 3.61 ppm is assigned to the -COOCH$_3$ protons. The signals observed at 0.85 and 1.03 ppm arise from the -CH$_3$ groups, whilst the -CH$_2$- protons give rise to the peaks between 1.8 and 2.0 ppm.[296] These peaks are all present in the spectrum of FLG-*g-f*-1400, confirming that PMMA is introduced on the graphene layers, and that graphenide does not cause ester cleavage during reaction. The signals of the -CH$_3$ protons are present at different intensities, indicating a different conformation of the polymer on FLG compared with the free polymer in solution. The peaks from the -CH$_2$- protons are weakened and broadened, suggesting that free rotation is restricted, by interactions with the graphene layers. The same signals were very weak for FLG-*g-f*-1000 and FLG-*g-f*-800, likely due to the lower polymer content, and hence, solubility. Similarly, in the grafting-to products, only very weak PMMA signals were detected.
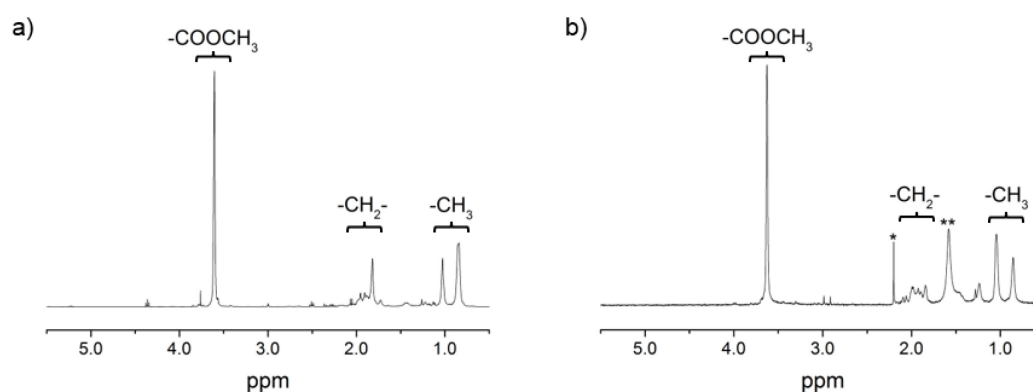
Figure 6.7. ^{1}H NMR a) PMMA-Br (M_n 5000 g mol^{-1}), and b) FLG-*g*-*f*-1400. * and ** indicate residual acetone and water, respectively.

6.1.3. Comparison of PMMA-FLG graft-to and -from routes

Analysis of the Raman spectra for the grafting-to products shows a small increase in the I_D/I_G ratio (from 0.31±0.04 in ar-FLG up to 0.42±0.03 in FLG-*g*-*t*-8000), suggesting that only very few defects have been introduced onto the carbon lattice (Figure 6.8). This result is unsurprising given the edge mode of functionalisation observed for alkyl grafting (Chapter 5, section 5.3.4) and the size of the polymers. Following grafting of one PMMA addend, neighbouring edge sites are inaccessible to another polymer chain, resulting in a sparse distribution of polymers. These conclusions are also consistent with the relatively low degree of grafting obtained by TGA. Only a slight increase in the degree of exfoliation is observed, with I_{2D}/I_G increasing from 0.59±0.07 in ar-FLG, up to 0.67±0.04 in FLG-*g*-*t*-10000 (Figure 6.9a), suggesting that the large polymers can only access outer faces and edges of the FLG stacks and therefore do not significantly aid exfoliation. In contrast to the grafting-to products, a much greater increase in I_D/I_G can be seen in the modified graphenes obtained from the grafting-from method. For all molecular weights, I_D/I_G increased to ~0.5 (Figure 6.9b), indicating that a similar number of initiation sites are present in each case, regardless of polymer M_n. The smaller MMA monomers are able to diffuse further into the sample, and graft more densely compared to the bulky PMMA polymers. Accordingly, I_{2D}/I_G also shows a much greater increase after functionalisation (from 0.59±0.07 in ar-FLG up to 0.77±0.05 in FLG-*g*-*f*-2300), this time increasing with increasing molecular weight. This observation suggests that the growth of longer polymers from the surface helped expand the graphene layers, encouraging exfoliation, and prevented restacking of the layers.
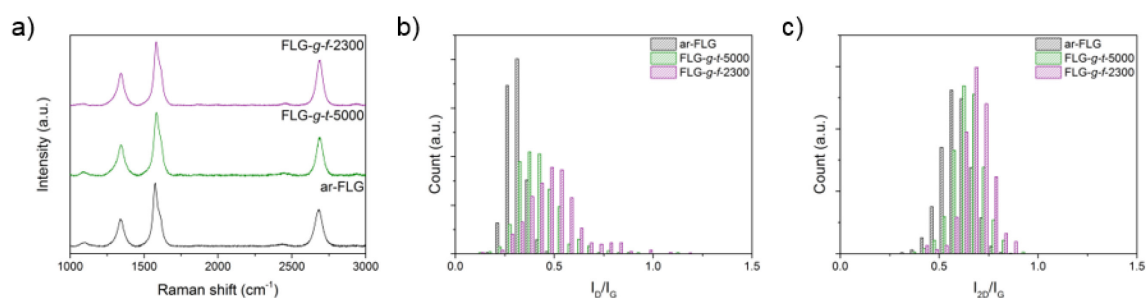
Figure 6.8. a) Averaged Raman spectra, and Raman histograms of b) I_D/I_G and c) I_{2D}/I_G ratio for ar-FLG (black), FLG-*g-t*-5000 (olive) and FLG-*g-f*-2300 (purple); spectra normalised to the G peak intensity and offset for clarity.
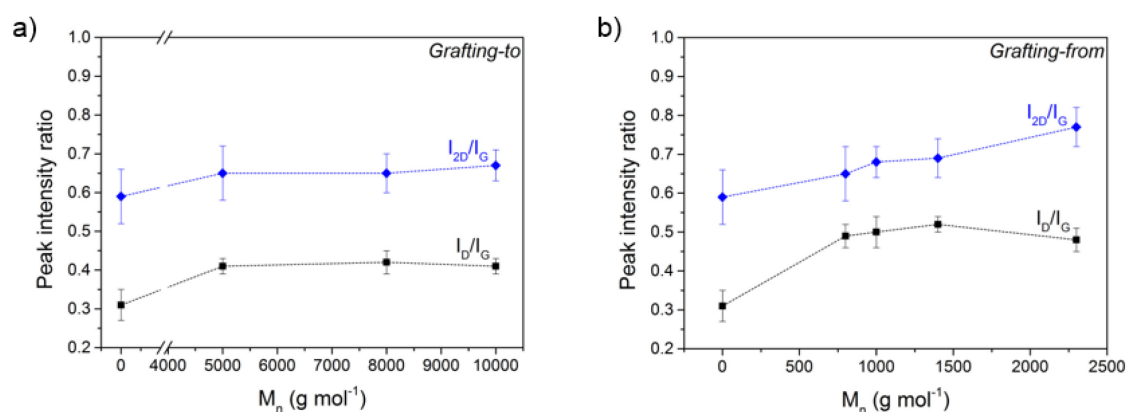
Figure 6.9. Average I_D/I_G and I_{2D}/I_G ratios of FLG-PMMA obtained using the a) grafting-to and b) grafting-from approaches. (All values can be found in Appendix II.)

Further evidence for covalent functionalisation was obtained by XPS (Figure 6.10). In ar-FLG, the main signal of the C1s peak at ~284.5 eV arises from the C=C and C-C bands (284.5 eV) with a small contribution from C-O and C=O (286.4 eV), COOR (288.7 eV) and the π-π* transition (290.7 eV) (Figure 6.10a (left)). Similar components are seen in the Na-THF-FLG spectrum, with a slight increase in oxygen content (5.2 at% from 3.9 at% in ar-FLG) (Figure 6.10b). This increase is attributed to the presence of a small amount of residual THF, also seen by TGA measurements, and corroborated by the presence of sodium (0.1 at%), rather than introduction of oxygen functionalities onto the graphene layers during reductive treatment. After the addition of PMMA, the C=C/C-C band in the high resolution C1s spectra of both FLG-*g-t*-5000 and FLG-*g-f*-2300 broadens due to the introduction of polymer C-C bonds (Figure 6.10c and d (left)); further, a significantly increased contribution from the COOR and C=O bands is observed, compared with ar-FLG and Na-THF-FLG (Figure 6.10a and b (left)). Correspondingly, a stronger core O1s signal is detected, consistent with the deconvoluted C1s peaks (Figure 6.10c and d (right)).
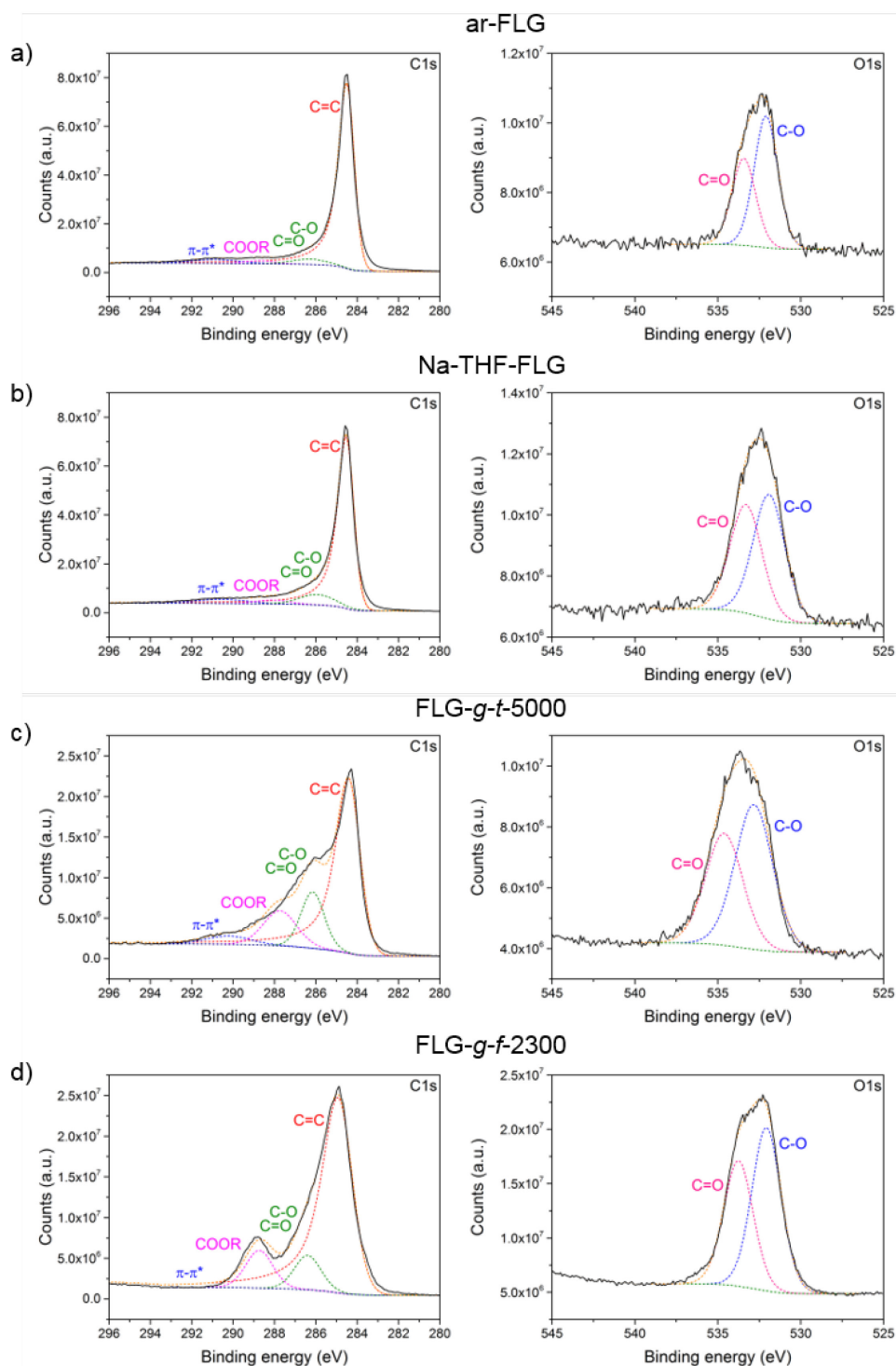
Figure 6.10. High resolution C1s (left) and O1s (right) XPS data for a) ar-FLG, b) Na-THF-FLG, c) FLG-*g-t*-5000, and d) FLG-*g-f*-2300.

Compositional analysis of the samples obtained by the grafting-to approach shows an increased O/C ratio relative to ar-FLG (up to 0.11 from 0.04), indicative of the presence of PMMA. The oxygen content decreases from 9.6 at% to 8.2 at% with increasing length of polymer (Table 6.4) consistent with decreasing GR results (20.3% to 12.6%) obtained by TGA

(Table 6.1). The amount of oxygen increases much more significantly in the grafting-from products, reaching an O/C ratio of 0.31 in FLG-*g-f*-2300; using this grafting approach, the oxygen content increases with the size of polymer (9.9-23.5 at%), in line with TGA GR values (44.5-126.5%, Table 6.3). The XPS data were used to calculate C/PMMA values. As a simplification, the amount of solvent remaining was assumed to be the same in every sample, and equal to the amount in Na-THF-FLG. The C/PMMA values for the grafting-to products estimated by XPS are generally slightly lower than those obtained by TGA. XPS is highly surface sensitive and polymers grafted and wrapped around the edges and surfaces are detected preferentially, but the overall trend is in good agreement with TGA calculations (Table 6.4). For the samples obtained by the grafting-from method, the grafted densities calculated from XPS data varied between 45 and 250, reasonably close to the estimate obtained from reaction with TFAA.

Table 6.4. XPS atomic compositions and grafting densities of PMMA-grafted FLGs.

Sample	at% C	at% O	C/PMMA (XPS)	C/PMMA (TGA)
ar-FLG	95.9	3.9	-	-
Na-THF-FLG	94.3	5.2	-	-
FLG-*g-t*-5000	89.7	9.6	1440	2055
FLG-*g-t*-8000	90.9	9.0	3630	4421
FLG-*g-t*-10000	91.6	8.2	4540	6615
FLG-*g-f*-800	89.7	9.9	210	149[†]
FLG-*g-f*-1000	89.2	10.1	250	149[†]
FLG-*g-f*-1400	79.6	20.2	50	149[†]
FLG-*g-f*-2300	75.6	23.5	45	149[†]

[†]Estimated from FLG-COCF$_3$ and assumed to be constant.

The characteristic graphite (002) signal at 2θ ~26.0° is present in the XRD measurements of all the PMMA-grafted FLG samples (Appendix II, Figure II.3). The weak and broad diffraction pattern is indicative of a well-exfoliated material; there are an estimated 13 layers per stack in the starting material (Chapter 5, section 5.3.1.5). After polymerisation, a small broadening of the (002) peak is observed in all samples, indicating further exfoliation of the FLG material.[297] A slightly greater degree of exfoliation is achieved in the grafting-from products, where the average number of layers in each coherent stack is reduced to ~6, compared with ~11 in the grafting-to approach (Table 6.5). In the XRD pattern for FLG-*g-f*-2300, the intensity of the (002) peak is very significantly reduced (compared with the other identically prepared samples), suggesting almost complete loss of any graphitic domains. An additional broad signal detected around 12.4° in FLG-*g-f*-1000 and FLG-*g-f*-2300 is attributed to regions of loosely stacked graphene separated by grafted PMMA chains, and corresponds to an interlayer spacing of 7.2 Å. The smaller layer numbers for the grafting-from products obtained by XRD are consistent with the trend of higher I_{2D}/I_G ratios (up to 0.77±0.05) observed in the Raman data, both indicative of more successful exfoliation than the grafting-to approach.

Table 6.5. XRD data for grafting-to and grafting-from products.

Sample	d_{002} (nm)	Layer number*	Raman I_{2D}/I_G
ar-FLG	0.337	13	0.59±0.07
Na-THF-FLG	0.340	16	0.61±0.04
FLG-*g-t*-5000	0.344	9	0.65±0.07
FLG-*g-t*-8000	0.345	11	0.65±0.05
FLG-*g-t*-10000	0.339	12	0.67±0.04
FLG-*g-f*-800	0.341	7	0.65±0.07
FLG-*g-f*-1000	0.343	6	0.68±0.04
FLG-*g-f*-1400	0.344	6	0.69±0.05
FLG-*g-f*-2300	0.343	6	0.77±0.05

*Estimated using the Scherrer equation with $K = 0.91$ and taking instrumental line broadening as 0.12°.

The degree of exfoliation of the FLG-PMMA materials was further investigated by AFM (Figure 6.11). In ar-FLG, the average height of the agglomerated stacks is 21±5 nm, corresponding to around 60 graphene layers. Reductive treatment of FLG effectively separates these aggregates, yielding smaller flakes with lateral size 640±170 nm, and thicknesses of 4.4±0.6 nm, or approximately 12 layers. Introduction of polymer chains further improves the degree of exfoliation, with an average flake thickness of 3.1±0.4 nm observed in FLG-*g-f*-2300. This thickness corresponds to ~9 graphene layers, or, assuming the graphene sheets are loosely separated by grafted PMMA chains, and using the interlayer spacing obtained from XRD (7.2 Å), ~4 polymer-grafted layers. These values obtained by AFM are in good agreement with those calculated from XRD, and confirm successful exfoliation occurs with polymer grafting.
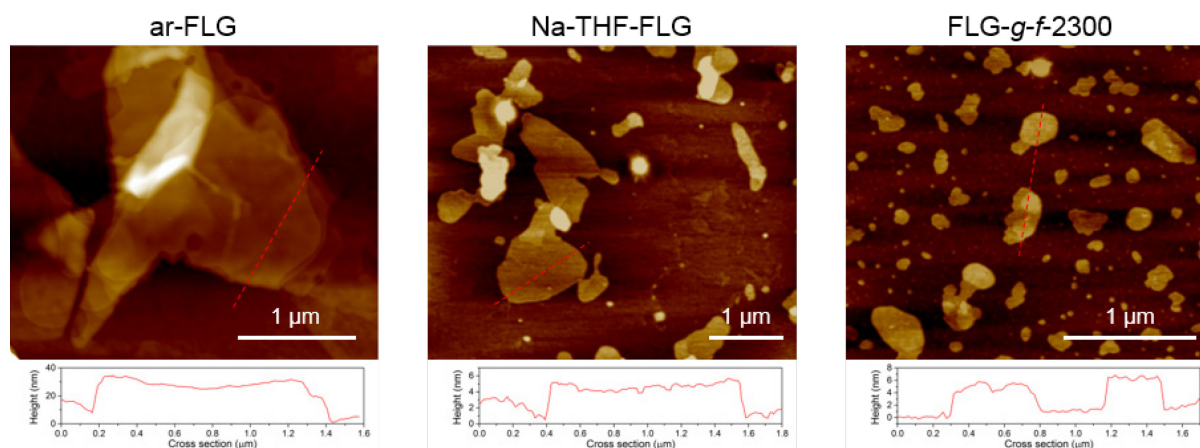
Figure 6.11. AFM images of as-received, Na-THF- and FLG-*g-f*-2300; height profiles indicated by the red line.

Little change in the shape or morphology of the graphene layers, compared to the starting material, can be seen in the TEM images of Na-THF-FLG and FLG-*g-f*-2300 (Figure 6.12). The apparent lateral dimensions also remain the same (200 nm), indicating that the exfoliation and functionalisation procedure with PMMA did not damage the graphene sheets. Compared

with AFM measurements, the flakes appear smaller due to wrinkling and folding; possibly due to the rates of solvent drying on different substrates.
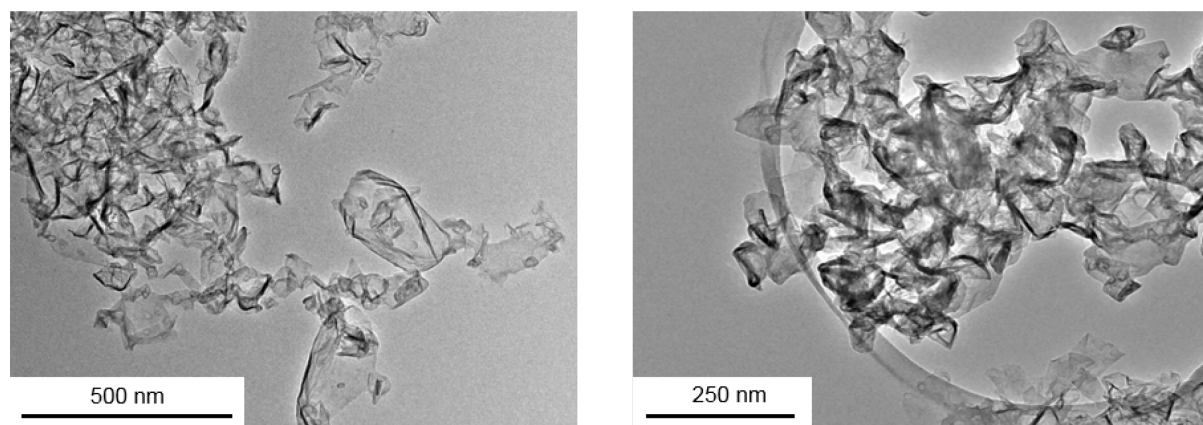
Figure 6.12. TEM images of Na-THF- (left) and FLG-*g-f-*2300 (right).

6.1.4. Trends in grafting and solubility

In the grafting-to approach, the grafting ratio obtained from TGA measurements (Table 6.1) shows a slight decrease with increasing molecular weight of polymer (Figure 6.13), with a corresponding increase in C/PMMA; this observation is attributed to steric effects limiting grafting density. The balance between the lower grafting density and the higher molar mass of the polymers results in a relatively constant mass of polymer attached to the graphene surface (12.6-20.3%). A similar trend was observed in the grafting ratio of SWCNTs functionalised with polystyrene of varying M_n.[233] In contrast, the grafting ratio increases, from 44.6% in FLG-*g-f*-800 to 126.5% in FLG-*g-f*-2300 (Table 6.3), with increasing M_n, for products obtained by the grafting-from method. The small MMA monomers can achieve a much higher grafting density initially, and growth of the polymers from the surface aids exfoliation of the graphene layers. These results are in contrast to a previous report comparing the grafting-to and grafting-from of PMMA to rGO,[197] which found that a higher graft density was achieved by the grafting-to method, but that higher molecular weight polymers could be achieved by grafting-from. This difference could likely be due to the mechanism of polymerisation (RAFT), and the fact that in the grafting-from approach, initiation sites are limited to those introduced by a previous cycloaddition step, whereas for anionic polymerisation from graphenide, the number of initiations is theoretically only limited by the amount of charge available initially.
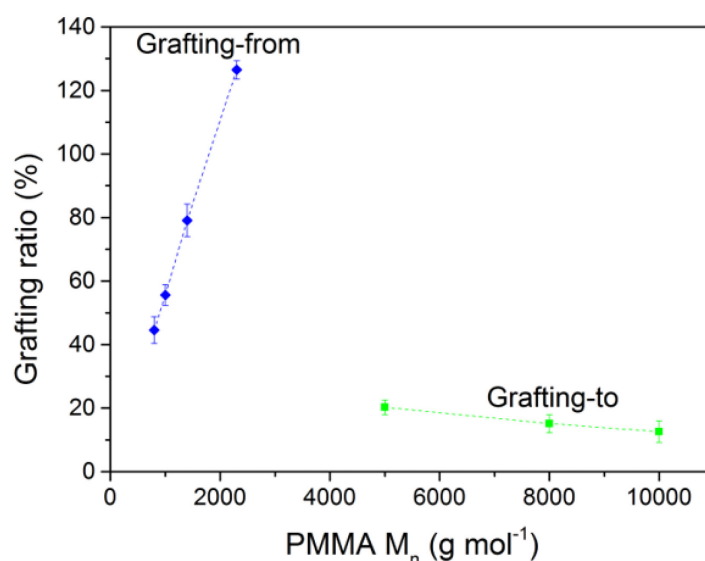
Figure 6.13. Grafting ratio vs PMMA molar mass for the grafting-to and grafting-from approaches.

The conformation of grafted PMMA chains can be predicted by comparing the average separation, D, between grafting sites, to the theoretical Flory radius of each polymer ($R_F = N^{3/5}l$, where l is the Kuhn length of PMMA,[298] and N is the number of Kuhn segments per chain).[299] The value of D, and the surface concentration of grafted polymer were estimated using the specific surface area for Na-THF-FLG (420 ± 5 m^2 g^{-1}) (Table 6.6). For the grafting-to products, the average separation between chains ranges from 5.48 to 9.55 nm, assuming a uniform grafting density.

Table 6.6. Polymer grafting data for PMMA-FLGs.

Sample	Surface concentration of PMMA (μmol m^{-2})*	PMMA separation, D (nm)	R_F (nm)[†]
FLG-g-t-5000	0.07	5.48	5.81
FLG-g-t-8000	0.03	8.01	7.70
FLG-g-t-10000	0.02	9.55	8.80
FLG-g-f-800	0.85	1.58	1.93
FLG-g-f-1000	0.79	1.63	2.21
FLG-g-f-1400	0.66	1.79	2.71
FLG-g-f-2300	0.49	2.08	3.65

*Calculated using the mass of PMMA obtained from TGA measurements and the specific surface area of Na-THF-FLG; [†]using Kuhn length, l = 1.4 nm.[298]

For the two higher molecular weights, these are larger than the calculated Flory radius, suggesting that the polymer adopts a mushroom-like conformation and coils up on itself.[299] For FLG-g-t-5000, and the grafting-from samples, the separation is smaller than R_F, and de Gennes' model predicts that the polymers conform to a brush-like regime. Whilst these calculations are based on the specific surface area obtained for Na-THF-FLG, which is less exfoliated than the grafting-from products, and would therefore have a smaller surface area,

they provide a reasonable approximation of the expected polymer conformations on the graphene surface. For a proposed edge-initiated mode of grafting, where polymers are more densely grouped near edge sites, a transition to brush-like grafting might be expected.

PMMA dissolves readily in acetone,[300] and the dispersibility of the FLG material was dramatically increased after functionalisation with PMMA. The initial dispersibility of ar-FLG in acetone was low (3.8 µg mL^{-1}), but increased substantially in Na-THF-FLG (530 µg mL^{-1}). Modification with polymer further enhanced the solubility, by up to 190 times using the grafting-to approach (FLG-*g-t*-10000 710 µg mL^{-1}), and up to 250 times by the grafting-from route (FLG-*g-f*-2300 920 µg mL^{-1}) (Table 6.7). The incorporation of different molecular weight polymer chains onto the surface of FLG, by the grafting-to approach, can have two competing and opposing effects on the solubility of the graphene sheets. The longer polymer chains grafted on FLG resulted in improved polymer-solvent interactions and, therefore, an increased solubility. However, the lower grafting density resulting from steric interactions means that a smaller amount of polymer can be introduced onto the graphene surface, thus reducing the amount of steric stabilisation to prevent aggregation. The dispersibility of the grafting-to products varies only slightly with the M_n of the attached polymers, with FLG-*g-t*-10000 achieving the highest solubility. Despite having the lowest grafting density, the longer polymer chains are more effective at stabilising graphene sheets in solution; therefore, the polymer length dominates the materials' solubility properties by this approach. However, the difference is not large, likely because the grafting ratio is relatively similar in all cases and therefore the total amount of polymer remains approximately the same, regardless of chain length. Conversely, the samples obtained from the grafting-from reactions show an increasing solubility with increasing polymer size, and grafting ratio, because the larger amount of polymer can provide greater stability against aggregation.

Table 6.7. Summary of dispersibility data for PMMA-FLGs.

Sample	Grafting ratio (%)	Dispersibility (µg mL^{-1})
ar-FLG	-	3.8
Na-THF-FLG	-	530
FLG-*g-t*-5000	20.3	650
FLG-*g-t*-8000	15.1	670
FLG-*g-t*-10000	12.6	710
FLG-*g-f*-1100	44.6	720
FLG-*g-f*-1300	55.6	760
FLG-*g-f*-1900	79.1	875
FLG-*g-f*-2800	126.5	920

The dispersibilities of the grafting-from products achieved in this study are higher than values reported in the literature for rGO grafted with PMMA polymers of higher M_n, but with lower

grafting density,[197] suggesting that in the grafting-from products, the grafting density is the dominant factor affecting solubility. Overall, the samples obtained by the grafting-from approach show a higher degree of dispersibility than the grafting-to products (Figure 6.14), in line with the grafting ratios achieved. This increased dispersibility might also be due to more effective exfoliation during the grafting-from reaction, caused by the growth of polymers expanding the interlayer spaces, resulting in fewer large aggregates which easily agglomerate and sediment. These improved solubility results are very promising for potential incorporation of PMMA-grafted FLGs into different polymer matrices.
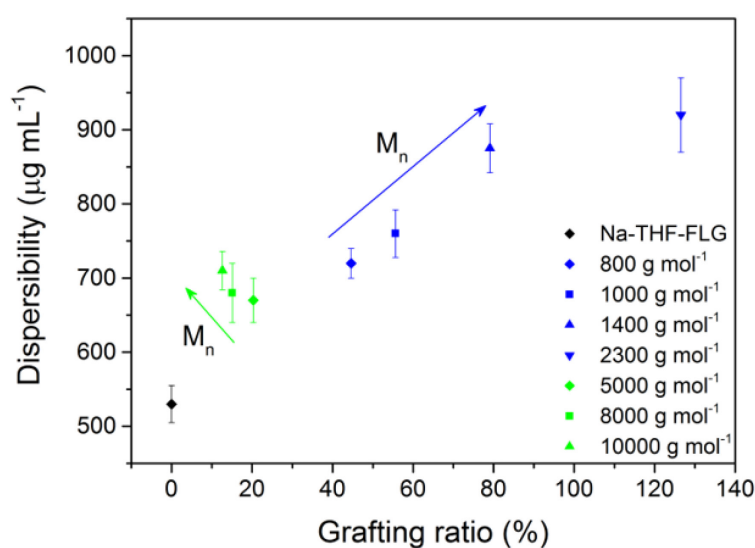
Figure 6.14. Dispersibility vs grafting ratio for the grafting-to (green) and grafting-from (blue) products.

6.2. Extension to natural flake graphite

Successful reaction of reduced FLG with brominated PMMA and MMA monomer effectively improved solubility and exfoliation. The grafting-to and -from methods can also be applied to other graphite starting materials, where exfoliation and solubility is inherently a larger problem. In the following section, these grafting approaches are applied to natural flake graphite. Characterisation of the as-received material can be found in Chapter 5, section 5.1.1.

6.2.1. Comparison of solvent and grafting in NFG-*g-t* and NFG-*g-f*

Following the same procedures for FLG (Chapter 6, sections 6.1.1.2 and 6.1.2), a graphenide-containing solution from natural flake graphite was reacted with bromine-terminated PMMA (M_n ~5000 g mol^{-1}) in a grafting-to approach, to obtain the product NFG-*g-t*. In parallel, dried and degassed MMA monomer was added in the ratio MMA/Na = 30 to a charged solution of

NFG, to produce the grafting-from product NFG-*g-f*. These conditions were selected since PMMA-Br with M_n ~5000 g mol^{-1} achieved the highest grafting ratio with FLG (20.3%), whilst the MMA/Na = 30 ratio resulted in the least amount of solvent trapped (C/THF of 58), with a high grafting ratio (55.6%).

TGA-MS data show the same two-step weight loss (at 150-350 °C and 350-650 °C) characteristic of intercalated Na-THF, but in addition to THF fragments *m/z* 41 and 72, PMMA fragments *m/z* 41, 59, 69 and 100 were also detected in the same temperature range (Figure 6.15). A greater apparent weight loss is seen for NFG-*g-t* (21.1 wt%) compared with NFG-*g-f* (15.9 wt%). However, further analysis of the MS fragments *m/z* 41 and 69, using the method applied previously (refer to Chapter 4, section 4.4.1.1), indicates that more polymer is present in the grafting-from product (consistent with FLG); the weight loss in the grafting-to product arises mostly from solvent, with a C/THF ratio of 23, compared with 37 in NFG-*g-f* (Table 6.8). These results suggest that the presence of more polymer in NFG-*g-f* can effectively prevent close restacking of graphene layers, allowing some removal of residual THF.
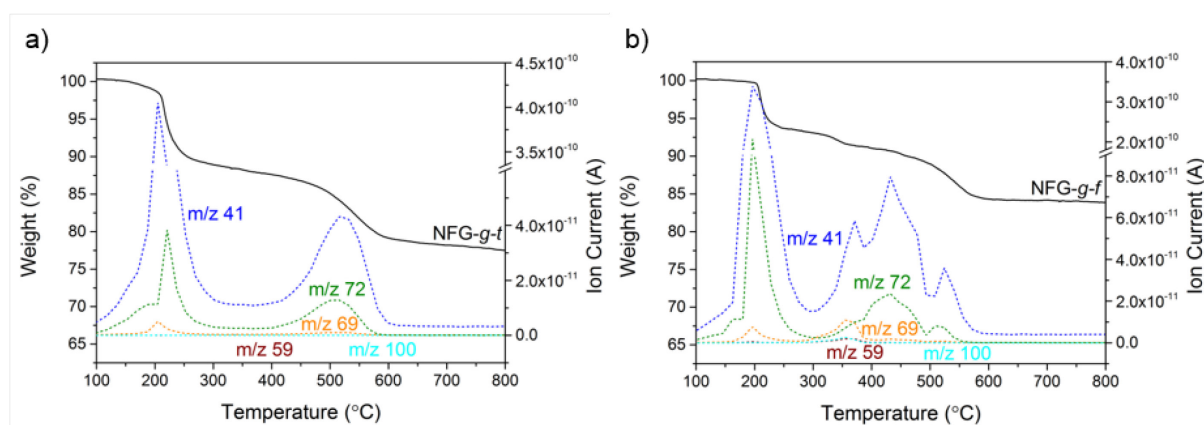
Figure 6.15. TGA-MS profiles of a) NFG-*g-t* and b) NFG-*g-f*; *m/z* 41 (-CH$_2$C(CH$_3$)-$^+$) or (-CHCH$_2$CH$_2$-$^+$), 59 (-COOCH$_3$$^+$), 69 (-CH$_2$C(CH$_3$)(CO)-$^+$), 72 (C$_4H_8O^+$), and 100 (-CH$_2$C(CH$_3$)(COOCH$_3$)-$^+$).

Table 6.8. Summary of grafting data for PMMA-NFGs.

Sample	GR (%)	C/PMMA (TGA)	C/PMMA (Raman)	C/THF	M_n (g mol^{-1})
NFG-*g-t*	1.2	34338	6336	23	5000
NFG-*g-f*	2.6	-	3987	37	1247*

*M_n calculated using grafting ratio obtained by TGA and C/PMMA from Raman analysis.

Raman spectroscopy provides evidence for functionalisation; in both reactions, the I_D/I_G ratio increases very slightly (0.07±0.09 in NFG-*g-t* and 0.1±0.2 in NFG-*g-f*, from 0.05±0.05 in ar-NFG) with the introduction of sp^3 defects onto the carbon lattice (Figure 6.16). The grafting-to approach introduces fewer grafting sites, presumably because the large steric bulk of the polymer prevents ready diffusion into the sample, and once grafting occurs, nearby sites are

blocked from further reaction. However, the difference is not so significant, consistent with the proposed model that grafting is edge initiated since these sites are more available; whilst MMA monomers are able to diffuse more easily into the graphene layers (for grafting-from), reactions are initiated close to the layer edges, which are then more available for further reaction, and subsequent anionic polymerisation is preferable to direct attachment of monomer to the graphene basal plane. This trend is consistent with that observed in the reactions with FLG, although the grafting ratios obtained are far lower (1.2% for NFG-*g-t* compared with 20.3% in FLG-*g-t*-5000, and 2.6% for NFG-*g-f* against 55.6% in FLG-*g-f*-1000), owing to the reduced edge to flake area ratio, similar to the trend seen in grafting of dodecyl bromide (Chapter 5, section 5.3.4).
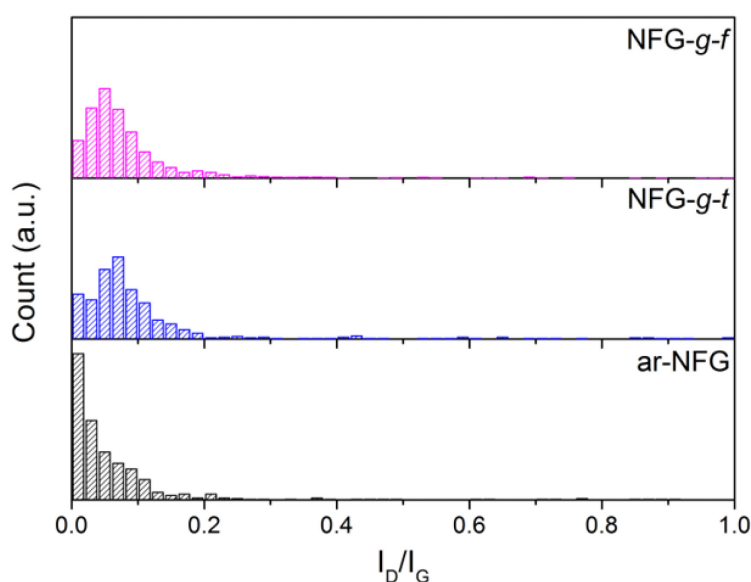
Figure 6.16. Raman histogram of I_D/I_G ratios of ar-NFG (black), NFG-*g-t* (blue) and NFG-*g-f* (magenta).

The C/PMMA ratio for NFG-*g-f* obtained by Raman (3987) and the GR derived from TGA-MS analysis were used to estimate the length of PMMA chains, assuming even chain growth (Table 6.8). In reality, the C/PMMA ratio from Raman is expected to be an underestimate, since it is based on an assumed even distribution of grafting; therefore, the obtained M_n of 1247 g mol^{-1} is an upper estimate. The grafting ratio achieved (2.6%) is far lower than the theoretical maximum if all monomer was consumed in the polymerisation reaction (2083%); it is likely that side reactions resulting in chain transfer and early termination occurred,[295] and ungrafted oligomeric species were subsequently washed away. In reality, it is unlikely that homogeneous chain growth occurs due to the heterogeneity of the starting graphite and therefore the accessibility of different initiation sites. The same initial loading of monomer (C/Na = 30) resulted in a similar length polymer on natural flake graphite (M_n 1247 g mol^{-1})

and FLG (M_n 995 g mol^{-1}), although the number of initiation sites is far lower for the larger flake size (3987 in NFG-*g-f* and 149 in FLG-*g-f*-1000). The C/PMMA value for the grafting-to product obtained by Raman (6336) is much lower than that calculated by TGA (34338). This discrepancy may be due to the difficulty in detecting such small quantities of polymer in the mass spectrometer, or the presence of edges affecting the Raman I_D/I_G values, resulting in a higher grafting density compared to TGA.

6.2.2. Exfoliation and solubility in NFG-*g-t* and NFG-*g-f*

According to statistical Raman analysis of the I_D/I_G ratio (Figure 6.16), there is little difference between the grafting densities in the grafting-to and grafting-from approaches on NFG, despite the large difference in size of the grafted moieties; however, the 2D peak reveals a significant difference (Table 6.9). In the grafting-to product, the I_{2D}/I_G histogram (Figure 6.17a) shows a bimodal distribution reflecting a mixture of highly intercalated areas, where the 2D peak intensity is extremely weak, and regions which remain unchanged and unexfoliated (Figure 6.17b). The spectrum from area (i) shows an upshifted G peak and a very weak 2D intensity, indicative of doping arising from Na-THF intercalation. The slight splitting of the G peak in area (ii) is a result of partial intercalation, whilst the rounded 2D band suggests only a slight degree of exfoliation.
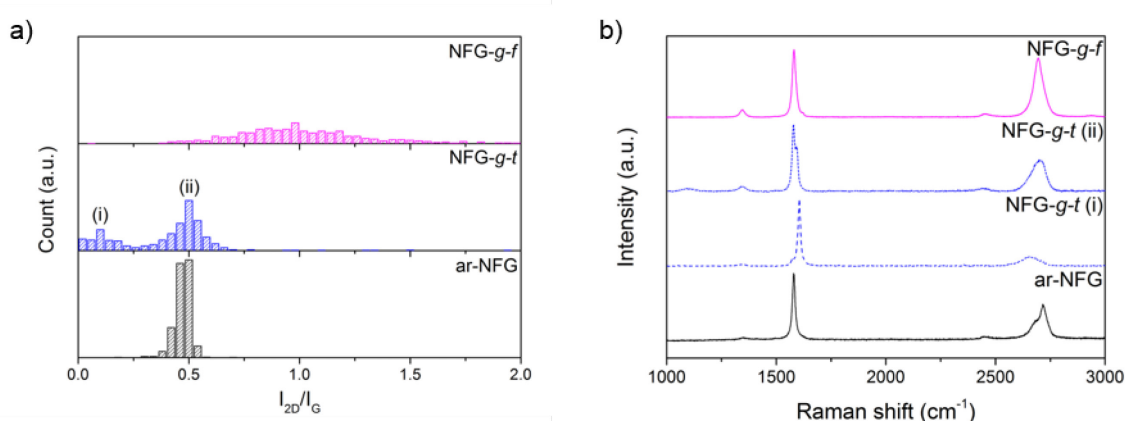
Figure 6.17. a) Raman histograms of I_{2D}/I_G ratios, and b) averaged Raman spectra of ar-NFG (black), NFG-*g-t* (blue) and NFG-*g-f* (magenta); point spectra for NFG-*g-t* labelled (i) and (ii) correspond to areas marked in a); spectra normalised to the G peak intensity and offset for clarity.

The grafting-to approach does not significantly affect exfoliation because the large polymers can only access the sheet edges. In the grafting-from approach, MMA monomers may diffuse further into the interlayer spaces and the attachment of a small molecule and subsequent initiation of polymerisation can effectively push apart the graphene layers during reaction. Even after drying, the presence of polymer was enough to prevent perfect restacking of the

graphene layers. This effect is seen in the greatly increased I_{2D}/I_G ratio and the symmetrical, but broad 2D band (Γ_{2D} 50±9 cm^{-1}) (Figure 6.17, Table 6.9), characteristic of turbostratically stacked graphites.[271] The histogram is also significantly broadened, indicating inhomogeneity in the sample.

Table 6.9. Summary of Raman and XRD data for PMMA–NFGs.

Sample	I_D/I_G	I_{2D}/I_G	Γ_{2D} (cm^{-1})	2D position (cm^{-1})	XRD layer number*
ar-NFG	0.05±0.05	0.47±0.04	52±14	2712±16	205
Na-THF-NFG	0.06±0.08	0.49±0.13	82±12	2694±13	82
NFG-*g-t*	0.07±0.09	0.4±0.2	87±16	2690±26	39
NFG-*g-f*	0.1±0.2	1.0±0.3	50±9	2690±6	19

*Estimated using the Scherrer equation with $K = 0.91$ and taking instrumental line broadening as 0.12°.

Further evidence of exfoliation can be seen in the XRD patterns. In identically prepared samples, the intensity of the graphite (002) peak is significantly reduced in both NFG-*g-f* and NFG-*g-t* compared with ar-NFG, suggesting the loss of long-range graphitic order in both samples (Figure 6.18). The number of layers in these remaining graphitic domains reduces from 205 in ar-NFG, to 39 in NFG-*g-t* and 19 in NFG-*g-f* (Table 6.9), showing a higher degree of exfoliation than the unfunctionalised control Na-THF-NFG (82 layers). In NFG-*g-t*, residual stage 1A intercalation structure can be seen from the peaks at 15.9° and 24.1°, with a higher intensity with those in Na-THF-NFG; the small peak at 12.1° indicates that traces of stage 1B structure are also present. These results indicate that the grafting of large polymers prevents diffusion and escape of solvent molecules. In contrast, no ordered GIC structure is discernible in NFG-*g-f*, but the broad peak around 25.4° (also present in NFG-*g-t* and Na-THF-NFG) shows that the sample is mostly a disordered random stage structure.[284] These results are consistent with Raman and TGA data, suggesting that grafting of large polymers at flake edges does not allow much movement of residual solvent, whereas the grafting-from approach enables more exfoliation allowing gradual escape of residual solvent from the interlayer spaces and rearrangement of the defined stage 1A and 1B structures, leaving only disordered intercalated areas.

The exfoliation data from Raman and XRD together imply that a considerable amount of ordered GIC structure is present in solution, after charging; large PMMA-Br polymers can only access the edges and outer surfaces of these stacks, and the product therefore contains traces of residual GIC structure. On the other hand, growth of the polymers in the grafting-from approach promotes exfoliation of the graphene layers, which is supported by the pronounced 2D peak in Raman, and lack of any ordered GIC structure by XRD.
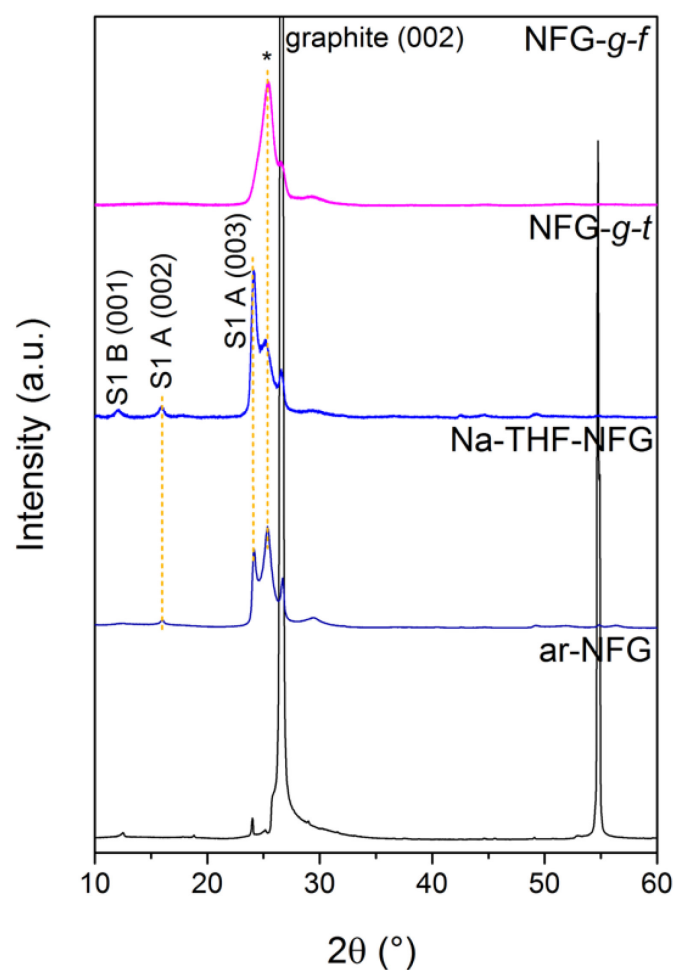
Figure 6.18. XRD patterns for ar-NFG, Na-THF-NFG, NFG-*g-t* and NFG-*g-f*.

Large exfoliated graphene sheets in NFG-*g-f* are also evident by TEM and AFM (Figure 6.19). In the TEM images, few-layers of tens of microns in lateral size can be seen to be wrinkled and folded (Figure 6.19a and b), but overall less trapped solvent is observed compared with the alkyl grafted samples (Chapter 5, section 5.1.3). The wrinkled morphology of the large flakes is also visible by AFM (Figure 6.19c and d). The two highlighted regions reveal stacks of between 5 and 13 nm thick, corresponding to 15-40 layers of graphite, in reasonable agreement with results obtained by XRD. Alternatively, assuming the presence of polymer increases the interlayer spacing in the same way as FLG, to 7.2 Å (section 6.1.3), these thicknesses correspond to 7-18 layers of stacked polymer-grafted sheets.
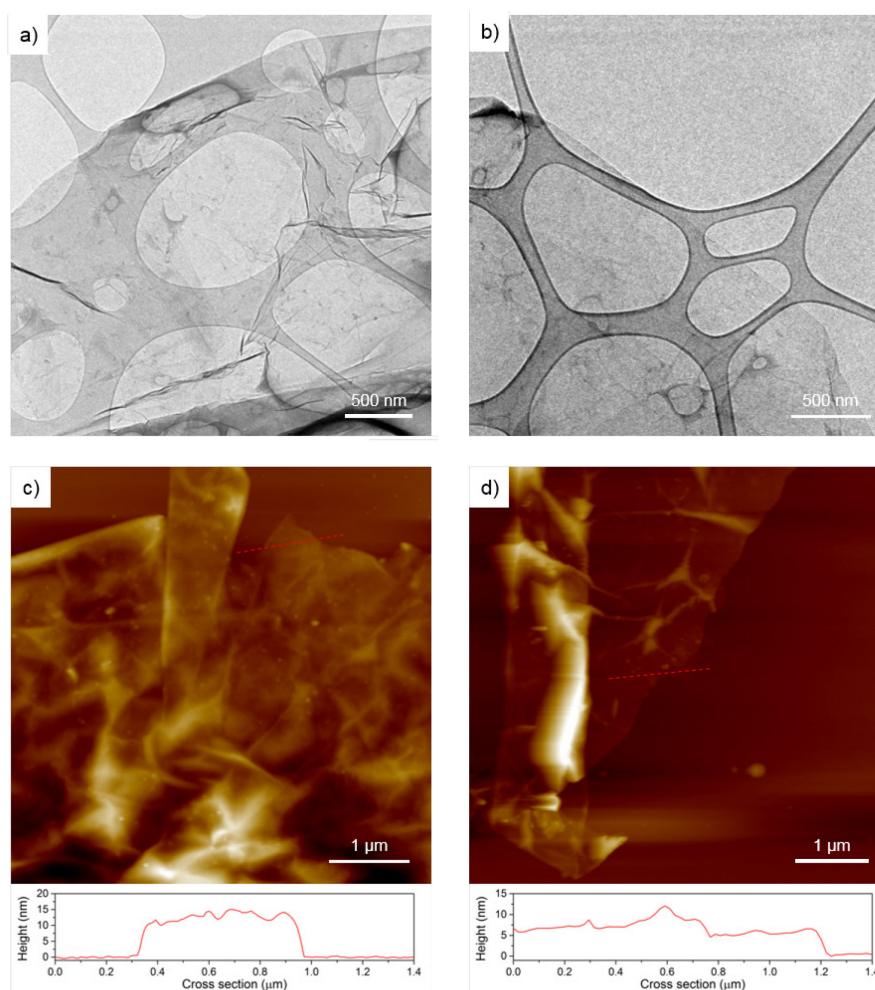
Figure 6.19. a-b) TEM and c-d) AFM images of NFG-*g-f*; height profile indicated by red line.

The differences in grafting ratio are also evident from the difference in solubility between the grafting-to and grafting-from products. Natural flake graphite starting material could not be dispersed in acetone to any significant degree. After functionalisation with PMMA *via* the grafting-to approach, solubility increased to 25.3 µg mL^{-1}, indicating the presence of polymer on the graphene. NFG-*g-f* achieved a solubility of 62.4 µg mL^{-1}, confirming that a greater amount of PMMA had been grafted to successfully stabilise graphene flakes in solution. The solubility values obtained here are lower compared to other methods of polymer functionalisation on natural flake graphite; for example, PEG[202] and PAMAM[203] grafting on graphite by cycloaddition reactions achieved solubilities of 100 µg mL^{-1} and 520 µg mL^{-1} in DMF, respectively. However, these other approaches generally involve intensive sonication exfoliation steps before functionalisation, resulting in much smaller flakes, of around 1-2 µm in lateral size. In comparison to other reductively-functionalised graphites, these solubility values are reasonably high, with alkyl grafting reaching solubilities of 3-37 µg mL^{-1} depending on alkyl length,[13, 15] and PEG-grafted graphene achieving 35 µg mL^{-1} in water;[245] optimisation of reaction conditions could further increase solubility.

6.3. Summary

FLG and natural graphite were grafted with PMMA polymers using reductive chemistry, comparing grafting-to and -from approaches. Pre-synthesised PMMA chains with an activated end group were directly attached in a graft-to approach, similar to the covalent functionalisation with alkyl bromides, described in Chapter 5. Conversely, graphenide can directly initiate anionic polymerisation of MMA, by a graft-from methodology. Based on an assumed constant grafting density between samples, an increased monomer loading results in polymers with larger M_n, and therefore higher grafting ratios. The solubility in acetone of the FLG-PMMA products obtained from the grafting-from approach is directly related to the M_n and grafting ratios; however, it is difficult to control the M_n of the polymer attached to the graphene surface. In contrast, whilst the grafting-to approach allows total control of the polymer size, the obtained solubilities and grafting ratios were lower than those achieved by grafting-from.

Similarly, in natural flake graphite, a higher grafting ratio and graft density were obtained for the grafting-from product, compared with the sample obtained by grafting-to. NFG-*g-f* was correspondingly more soluble than NFG-*g-t*, and showed a far higher degree of exfoliation, confirming that the polymerisation process could effectively separate the graphene layers. In natural flake graphite, the grafting density achieved by reaction with PMMA-Br is lower than that obtained from the analogous grafting reaction with 1-bromododecane, indicating that steric bulk is an important contributing factor in determining grafting density. Following the trend for alkyl grafting on different flake sizes, the grafting density is also lower in natural flake graphite compared with FLG, as expected.

Extension of the reductive functionalisation method for polymer grafting, by both grafting-to and grafting-from approaches, could allow the introduction of a wide variety of polymers and copolymers on graphene. Generally, the grafting-from approach is more suitable for functionalisation of bulk graphitic materials, since the growth of polymers encourages exfoliation, whilst a higher grafting density, and resulting solubility, can be achieved, despite the lower molecular weight obtained by anionic polymerisation. This synthetic route should be applicable to a range of other graphitic starting materials, and the produced polymer-graphene hybrids could have potential use in a wide range of applications, such as sensors, energy storage devices, conductive coatings, or biomedical materials.

7. Brominated graphene as a versatile precursor for multifunctional grafting

In addition to reactions with activated electrophiles, graphenide solutions can effectively initiate anionic polymerisation reactions, illustrated in Chapter 6 by reaction with MMA. However, anionic polymerisation is extremely sensitive to oxygen, moisture or any other protic or carbanion-sensitive impurities, which must therefore be rigorously excluded to prevent quenching and termination of polymer growth. Furthermore, due to the strongly reducing reaction conditions, the choice of monomers is limited to only those stable in the presence of graphenide, or else additional reaction steps must first be taken in order to protect sensitive functional groups.

An alternative and complementary approach to direct polymer grafting on graphenide is discussed in this chapter. Directly brominated few-layer graphene is prepared by reductive chemistry as an air-stable precursor for a variety of further transformations. The versatility of this method is illustrated by using the brominated graphene species as an initiator for atom transfer radical polymerisation of PMMA. In addition, the brominated sites may undergo substitution by reaction with suitable nucleophiles. This approach provides a means of easy access to modified few-layer graphene with improved and tunable dispersibility, critical in bulk applications requiring compatibility with common organic solvents and polymer matrices.

7.1. Bromination of few-layer graphene

7.1.1. Characterisation of few-layer graphene

This study is complementary to the grafting-to and grafting-from investigations discussed in Chapter 6, and FLG was used as a starting material again, to allow easy comparison between the studies. In addition, bromine intercalation compounds of graphite are known to be very stable;[214] smaller, more exfoliated flakes were used with the aim of minimising contributions from stably adsorbed bromine, and residual solvent (Chapter 5, section 5.3). This study was performed with a second batch of FLG (FLG2) supplied by Cambridge Nanosystems. However, characterisation showed that it was very similar to the first; specifically, a similar wrinkled and crumpled morphology was observed (Figure 7.1b) and the lateral flake size lies in a similar range (0.25 to 1.5 µm) as before. The same low degree of c-axis coherence is observed by XRD (Figure 7.1c), with as-received FLG2 (ar-FLG2) showing a weak and broad (002) peak, which is slightly shifted and corresponds to an expanded d-spacing of 3.43 Å; as

before, the estimated number of layers is ~13. A larger D peak (mean I_D/I_G = 0.40±0.03) can be seen in the Raman spectrum (Figure 7.1d), and the 2D peak centred at 2694.3±0.6 cm^{-1} is highly symmetrical and intense, indicative of the highly exfoliated nature of the material. The high degree of graphitisation is reflected in the well-defined G band at ~1580 cm^{-1}.
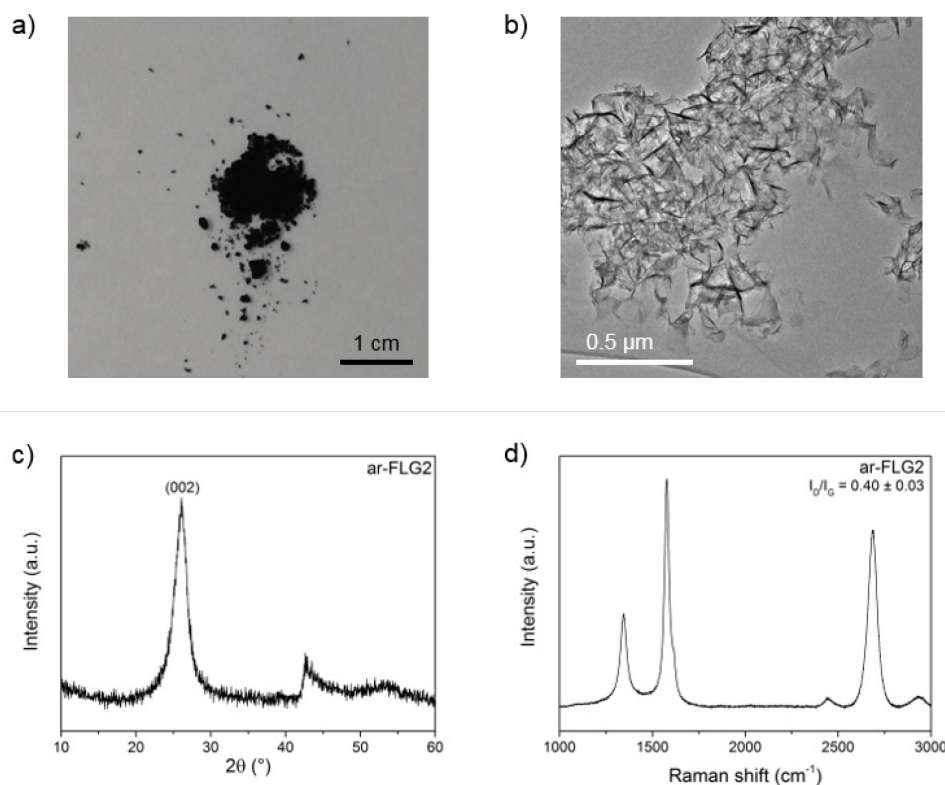
Figure 7.1. a) Photograph, b) TEM image, c) XRD pattern, and d) Raman spectrum of ar-FLG2.

7.1.2. Synthesis and characterisation of FLG2-Br

Following the previously described functionalisation sequence, reduced FLG was prepared by treatment with sodium naphthalide in THF. The black, graphenide-containing dispersion was reacted with bromine liquid to yield brominated graphene (FLG2-Br) (Scheme 7.1). Upon addition of bromine, the FLG flakes sedimented, leaving a brown supernatant. After quenching, the product was washed with DMAc instead of water to remove residual NaBr, since water can react with the bromine addends (more details in section 7.2.2).

The stability of bromine-containing GICs is well-known in the literature[88, 214, 301, 302] and therefore, reductive activation of FLG to form a reactive intermediate is required for covalent functionalisation to take place, similar to the reaction on SWCNTs.[221] In general, bromine intercalation of graphite has been carried out on large natural flake materials,[88, 214] allowing easy adsorption of bromine molecules inside the interlayer galleries. However, as is the case for sodium-THF GICs, adsorbed species lead to complications when determining

functionalisation. In this chapter, the exfoliated nature of the FLG starting material and the small lateral flake size mean that non-covalently adsorbed bromine should be easier to remove after reaction; compared to larger, flatter sheets, quantification of grafting should be more straightforward.
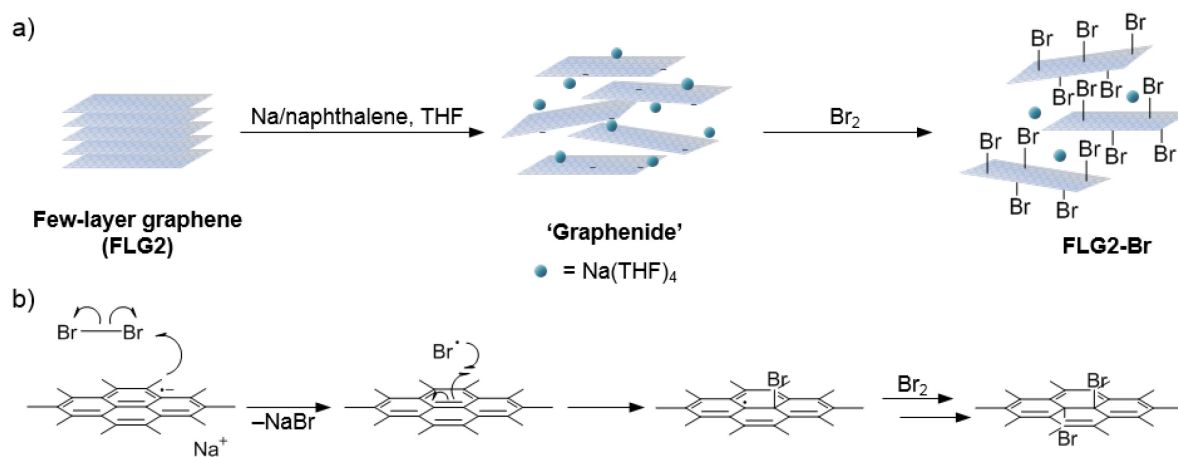
Scheme 7.1. a) Bromine functionalisation of FLG2 to FLG2-Br *via* reduction with sodium naphthalide in THF, followed by reaction with Br2; b) proposed mechanism for reaction of reduced FLG2 with bromine.

TGA-MS under nitrogen confirmed the introduction of bromine species on the FLG starting material (Figure 7.2). Mass fragments *m/z* 79, 81 are detected in the weight loss region between 200 and 450 °C; these signals show a characteristic isotopic distribution of 1:1, and can therefore be assigned to the detachment of bromine addends.[217, 221]
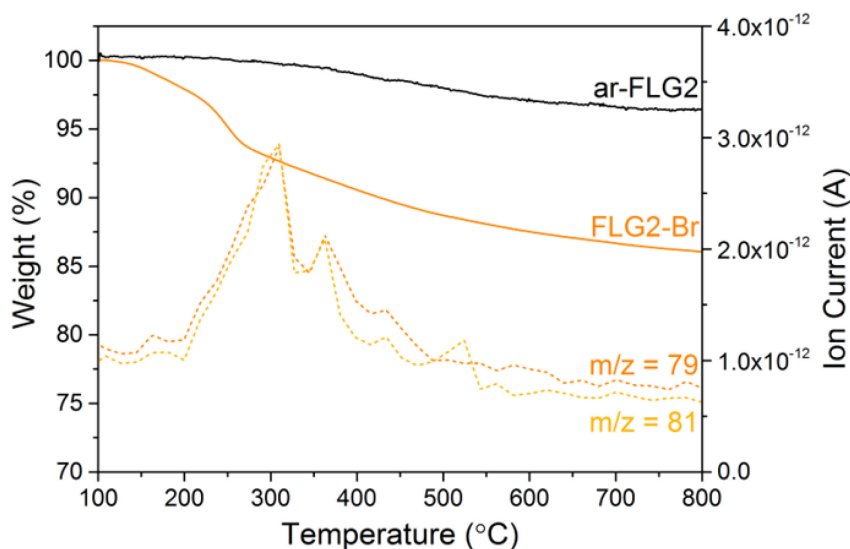
Figure 7.2. TGA-MS profile of ar-FLG2 and FLG2-Br, and corresponding *m/z* 71, 81 (-Br+).

As mentioned above, bromine adsorption on graphite results in stable Br_2-GICs, but desorption occurs at relatively low temperatures (80-180 °C).[303] A reference experiment mixing bromine with uncharged FLG2 (FLG2+Br_2) showed that the washing procedure effectively removed all physisorbed bromine species. No bromine fragments were detected by MS, in the same temperature range, suggesting that bromine species detected in the functionalised product are covalently bound (Figure 7.3a). MS fragments attributed to residual THF were detected in both FLG2+Br_2 and FLG2-Br, due to some solvent trapped within the sample (Figure 7.3). Since bromine and THF have no common mass fragments, the method applied in Chapters 5 and 6 cannot be used to calculate the grafting ratio definitively from TGA alone. However, by taking the total mass loss during pyrolysis (8.4 wt%), an upper bound for the grafting ratio is 9.3%, corresponding to a C/Br of 71 (Table 7.1).
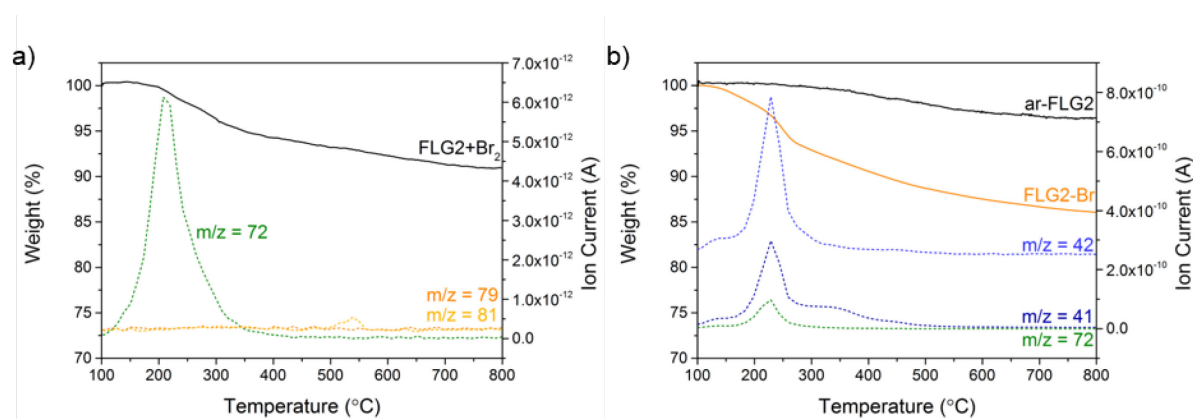
Figure 7.3. TGA-MS data for a) FLG2+Br_2 control; m/z 72 (THF), 79, 81 (-Br^+); and b) FLG2-Br with THF fragments m/z 41, 42 and 72.

Further evidence for covalent functionalisation was obtained by XPS. In the wide survey XPS spectra of ar-FLG2, FLG2-Br and FLG2+Br_2 (Figure 7.4f), the major peak at 284.6 eV arises from C1s of sp^2 hybridised carbon. In FLG2-Br, additional peaks corresponding to Br3s, $3p_{1/2}/3p_{3/2}$ and 3d appear at 257.1, 190.1/184.1 and 70.2 eV, respectively; these signals are absent in the starting material and the bromine adsorption control. In the high resolution bromine spectrum of FLG2-Br (Figure 7.4b), the deconvoluted Br3d peaks at 70.1 and 71.1 eV are characteristic of covalently-bound Br,[215] although a small fraction (~12%) of adsorbed bromine or residual sodium bromide was detected, around 68.5 eV,[209, 304-306] consistent with these species being intercalated between graphene layers. A corresponding C-Br peak at 285.3 eV can be identified in the deconvoluted C1s core-level spectrum of FLG2-Br,[187] but is absent in FLG2, confirming that Br atoms have been covalently attached to the graphene sheets (Figure 7.4d and e). Additional peaks at 286.1 and 286.9 eV are assigned to C-O and C=O, respectively, also present in the starting material. No Br3d peak was detected in the as-received sample (Figure 7.4a) whilst only a trace amount of adsorbed Br_2 was found in

FLG2+Br_2 control (0.1 at% Br) (Figure 7.4c). The XPS data therefore present strong evidence for direct covalent Br attachment in FLG2-Br, consistent with reports in the literature concerning bromine functionalisation of graphite by microwave irradiation[15] or of various CNMs by plasma-chemical treatment.[187, 209, 218] Analysis of the higher resolution data indicates a composition of 0.9 at% covalent Br to 95.6 at% C (and 3.4 at% O) after functionalisation, giving a C/Br of 108 (Table 7.1) and grafting ratio of 6.2%. The relative amount of oxygen and carbon in FLG2-Br or FLG2-Br_2 (95.4 at% C, 4.5 at% O) does not vary substantially compared to FLG2 starting material (96.5 at% C, 3.5 at% O) suggesting that the THF content in both samples is insignificant. The GRs by TGA and XPS are in good agreement, given the differences in surface sensitivity. The number density of bromine calculated from XPS data (3.5×10^{13} cm^{-2}), therefore, also agrees well with that obtained from TGA (5.4×10^{13} cm^{-2}) (see Appendix III for calculations).
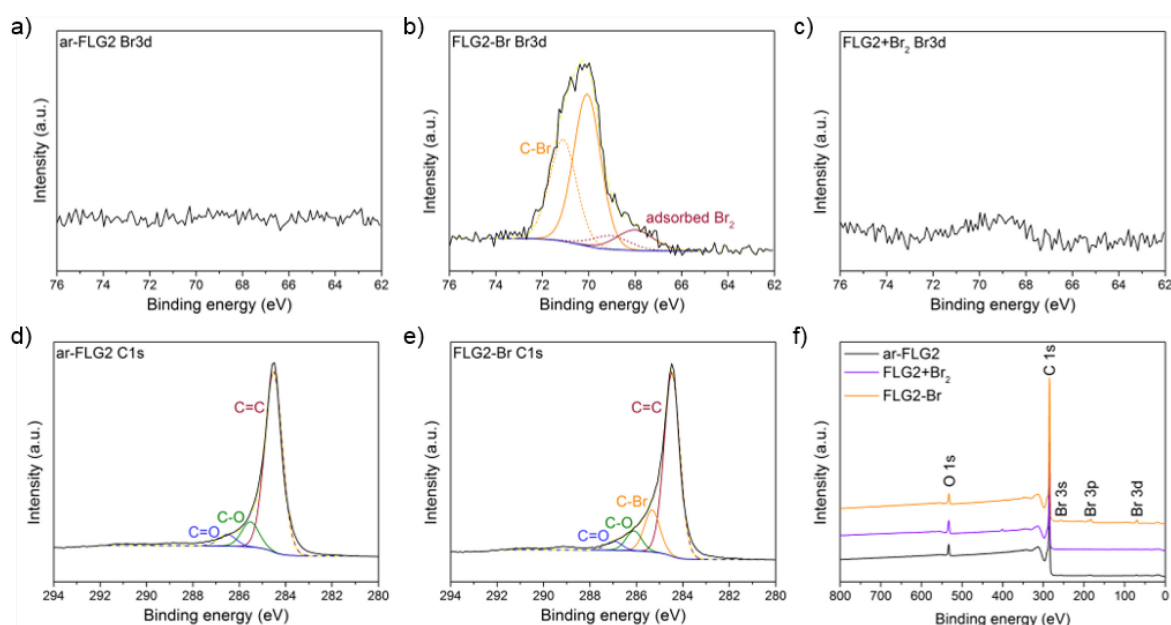
Figure 7.4. Core level Br3d spectrum for a) ar-FLG2, b) FLG2-Br (dashed lines denote $3d_{3/2}$, solid $3d_{5/2}$), and c) FLG2+Br_2; core level C1s spectrum for d) ar-FLG2, and e) FLG2-Br; f) wide survey XPS spectra of ar-FLG2, FLG2+Br_2 and FLG2-Br.

Table 7.1. XPS atomic compositions and C/Br ratios of bromine reactions with FLG.

Sample	at% C	at% O	at% Br	C/Br (TGA)*	C/Br (XPS)*
ar-FLG2	96.5	3.5	-	-	-
FLG2+Br_2	95.4	4.5	0.1	-	-
FLG2-Br	95.6	3.4	0.9	71	108

*Number of graphene basal carbons per grafted bromine addend.

Statistical Raman analysis of the bulk sample shows an I_D/I_G of 0.40±0.03 in the FLG starting material (Figure 7.5a); the large D peak arises from edge scattering,[266] because many flakes are smaller than the laser spot size. For the bromine adsorption control, FLG2+Br_2, the I_D/I_G

ratio (0.40±0.09) remains essentially unchanged, confirming that no bromine functionalisation occurs without reductive treatment (Figure 7.5a). In contrast, I_D/I_G increases to 0.58±0.02 in FLG2-Br (Figure 7.5a) suggesting that bulk covalent functionalisation has indeed occurred.[13, 15] However, the high grafting densities implied by the TGA and XPS data[255, 307] suggest that FLG2-Br falls in the high defect density regime, where the I_D/I_G trend is inverted[267] and the peaks broaden, since the defect spacing should be below the Tuinstra-Koenig limit,[267, 290] if uniformly distributed. FLG2 and its functionalised derivatives do have wider FWHM values (Appendix III, Table III.1) for the D and G bands than those quoted in the literature for graphitic carbon with a low density of defects (typically $\Gamma_D < 30$ cm^{-1} and $\Gamma_G < 14$ cm^{-1});[255, 267] but line broadening in these samples likely occurs due to edge effects and surface oxides, and the crumpled nature of the sheets. The D, G and 2D peaks still have very well-defined lineshapes (Figure 7.5b), and so the samples can be classified within the low defect density regime. The I_D/I_G ratios therefore underestimate the degree of grafting, implying that grafting does not occur uniformly, but rather in clusters nucleating from defects and edges, consistent with alkyl grafting results discussed in Chapter 5. The density of grafted sites ($n_D = 5.0 \times 10^{11}$ cm^{-1}) and C/Br ratio of 765, obtained from the I_D/I_G ratio, diverge from the values obtained by TGA and XPS. This discrepancy is consistent with defect clusters and supported by the apparent lower density of defects seen by Raman spectroscopy, since large areas of the carbon lattice will remain intact, resulting in comparatively little change in the G band intensity relative to the D.
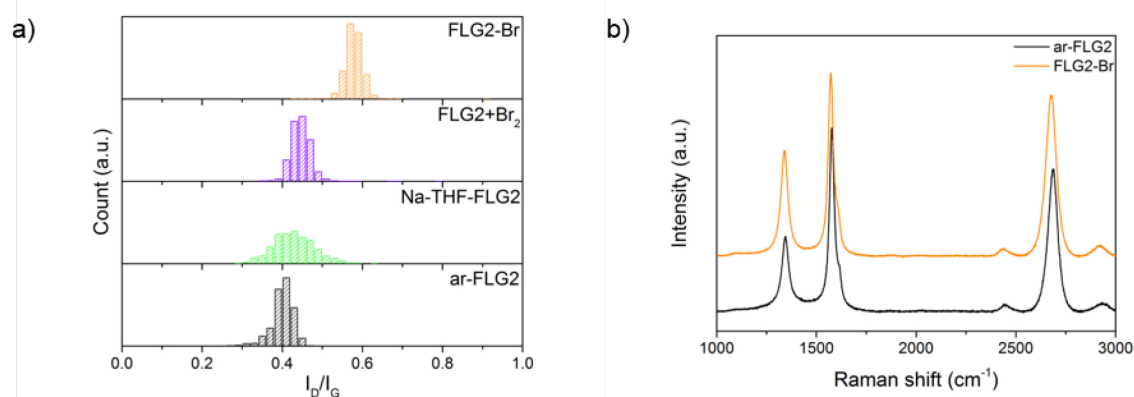
Figure 7.5. a) Raman histograms of I_D/I_G ratio of ar-FLG2, Na-THF-FLG2, FLG2+Br$_2$ and FLG2-Br; b) averaged Raman spectra of ar-FLG2 and FLG2-Br; spectra normalised to the G peak intensity and offset for clarity.

Additional analysis of the D' band at ~1615 cm^{-1} (Figure 7.6) shows an increase in $I_D/I_{D'}$ after functionalisation (from 3.0±0.6 to 3.9±0.4) which is consistent with an increase in the ratio of sp^3 defects to edge-type defects,[270] and therefore indicates that covalent grafting occurs, with retention of lattice connectivity. In FLG2-Br, the distribution width of I_D/I_G ratio remains

essentially unchanged (Figure 7.5a), suggesting that all the flakes in the sample react equally. The 2D peaks indicate the extent of exfoliation and are discussed below (section 7.2.3).
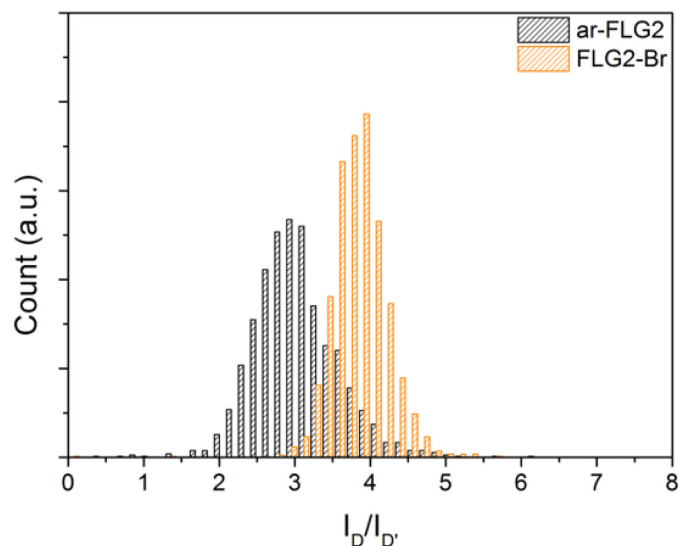
Figure 7.6. Raman histograms of $I_D/I_{D'}$ ratio of ar-FLG2 and FLG2-Br.

7.2. Polymer grafting

Polymer grafting is useful for increasing solubility and compatibility with polymeric matrices (Chapter 2, section 2.3.1). Covalently-bound bromine is attractive as a synthetic handle, and FLG2-Br can act as a useful precursor for further transformations. As discussed in Chapter 6, a 'grafting-to' approach allows control of polymer properties[197] but the steric bulk of the chains limits grafting density. Conversely, surface-initiated anionic polymerisation can achieve densely-grown polymers,[222] but requires rigorously dry reaction conditions to allow full control over the molar mass and dispersity of the grown polymers. An alternative grafting-from route, ATRP, could afford more control over polymer growth in more accessible reaction conditions,[308] whilst retaining a high graft density; therefore FLG2-Br was used as an initiator to grow PMMA chains from the graphene surface (Scheme 7.2 i). In a complementary approach, bromine addends were replaced with polyethylene glycol or hydroxyl groups, in a direct nucleophilic substitution reaction (Scheme 7.2 ii).
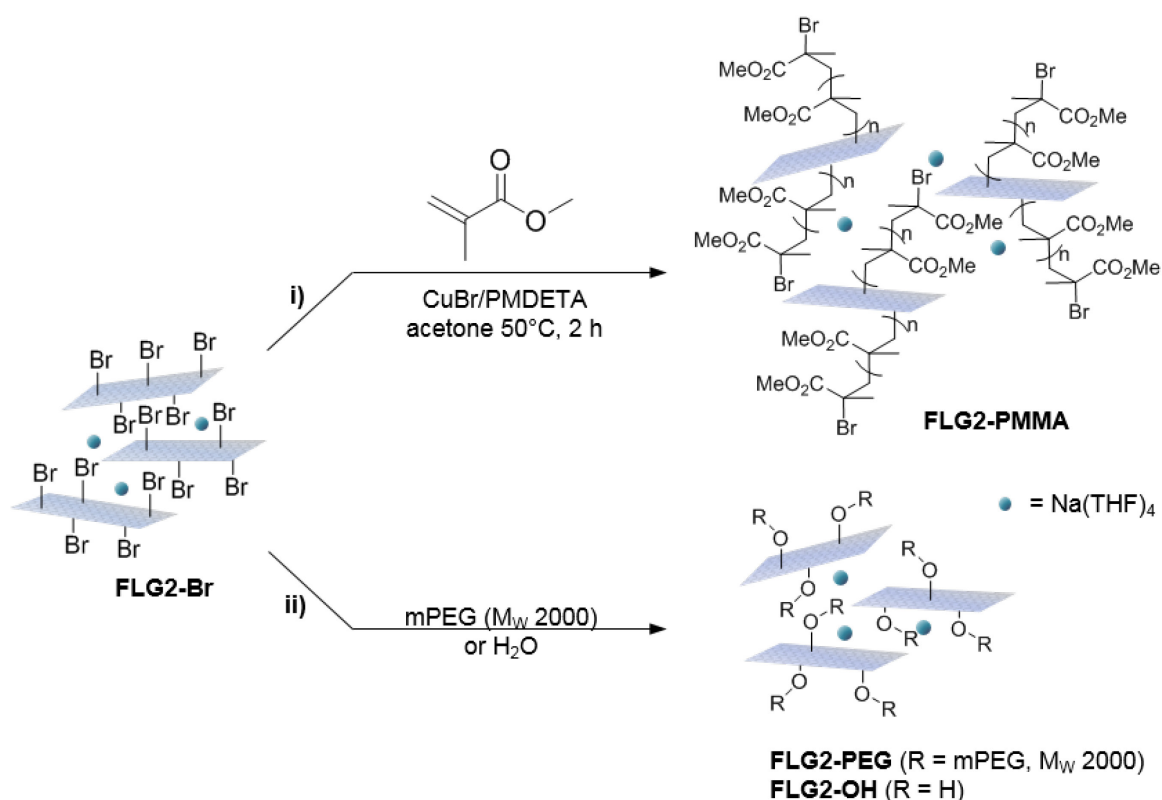
Scheme 7.2. Polymer functionalisation of FLG2-Br: i) synthesis of FLG2-PMMA *via* ATRP; or ii) nucleophilic substitution of FLG2-Br with mPEG or water, yielding FLG2-PEG and FLG2-OH, respectively.

7.2.1. FLG2-Br as a precursor to PMMA-grafted graphene *via* ATRP

Previous examples of ATRP from nanomaterial surfaces include the polymerisation of styrene, methyl methacrylate and glycidyl methacrylate from GO, CNTs and BNNTs.[182, 226, 227, 234-237] In these procedures, bromine-containing initiator molecules are grafted first (usually *via* multi-step reactions), rather than directly attaching an active bromine atom to the surface. PMMA is a well-known ATRP target and has been used as a compatibiliser for various fillers, such as glass fibre[16] and nanoclays,[17] in epoxy resins. FLG2-Br was therefore used as a precursor to obtain PMMA-grafted graphene as both a model system and for practical purposes, providing a useful comparison to the work detailed in Chapter 6. Using FLG2-Br as the initiator molecule and following standard ATRP procedures in the literature, FLG2-PMMA was obtained from the polymerisation of MMA[309] (Scheme 7.2 i). Briefly, under inert conditions, distilled MMA was stirred with CuBr, CuBr$_2$, PMDETA, and FLG2-Br in acetone, at 50 °C for 2 h. FLG2-PMMA was obtained as a black powder after washing with THF and drying under vacuum.

TGA-MS analysis of the product shows an increased mass loss (16.2 wt%), and correspondingly larger grafting ratio (19.5%), compared to FLG2-Br, in the range 200 to 550 °C (Figure 7.7a); the accompanying mass fragments correspond to PMMA polymer,

including m/z 41 ($-CH_2C(CH_3)-^+$), 59 ($-COOCH_3^+$), 69 ($-CH_2C(CH_3)(CO)-^+$), and 100 ($-CH_2C(CH_3)(COOCH_3)-^+$) (Figure 7.7b). This weight loss temperature is also consistent with the expected thermal degradation of PMMA.[227] A control reaction mixing MMA monomer with uncharged FLG (FLG2+MMA) shows a small mass loss of 7.0 wt% in the same temperature range which may be attributed to residual solvent trapped between the graphene layers (Figure 7.7). The fragment m/z 41 is common to PMMA and THF; since the mass spectrum shows no other fragments corresponding to PMMA, this particular m/z peak may be attributed to THF. Any polymer detected in FLG2-PMMA is therefore assumed to be covalently grafted.
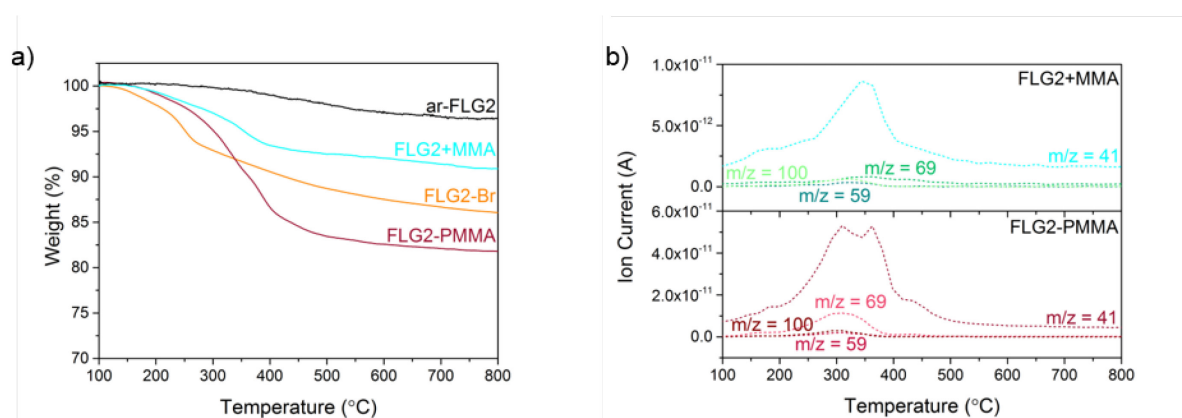
Figure 7.7. a) TGA profiles of ar-FLG2, FLG2+MMA, FLG2-Br and FLG2-PMMA, and b) corresponding MS signals for FLG2+MMA and FLG2-PMMA; m/z 41 ($-CH_2C(CH_3)-^+$) or ($-CHCH_2CH_2-^+$), 59 ($-COOCH_3^+$), 69 ($-CH_2C(CH_3)(CO)-^+$), 100 ($-CH_2C(CH_3)(COOCH_3)-^+$).

XPS data for FLG2-PMMA show an increase in oxygen content compared with ar-FLG2 and FLG2-Br (Figure 7.8), with a composition of 92.6 at% C and 6.9 at% O (Table 7.2); the bromine content decreases to 0.5 at% from 0.9 at% in FLG2-Br. From these values, assuming that approximately half the bromine addends served as initiators in the ATRP reaction, the polymer chains are estimated to have an average molar mass in the range 370 to 590 Da, based on the number of bromine initiation sites obtained from TGA and XPS (C/Br = 71 and 108, respectively) (see section 7.1.2, and Appendix III for calculations). The carbon and oxygen contents from XPS are in good agreement with calculated compositional values based on C/PMMA = 250, M_n ~590 g mol^{-1} (92.7 at% C, 6.8 at% O and 0.4 at% Br); the estimated grafting ratio from XPS is 21.4%, close to the value obtained by TGA (19.5%). These calculated compositional values from XPS suggest that no THF remains; TGA-MS also shows only a trace amount of THF in FLG2-PMMA. The introduction of polymer on the graphene surface likely preserves an open pathway between layers, allowing diffusion of sodium and THF during the washing steps.
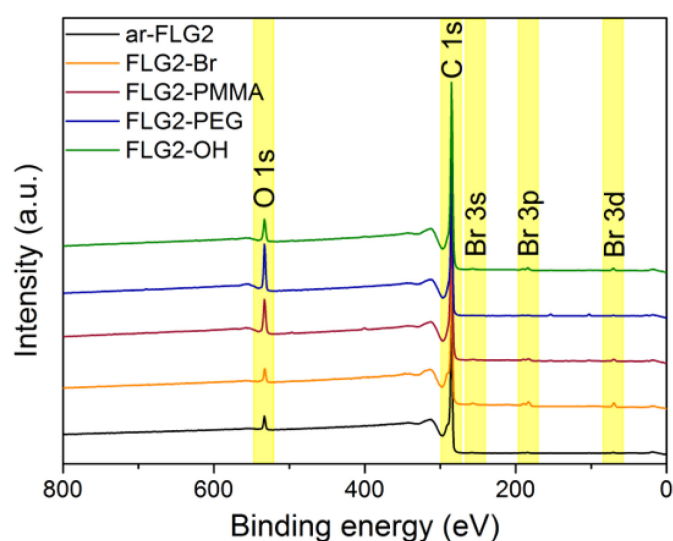
Figure 7.8. Wide survey XPS spectra of ar-FLG2, FLG2-Br, FLG2-PMMA, FLG2-PEG and FLG2-OH. The increase in the O1s peak for FLG2-PMMA, FLG2-PEG and FLG2-OH is consistent with subsequent grafting reactions.

Table 7.2. XPS atomic compositions and grafting ratios of functionalised FLGs.

Sample	at% C	at% O	at% Br	GR (TGA)*	GR (XPS)*
ar-FLG2	96.5	3.5	-	-	-
FLG2-Br	95.6	3.4	0.9	9.3	6.2
FLG2-PMMA	92.6	6.9	0.5	19.5	21.4
FLG2-PEG	90.9	9.0	0.1	23.8	26.2
FLG2-OH	94.7	4.9	0.4	6.5	3.8

*Grafting moiety/FLG mass ratios, %. For details of these calculations, see Appendix III.

Raman spectra of FLG2-PMMA show that peak width and definition remain the same after reaction (Appendix III, Figure III.1). Statistical analysis of the FLG2-PMMA product indicates that the initial density of defects in FLG2-Br is hardly changed (I_D/I_G 0.58±0.02 to 0.53±0.03) after PMMA growth from the surface (Figure 7.9); therefore, no additional sp^3 centres were introduced during this part of the reaction sequence. $I_D/I_{D'}$ is also unchanged (4.0±0.6), confirming no increase in sp^3 to edge sites (Appendix III, Table III.1). In the control FLG2+MMA experiment, using only FLG2 as the ATRP initiator, the I_D/I_G ratio (0.43±0.03) is essentially unchanged compared to ar-FLG2, and is in agreement with the TGA results that no MMA is introduced on the graphene surface. This result suggests that the reaction does not take place on the original FLG surface, and demonstrates that brominated sites are necessary to initiate polymerisation.
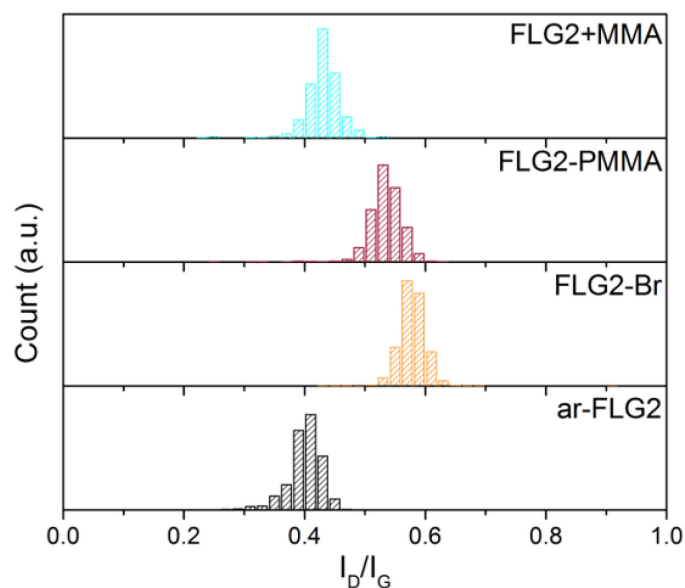
Figure 7.9. Raman histograms of I_D/I_G ratio of ar-FLG2, FLG2-Br, FLG2-PMMA and FLG2+MMA.

7.2.2. Nucleophilic substitution of FLG2-Br

An alternative route to polymer-grafted graphene, and further proof of the versatility of bromine functionalisation, is provided by nucleophilic substitution of the bromine addends with polyethylene glycol (Scheme 7.2 ii). To obtain the PEG-substituted product, FLG2-Br was dispersed in dry THF and dichloromethane by brief and mild bath sonication. After addition of mPEG (M_w 2000 g mol^{-1}), the suspension was stirred at 40 °C for 2.5 h, and FLG2-PEG was obtained after filtering and washing with THF, water and ethanol, and drying under vacuum.

The weight loss during TGA pyrolysis of FLG2-PEG in the range 300-500 °C is accompanied by mass fragments which can be attributed to mPEG (m/z 15 ($-CH_3^+$), 31 ($-OCH_3^+$), 44 ($-CH_2CH_2O-^+$)), confirming successful introduction of PEG on the graphene surface (Figure 7.10). No significant weight loss or mPEG mass fragments were detected in the physisorption control reaction FLG2+PEG, so it can be assumed that any polymer present in FLG2-PEG is covalently grafted.

The mass loss of 18.7 wt% implies an incomplete reaction of ~1 in 6 bromine addends (based on C/Br from XPS); this partial substitution by mPEG may be explained by the steric bulk of the polymer chains. A large increase in oxygen content can be seen by XPS (Figure 7.8); C and O atomic percentages obtained by XPS (Table 7.2) are consistent with the proposed substitution of 1 in 6 addends, although the bromine content is lower than expected. This lower Br content could potentially result from the washing process; water introduced to remove residual ungrafted mPEG chains could substitute remaining bromine groups, since the small

hydroxyl addends can access sites blocked to larger PEG polymers. However, OH fragments are not detected by TGA-MS, possibly because of the insignificant amount compared to PEG. The grafting ratio from TGA (23.8%) is in good agreement with that implied by the XPS data (26.2%).
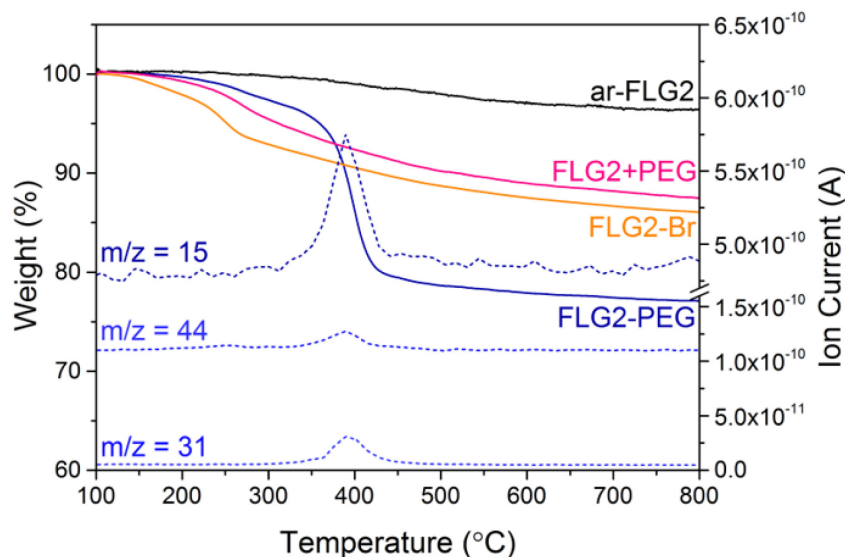
Figure 7.10. TGA-MS profile of ar-FLG2, FLG2-Br, FLG2-PEG and FLG+PEG, and corresponding m/z 15 (-CH$_3^+$), 31 (-OCH$_3^+$), 44 (-CH$_2$CH$_2$O^{-+}) for FLG2-PEG.

To explore whether substitution efficiency was affected by nucleophile size, FLG2-Br was reacted with water under the same conditions for PEG substitution, to obtain the hydroxyl-functionalised product FLG2-OH. XPS data show that the reaction is more effective in this case, achieving a greater degree of substitution with over half (0.6) of the bromine addends replaced with hydroxyl groups (Table 7.2). This observation is unsurprising given the difference in size between the two nucleophiles. The reduced TGA weight loss (6.1 wt%) is also consistent with the substitution of this proportion of addends (see Appendix III for calculations). Hydroxyl groups and water (m/z 17, 18) are detected by TGA-MS (Figure 7.11), as well as some residual solvent. However, bromine fragments are not seen, possibly because the low concentration cannot be detected by the MS; even in FLG2-Br, the bromine m/z fragments give only a very weak signal.

As is the case for FLG2-PMMA, in the Raman spectra for the PEG- and OH-substituted products, the I_D/I_G ratios of 0.56±0.03 and 0.57±0.09 (Figure 7.12), respectively, indicate that no further defects are introduced during subsequent reaction, and that substitution occurs exclusively at existing grafted sites. Unchanged $I_D/I_{D'}$ values (3.9±0.6 for FLG2-PEG and 4.0±1.3 for FLG2-OH) further support this assertion. Overall, the TGA, Raman and XPS data

indicate that successful growth of PMMA by ATRP, or nucleophilic substitution, illustrated by mPEG and water, can be achieved from brominated FLG, without the creation of further defects.
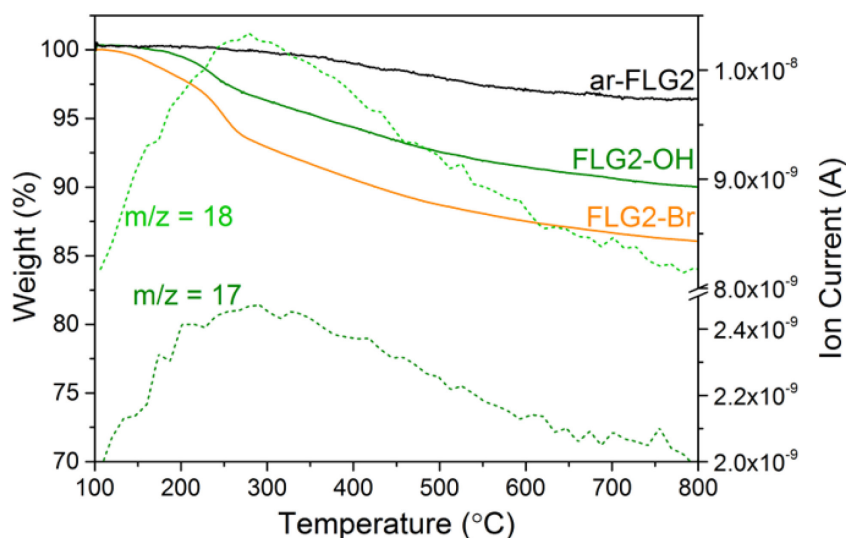
Figure 7.11. TGA-MS profile of ar-FLG2, FLG2-Br and FLG2-OH, and corresponding *m/z* 17 (-OH$^+$), 18 (H$_2$O$^+$).
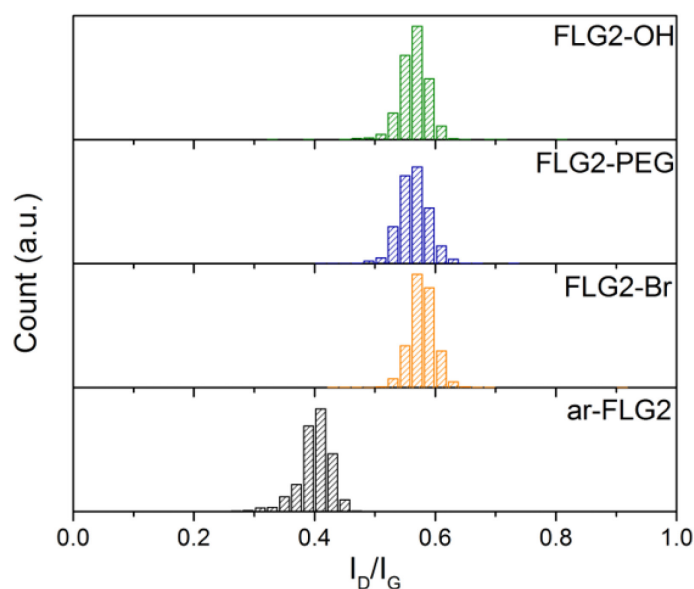
Figure 7.12. Raman histograms of I$_D$/I$_G$ ratio of ar-FLG2, FLG2-Br, FLG2-PEG and FLG2-OH.

7.2.3. Exfoliation and dispersion

After bromine grafting, the I$_{2D}$/I$_G$ ratio increases only slightly (from 0.97±0.04 to 1.02±0.05), since bromine addends are not large and do not significantly aid further exfoliation (Figure

7.13a). Following PMMA functionalisation, this value increases again to 1.06±0.05 suggesting that as ATRP progresses, graphene layers are pushed apart and prevented from restacking and aggregation by grafted polymer chains, similar to the effect for anionic polymerisation (Chapter 6, section 6.1.3). An accompanying decrease in Γ_{2D} (Figure 7.13b) also implies that the grafted samples are more exfoliated than the starting material.[310] In FLG2-PEG, there is no significant change in either I_{2D}/I_G or Γ_{2D} (Figure 7.13) from FLG2-Br; in this 'grafting-to' reaction the large polymer chains cannot diffuse through the interlayer galleries so easily and therefore only substitute the more readily accessible bromine sites. As a result, no further exfoliation occurs, and the I_{2D}/I_G ratio remains unchanged. The same exfoliation trends were observed for the grafting-to and grafting-from products directly on graphenide (Chapter 6, section 6.1). There is little change in I_{2D}/I_G or Γ_{2D} in FLG2-OH, despite the higher degree of substitution; hydroxyl addends are small and do not significantly expand the layers or prevent restacking after drying.
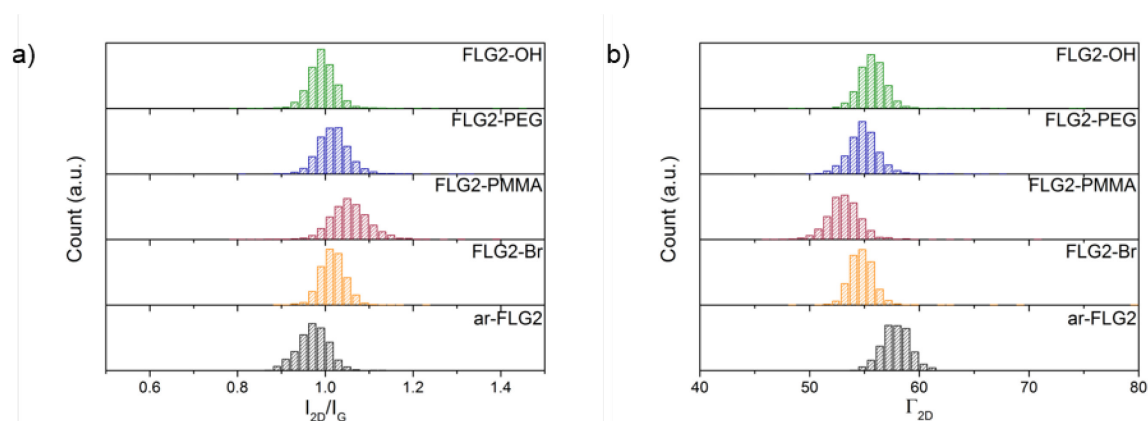
Figure 7.13. Raman histograms of a) I_{2D}/I_G ratio, and b) Γ_{2D}, of ar-FLG2, FLG2-Br, FLG2-PMMA, FLG2-PEG and FLG2-OH.

TEM images of FLG2-PMMA and FLG2-PEG reveal little significant difference in exfoliation after grafting (Figure 7.14). The crumpled nature of the sheets can be seen, and the morphology and dimensions of the layers remain unaffected, compared with the starting material (Figure 7.1b). These results confirm that neither the bromination procedure, or either subsequent polymer-grafting process damaged the graphene sheets.
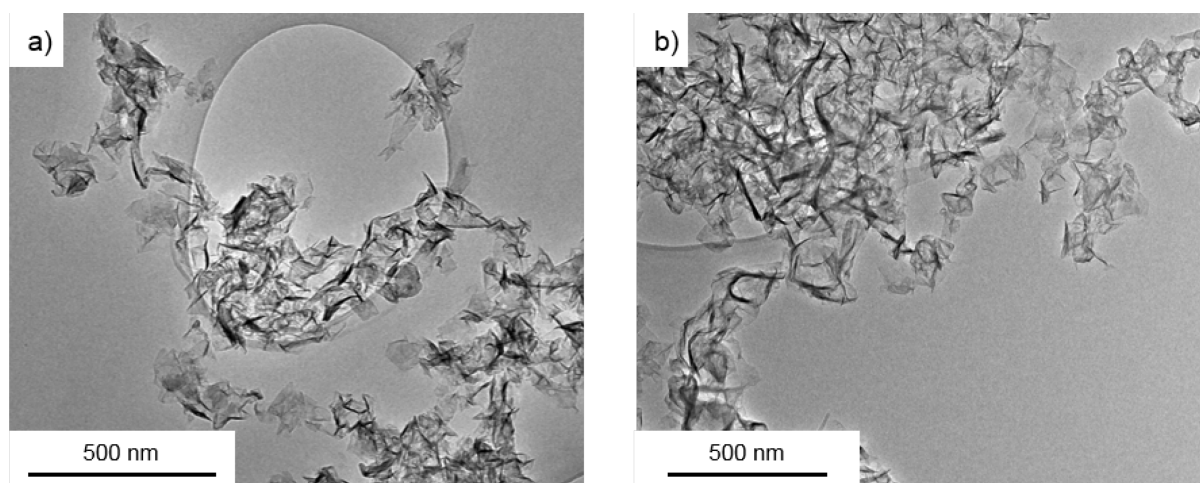
Figure 7.14. TEM images of a) FLG2-PMMA, and b) FLG2-PEG.

The dispersibility of the polymer-grafted graphenes was measured by UV-vis absorbance (Appendix III, Figure III.2). Covalent grafting significantly improved the dispersibility of the material, with FLG2-PMMA reaching a concentration of 200 $\mu g\ mL^{-1}$ in acetone, and FLG2-PEG 255 $\mu g\ mL^{-1}$ in ethanol. In the case of FLG2-PMMA, even the addition of low molecular weight polymer chains was enough to increase dispersibility six-fold in acetone. FLG2-PEG was three and a half times more soluble than FLG2 in ethanol; despite a low grafting density, the longer mPEG chains were relatively effective in stabilising the graphene sheets. Hydroxyl groups increased the solubility of FLG2 in water, from 8.51 $\mu g\ mL^{-1}$ to 96.4 $\mu g\ mL^{-1}$ (Table 7.3).

Table 7.3. Calculated concentrations of ar-FLG2 and polymer-grafted derivatives in acetone, ethanol and water, obtained from UV/vis absorption spectra.

Sample	Solvent	Concentration ($\mu g\ mL^{-1}$)*
ar-FLG2	acetone	31.8
FLG2-PMMA	acetone	200
ar-FLG2	ethanol	82.0
FLG2-PEG	ethanol	255
ar-FLG2	water	8.51
FLG2-OH	water	96.4

*The absorption at 660 nm and the extinction coefficient for dispersed graphene in solution (ε_{660} = 2460 L $g^{-1}\ m^{-1}$)[52] were used to estimate the concentrations of the different solutions using the Beer-Lambert law.

7.3. Summary

Brominated graphene was synthesised by reacting exfoliated Na-based GICs with bromine. In contrast to harsher methods, this reductive approach results only in a low concentration of sp^3 defects, localised in clusters, and the underlying connectivity of the carbon network is therefore retained.

The brominated FLG serves as a convenient and versatile precursor to modified graphenes. The FLG2-Br can act as an initiator in the polymerisation of MMA by ATRP, resulting in PMMA-grafted graphene. FLG2-PMMA showed improved exfoliation and dispersibility in acetone, with the addition of only low molecular weight polymers; although the grafting ratio of PMMA achieved by this method is far lower than by anionic polymerisation (19.5% compared with 126.5%, Chapter 6, section 6.1.2.2), optimising polymerisation conditions and careful selection of other polymer targets could further increase dispersibility in different solvents. Furthermore, in contrast to direct anionic polymerisation from reduced graphite/graphenides, this methodology offers greater versatility with a wide choice of monomers including those that may be unstable to graphenide, for example glycidyl methacrylate or aminoethyl methacrylate.

In addition, the bromine addends may easily undergo nucleophilic substitutions, as illustrated by reactions with mPEG and water, without introducing any additional sp^3 centres on the carbon framework. A higher grafting ratio was achieved for mPEG grafting on FLG2-Br (23.8%) than for direct reaction with of graphenide with PMMA-Br (20.3%, Chapter 6, section 6.1.1.2), and this method may be useful for attaching defined-length polymers with functionalities which are sensitive to reducing conditions. In this generalised reaction, brominated graphenes represent versatile, air-stable starting materials for the generation of grafted graphenes with a wide variety of functional moieties, affording the opportunity to create tailored materials with specific properties.

8. Conclusions and outlook

8.1. Overview

The work presented in this thesis illustrates the use of a simple reductive functionalisation methodology as a means of exfoliating and covalently modifying bulk graphite precursors, to produce functionalised GRMs with significantly improved dispersibility in common organic solvents. Sodium naphthalide can reduce and exfoliate bulk graphite in THF; these graphenide species were successfully functionalised by reaction with 1-bromododecane to form alkyl-grafted graphene, resulting in only a small number of defects introduced on the carbon lattice, as determined by Raman spectroscopy. The method is non-damaging, and also showed successful grafting in two other solvent systems, DMAc and DME. Surprisingly, given its effectiveness at stabilising CNTs in solution, very little exfoliation was achieved in DMAc, attributed to the high stability of the Na-DMAc-GIC structure. Conversely, reductive treatment in DME resulted in a high degree of functionalisation (C/R = 209) and exfoliation, although the unfunctionalised control reaction suggested that inadvertent functionalisation by solvent also occurred. The versatility of the method was demonstrated by application to five different graphite starting materials, of varying flake size and morphology: large flake graphite, natural flake graphite, graphite platelets, graphite nanofibres, and few-layer graphene. C/R varied between 55 and 1246, generally decreasing with flake size. The trend in grafting density shows a linear relation with lateral flake size; these results indicate that functionalisation is edge-dominated, since for basal plane grafting the electrophile must first intercalate the graphene layers, resulting in functionalisation occurring more readily near the more accessible edge sites. Further confirmation was obtained from mapping analysis of the Raman I_D/I_G and $I_D/I_{D'}$ ratios, which showed that grafting occurred predominantly around flake edges, supporting the proposed edge-initiated mechanism of grafting. Generally, grafting of alkyl moieties increased the degree of exfoliation, and the solubility was also increased, far more significantly for the smaller graphite materials, in line with the grafting ratio.

The functionalisation methodology was extended to the grafting of PMMA polymer on FLG, comparing the effectiveness of direct reaction with various molecular weight PMMA-Br polymers, and graphenide-initiated anionic polymerisation of MMA with different loadings. In the grafting-to approach, the steric bulk of the PMMA chains prevented close grafting (C/PMMA 2055-6615), resulting in GRs of 12.6-20.3%, whereas by the grafting-from method, the smaller monomer size allowed a much higher grafting density (C/PMMA 149) to be

reached, with different grafting ratios obtained by varying the monomer loading. The grafting ratios (44.6-126.5%) achieved by the grafting-from route exceed those observed for the grafting-to products, and the presence of more polymer is also reflected in the exceptional solubility of these materials, up to 920 µg mL^{-1} in acetone. Application of the same grafting protocols to natural flake graphite yielded similar results, with a higher grafting ratio, graft density, and solubility obtained for the grafting-from product. In comparison to functionalisation of FLG, the grafting density is much lower in NFG, in line with the alkyl grafting trend observed on different flake sizes. For both flake sizes, the grafting density achieved by reaction with PMMA-Br was lower than that observed by analogous reaction with 1-bromododecane, indicating that steric bulk plays an important role in governing grafting density. Despite the lower grafting densities in the polymer-functionalised materials, the solubilities obtained were significantly improved, showing that the much longer chains could greatly stabilise sheets in solution. For functionalised FLG and NFG, greater exfoliation was observed for the grafting-from products, confirming that anionic polymerisation initiated from the graphenide surface could effectively expand the interlayer spaces. A full grafting comparison of different molecular weight PMMA polymers, and different initial MMA loadings on natural flake graphite would be useful for direct comparison with grafting on smaller flake FLG.

Bromination of FLG was also achieved by reductive treatment and subsequent reaction with bromine. In contrast to harsher literature methods, bromination by this route results in only in a low concentration of sp^3 defects (C/Br 108). Raman analysis confirms that the underlying connectivity of the carbon network is retained, suggesting that functionalisation occurs in clusters. The brominated sites are a useful reactive handle for subsequent chemical modifications. FLG-Br was used as an initiator for polymerisation of MMA by ATRP; the polymers were estimated to have M_n ~600 g mol^{-1}, but even at this low molecular weight the resulting PMMA-grafted graphene showed improved exfoliation and dispersibility in acetone. In addition, the bromine addends underwent nucleophilic substitution, illustrated by reactions with mPEG and water. The degree of substitution was governed by the steric bulk of the nucleophile with OH substitution occurring more effectively than mPEG, similar to the effects seen for PMMA-Br grafting. In both cases, the solubility was greatly improved. Optimisation of the polymerisation conditions, including concentration, temperature, and reaction time, could increase the grafting ratio, and hence, further improve dispersibility in different solvents. Brominated graphene therefore shows scope as a versatile, air-stable precursor to a variety of modified graphenes.

Residual solvent remained in all samples, coordinated to sodium. In the larger flakes, areas of GIC structure remained; the amount of residual GIC varied with the solvent used, with

DMAc, especially, forming very air-stable GIC structures. A method of quantification of grafting and residual solvent was developed from TGA-MS data; analysis of solvent trapping is little discussed in the literature, but it is an important factor in determining true grafting yields. In general, grafting of addends reduced the amount of solvent remaining between the graphene layers by preventing close restacking, and smaller flakes trapped less solvent. Further study of the work up and drying procedures is needed to ensure full solvent removal.

In summary, the versatility of the reductive functionalisation method has been illustrated by reactions of graphenide with a variety of electrophiles. The graphitic starting material has a strong influence on the degree of grafting and residual solvent, with smaller flakes achieving a higher degree of functionalisation, due to the higher edge:basal carbon ratio, and generally trapping less solvent. Functionalisation by both grafting-to and grafting-from approaches may be exploited, with varying outcomes regarding polymer characteristics, grafting density and degree of exfoliation. Introduction of bromine species onto the graphenide surface further extends the range of chemical modifications available. These conclusions will have important implications when considering these graphene derivatives for subsequent applications. Sheet size and quality, for example, will be important for electrical conductivity, and therefore edge-functionalised LFG may benefit these applications; on the other hand, mechanical reinforcement of composites depends strongly on interfacial interactions, and thus a smaller, but highly-functionalised graphene may be preferable. Tuning the degree and type of functionality, and starting graphite, creates a broad panel of modified graphenes which may benefit a vast range of functional materials.

8.2. Future work

Solvent trapping and incomplete charge quenching can be mitigated to a certain extent by functionalisation, but both remain a fundamental issue of interest. Two recent reports investigating quenching in graphenides found that complete charge removal could be achieved by treatment with the solvent benzonitrile,[262] or with discharging reagents such as iodine, fullerene, and triphenylmethyl chloride.[261] These studies used the binary intercalation compound KC_8, dispersed in benzonitrile, or NMP, respectively. For the ternary compounds described in this thesis, these methods may provide a possible route to full discharging and sodium-THF removal from the interlayer galleries of the Na-THF-GICs. A slower work up procedure may also encourage diffusion of sodium ions out of the interlayer galleries, which may be another modification worth exploring. Interestingly, grafting of PMMA did not have a very significant effect on reducing the residual THF compared with alkyl addends, which may be due to the strong affinity between THF and PMMA; solvent exchange methods could be a useful means of removing residual THF, allowing diffusion of THF molecules from out of the

interlayer galleries into a solvent which has a good miscibility with THF but a poor affinity for graphene. The inaccessibility of the carbon basal planes resulting in predominantly edge grafting, and the small number of single layers in solution, suggests that less spontaneous exfoliation occurs in solution than previously observed.[13] Interestingly, the single layer flakes identified by Raman spectroscopy generally show a higher degree of functionalisation than the bulk sample, in line with other studies confirming higher reactivity of single layers compared with bulk graphite.[191, 248] These results suggest that functionalisation is effective for individualised layers in solution, but for less exfoliated parts of the sample, grafting can only occur at the more accessible edge regions. Therefore, re-optimisation of the charging conditions should be carried out, to maximise the number of dispersed graphenide sheets prior to functionalisation. It is likely that for each graphite starting material, the optimal conditions should vary, so a systematic study is required for all graphite precursors.

The exact mechanisms of grafting also remain an interesting topic of study. In the larger flake graphites, it is worth noting the two discrete temperatures at which decomposition of covalent addends occurs, and their coincidence with solvent loss. Whilst it was shown that alkyl chains were covalently grafted, and solvent is physisorbed, (by comparison of the Raman I_D/I_G ratios of the functionalised sample and the quenched control,) Raman spectroscopy of the functionalised materials whilst heating incrementally to 800 °C may provide insight into the temperature at which grafted moieties and solvent are lost, by monitoring the D and 2D peaks, respectively. It may be that whilst detachment of alkyl addends occurs at a certain temperature independent of solvent loss, the fragments remain trapped within pockets also containing solvent, and can only escape when a critical pressure/temperature is reached. The difference in decomposition temperature may arise from different grafting environments in the flake; spatial mapping whilst heating could be useful to determine the grafting locations.

To prove unequivocally that functionalisation is predominantly edge-initiated, grafting of a small molecule containing a thiol or sulfide would enable coordination of Au nanoparticles, subsequently allowing imaging of the grafting locations by TEM. Similar mapping may be achieved by EDX of other detectable species. Preliminary work into sulfide grafting has been conducted on FLG, showing applicability of the grafting method to these molecules (Appendix IV, Figure IV.1).

While covalent modification of bulk graphite is useful for large-scale processing, application of the reductive functionalisation method to smaller, well-defined polyaromatic systems, as graphene models, could provide insight into the grafting mechanism and location. Smaller molecules such as hexabenzocoronene ($C_{42}H_{18}$) ranging up to $C_{222}H_{42}$ (Figure 8.1), with a finite number of carbon environments, allows access to analytical techniques such as NMR to

provide definitive identification of grafting sites. As initial work, HBC was first synthesised following a literature protocol,[311] and then reductively functionalised by charging with sodium naphthalide in THF (applying the same charge ratio and concentration as before, almost certainly not the optimum conditions). Preliminary characterisation by MS indicates a mixture of grafting products (Appendix IV, Figure IV.2). Further separation and analysis should provide information regarding edge versus basal plane grafting. In addition, HBC can be used as a model system for a variety of electrophiles; for example, whilst alkylation or hydrogenation might proceed *via* a Birch-type reaction at the molecule edges, electron transfer from the basal plane could be the initiation mechanism for anionic polymerisation of vinyl monomers. NMR analysis of the products may be useful in determining exactly how the reactions proceed, and by extension, the specific reactivity of graphenide towards these different reagents.

$C_{42}H_{18}$ $C_{96}H_{24}$ $C_{222}H_{42}$
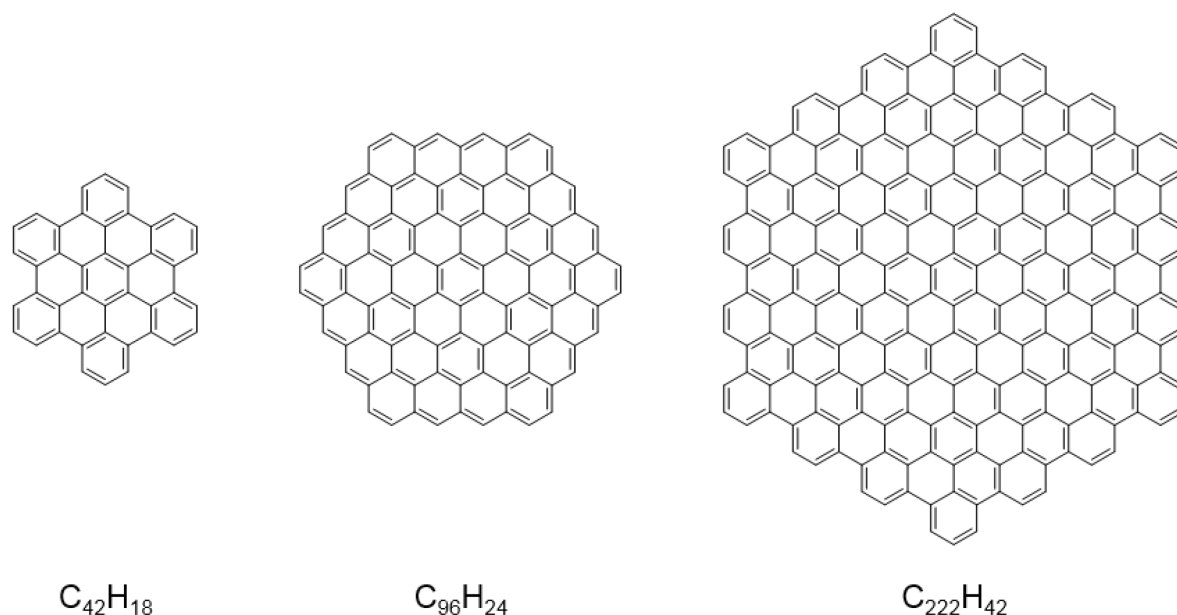
Figure 8.1. Large polyaromatic molecules as model graphene systems.

In the larger graphite starting materials, it may be possible to increase the degree of grafting and exfoliation by repeating the charging and functionalisation methodology in cycles, until the desired level of modification is reached. This cycling has been applied to graphene previously, with alkyl grafting;[244] extension to polymer grafting may be of particular interest. Furthermore, Raman mapping of the materials after each cycle could provide insight into propagation of grafting sites, to see whether the grafting 'edge' moves gradually inwards on the flake in a uniform way, which would be a useful study in conjunction with the studies discussed above.

The grafting-to and grafting-from approaches for polymer functionalisation should be similarly applicable to the other graphite precursors; additionally, selection of other polymer targets would allow tunable solubility in various organic solvents. To obtain the best exfoliation results,

grafting-from, by both anionic polymerisation and ATRP, is the more promising approach. To better determine the number of initiator sites and the molar mass of the resulting chains, the polymers could be tagged with detectable end groups, for example, with a pyrene-containing molecule which may be detected by fluorescence spectroscopy, or a heteroatom such as sulfur, which can easily be quantified by XPS measurements. These detectable groups would in principle allow the mapping of functional sites, although consideration of the termination mechanism would first be required. There is potential to introduce many useful functionalities by these methods, including amine species or epoxide groups, particularly relevant in epoxy composite applications where these reactive moieties would enable crosslinking in the matrix. Potential monomers of interest include glycidyl methacrylate and aminoethyl methacrylate, which may be grafted directly by ATRP, although by anionic polymerisation sensitive groups must first be protected.

In principle, bromination of all the different graphite precursors should be possible, although the formation of stable bromine GICs in the larger flakes may complicate straightforward characterisation of covalent grafting. Preliminary work on bromination of natural flake graphite shows that bromine can be covalently introduced, although a large amount of adsorbed Br_2 detected by XPS is difficult to remove, requiring extensive washing (Appendix IV, Figure IV.3). Finally, this range of modified graphenes should be incorporated into epoxy resins to investigate the effects of flake size, exfoliation, polymer functionality and loading on mechanical reinforcement in epoxy composites.

8.3. Concluding remarks

Graphene has survived the hype surrounding its discovery and proved to be an enduring field of interest, on both a fundamental and practical level. While the quest for perfect graphene is ongoing, many of the graphene products available already benefit a variety of applications. Covalently-grafted graphene is one example where modification can reduce the requirements on graphene flake size and quality. The grafting strategies and resulting functionalised graphenes described in this thesis contribute further understanding into the chemistry and reactivity of graphene, and could find use in many different fields, depending on the properties required; indeed, the methodologies discussed are not limited to graphene but can be applied to other nanomaterials of interest. The ability to introduce a wide variety of polymers and copolymers on graphene without destruction of the carbon framework, and therefore intrinsic properties, has significant potential to benefit many existing and emerging technologies.

References

1. K. S. Novoselov, V. I. Falko, L. Colombo, P. R. Gellert, M. G. Schwab and K. Kim, *Nature*, 2012, **490**, 192-200.
2. M. Cai, D. Thorpe, D. H. Adamson and H. C. Schniepp, *Journal of Materials Chemistry*, 2012, **22**, 24992-25002.
3. A. Ciesielski and P. Samori, *Chemical Society Reviews*, 2014, **43**, 381-398.
4. R. S. Edwards and K. S. Coleman, *Nanoscale*, 2013, **5**, 38-51.
5. T. Gatti, N. Vicentini, M. Mba and E. Menna, *European Journal of Organic Chemistry*, 2016, **2016**, 1071-1090.
6. V. Mittal, *Macromolecular Materials and Engineering*, 2014, **299**, 906-931.
7. C. Valles, A. M. Abdelkader, R. J. Young and I. A. Kinloch, *Faraday Discussions*, 2014, **173**, 379-390.
8. L. Rodriguez-Perez, M. a. A. Herranz and N. Martin, *Chemical Communications*, 2013, **49**, 3721-3735.
9. I. A. Vacchi, C. Ménard-Moyon and A. Bianco, *Physical Sciences Reviews*, 2017, **2**.
10. V. Georgakilas, M. Otyepka, A. B. Bourlinos, V. Chandra, N. Kim, K. C. Kemp, P. Hobza, R. Zboril and K. S. Kim, *Chemical Reviews*, 2012, **112**, 6156-6214.
11. T. Lin, W.-D. Zhang, J. Huang and C. He, *The Journal of Physical Chemistry B*, 2005, **109**, 13755-13760.
12. K. S. Novoselov, A. K. Geim, S. V. Morozov, D. Jiang, Y. Zhang, S. V. Dubonos, I. V. Grigorieva and A. A. Firsov, *Science*, 2004, **306**, 666-669.
13. T. Morishita, A. J. Clancy and M. S. P. Shaffer, *Journal of Materials Chemistry A*, 2014, **2**, 15022-15028.
14. R. A. Schäfer, D. Dasler, U. Mundloch, F. Hauke and A. Hirsch, *Journal of the American Chemical Society*, 2016, **138**, 1647-1652.
15. K. C. Knirsch, J. M. Englert, C. Dotzer, F. Hauke and A. Hirsch, *Chemical Communications*, 2013, **49**, 10811-10813.
16. D. Olmos, K. Bagdi, J. Mózcó, B. Pukánszky and J. González-Benito, *Journal of Colloid and Interface Science*, 2011, **360**, 289-299.
17. M. Hernandez, B. Sixou, J. Duchet and H. Sautereau, *Polymer*, 2007, **48**, 4075-4086.
18. H. W. Kroto, J. R. Heath, S. C. O'Brien, R. F. Curl and R. E. Smalley, *Nature*, 1985, **318**, 162-163.
19. R. Taylor, J. P. Hare, A. a. K. Abdul-Sada and H. W. Kroto, *Journal of the Chemical Society, Chemical Communications*, 1990, 1423-1425.
20. F. H. Hennrich, R. H. Michel, A. Fischer, S. Richard-Schneider, S. Gilb, M. M. Kappes, D. Fuchs, M. Bürk, K. Kobayashi and S. Nagase, *Angewandte Chemie International Edition*, 1996, **35**, 1732-1734.
21. S. Iijima, *Nature*, 1991, **354**, 56-58.
22. S. Iijima and T. Ichihashi, *Nature*, 1993, **363**, 603-605.
23. A. Bianco, H.-M. Cheng, T. Enoki, Y. Gogotsi, R. H. Hurt, N. Koratkar, T. Kyotani, M. Monthioux, C. R. Park, J. M. D. Tascon and J. Zhang, *Carbon*, 2013, **65**, 1-6.
24. X. Cui, C. Zhang, R. Hao and Y. Hou, *Nanoscale*, 2011, **3**, 2118-2126.
25. I. Suarez-Martinez, N. Grobert and C. P. Ewels, *Carbon*, 2012, **50**, 741-747.
26. S. Eigler and A. Hirsch, *Angewandte Chemie International Edition*, 2014, **53**, 7720-7738.
27. Q. Tang, Z. Zhou and Z. Chen, *Nanoscale*, 2013, **5**, 4541-4583.
28. Y. Zhang, L. Zhang and C. Zhou, *Accounts of Chemical Research*, 2013, **46**, 2329-2339.

29.   C. Mattevi, H. Kim and M. Chhowalla, *Journal of Materials Chemistry*, 2011, **21**, 3324-3334.
30.   M. Yi and Z. Shen, *Journal of Materials Chemistry A*, 2015, **3**, 11700-11715.
31.   M. Eizenberg and J. M. Blakely, *Surface Science*, 1979, **82**, 228-236.
32.   S. Bae, H. Kim, Y. Lee, X. Xu, J.-S. Park, Y. Zheng, J. Balakrishnan, T. Lei, H. Ri Kim, Y. I. Song, Y.-J. Kim, K. S. Kim, B. Ozyilmaz, J.-H. Ahn, B. H. Hong and S. Iijima, *Nature Nanotechnology*, 2010, **5**, 574-578.
33.   H. Tetlow, J. Posthuma de Boer, I. J. Ford, D. D. Vvedensky, J. Coraux and L. Kantorovich, *Physics Reports*, 2014, **542**, 195-295.
34.   W. A. de Heer, C. Berger, X. Wu, P. N. First, E. H. Conrad, X. Li, T. Li, M. Sprinkle, J. Hass, M. L. Sadowski, M. Potemski and G. Martinez, *Solid State Communications*, 2007, **143**, 92-100.
35.   J. Cai, P. Ruffieux, R. Jaafar, M. Bieri, T. Braun, S. Blankenburg, M. Muoth, A. P. Seitsonen, M. Saleh, X. Feng, K. Mullen and R. Fasel, *Nature*, 2010, **466**, 470-473.
36.   J. J. Wang, M. Y. Zhu, R. A. Outlaw, X. Zhao, D. M. Manos, B. C. Holloway and V. P. Mammana, *Applied Physics Letters*, 2004, **85**, 1265-1267.
37.   Z. Wang, M. Shoji and H. Ogata, *Applied Surface Science*, 2011, **257**, 9082-9085.
38.   Z. Wang, H. Ogata, S. Morimoto, M. Fujishige, K. Takeuchi, Y. Hashimoto and M. Endo, *Carbon*, 2014, **72**, 421-424.
39.   Z. Wang, H. Ogata, S. Morimoto, M. Fujishige, K. Takeuchi, H. Muramatsu, T. Hayashi, J. Ortiz-Medina, M. Z. Mohd Yusop, M. Tanemura, M. Terrones, Y. Hashimoto and M. Endo, *Journal of Materials Chemistry A*, 2015, **3**, 14545-14549.
40.   H. Murayama and T. Maeda, *Nature*, 1990, **345**, 791-793.
41.   A. C. Ferrari, J. C. Meyer, V. Scardaci, C. Casiraghi, M. Lazzeri, F. Mauri, S. Piscanec, D. Jiang, K. S. Novoselov, S. Roth and A. K. Geim, *Physical Review Letters*, 2006, **97**, 187401.
42.   F. Bonaccorso, A. Lombardo, T. Hasan, Z. Sun, L. Colombo and A. C. Ferrari, *Materials Today*, 2012, **15**, 564-589.
43.   A. Del Rio-Castillo, C. Merino, E. Díez-Barra and E. Vázquez, *Nano Research*, 2014, **7**, 963-972.
44.   M. Mao, S. Chen, P. He, H. Zhang and H. Liu, *Journal of Materials Chemistry A*, 2014, **2**, 4132-4135.
45.   Y. Lv, L. Yu, C. Jiang, S. Chen and Z. Nie, *RSC Advances*, 2014, **4**, 13350-13354.
46.   I.-Y. Jeon, Y.-R. Shin, G.-J. Sohn, H.-J. Choi, S.-Y. Bae, J. Mahmood, S.-M. Jung, J.-M. Seo, M.-J. Kim, D. Wook Chang, L. Dai and J.-B. Baek, *Proceedings of the National Academy of Sciences*, 2012, **109**, 5588-5593.
47.   I.-Y. Jeon, H.-J. Choi, S.-M. Jung, J.-M. Seo, M.-J. Kim, L. Dai and J.-B. Baek, *Journal of the American Chemical Society*, 2013, **135**, 1386-1393.
48.   K. R. Paton, E. Varrla, C. Backes, R. J. Smith, U. Khan, A. O'Neill, C. Boland, M. Lotya, O. M. Istrate, P. King, T. Higgins, S. Barwich, P. May, P. Puczkarski, I. Ahmed, M. Moebius, H. Pettersson, E. Long, J. Coelho, S. E. O'Brien, E. K. McGuire, B. M. Sanchez, G. S. Duesberg, N. McEvoy, T. J. Pennycook, C. Downing, A. Crossley, V. Nicolosi and J. N. Coleman, *Nature Materials*, 2014, **13**, 624-630.
49.   L. Liu, Z. Shen, M. Yi, X. Zhang and S. Ma, *RSC Advances*, 2014, **4**, 36464-36470.
50.   E. Varrla, K. R. Paton, C. Backes, A. Harvey, R. J. Smith, J. McCauley and J. N. Coleman, *Nanoscale*, 2014, **6**, 11810-11819.
51.   M. Yi and Z. Shen, *Carbon*, 2014, **78**, 622-626.
52.   Y. Hernandez, V. Nicolosi, M. Lotya, F. M. Blighe, Z. Sun, S. De, I. T. McGovern, B. Holland, M. Byrne, Y. K. Gun'Ko, J. J. Boland, P. Niraj, G. Duesberg, S. Krishnamurthy, R. Goodhue, J. Hutchison, V. Scardaci, A. C. Ferrari and J. N. Coleman, *Nature Nanotechnology*, 2008, **3**, 563-568.
53.   L. Guardia, M. J. Fernández-Merino, J. I. Paredes, P. Solís-Fernández, S. Villar-Rodil, A. Martínez-Alonso and J. M. D. Tascón, *Carbon*, 2011, **49**, 1653-1662.

54. X. Zhang, A. C. Coleman, N. Katsonis, W. R. Browne, B. J. van Wees and B. L. Feringa, *Chemical Communications*, 2010, **46**, 7539-7541.
55. U. Khan, A. O'Neill, M. Lotya, S. De and J. N. Coleman, *Small*, 2010, **6**, 864-871.
56. U. Khan, A. O'Neill, H. Porwal, P. May, K. Nawaz and J. N. Coleman, *Carbon*, 2012, **50**, 470-475.
57. U. Khan, H. Porwal, A. O'Neill, K. Nawaz, P. May and J. N. Coleman, *Langmuir*, 2011, **27**, 9077-9082.
58. M. Lotya, P. J. King, U. Khan, S. De and J. N. Coleman, *ACS Nano*, 2010, **4**, 3155-3162.
59. A. B. Bourlinos, V. Georgakilas, R. Zboril, T. A. Steriotis, A. K. Stubos and C. Trapalis, *Solid State Communications*, 2009, **149**, 2172-2176.
60. T. Skaltsas, N. Karousis, H.-J. Yan, C.-R. Wang, S. Pispas and N. Tagmatarchis, *Journal of Materials Chemistry*, 2012, **22**, 21507-21512.
61. Y. T. Liang and M. C. Hersam, *Journal of the American Chemical Society*, 2010, **132**, 17661-17663.
62. P. May, U. Khan, J. M. Hughes and J. N. Coleman, *The Journal of Physical Chemistry C*, 2012, **116**, 11393-11400.
63. L. Xu, J.-W. McGraw, F. Gao, M. Grundy, Z. Ye, Z. Gu and J. L. Shepherd, *The Journal of Physical Chemistry C*, 2013, **117**, 10730-10742.
64. L. X. Benedict, N. G. Chopra, M. L. Cohen, A. Zettl, S. G. Louie and V. H. Crespi, *Chemical Physics Letters*, 1998, **286**, 490-496.
65. L. A. Girifalco and R. J. Good, *The Journal of Physical Chemistry*, 1957, **61**, 904-909.
66. R. Zacharia, H. Ulbricht and T. Hertel, *Physical Review B*, 2004, **69**, 155406.
67. Y. Hernandez, M. Lotya, D. Rickard, S. D. Bergin and J. N. Coleman, *Langmuir*, 2009, **26**, 3208-3213.
68. A. Reina, S. Thiele, X. Jia, S. Bhaviripudi, M. S. Dresselhaus, J. A. Schaefer and J. Kong, *Nano Research*, 2009, **2**, 509-516.
69. T. Skaltsas, X. Ke, C. Bittencourt and N. Tagmatarchis, *The Journal of Physical Chemistry C*, 2013, **117**, 23272-23278.
70. M. Yi, Z. Shen, S. Liang, L. Liu, X. Zhang and S. Ma, *Chemical Communications*, 2013, **49**, 11059-11061.
71. M. V. Bracamonte, G. I. Lacconi, S. E. Urreta and L. E. F. Foa Torres, *The Journal of Physical Chemistry C*, 2014, **118**, 15455-15459.
72. J. N. Coleman, *Accounts of Chemical Research*, 2012, **46**, 14-22.
73. C. Backes, T. M. Higgins, A. Kelly, C. Boland, A. Harvey, D. Hanlon and J. N. Coleman, *Chemistry of Materials*, 2016, **29**, 243-255.
74. D. R. Dreyer, S. Park, C. W. Bielawski and R. S. Ruoff, *Chemical Society Reviews*, 2010, **39**, 228-240.
75. M. S. Dresselhaus and G. Dresselhaus, *Advances in Physics*, 2002, **51**, 1-186.
76. P. Schaffautl, *Journal für Praktische Chemie*, 1840, **21**, 155.
77. U. Hoffmann and A. Frenzel, *Zeitschrift für Elektrochemie*, 1931, **37**, 613.
78. T. Enoki, M. Suzuki and M. Endo, *Graphite Intercalation Compounds and Applications*, Oxford University Press, 2003.
79. D. E. Nixon and G. S. Parry, *Journal of Physics D: Applied Physics*, 1968, **1**, 291.
80. Y. Wang, P. Puech, I. Gerber and A. Pénicaud, *Journal of Raman Spectroscopy*, 2014, **45**, 219-223.
81. T. Sasa, Y. Takahashi and T. Mukaibo, *Carbon*, 1971, **9**, 407-416.
82. J. G. Hooley and M. Bartlett, *Carbon*, 1967, **5**, 417-422.
83. W. Zhao, P. H. Tan, J. Liu and A. C. Ferrari, *Journal of the American Chemical Society*, 2011, **133**, 5941-5946.
84. E. R. Falardeau, L. R. Hanlon and T. E. Thompson, *Inorganic Chemistry*, 1978, **17**, 301-303.

85. G. M. Gualberto, C. Underhill, S. Y. Leung and G. Dresselhaus, *Physical Review B*, 1980, **21**, 862-868.
86. M. Zanini, S. Basu and J. E. Fischer, *Carbon*, 1978, **16**, 211-212.
87. S. Chakraborty, J. Chattopadhyay, W. Guo and W. E. Billups, *Angewandte Chemie International Edition*, 2007, **46**, 4486-4488.
88. G. A. Saunders, A. R. Ubbelohde and D. A. Young, *Proceedings of the Royal Society of London A: Mathematical, Physical and Engineering Sciences*, 1963, **271**, 499-511.
89. A. M. Dimiev, G. Ceriotti, N. Behabtu, D. Zakhidov, M. Pasquali, R. Saito and J. M. Tour, *ACS Nano*, 2013, **7**, 2773-2780.
90. N. Daumas and A. Herold, *Comptes Rendus Hebdomadaires Des Seances De L'Academie Des Sciences Serie C*, 1969, **268**, 373-382.
91. W. Rüdorff, E. Schulze and O. Rubisch, *Zeitschrift für anorganische und allgemeine Chemie*, 1955, **282**, 232-240.
92. Z. Yang, Y. Sun, L. B. Alemany, T. N. Narayanan and W. E. Billups, *Journal of the American Chemical Society*, 2012, **134**, 18689-18694.
93. E. M. Milner, N. T. Skipper, C. A. Howard, M. S. P. Shaffer, D. J. Buckley, K. A. Rahnejat, P. L. Cullen, R. K. Heenan, P. Lindner and R. Schweins, *Journal of the American Chemical Society*, 2012, **134**, 8302-8305.
94. R. A. Schäfer, J. M. Englert, P. Wehrfritz, W. Bauer, F. Hauke, T. Seyller and A. Hirsch, *Angewandte Chemie International Edition*, 2013, **52**, 754-757.
95. T. Abe, Y. Mizutani, T. Tabuchi, K. Ikeda, M. Asano, T. Harada, M. Inaba and Z. Ogumi, *Journal of Power Sources*, 1997, **68**, 216-220.
96. F. Beguin, R. Setton, F. Beguin, R. Setton, A. Hamwi and P. Touzain, *Materials Science and Engineering*, 1979, **40**, 167-173.
97. M. Inagaki and O. Tanaike, *Synthetic Metals*, 1995, **73**, 77-81.
98. M. Inagaki and O. Tanaike, *Journal of Physics and Chemistry of Solids*, 1996, **57**, 795-798.
99. T. Maluangnont, G. T. Bui, B. A. Huntington and M. M. Lerner, *Chemistry of Materials*, 2011, **23**, 1091-1095.
100. H. Zhang and M. M. Lerner, *Inorganic Chemistry*, 2016, **55**, 8281-8284.
101. R. Setton, F. Beguin, L. Facchini, M. F. Quinton, A. P. Legrand, B. Ruisinger and H. P. Boehm, *Journal of the Chemical Society, Chemical Communications*, 1983, 36-37.
102. Z. Wang, S. M. Selbach and T. Grande, *RSC Advances*, 2014, **4**, 4069-4079.
103. N. N. Yurii and E. V. p. Mark, *Russian Chemical Reviews*, 1971, **40**, 733.
104. F. L. Vogel, G. M. T. Foley, C. Zeller, E. R. Falardeau and J. Gan, *Materials Science and Engineering*, 1977, **31**, 261-265.
105. N. B. Hannay, T. H. Geballe, B. T. Matthias, K. Andres, P. Schmidt and D. MacNair, *Physical Review Letters*, 1965, **14**, 225-226.
106. W.-Q. Deng, X. Xu and W. A. Goddard, *Physical Review Letters*, 2004, **92**, 166103.
107. J. O. Besenhard, *Carbon*, 1976, **14**, 111-115.
108. M. Inagaki, K. Muramatsu, Y. Maeda and K. Maekawa, *Synthetic Metals*, 1983, **8**, 335-342.
109. X. van Heerden and H. Badenhorst, *Carbon*, 2015, **88**, 173-184.
110. S. Malik, A. Vijayaraghavan, R. Erni, K. Ariga, I. Khalakhan and J. P. Hill, *Nanoscale*, 2010, **2**, 2139-2143.
111. K. Arapov, R. Abbel, G. de With and H. Friedrich, *Faraday Discussions*, 2014, **173**, 323-336.
112. E. H. L. Falcao, R. G. Blair, J. J. Mack, L. M. Viculis, C.-W. Kwon, M. Bendikov, R. B. Kaner, B. S. Dunn and F. Wudl, *Carbon*, 2007, **45**, 1367-1369.
113. T. Wei, Z. Fan, G. Luo, C. Zheng and D. Xie, *Carbon*, 2009, **47**, 337-339.
114. Z. Wang, J. Liu, W. Wang, H. Chen, Z. Liu, Q. Yu, H. Zeng and L. Sun, *Chemical Communications*, 2013, **49**, 10835-10837.

115. C.-J. Shih, A. Vijayaraghavan, R. Krishnan, R. Sharma, J.-H. Han, M.-H. Ham, Z. Jin, S. Lin, G. L. C. Paulus, N. F. Reuel, Q. H. Wang, D. Blankschtein and M. S. Strano, *Nature Nanotechnology*, 2011, **6**, 439-445.

116. A. M. Dimiev, S. M. Bachilo, R. Saito and J. M. Tour, *ACS Nano*, 2012, **6**, 7842-7849.

117. A. M. Dimiev, G. Ceriotti, A. Metzger, N. D. Kim and J. M. Tour, *ACS Nano*, 2015, **10**, 274-279.

118. S. Eigler, *Chemical Communications*, 2015, **51**, 3162-3165.

119. X. Geng, Y. Guo, D. Li, W. Li, C. Zhu, X. Wei, M. Chen, S. Gao, S. Qiu, Y. Gong, L. Wu, M. Long, M. Sun, G. Pan and L. Liu, *Scientific Reports*, 2013, **3**.

120. J. Zheng, C.-a. Di, Y. Liu, H. Liu, Y. Guo, C. Du, T. Wu, G. Yu and D. Zhu, *Chemical Communications*, 2010, **46**, 5728-5730.

121. G. S. Manning, *Accounts of Chemical Research*, 1979, **12**, 443-449.

122. G. Yoon, D.-H. Seo, K. Ku, J. Kim, S. Jeon and K. Kang, *Chemistry of Materials*, 2015, **27**, 2067-2073.

123. A. Pénicaud, P. Poulin, A. Derré, E. Anglaret and P. Petit, *Journal of the American Chemical Society*, 2004, **127**, 8-9.

124. D. Voiry, C. Drummond and A. Penicaud, *Soft Matter*, 2011, **7**, 7998-8001.

125. C. Vallés, C. Drummond, H. Saadaoui, C. A. Furtado, M. He, O. Roubeau, L. Ortolani, M. Monthioux and A. Pénicaud, *Journal of the American Chemical Society*, 2008, **130**, 15802-15804.

126. A. Catheline, L. Ortolani, V. Morandi, M. Melle-Franco, C. Drummond, C. Zakri and A. Penicaud, *Soft Matter*, 2012, **8**, 7882-7887.

127. A. Catheline, C. Valles, C. Drummond, L. Ortolani, V. Morandi, M. Marcaccio, M. Iurlo, F. Paolucci and A. Penicaud, *Chemical Communications*, 2011, **47**, 5470-5472.

128. K. Huang, G. Delport, L. Orcin-Chaix, C. Drummond, J.-S. Lauret and A. Penicaud, *Nanoscale*, 2016, **8**, 8810-8818.

129. R. Schlögl and H. P. Boehm, *Carbon*, 1984, **22**, 341-349.

130. G. Bepete, E. Anglaret, L. Ortolani, V. Morandi, K. Huang, A. Penicaud and C. Drummond, *Nature Chemistry*, 2017, **9**, 347-352.

131. G. Bepete, A. Pénicaud, C. Drummond and E. Anglaret, *The Journal of Physical Chemistry C*, 2016, **120**, 28204-28214.

132. P. Yu, S. E. Lowe, G. P. Simon and Y. L. Zhong, *Current Opinion in Colloid & Interface Science*, 2015, **20**, 329-338.

133. A. M. Abdelkader, I. A. Kinloch and R. A. W. Dryfe, *ACS Applied Materials & Interfaces*, 2014, **6**, 1632-1639.

134. J. Wang, K. K. Manga, Q. Bao and K. P. Loh, *Journal of the American Chemical Society*, 2011, **133**, 8888-8891.

135. K. Parvez, Z.-S. Wu, R. Li, X. Liu, R. Graf, X. Feng and K. Müllen, *Journal of the American Chemical Society*, 2014, **136**, 6083-6091.

136. F. Torrisi, T. Hasan, W. Wu, Z. Sun, A. Lombardo, T. S. Kulmala, G.-W. Hsieh, S. Jung, F. Bonaccorso, P. J. Paul, D. Chu and A. C. Ferrari, *ACS Nano*, 2012, **6**, 2992-3006.

137. K. Arapov, E. Rubingh, R. Abbel, J. Laven, G. de With and H. Friedrich, *Advanced Functional Materials*, 2016, **26**, 586-593.

138. D. J. Finn, M. Lotya, G. Cunningham, R. J. Smith, D. McCloskey, J. F. Donegan and J. N. Coleman, *Journal of Materials Chemistry C*, 2014, **2**, 925-932.

139. J. Liu, J. Tang and J. J. Gooding, *Journal of Materials Chemistry*, 2012, **22**, 12435-12452.

140. X. Huang, X. Qi, F. Boey and H. Zhang, *Chemical Society Reviews*, 2012, **41**, 666-686.

141. J. Ma, Q. Meng, A. Michelmore, N. Kawashima, Z. Izzuddin, C. Bengtsson and H.-C. Kuan, *Journal of Materials Chemistry A*, 2013, **1**, 4255-4264.

142. L. Gong, I. A. Kinloch, R. J. Young, I. Riaz, R. Jalil and K. S. Novoselov, *Advanced Materials*, 2010, **22**, 2694-2697.

143. R. J. Young, L. Gong, I. A. Kinloch, I. Riaz, R. Jalil and K. S. Novoselov, *ACS Nano*, 2011, **5**, 3079-3084.
144. W. K. Chee, H. N. Lim, N. M. Huang and I. Harrison, *RSC Advances*, 2015, **5**, 68014-68051.
145. R. J. Young, I. A. Kinloch, L. Gong and K. S. Novoselov, *Composites Science and Technology*, 2012, **72**, 1459-1476.
146. M. Ghislandi, E. Tkalya, S. Schillinger, C. E. Koning and G. de With, *Composites Science and Technology*, 2013, **80**, 16-22.
147. M. A. Rafiee, J. Rafiee, I. Srivastava, Z. Wang, H. Song, Z.-Z. Yu and N. Koratkar, *Small*, 2010, **6**, 179-183.
148. T. Ramanathan, A. A. Abdala, S. Stankovich, D. A. Dikin, M. Herrera Alonso, R. D. Piner, D. H. Adamson, H. C. Schniepp, C. X, R. S. Ruoff, S. T. Nguyen, I. A. Aksay, R. K. Prud'Homme and L. C. Brinson, *Nature Nanotechnology*, 2008, **3**, 327-331.
149. S. Stankovich, D. A. Dikin, G. H. B. Dommett, K. M. Kohlhaas, E. J. Zimney, E. A. Stach, R. D. Piner, S. T. Nguyen and R. S. Ruoff, *Nature*, 2006, **442**, 282-286.
150. M. Fang, Z. Zhang, J. Li, H. Zhang, H. Lu and Y. Yang, *Journal of Materials Chemistry*, 2010, **20**, 9635-9643.
151. R. K. Layek, A. Kuila, D. P. Chatterjee and A. K. Nandi, *Journal of Materials Chemistry A*, 2013, **1**, 10863-10874.
152. X. Wang, W. Xing, X. Feng, B. Yu, L. Song and Y. Hu, *Polymer Chemistry*, 2014, **5**, 1145-1154.
153. F. Liu, L. Wu, Y. Song, W. Xia and K. Guo, *RSC Advances*, 2015, **5**, 45987-45995.
154. H. Ribeiro, W. M. da Silva, J. C. Neves, H. D. R. Calado, R. Paniago, L. M. Seara, D. d. Mercês Camarano and G. G. Silva, *Polymer Testing*, 2015, **43**, 182-192.
155. S. Park and R. S. Ruoff, *Nature Nanotechnology*, 2009, **4**, 217-224.
156. H. Kim, H. Thomas Hahn, L. M. Viculis, S. Gilje and R. B. Kaner, *Carbon*, 2007, **45**, 1578-1582.
157. X. Xiao, T. Xie and Y.-T. Cheng, *Journal of Materials Chemistry*, 2010, **20**, 3508-3514.
158. J. Wang, Z. Shi, Y. Ge, Y. Wang, J. Fan and J. Yin, *Materials Chemistry and Physics*, 2012, **136**, 43-50.
159. M. Castelain, G. Martinez, G. Ellis and H. J. Salavagione, *Chemical Communications*, 2013, **49**, 8967-8969.
160. S. Araby, I. Zaman, Q. Meng, N. Kawashima, A. Michelmore, H.-C. Kuan, P. Majewski, J. Ma and L. Zhang, *Nanotechnology*, 2013, **24**, 165601.
161. I. Zaman, T. T. Phan, H.-C. Kuan, Q. Meng, L. T. Bao La, L. Luong, O. Youssf and J. Ma, *Polymer*, 2011, **52**, 1603-1611.
162. A. Ciesielski and P. Samori, *Advanced Materials*, 2016, **28**, 6030-6051.
163. D. Kiessling, R. D. Costa, G. Katsukis, J. Malig, F. Lodermeyer, S. Feihl, A. Roth, L. Wibmer, M. Kehrer, M. Volland, P. Wagner, G. G. Wallace, D. L. Officer and D. M. Guldi, *Chemical Science*, 2013, **4**, 3085-3098.
164. J. Xu, D. K. Dang, V. T. Tran, X. Liu, J. S. Chung, S. H. Hur, W. M. Choi, E. J. Kim and P. A. Kohl, *Journal of Colloid and Interface Science*, 2014, **418**, 37-42.
165. L. Zhang, Z. Zhang, C. He, L. Dai, J. Liu and L. Wang, *ACS Nano*, 2014, **8**, 6663-6670.
166. D.-W. Lee, T. Kim and M. Lee, *Chemical Communications*, 2011, **47**, 8259-8261.
167. S. Hu, S. Chen, R. Menzel, A. D. Goode, M. P. Ryan, A. E. Porter and M. S. P. Shaffer, *Faraday Discussions*, 2014, **173**, 273-285.
168. K. P. Loh, Q. Bao, P. K. Ang and J. Yang, *Journal of Materials Chemistry*, 2010, **20**, 2277-2289.
169. W. S. Hummers and R. E. Offeman, *Journal of the American Chemical Society*, 1958, **80**, 1339-1339.
170. A. Lerf, H. He, M. Forster and J. Klinowski, *The Journal of Physical Chemistry B*, 1998, **102**, 4477-4482.
171. D. Li, M. B. Muller, S. Gilje, R. B. Kaner and G. G. Wallace, *Nature Nanotechnology*, 2008, **3**, 101-105.

172. H. C. Schniepp, J.-L. Li, M. J. McAllister, H. Sai, M. Herrera-Alonso, D. H. Adamson, R. K. Prud'homme, R. Car, D. A. Saville and I. A. Aksay, *The Journal of Physical Chemistry B*, 2006, **110**, 8535-8539.

173. J. I. Paredes, S. Villar-Rodil, A. Martínez-Alonso and J. M. D. Tascón, *Langmuir*, 2008, **24**, 10560-10564.

174. K. E. Lee, J. E. Kim, U. N. Maiti, J. Lim, J. O. Hwang, J. Shim, J. J. Oh, T. Yun and S. O. Kim, *ACS Nano*, 2014, **8**, 9073-9080.

175. D. R. Dreyer, H.-P. Jia, A. D. Todd, J. Geng and C. W. Bielawski, *Organic & Biomolecular Chemistry*, 2011, **9**, 7292-7295.

176. S. Stankovich, D. A. Dikin, R. D. Piner, K. A. Kohlhaas, A. Kleinhammes, Y. Jia, Y. Wu, S. T. Nguyen and R. S. Ruoff, *Carbon*, 2007, **45**, 1558-1565.

177. H.-J. Shin, K. K. Kim, A. Benayad, S.-M. Yoon, H. K. Park, I.-S. Jung, M. H. Jin, H.-K. Jeong, J. M. Kim, J.-Y. Choi and Y. H. Lee, *Advanced Functional Materials*, 2009, **19**, 1987-1992.

178. G. Wang, J. Yang, J. Park, X. Gou, B. Wang, H. Liu and J. Yao, *The Journal of Physical Chemistry C*, 2008, **112**, 8192-8195.

179. C. Mattevi, G. Eda, S. Agnoli, S. Miller, K. A. Mkhoyan, O. Celik, D. Mastrogiovanni, G. Granozzi, E. Garfunkel and M. Chhowalla, *Advanced Functional Materials*, 2009, **19**, 2577-2583.

180. L. Zhang, Z. Wang, Z. Lu, H. Shen, J. Huang, Q. Zhao, M. Liu, N. He and Z. Zhang, *Journal of Materials Chemistry B*, 2013, **1**, 749-755.

181. Y. Yang, J. Wang, J. Zhang, J. Liu, X. Yang and H. Zhao, *Langmuir*, 2009, **25**, 11808-11814.

182. S. H. Lee, D. R. Dreyer, J. An, A. Velamakanni, R. D. Piner, S. Park, Y. Zhu, S. O. Kim, C. W. Bielawski and R. S. Ruoff, *Macromolecular Rapid Communications*, 2010, **31**, 281-288.

183. G. Gao, D. Liu, S. Tang, C. Huang, M. He, Y. Guo, X. Sun and B. Gao, *Scientific Reports*, 2016, **6**, 20034.

184. L. Zhang, J. Yu, M. Yang, Q. Xie, H. Peng and Z. Liu, *Nature Communications*, 2013, **4**, 1443.

185. X. Zhang, M. Han, S. Chen, L. Bao, L. Li and W. Xu, *RSC Advances*, 2013, **3**, 17689-17692.

186. M. Liras, O. Garcia, I. Quijada-Garrido, G. Ellis and H. J. Salavagione, *Journal of Materials Chemistry C*, 2014, **2**, 1723-1729.

187. T. Sainsbury, M. Passarelli, M. Naftaly, S. Gnaniah, S. J. Spencer and A. J. Pollard, *ACS Applied Materials & Interfaces*, 2016, **8**, 4870-4877.

188. B. Li, L. Zhou, D. Wu, H. Peng, K. Yan, Y. Zhou and Z. Liu, *ACS Nano*, 2011, **5**, 5957-5961.

189. E. Bekyarova, M. E. Itkis, P. Ramesh, C. Berger, M. Sprinkle, W. A. de Heer and R. C. Haddon, *Journal of the American Chemical Society*, 2009, **131**, 1336-1337.

190. R. Sharma, J. H. Baik, C. J. Perera and M. S. Strano, *Nano Letters*, 2010, **10**, 398-405.

191. F. M. Koehler, A. Jacobsen, K. Ensslin, C. Stampfer and W. J. Stark, *Small*, 2010, **6**, 1125-1130.

192. C. Peng, Y. Xiong, Z. Liu, F. Zhang, E. Ou, J. Qian, Y. Xiong and W. Xu, *Applied Surface Science*, 2013, **280**, 914-919.

193. Z. Xia, F. Leonardi, M. Gobbi, Y. Liu, V. Bellani, A. Liscio, A. Kovtun, R. Li, X. Feng, E. Orgiu, P. Samorì, E. Treossi and V. Palermo, *ACS Nano*, 2016, **10**, 7125-7134.

194. J. R. Lomeda, C. D. Doyle, D. V. Kosynkin, W.-F. Hwang and J. M. Tour, *Journal of the American Chemical Society*, 2008, **130**, 16201-16206.

195. Z. Sun, S.-i. Kohama, Z. Zhang, J. Lomeda and J. Tour, *Nano Research*, 2010, **3**, 117-125.

196. Z. Jin, T. P. McNicholas, C.-J. Shih, Q. H. Wang, G. L. C. Paulus, A. J. Hilmer, S. Shimizu and M. S. Strano, *Chemistry of Materials*, 2011, **23**, 3362-3370.

197. Y.-S. Ye, Y.-N. Chen, J.-S. Wang, J. Rick, Y.-J. Huang, F.-C. Chang and B.-J. Hwang, *Chemistry of Materials*, 2012, **24**, 2987-2997.
198. F. M. Koehler and W. J. Stark, *Accounts of Chemical Research*, 2012, **46**, 2297-2306.
199. M. Fang, K. Wang, H. Lu, Y. Yang and S. Nutt, *Journal of Materials Chemistry*, 2009, **19**, 7098-7105.
200. M. Maggini, G. Scorrano and M. Prato, *Journal of the American Chemical Society*, 1993, **115**, 9798-9799.
201. V. Georgakilas, K. Kordatos, M. Prato, D. M. Guldi, M. Holzinger and A. Hirsch, *Journal of the American Chemical Society*, 2002, **124**, 760-761.
202. M. Quintana, K. Spyrou, M. Grzelczak, W. R. Browne, P. Rudolf and M. Prato, *ACS Nano*, 2010, **4**, 3527-3533.
203. M. Quintana, A. Montellano, A. E. del Rio Castillo, G. V. Tendeloo, C. Bittencourt and M. Prato, *Chemical Communications*, 2011, **47**, 9330-9332.
204. M. Quintana, E. Vazquez and M. Prato, *Accounts of Chemical Research*, 2013, **46**, 138-148.
205. S. Sarkar, E. Bekyarova, S. Niyogi and R. C. Haddon, *Journal of the American Chemical Society*, 2011, **133**, 3324-3327.
206. X. Zhang, W. R. Browne and B. L. Feringa, *RSC Advances*, 2012, **2**, 12173-12176.
207. T. A. Strom, E. P. Dillon, C. E. Hamilton and A. R. Barron, *Chemical Communications*, 2010, **46**, 4097-4099.
208. L.-H. Liu, M. M. Lerner and M. Yan, *Nano Letters*, 2010, **10**, 3754-3756.
209. J. Zheng, H.-T. Liu, B. Wu, C.-A. Di, Y.-L. Guo, T. Wu, G. Yu, Y.-Q. Liu and D.-B. Zhu, *Scientific Reports*, 2012, **2**.
210. R. Stine, W.-K. Lee, K. E. Whitener, J. T. Robinson and P. E. Sheehan, *Nano Letters*, 2013, **13**, 4311-4316.
211. K. S. Coleman, A. K. Chakraborty, S. R. Bailey, J. Sloan and M. Alexander, *Chemistry of Materials*, 2007, **19**, 1076-1081.
212. N. A. Nebogatikova, I. V. Antonova, V. A. Volodin and V. Y. Prinz, *Physica E: Low-dimensional Systems and Nanostructures*, 2013, **52**, 106-111.
213. K. E. Whitener, R. Stine, J. T. Robinson and P. E. Sheehan, *The Journal of Physical Chemistry C*, 2015, **119**, 10507-10512.
214. P. C. Eklund, N. Kambe, G. Dresselhaus and M. S. Dresselhaus, *Physical Review B*, 1978, **18**, 7069-7079.
215. L. G. Bulusheva, A. V. Okotrub, E. Flahaut, I. P. Asanov, P. N. Gevko, V. O. Koroteev, Y. V. Fedoseeva, A. Yaya and C. P. Ewels, *Chemistry of Materials*, 2012, **24**, 2708-2715.
216. J. Gao, F. Bao, Q. Zhu, Z. Tan, T. Chen, H. Cai, C. Zhao, Q. Cheng, Y. Yang and R. Ma, *Polymer Chemistry*, 2013, **4**, 1672-1679.
217. D. Hines, M. H. Rummeli, D. Adebimpe and D. L. Akins, *Chemical Communications*, 2014, **50**, 11568-11571.
218. J. F. Friedrich, S. Wettmarshausen, S. Hanelt, R. Mach, R. Mix, E. B. Zeynalov and A. Meyer-Plath, *Carbon*, 2010, **48**, 3884-3894.
219. O. Jankovsky, P. Simek, K. Klimova, D. Sedmidubsky, S. Matejkova, M. Pumera and Z. Sofer, *Nanoscale*, 2014, **6**, 6065-6074.
220. Y. Yao, J. Gao, F. Bao, S. Jiang, X. Zhang and R. Ma, *RSC Advances*, 2015, **5**, 42754-42761.
221. F. Hof, F. Hauke and A. Hirsch, *Chemical Communications*, 2014, **50**, 6582-6584.
222. F. Liang, J. M. Beach, K. Kobashi, A. K. Sadana, Y. I. Vega-Cantu, J. M. Tour and W. E. Billups, *Chemistry of Materials*, 2006, **18**, 4764-4767.
223. A. Chakravarty, K. Bhowmik, G. De and A. Mukherjee, *New Journal of Chemistry*, 2015, **39**, 2451-2458.
224. S. Zhang, P. Xiong, X. Yang and X. Wang, *Nanoscale*, 2011, **3**, 2169-2174.
225. M. Castelaín, G. Martínez, C. Marco, G. Ellis and H. J. Salavagione, *Macromolecules*, 2013, **46**, 8980-8987.

226. H. Roghani-Mamaqani, *RSC Advances*, 2015, **5**, 53357-53368.
227. G. Goncalves, P. A. A. P. Marques, A. Barros-Timmons, I. Bdkin, M. K. Singh, N. Emami and J. Gracio, *Journal of Materials Chemistry*, 2010, **20**, 9927-9934.
228. Z. Liu, Z. Xu, X. Hu and C. Gao, *Macromolecules*, 2013, **46**, 6931-6941.
229. W. Lu, G. Ruan, B. Genorio, Y. Zhu, B. Novosel, Z. Peng and J. M. Tour, *ACS Nano*, 2013, **7**, 2669-2675.
230. L. Sun, M. Xiao, J. Liu and K. Gong, *European Polymer Journal*, 2006, **42**, 259-264.
231. H. Shioyama, *Journal of Materials Chemistry*, 2001, **11**, 3307-3309.
232. C. M. Homenick, G. Lawson and A. Adronov, *Polymer Reviews*, 2007, **47**, 265-290.
233. R. C. Chadwick, U. Khan, J. N. Coleman and A. Adronov, *Small*, 2013, **9**, 552-560.
234. S. Qin, D. Qin, W. T. Ford, D. E. Resasco and J. E. Herrera, *Macromolecules*, 2004, **37**, 752-757.
235. D. Baskaran, J. W. Mays and M. S. Bratcher, *Angewandte Chemie International Edition*, 2004, **43**, 2138-2142.
236. H. Kong, C. Gao and D. Yan, *Journal of the American Chemical Society*, 2004, **126**, 412-413.
237. M. Ejaz, S. C. Rai, K. Wang, K. Zhang, W. Zhou and S. M. Grayson, *Journal of Materials Chemistry C*, 2014, **2**, 4073-4079.
238. D. Voiry, O. Roubeau and A. Penicaud, *Journal of Materials Chemistry*, 2010, **20**, 4385-4391.
239. A. Molina-Ontoria, M. N. Chaur, M. E. Plonska-Brzezinska and L. Echegoyen, *Chemical Communications*, 2013, **49**, 2406-2408.
240. J. Chattopadhyay, A. Mukherjee, S. Chakraborty, J. Kang, P. J. Loos, K. F. Kelly, H. K. Schmidt and W. E. Billups, *Carbon*, 2009, **47**, 2945-2949.
241. F. Hof, R. A. Schäfer, C. Weiss, F. Hauke and A. Hirsch, *Chemistry – A European Journal*, 2014, **20**, 16644-16651.
242. J. M. Englert, C. Dotzer, G. Yang, M. Schmid, C. Papp, J. M. Gottfried, H.-P. Steinrück, E. Spiecker, F. Hauke and A. Hirsch, *Nature Chemistry*, 2011, **3**, 279-286.
243. P. Vecera, K. Edelthalhammer, F. Hauke and A. Hirsch, *Physica Status Solidi B*, 2014, **251**, 2536-2540.
244. L. Feng, Y.-W. Liu, X.-Y. Tang, Y. Piao, S.-F. Chen, S.-L. Deng, S.-Y. Xie, Y. Wang and L.-S. Zheng, *Chemistry of Materials*, 2013, **25**, 4487-4496.
245. H. S. Leese, L. Govada, E. Saridakis, S. Khurshid, R. Menzel, T. Morishita, A. J. Clancy, E. R. White, N. E. Chayen and M. S. P. Shaffer, *Chemical Science*, 2016, **7**, 2916-2923.
246. K. C. Knirsch, F. Hof, V. Lloret, U. Mundloch, F. Hauke and A. Hirsch, *Journal of the American Chemical Society*, 2016, **138**, 15642-15647.
247. K. E. Whitener, W. K. Lee, P. M. Campbell, J. T. Robinson and P. E. Sheehan, *Carbon*, 2014, **72**, 348-353.
248. X. Zhang, Y. Huang, S. Chen, N. Y. Kim, W. Kim, D. Schilter, M. Biswal, B. Li, Z. Lee, S. Ryu, C. W. Bielawski, W. S. Bacsa and R. S. Ruoff, *Journal of the American Chemical Society*, 2016, **138**, 14980-14986.
249. S. Pekker, J. P. Salvetat, E. Jakab, J. M. Bonard and L. Forró, *The Journal of Physical Chemistry B*, 2001, **105**, 7938-7943.
250. L. M. Viculis, J. J. Mack and R. B. Kaner, *Science*, 2003, **299**, 1361.
251. L. M. Viculis, J. J. Mack, O. M. Mayer, H. T. Hahn and R. B. Kaner, *Journal of Materials Chemistry*, 2005, **15**, 974-978.
252. D. E. Bergbreiter and J. M. Killough, *Journal of the American Chemical Society*, 1978, **100**, 2126-2134.
253. K. C. Knirsch, R. A. Schäfer, F. Hauke and A. Hirsch, *Angewandte Chemie International Edition*, 2016, **55**, 5861-5864.
254. R. A. Schäfer, K. Weber, M. Kolesnik-Gray, F. Hauke, V. Krstic, B. Meyer and A. Hirsch, *Angewandte Chemie International Edition*, 2016, **55**, 14858-14862.

255. J. M. Englert, P. Vecera, K. C. Knirsch, R. A. Schäfer, F. Hauke and A. Hirsch, *ACS Nano*, 2013, **7**, 5472-5482.
256. J. M. Englert, K. C. Knirsch, C. Dotzer, B. Butz, F. Hauke, E. Spiecker and A. Hirsch, *Chemical Communications*, 2012, **48**, 5025-5027.
257. B. Genorio, W. Lu, A. M. Dimiev, Y. Zhu, A.-R. O. Raji, B. Novosel, L. B. Alemany and J. M. Tour, *ACS Nano*, 2012, **6**, 4231-4240.
258. A. García-Gallastegui, I. Obieta, I. Bustero, G. Imbuluzqueta, J. Arbiol, J. I. Miranda and J. M. Aizpurua, *Chemistry of Materials*, 2008, **20**, 4433-4438.
259. S. A. Hodge, H. H. Tay, D. B. Anthony, R. Menzel, D. J. Buckley, P. L. Cullen, N. T. Skipper, C. A. Howard and M. S. P. Shaffer, *Faraday Discussions*, 2014, **172**, 311-325.
260. F. Hof, S. Bosch, S. Eigler, F. Hauke and A. Hirsch, *Journal of the American Chemical Society*, 2013, **49**, 18385–18395.
261. S. A. Hodge, D. J. Buckley, H. C. Yau, N. T. Skipper, C. A. Howard and M. S. P. Shaffer, *Nanoscale*, 2017, **9**, 3150-3158.
262. P. Vecera, J. Holzwarth, K. F. Edelthalhammer, U. Mundloch, H. Peterlik, F. Hauke and A. Hirsch, *Nature Communications*, 2016, **7**.
263. F. Liang, A. K. Sadana, A. Peera, J. Chattopadhyay, Z. Gu, R. H. Hauge and W. E. Billups, *Nano Letters*, 2004, **4**, 1257-1260.
264. C. Jiang, A. Saha and A. A. Martí, *Nanoscale*, 2015, **7**, 15037-15045.
265. A. J. Marsden, P. Brommer, J. J. Mudd, M. A. Dyson, R. Cook, M. Asensio, J. Avila, A. Levy, J. Sloan, D. Quigley, G. R. Bell and N. R. Wilson, *Nano Research*, 2015, **8**, 2620-2635.
266. A. C. Ferrari and D. M. Basko, *Nature Nanotechnology*, 2013, **8**, 235-246.
267. L. G. Cançado, A. Jorio, E. H. M. Ferreira, F. Stavale, C. A. Achete, R. B. Capaz, M. V. O. Moutinho, A. Lombardo, T. S. Kulmala and A. C. Ferrari, *Nano Letters*, 2011, **11**, 3190-3196.
268. M. M. Lucchese, F. Stavale, E. H. M. Ferreira, C. Vilani, M. V. O. Moutinho, R. B. Capaz, C. A. Achete and A. Jorio, *Carbon*, 2010, **48**, 1592-1597.
269. F. Tuinstra and J. L. Koenig, *The Journal of Chemical Physics*, 1970, **53**, 1126-1130.
270. A. Eckmann, A. Felten, A. Mishchenko, L. Britnell, R. Krupke, K. S. Novoselov and C. Casiraghi, *Nano Letters*, 2012, **12**, 3925-3930.
271. A. C. Ferrari, *Solid State Communications*, 2007, **143**, 47-57.
272. B. K. Saikia, R. K. Boruah and P. K. Gogoi, *Journal of Chemical Sciences*, 2009, **121**, 103-106.
273. M. S. Seehra and A. S. Pavlovic, *Carbon*, 1993, **31**, 557-564.
274. J. C. Meyer, A. K. Geim, M. I. Katsnelson, K. S. Novoselov, T. J. Booth and S. Roth, *Nature*, 2007, **446**, 60-63.
275. T. Sarbu, K.-Y. Lin, J. Ell, D. J. Siegwart, J. Spanswick and K. Matyjaszewski, *Macromolecules*, 2004, **37**, 3120-3127.
276. H. Badenhorst, *Carbon*, 2014, **66**, 674-690.
277. N. G. Connelly and W. E. Geiger, *Chemical Reviews*, 1996, **96**, 877-910.
278. C. Jiang, A. Saha, C. Xiang, C. C. Young, J. M. Tour, M. Pasquali and A. A. Martí, *ACS Nano*, 2013, **5**, 4503–4510.
279. A. Suri and K. S. Coleman, *Journal of Nanoscience and Nanotechnology*, 2012, **12**, 2929-2933.
280. Y. Martinez-Rubi, J. Guan, S. Lin, C. Scriver, R. E. Sturgeon and B. Simard, *Chemical Communications*, 2007, **0**, 5146-5148.
281. A. J. Clancy, J. Melbourne and M. S. P. Shaffer, *Journal of Materials Chemistry A*, 2015, **3**, 16708-16715.
282. D. Voiry, G. Pagona, E. D. Canto, L. Ortolani, V. Morandi, L. Noe, M. Monthioux, N. Tagmatarchis and A. Penicaud, *Chemical Communications*, 2015, **51**, 5017-5019.
283. G. D. Sargent and G. A. Lux, *Journal of the American Chemical Society*, 1968, **90**, 7160-7162.

284. O. Tanaike and M. Inagaki, *Carbon*, 1997, **35**, 831-836.
285. M. S. Dresselhaus, G. Dresselhaus, K. Sugihara, I. L. Spain and H. A. Goldberg, *Graphite Fibers and Filaments*, Springer-Verlag Berlin Heidelberg, 1 edn., 1988.
286. S. A. Solin, *Physica B+C*, 1980, **99**, 443-452.
287. J. C. Chacón-Torres, L. Wirtz and T. Pichler, *ACS Nano*, 2013, **7**, 9249-9259.
288. M. Rosillo-Lopez, T. J. Lee, M. Bella, M. Hart and C. G. Salzmann, *RSC Advances*, 2015, **5**, 104198-104202.
289. Z. Q. Li, C. J. Lu, Z. P. Xia, Y. Zhou and Z. Luo, *Carbon*, 2007, **45**, 1686-1695.
290. A. C. Ferrari and J. Robertson, *Physical Review B*, 2000, **61**, 14095-14107.
291. F. Hof, S. Bosch, J. M. Englert, F. Hauke and A. Hirsch, *Angewandte Chemie International Edition*, 2012, **51**, 11727-11730.
292. S. Deng, Y. Zhang, A. H. Brozena, M. L. Mayes, P. Banerjee, W.-A. Chiou, G. W. Rubloff, G. C. Schatz and Y. Wang, *Nature Communications*, 2011, **2**, 382.
293. C. M. Gomez and C. B. Bucknall, *Polymer*, 1993, **34**, 2111-2117.
294. G. Viswanathan, N. Chakrapani, H. Yang, B. Wei, H. Chung, K. Cho, C. Y. Ryu and P. M. Ajayan, *Journal of the American Chemical Society*, 2003, **125**, 9258-9259.
295. M. Frankel, A. Ottolenghi, M. Albeck and A. Zilkha, *Journal of the Chemical Society (Resumed)*, 1959, 3858-3864.
296. A. J. White and F. E. Filisko, *Journal of Polymer Science: Polymer Letters Edition*, 1982, **20**, 525-529.
297. H. Fujimoto, *Carbon*, 2003, **41**, 1585-1592.
298. J. Sacristan, C. Chen and J. K. Maranas, *Macromolecules*, 2008, **41**, 5466-5476.
299. P. G. de Gennes, *Macromolecules*, 1980, **13**, 1069-1075.
300. J. Brandrup, E. H. Immergut, E. A. Grulke, A. Abe and D. R. Bloch, *Polymer Handbook (4th Edition)*, John Wiley & Sons, 1999.
301. E. Widenkvist, D. W. Boukhvalov, S. Rubino, S. Akhtar, J. Lu, R. A. Quinlan, M. I. Katsnelson, K. Leifer, H. Grennberg and U. Jansson, *Journal of Physics D: Applied Physics*, 2009, **42**, 112003.
302. D. A. Young, *Carbon*, 1977, **15**, 373-377.
303. J. S. Culik and D. D. L. Chung, *Materials Science and Engineering*, 1980, **44**, 129-137.
304. E. Papirer, R. Lacroix, J.-B. Donnet, G. Nanse and P. Fioux, *Carbon*, 1994, **32**, 1341-1358.
305. J. Li, L. Vaisman, G. Marom and J.-K. Kim, *Carbon*, 2007, **45**, 744-750.
306. A. E. Mansour, S. Dey, A. Amassian and M. H. Tanielian, *ACS Applied Materials & Interfaces*, 2015, **7**, 17692-17699.
307. S. Eigler, F. Hof, M. Enzelberger-Heim, S. Grimm, P. Müller and A. Hirsch, *The Journal of Physical Chemistry C*, 2014, **118**, 7698-7704.
308. S. Edmondson and S. P. Armes, *Polymer International*, 2009, **58**, 307-316.
309. T. Sarbu, K.-Y. Lin, J. Spanswick, R. R. Gil, D. J. Siegwart and K. Matyjaszewski, *Macromolecules*, 2004, **37**, 9694-9700.
310. L. M. Malard, M. A. Pimenta, G. Dresselhaus and M. S. Dresselhaus, *Physics Reports*, 2009, **473**, 51-87.
311. C. Kubel, K. Eckhardt, V. Enkelmann, G. Wegner and K. Mullen, *Journal of Materials Chemistry*, 2000, **10**, 879-886.

Appendix I

Supplementary figures for Chapter 5.

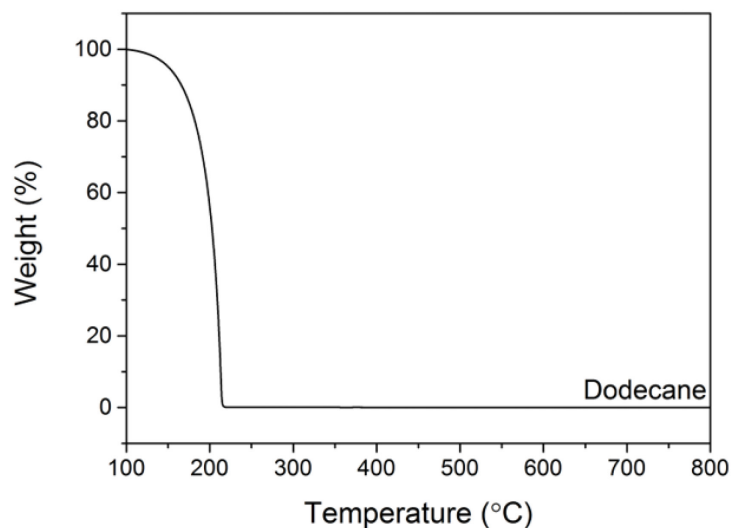

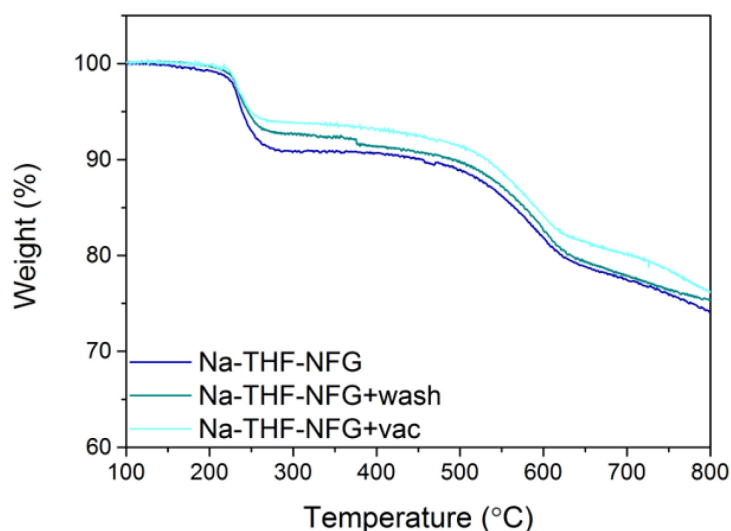Figure I.1. TGA profile of dodecane. Full decomposition occurs around 200 ℃.

Figure I.2. TGA profiles of Na-THF-NFG after extra washing and drying procedures; no significant difference in mass loss can be seen. For the additional washing process, the sample (5 mg) was suspended in 10 mL chloroform and 10 mL water, and bath sonicated for 10 min. The mixture was filtered through a 0.1 μm PTFE membrane, and washed thoroughly with water and THF. The product was collected and the procedure repeated twice more, before drying as before. Extra drying was achieved by heating at 120 ℃ under vacuum for 48 hours.
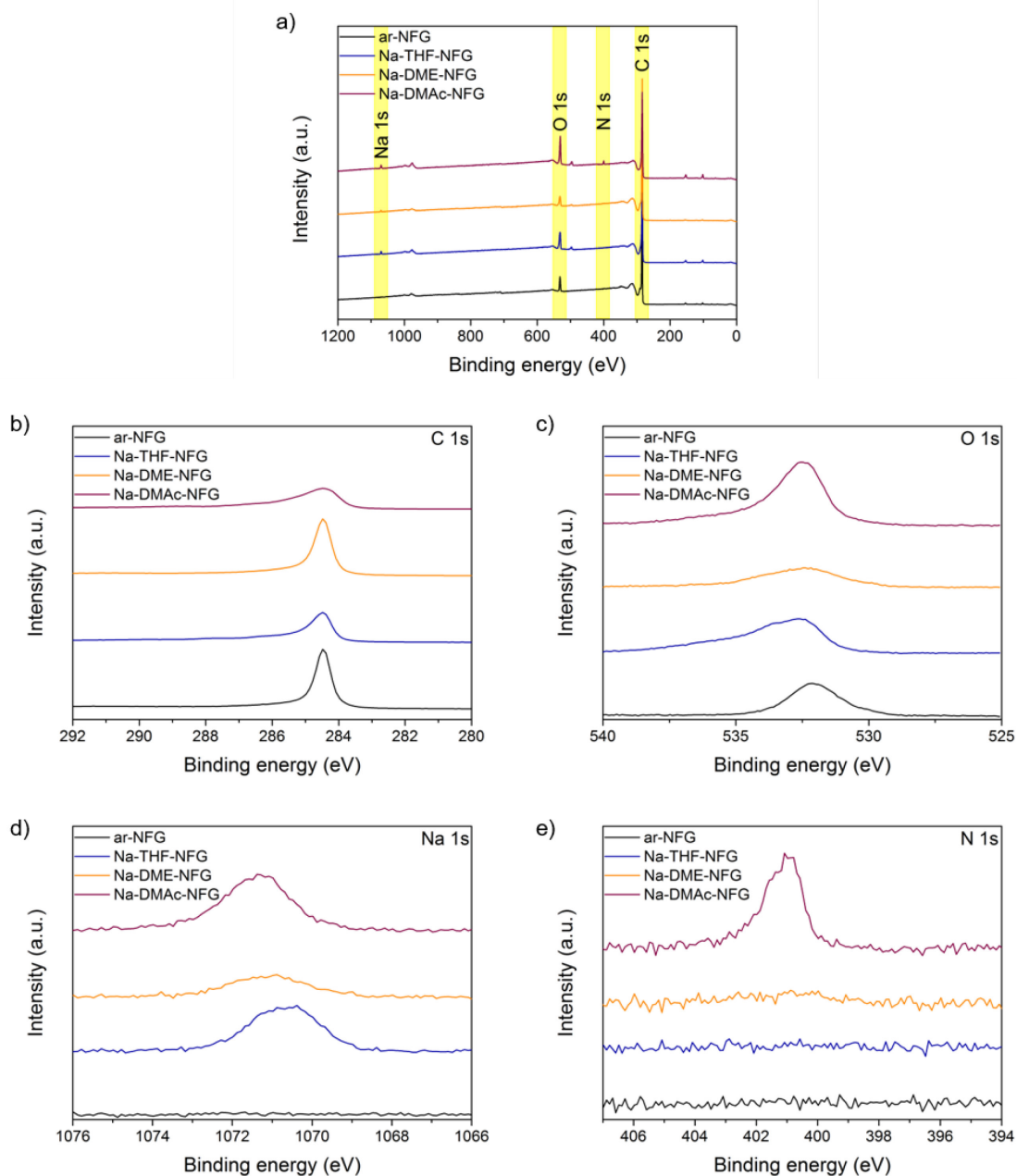
Figure I.3. a) Survey spectra and core level b) C1s, c) O1s, d) Na1s, and e) N1s spectra of ar-NFG (black), Na-THF-NFG (blue), Na-DME-NFG (orange) and Na-DMAc-NFG (red).
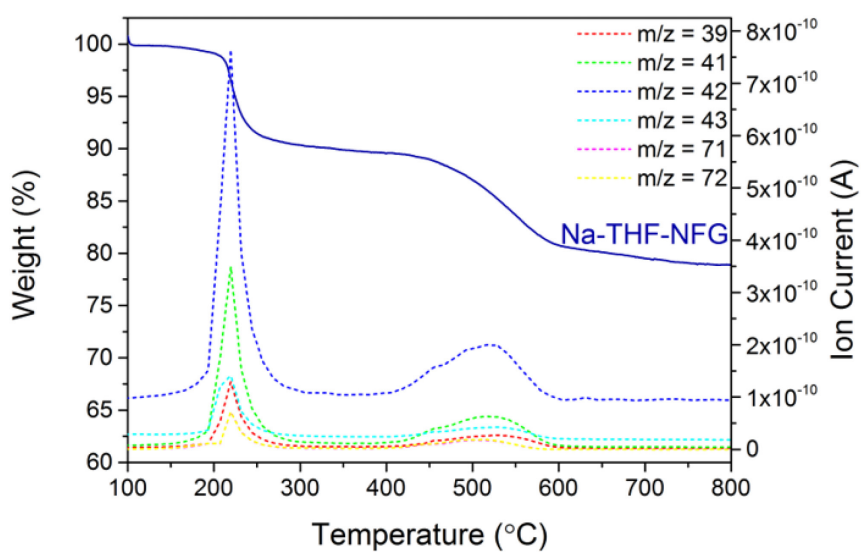
Figure I.4. TGA-MS profile of Na-THF-NFG, showing all m/z signals arising from THF.
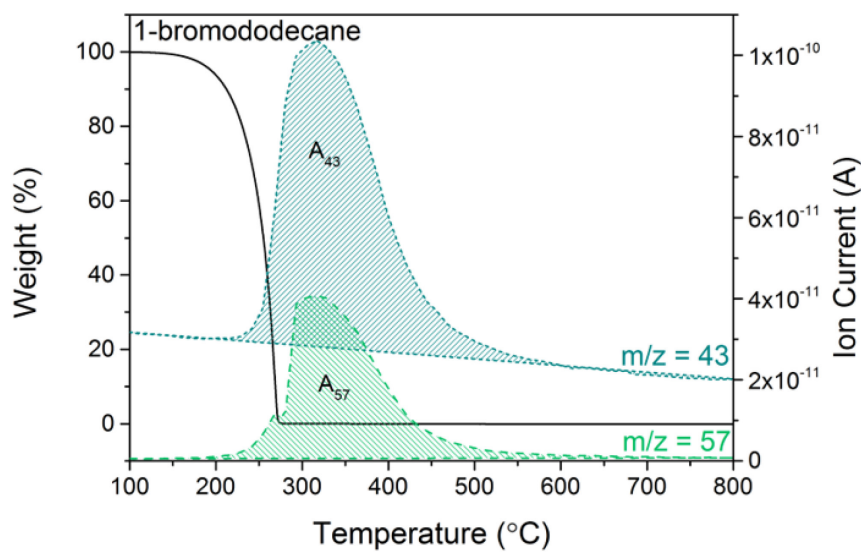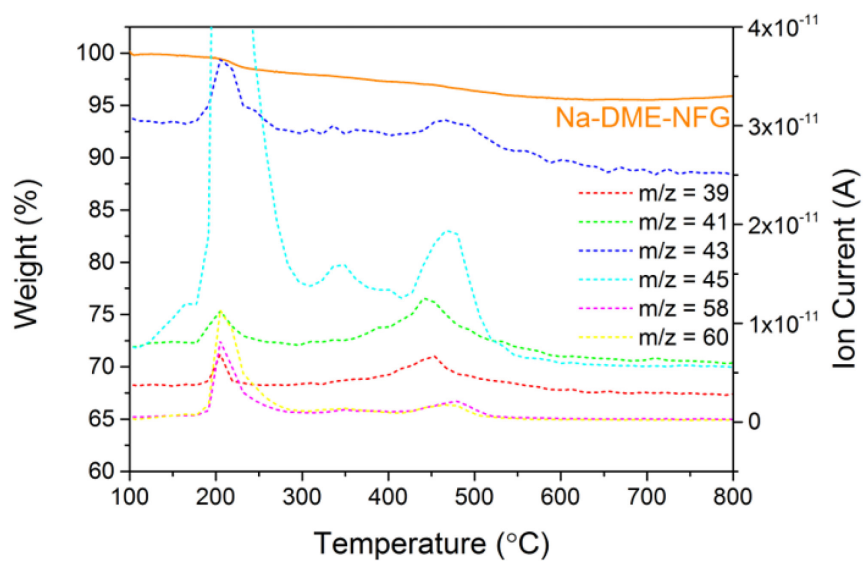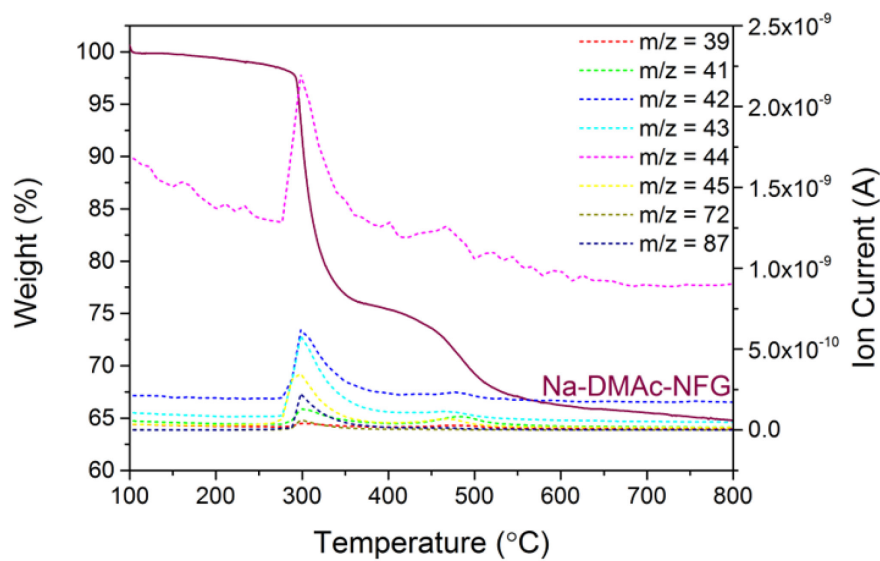

Figure I.5. TGA-MS of 1-bromododecane, and accompanying m/z fragments 43 ($C_3H_7^+$) and 57 ($C_4H_9^+$), used to calculate grafting ratio. These fragments appear in the relative ratio $A_{43}/A_{57} = 1.8$.

Figure I.6. TGA-MS profile of Na-DME-NFG, showing all *m/z* signals arising from DME.

Figure I.7. TGA-MS profile of Na-DMAc-NFG, showing all *m/z* signals arising from DMAc.
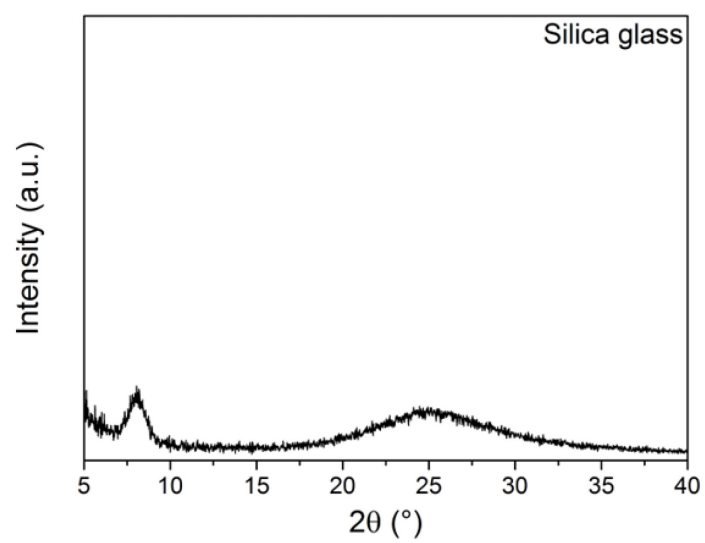
Figure I.8. XRD of blank silica glass showing peak at 8.1° and broad feature around 20-30°.

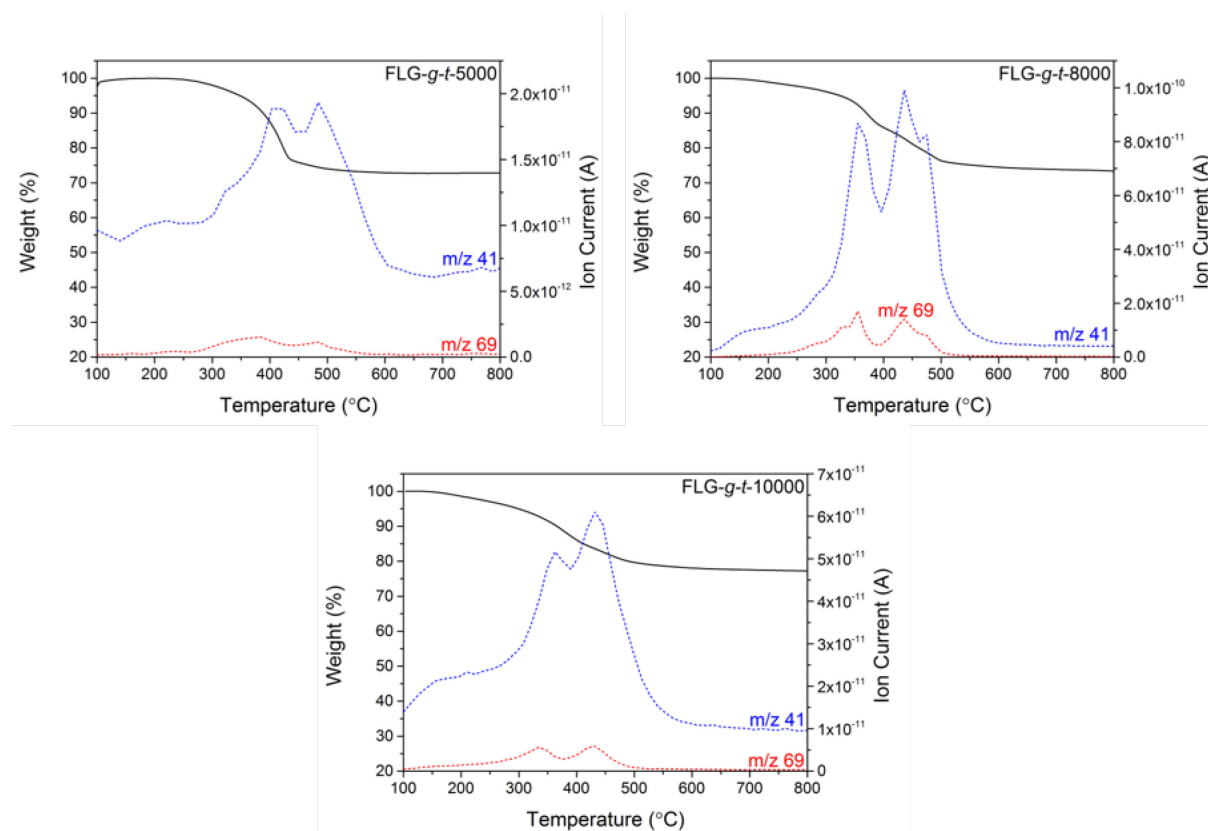# Appendix II

Supplementary figures for Chapter 6.

Figure II.1. TGA-MS profiles for grafting-to products with *m/z* fragments 41 (THF and PMMA) and 69 (PMMA).
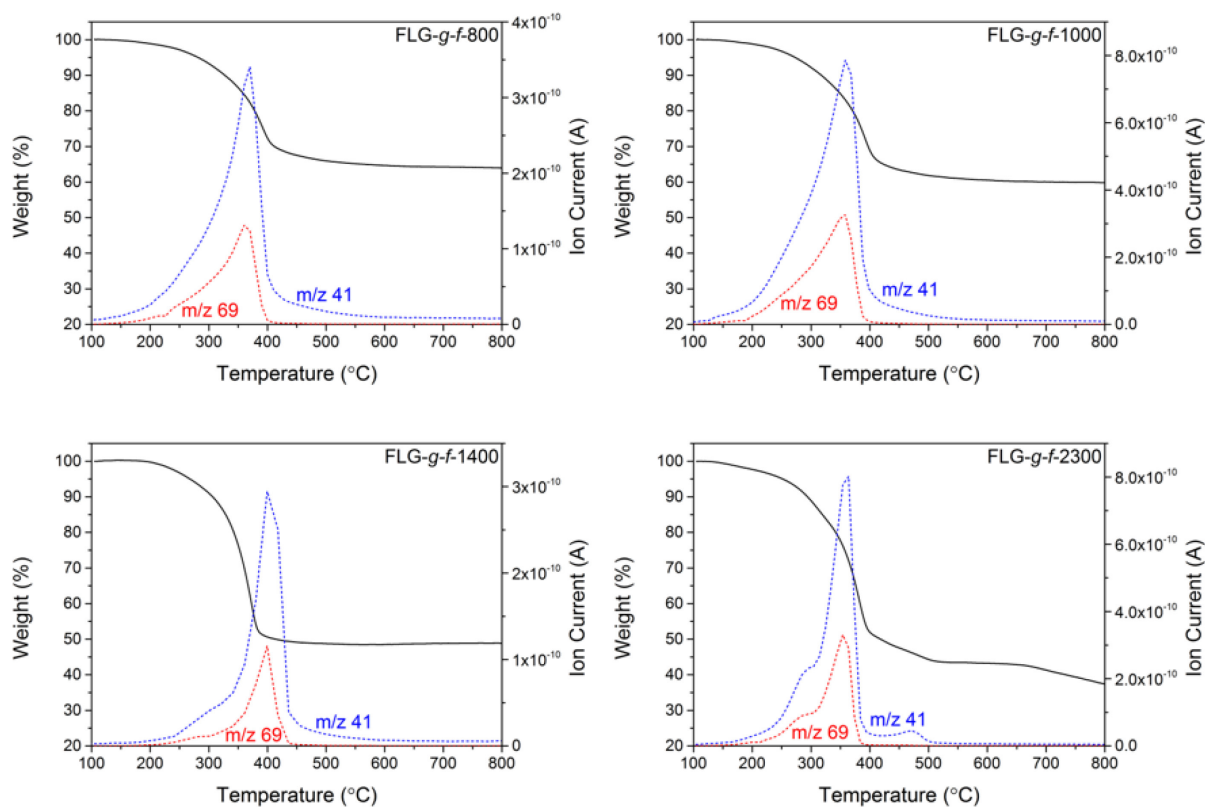
Figure II.2. TGA-MS profiles for grafting-from products with *m/z* fragments 41 (THF and PMMA) and 69 (PMMA).

Table II.1. Raman data for all PMMA-FLGs.

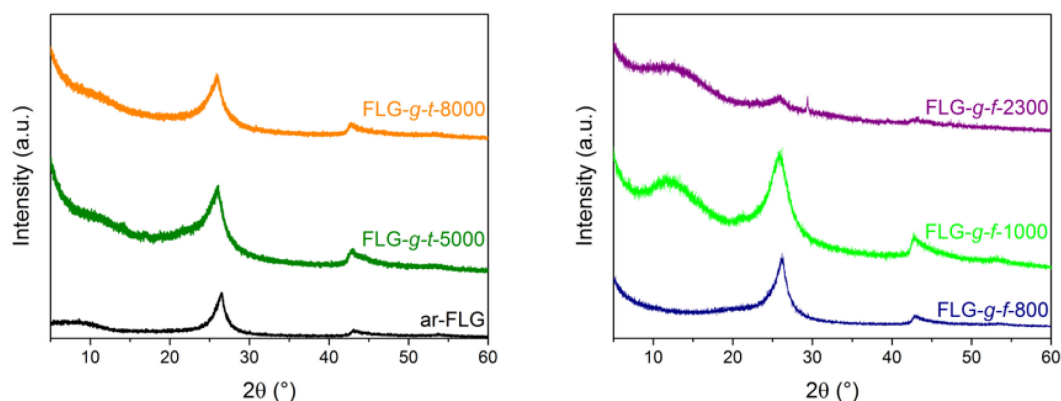| Sample	I_D/I_G	I_{2D}/I_G
ar-FLG	0.31±0.04	0.59±0.07
Na-THF-FLG	0.36±0.05	0.61±0.04
FLG-*g-t*-5000	0.41±0.02	0.65±0.07
FLG-*g-t*-8000	0.42±0.03	0.65±0.05
FLG-*g-t*-10000	0.41±0.02	0.67±0.04
FLG-*g-f*-800	0.49±0.03	0.65±0.07
FLG-*g-f*-1000	0.50±0.04	0.68±0.04
FLG-*g-f*-1400	0.52±0.02	0.69±0.05
FLG-*g-f*-2300	0.48±0.03	0.77±0.05

Figure II.3. XRD patterns of ar-FLG, and grafting-to and -from products.

Flory radius calculations and calculation derivations.

Calculation of surface concentration of PMMA:

The mass of PMMA in 1 g of sample is simply $\frac{wt\%_{PMMA}}{100}$. To convert to µmol, this value is multiplied by $\frac{10^6}{M_n PMMA}$; the surface concentration, moles per unit area (µmol m^{-2}), is therefore obtained by dividing the moles of PMMA by the specific surface area, S_{BET}:

$$C_{PMMA} = \frac{wt\%_{PMMA} \times 10^4}{M_n(PMMA) \times S_{BET}}$$

Calculation of polymer separation, D:

The surface area occupied by one polymer chain, a_{PMMA} (m^2), is calculated by dividing the area occupied by one mole of polymers, $\frac{10^6}{C_{PMMA}}$, by Avogadro's number, N_A:

$$a_{PMMA} = \frac{10^6}{C_{PMMA} \times N_A}$$

Assuming that polymer occludes a circular area on the graphene plane, the separation between polymers is twice the value of the radius of the circle with a_{PMMA}:

$$D\ (nm) = 2\sqrt{\frac{a_{PMMA}}{\pi}} \times 10^9 = \frac{2 \times 10^{12}}{\sqrt{\pi \times C_{PMMA} \times N_A}}$$
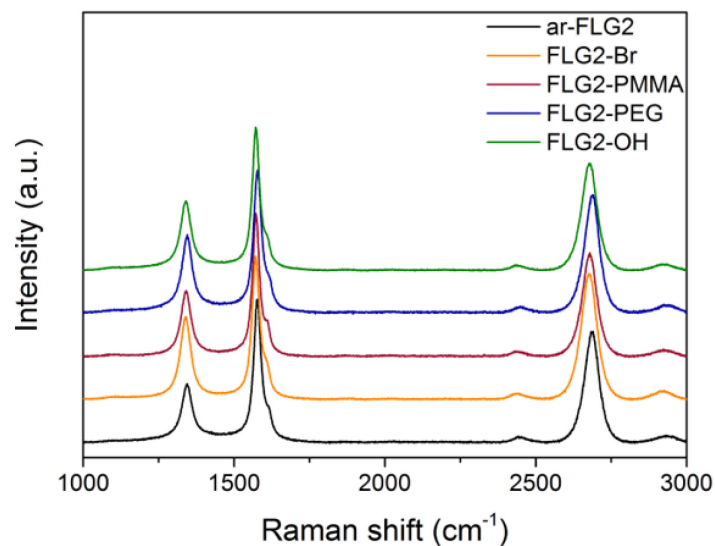
Appendix III

Figure III.1. Averaged Raman spectra of ar-FLG2, FLG2-Br, FLG2-PMMA, FLG2-PEG and FLG2-OH; point spectra normalised to the G peak intensity and offset for clarity. The D, G and 2D bands show narrow peaks with well-defined lineshapes.

Table III.1. Summary of Raman data* for functionalised FLGs.

	I_D/I_G	$I_D/I_{D'}$	I_{2D}/I_G	Γ_D (cm^{-1})	Γ_G (cm^{-1})	Γ_{2D} (cm^{-1})	2D peak position (cm^{-1})
ar-FLG2	0.40±0.03	3.0±0.6	0.97±0.04	53±6	32±2	58±1	2694.3±0.6
FLG2-Br	0.58±0.02	3.9±0.4	1.02±0.05	43±7	30±5	55±2	2694±2
FLG2-PMMA	0.53±0.03	4.0±0.6	1.06±0.05	43±4	29±1	53±1	2691.1±1.0
FLG2-PEG	0.56±0.03	3.9±0.6	1.02±0.04	43±4	30±1	55±2	2693.6±0.7
FLG2-OH	0.57±0.09	4.0±1.3	0.99±0.04	44±3	30±1	56±3	2693.8±0.6

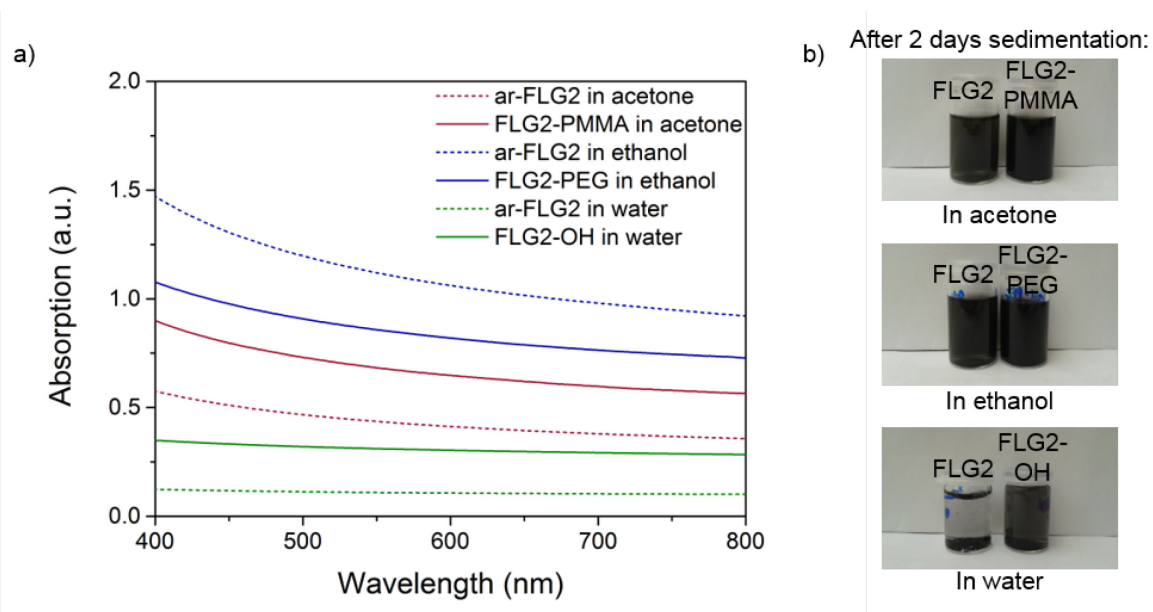*Mean values and standard deviation calculated from at least 500 spectra.

Figure III.2. a) UV-vis spectra of functionalised FLGs in acetone, ethanol and water. The samples were dispersed in different solvents by bath ultrasonication for 15 minutes and supernatants were taken after 2 days sedimentation. For measurement, FLG samples were diluted 2× and functionalised FLGs 8×; spectra values have been multiplied accordingly. b) Photographs of the supernatant solutions of functionalised FLGs. The extinction coefficient[52] for dispersed graphene in solution (ε_{660} = 2460 L g^{-1} m^{-1}) was used to estimate the concentrations of the different solutions.

Supplementary calculations for Chapter 7.

Determination of grafting data from TGA and XPS:

	Temperature range (°C)	%wt loss	End wt%*
ar-FLG2	100-800	3.6	96.4
FLG2-Br	200-450	8.4	89.5
FLG2-PMMA	200-550	16.2	83.0
FLG2-PEG	300-500	18.7	78.6
FLG2-OH	200-450	6.1	93.4

*Taken at the upper temperature of the range given in the table.

The grafting ratio (GR) is the mass fraction of grafted material, R, relative to the carbon framework, C, and can be deduced by taking the weight loss in the temperature range corresponding to the relevant m/z peaks, relative to the weight loss in as-received FLG, as the total amount of grafted material, ($wt\%_R$, assuming no residue after pyrolysis) and the residual weight as remaining FLG ($wt\%_C$):

$$\mathrm{GR} = \frac{wt\%_R}{wt\%_C} \times 100$$

The C/R ratio (the number of FLG carbons per grafted moiety) for FLG2-Br and FLG2-PEG is calculated from:

$$\mathrm{C/R} = \frac{MW_R}{wt\%_R} \times \frac{wt\%_C}{A_{rC}}$$

where MW_R and A_{rC} are the molecular weight of the grafted moiety and the atomic weight of carbon, respectively.

By XPS, C/Br for FLG2-Br may be straightforwardly determined from atomic composition data. The grafting ratio is obtained using:

$$\mathrm{GR} = \frac{A_{rBr}}{A_{rC}} \times \frac{1}{\mathrm{C/Br}} \times 100$$

Calculation of number density (TGA and XPS):

The area of the graphene lattice per grafted moiety, $area_R$ (nm^2), is given by:

$$area_R(nm^2) = \mathrm{C/R} \times area_C$$

Where $area_C$ is that occupied by one carbon in the lattice. Graphene's unit cell contains two carbon atoms and has an area of 0.0524 nm^2; therefore the area occupied by one carbon atom is 0.0262 nm^2.

The number density of grafting per cm^2, n_D, is obtained using the relation:

$$n_D \ (cm^{-2}) = \frac{10^{14}}{area_R}$$

Determination of PMMA molar mass and grafting ratio:

From the XPS data, approximately half (0.45) bromine addends serve as initiators, resulting in C/PMMA = 249 (using C/Br value obtained from XPS). The molar mass can then be deduced using:

$$MW_{PMMA} = \text{C/PMMA} \times A_{rC} \times \text{GR}/100$$

resulting in a value of 590 g mol^{-1}. Taking these proposed C/PMMA and M_n values of 249 and 590 g mol^{-1}, respectively, for each polymer (containing 29.5 C and 11.8 O) there are 249 C and 8.9 O in the FLG framework (O/C ratio obtained from FLG starting material). These values can be used to predict atomic composition by dividing the sum for each element by the total atomic mass.

	Actual	Predicted
at% C	92.6	92.7
at% O	6.9	6.8
at% Br	0.5	0.4

The atom percents for each element can then be multiplied by the relevant atomic weight to obtain relative masses, which can then be used to calculate grafting ratio:

$$\text{GR} = \frac{at\% \ C_{PMMA} \times A_{rC} + at\% \ O_{PMMA} \times A_{rO}}{at\% \ C_{FLG} \times A_{rC}} \times 100$$

	TGA	XPS
GR	19.5	21.4

Calculation of FLG2-PEG degree of substitution:

Degree of substitution can be calculated by:

$$degree \ of \ substitution = \frac{\text{C/PEG}}{\text{C/Br}}$$

where C/PEG is obtained from the TGA weight loss (disregarding bromine content) and has a value of 698.6.

For each PEG chain (containing 90 C and 45 O) there are 698.6 C and 25.7 O in the FLG framework. As before, these values are used to predict atomic composition and GR:

	Actual	Predicted
at% C	90.9	91.2
at% O	9.0	8.2
at% Br	0.1	0.6

	TGA	XPS
GR	23.8	26.2

Calculation of FLG-OH degree of substitution:

From XPS data, just over half (0.52) bromine addends were substituted by OH. The TGA weight loss for FLG2-Br is 8.366% so:

$$wt\%_{OH} = 0.52 \times wt\%_{Br} \times \frac{MW_{OH}}{A_{rBr}}$$

Resulting in a weight loss from OH addends of 0.93%. Summing the contributions from Br and OH and dividing by the new total (wt%OH + wt%Br + wt%C) results in a predicted TGA weight loss of 5.6% and a carbon weight of 94.4%, similar to actual values of 6.1% and 93.4%.

The C/OH ratio is 163 giving a GR of 3.8.

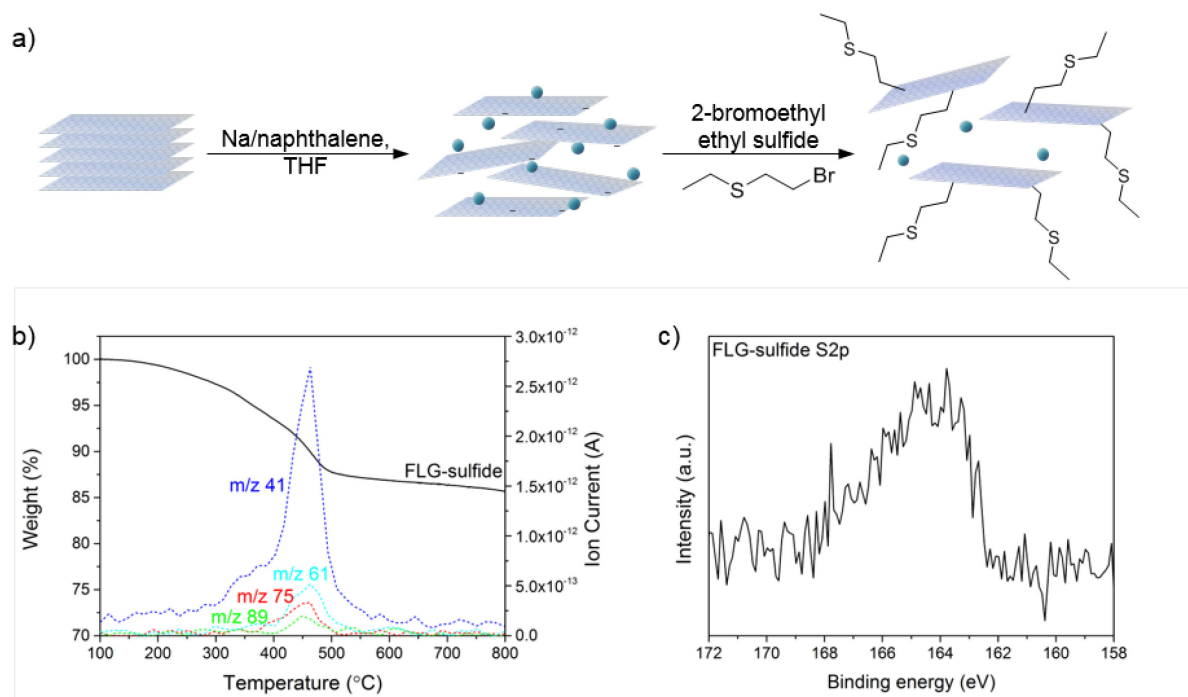# Appendix IV

Supplementary figures for Chapter 8.

Figure IV.1. a) Reaction of charged FLG with 2-bromoethyl ethyl sulfide; b) TGA-MS, and c) XPS S2p spectrum of FLG-sulfide.
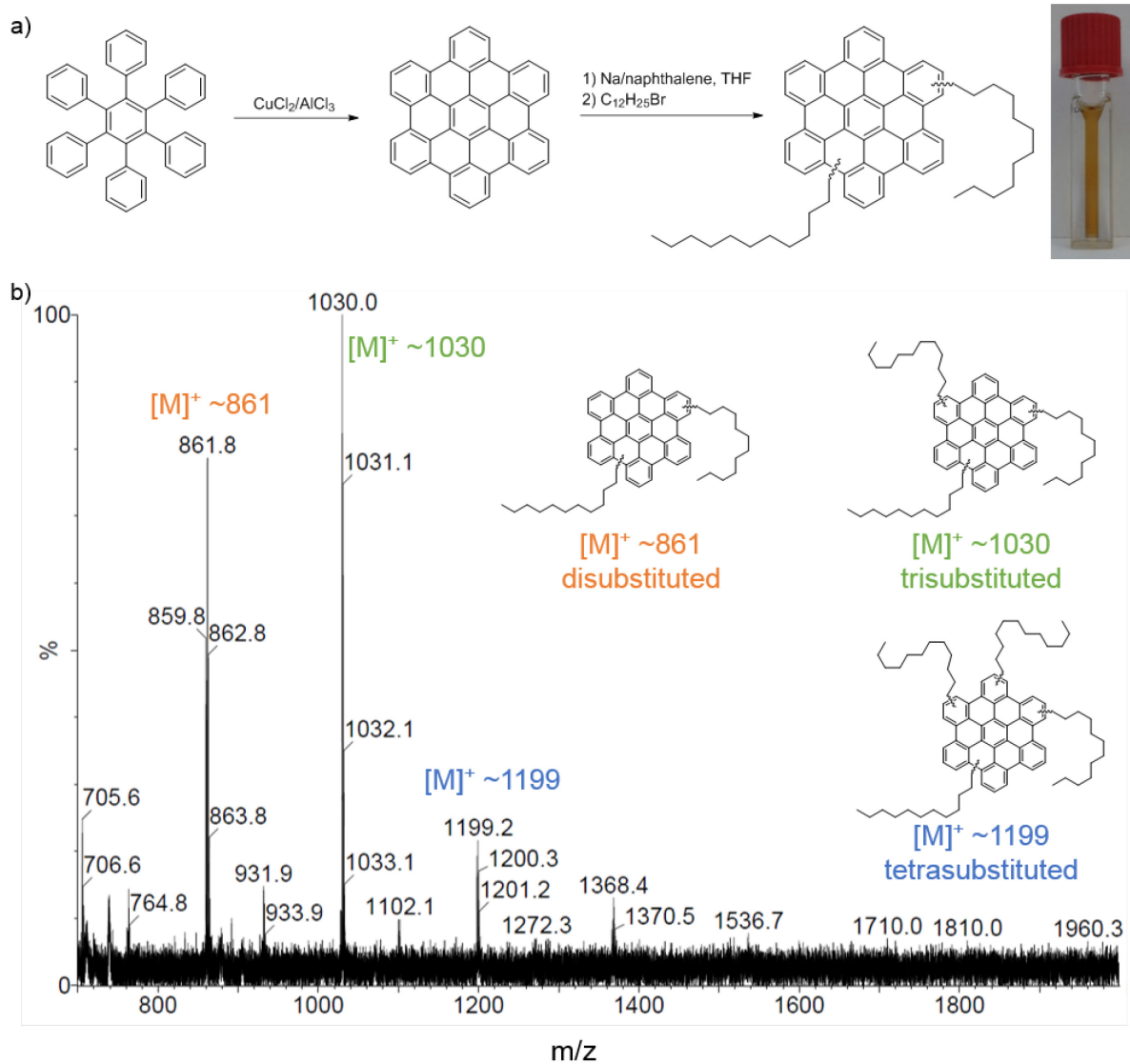
Figure IV.2. a) Synthesis of HBC and subsequent dodecyl functionalisation; b) MS characterisation of functionalised HBC.
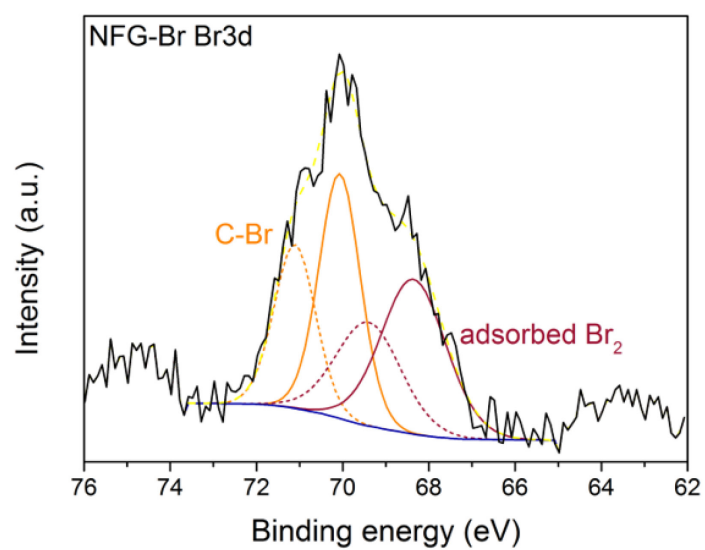
Figure IV.3. Core level Br3d XPS spectrum of NFG-Br showing covalently-bound and adsorbed bromine.

Acknowledgements

First and foremost, I would like to thank Milo Shaffer, for his invaluable supervision over the past four years. Without his ideas, knowledge and enthusiasm, this thesis would not have been possible.

To my fellow Graphene Girl, Noelia: thank you for always being kind and supportive, and brilliant to work with, a real rock. This project would not have been the same without you. To Hannah: I'm so glad you started in the Shaffer group at the same time as I did. You have been a fantastic colleague and a true and steadfast friend, from the very beginning of my PhD right up until the very last hour, and far beyond, I'm certain! Thank you to HH, for always being ready with a smile and kind words, and available for a cup of tea, in the flesh and on Skype. To Sandy, Cynthia, Martina: how lucky I've been to make and keep such a solid, caring, supportive and funny bunch of friends. Thanks also to Wonjun, for letting me smash at him in badminton – even if we are playing on the same team – to Adam, for having occasionally impeccable dress sense, Dave for his sometimes genius malapropisms, Hin Chun for always invading my personal space, Chris for all distractions bike-related, and to all the Shaffers present, past and honorary Hugo, Dave S, Rob M, Steve, Musty, Derrick, Ed, PJ, Takuya, Ismail, Buckley, Aaron, Francois, Rob W, James S, Eileen, Foivos, Jing, Jingjing, Jodie, Matt, Konzi, James F, Yoni, Alice, Andres, Seb, Martin, Nadir, Yulin, Jake, John, Maddy.

Thank you to my dearest Clareites, chemists and bosoms – always encouraging or ready with an amusing distraction. You've all been more support to me than you probably could know. To the Newlands crew, in particular, Sarah and Rosie: thank you for your many valiant attempts at understanding my convoluted explanations of this research, and of course for knowing how regularly to feed me – you're awesome.

Thank you to my wonderful brothers, who gave me a roof over my head when I was in need, fed me stupidly elaborate Nigella recipes, diverted me with un po' di musica, and let me watch endless re-runs of Friends and The Simpsons from their sofa.

Thank you to Tomi, for your endless support, care, and understanding; and most importantly, for showing me how to normalise histograms in Origin.

Finally, my biggest thanks are to my most excellent parents, who helped me to see it was not wholly impossible after all.